The role of excitation and inhibition in learning and memory formation

Victor Pedrosa

Thesis submitted for the degree of

Doctor of Philosophy

Bioengineering Department, Imperial College London

October 2019

I hereby declare that all work presented in this thesis was performed by me or was referenced otherwise.

Abstract

The neurons in the mammalian brain can be classified into two broad categories: excitatory and inhibitory neurons. The former has been historically associated to information processing whereas the latter has been linked to network homeostasis. More recently, inhibitory neurons have been related to several computational roles such as the gating of signal propagation, mediation of network competition, or learning. However, the ways by which excitation and inhibition can regulate learning have not been exhaustively explored. Here we explore several model systems to investigate the role of excitation and inhibition in learning and memory formation. Additionally, we investigate the effect that third factors such as neuromodulators and network state exert over this process. Firstly, we explore the effect of neuromodulators onto excitatory neurons and excitatory plasticity. Next, we investigate the plasticity rules governing excitatory connections while the neural network oscillates in a sleep-like cycle, shifting between Up and Down states. We observe that this plasticity rule depends on the state of the network. To study the role of inhibitory neurons in learning, we then investigate the mechanisms underlying place field emergence and consolidation. Our simulations suggest that dendrite-targeting interneurons play an important role in both promoting the emergence of new place fields and in ensuring place field

stabilization. Soma-targeting interneurons, on the other hand, are suggested to be related to quick, context-specific changes in the assignment of place and silent cells. We next investigate the mechanisms underlying the plasticity of synaptic connections from specific types of interneurons. Our experiments suggest that different types of interneurons undergo different synaptic plasticity rules. Using a computational model, we implement these plasticity rules in a simplified network. Our simulations indicate that the interaction between the different forms of plasticity account for the development of stable place fields across multiple environments. Moreover, these plasticity rules seems to be gated by the postsynaptic membrane voltage. Inspired by these findings, we propose a voltage-based inhibitory synaptic plasticity rule. As a consequence of this rule, the network activity is kept controlled by the imposition of a maximum pyramidal cell firing rate. Remarkably, this rule does not constrain the postsynaptic firing rate to a narrow range. Overall, through multiple stages of interactions between experiments and computational simulations, we investigate the effect of excitation and inhibition in learning. We propose mechanistic explanations for experimental data, and suggest possible functional implications of experimental findings. Finally, we proposed a voltage-based inhibitory synaptic plasticity model as a mechanism for flexible network homeostasis.

Acknowledgements

I would like to thank my supervisor Claudia Clopath for being an amazing supervisor and human being. I am immensely thankful for all the support and encouragement she gave me on hard days and all the cheering and excitement for each small accomplishment. She taught me not only almost everything I know about neuroscience, but how to support students and how to create an environment that feels welcoming to everyone in the group. I would also like to thank Andrei Kozlov and Tim Vogels for the invaluable feedback and constructive criticism on the thesis.

I would like to thank all my friends from the legendary Clopath lab for all the support, discussion, coffee breaks, and drinks over these years. I am also thankful for the Gabor wardening team and seniors, who became not just colleagues, but friends. Living in a hall of residence was/is an amazing experience and I would not be able to say the same without them.

Finally, I would like to thank my friends and family, both in the UK and in Brazil. I am especially grateful to Maria, my wife, for supporting me and believing in me throughout all these years. Going through the most difficult times of my life and creating some of the happiest memories as well. Without her, I would never be where I am.

Contents

Figures and Tables

Chapter 1

Chapter 2

Chapter 3

Chapter 4

Chapter 5

Chapter 6

Appendix

Chapter 1

Introduction

From learning to walk and to escape from predators to developing language and hunting strategies, animals have the remarkable capacity to learn and remember previous experiences. This ability to learn complex skills is intimately associated with the brains ability to adapt and change when exposed to different conditions. During the process of learning new skills, the connections between the neurons—the synapses—are thought to change in a process called synaptic plasticity. The final configuration of neurons and connections is thought to store the memory associated with the newly learned skill.

1.1 Receptive field formation and plasticity in young and adults

The same stimulus can trigger different responses for each neuron in the cortex. Indeed, each neuron can be associated to an area of the sensory space to which its response is more pronounced. In primary auditory cortex (A1), for example, a

neuron can be responsive to one sound frequency (pure tone) so that when this sound is presented to the animal, that neuron becomes active. In primary visual cortex (V1) a neuron can be associated with the direction of a bar presented to the animal. However, the activity of each neuron is not triggered by only one particular sound frequency or bar direction, instead its firing rate can be affected by a relatively large area of the sensory space. This area is called the receptive field of the neuron. A similar concept can also be applied to neurons in non-cortical regions. This concept is particularly important in the hippocampus, a brain region commonly associated with learning, memory formation, and spatial navigation. A subset of hippocampal pyramidal cells—named place cells—fire action potentials when the animal is in a specific location within the environment, the place fields [O'Keefe, 1976; O'Keefe and Dostrovsky, 1971; O'keefe and Nadel, 1978; Wilson and McNaughton, 1993].

Brain circuits are shaped by experience. These modifications can lead to the formation and refinement of receptive fields in cortical neurons and place fields in hippocampal neurons. In young animals, these receptive fields are extremely malleable [Dorrn et al., 2010], a characteristic that is associated to the extraordinary ability that young animals have to learn new skills. For young animals, the exposure to sensory stimulation by itself is enough to induce learning. Conversely, exposing adult animals to sensory stimulation is not sufficient to induce a change in receptive fields. At this stage, animals need something to communicate the importance of specific stimuli in order for any change in connectivity to be induced [Bakin and Weinberger, 1996; Bear and Singer, 1985; Chun et al., 2013; Drever, 2011; Froemke et al., 2007; Gu, 2002; Kilgard and Merzenich, 1998; Ma and Suga, 2005; Martins and Froemke, 2015; Shulz et al., 2000]. Neuromodulators are thought to be responsible for commu-

nicating the relevance of the behavioral context of sensory stimuli being presented to other brain regions [Gu, 2002; Shulz et al., 2000]. Nucleus Basalis and Locus Coeruleus, for example, are the main sources of acetylcholine and noradrenaline into the brain, respectively. These are two important neuromodulators for, amongst other things, cortical plasticity. They both have a disinhibitory effect on cortical networks, promoting the increase in cortical activity and later leading to learning.

1.2 Modelling neurons

In computational neuroscience, neurons are usually modelled as a set of differential equations and the complexity of these equations will depend on the level of detail required. In simulations in which the neuron spiking times are important but the details of the time course of action potentials is not necessary, integrate-and-fire neuron models [Gerstner and Kistler, 2002] are commonly used. In these models, the neuron's membrane voltage is described by one differential equation in which the neuron accumulates (integrates) the currents being injected into the neuron while a relaxation term pushes the membrane voltage back to its resting value. Once the membrane voltage reaches a fixed threshold, the neuron spikes an action potential and the membrane voltage is instantly reset to a lower value. In other words, the membrane voltage is determined by the equation

$$c_m \frac{dV}{dt} = -g_L(V - E_L) + \frac{I}{A} \quad ,$$

where c_m is the neuron's specific membrane capacitance, g_L is the leak conductance, E_L is the neuron's resting potential, I is the external current injected onto the neuron, and A is the total surface area of the neuron. This equation can be rewritten by

multiplying both sides by the neuron's specific membrane resistance $r_m = 1/g_L$, resulting in

$$\tau_m \frac{dV}{dt} = -(V - E_L) + R_m I \quad , \tag{1.1}$$

where $\tau_m = r_m c_m$ is the membrane time constant of the neuron and $R_m = r_m/A$ is the total membrane resistance. To simulate action potentials, the membrane voltage is reset to V_{reset} when the voltage crosses the threshold value V_{th}.

Neurons are connected to other neurons via synapses. These connections can be included in simulations of neural networks by introducing an extra term to equation 1.1

$$\tau_m \frac{dV}{dt} = -(V - E_L) - r_m g_s (V - E_s) + R_m I \quad ,$$

where g_s is the synaptic conductance and E_s is the synapse reversal potential. We can also include extra terms for different types of synapses, such as excitatory and inhibitory synapses. The synaptic conductance is increased every time the neuron receives a presynaptic action potential from neuron j such that $g_s \rightarrow g_s + \Delta g_s$, and decays exponentially otherwise with time constant τ_s. The increment in synaptic conductance is given by $\Delta g_s = \bar{g}_s w_j$, where $\bar{g}_s$ is a constant and w_j is the synaptic weight from presynaptic neuron j.

In simulation in which the evolution of the membrane voltage close to an action potential is important, the integrate-and-fire model described above is not adequate. In these cases, this model can be extended to a better approximation of real neurons. One example of such model is the adaptive-exponential integrate-and-fire neuron [Brette and Gerstner, 2005]. On the other hand, if the exact spike timing is not required but only the rate at which the neuron is spiking, the model described above

can be simplified to a rate-based model [Gerstner and Kistler, 2002]. Both of these models will be described in the following chapters.

1.3 Synaptic plasticity

The connections between neurons are not fixed. In fact, the change in receptive fields observed in both young and adult animals is due to a change in the strength of synaptic connections onto those neurons. The idea that changes in synaptic connections can be induced by targeted activation of individual neurons was first formulated by Hebb [Hebb, 1949]. In his now classic postulate, Hebb stated that when a neuron A repeatedly takes part in firing neuron B, the efficiency with which A fires B is increased [Hebb, 1949]. This postulate is usually summarized in the short version "neurons that fire together, wire together".

Several years later, the first spike-timing-dependent plasticity (STDP) model was proposed [Gerstner et al., 1996] and shortly after confirmed experimentally [Bi and Poo, 1998; Markram et al., 1997]. Synaptic connections following this STDP model are updated depending on the time window between pre- and postsynaptic spikes. More specifically, this rule states that presynaptic spikes preceding postsynaptic action potentials lead to potentiation, whereas depression is caused if the presynaptic neuron fires after the postsynaptic neuron (figure 1.1):

$$\Delta w^E = \begin{array}{l} + \textit{pre} \text{ before } \textit{post} \\ - \textit{post} \text{ before } \textit{pre} \end{array},$$

which in a rate-based version can be written as $\Delta w^E = pre \times post$ and thus recover Hebb's postulate. In a mathematical notation, the synaptic weight from presynaptic

neuron j to postsynaptic neuron i is updated following

$$\Delta w_{ij}(t) = \begin{cases} A_+ \exp(-t/\tau_+) & \text{if } t < 0 \\ A_- \exp(-t/\tau_-) & \text{if } t > 0 \end{cases} , \tag{1.2}$$

where $t = t_j^{(f)} - t_i^{(f)}$ is the difference between the postsynaptic and the presynaptic firing times, $A_+ > 0$ is the potentiation amplitude and $A_- < 0$ is the depression amplitude (see Methods for more detail). According to this rule, if the presynaptic action potential precedes the postsynaptic firing ($t < 0$) the synapse is potentiated, whereas the opposite ($t > 0$) leads to depression. This excitatory plasticity rule is known to be unstable as once a neuron induces another neuron to fire, the synaptic weight is increased and the neuron becomes more likely to induce the firing again, producing a positive feedback loop. Therefore, in order to prevent runaway activity, we need to impose other homeostatic mechanisms such as weight normalization or bounds.

This STDP rule — which we will name conventional STDP rule — can be modified by the action of neuromodulators. In chapter 2, we will explore the effect of several neuromodulators in cortical plasticity and will investigate the consequences of these effects on receptive field development. To do so, we will use 4 variations of this STDP rule in which the parameters A_+ and A_- will be determined by the presence of one or a few types of neuromodulators. Under these conditions, these parameters are not restricted to being positive or negative. Instead, their value and sign are determined by the influence of neuromodulators. This conventional STDP rule, although vastly used, does not capture the dependence of synaptic weight change on the frequency of stimulation during the plasticity induction protocol. To incorporate this dependency,

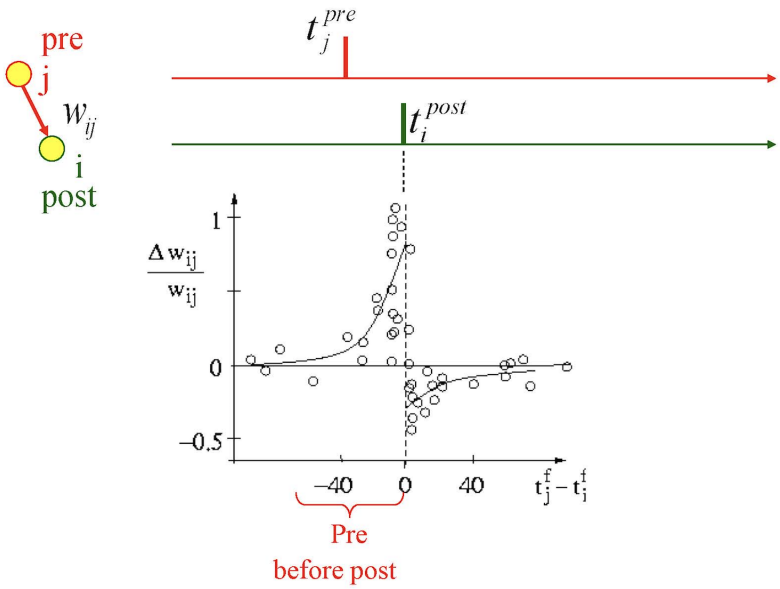

Figure 1. Excitatory STDP learning window. Relative change in excitatory synaptic weight as a function of the time window between pre- and postsynaptic spikes. Synaptic weights are potentiated for negative time windows (pre before post) and depressed in the opposite case (post before pre). This figure has been adapted from Sjöström et al. [2010].

we can implement a synaptic plasticity rule that depends on the interaction between triplets instead of pairs of spikes. The so-called triplet rule [Pfister and Gerstner, 2006] can be implemented by first defining two detectors for presynaptic events, r_1 and r_2, and two detectors for postsynaptic events, o_1 and o_2. These detectors are defined by the following set of equations:

$$\begin{aligned}
\frac{dr_1(t)}{dt} &= -\frac{r_1(t)}{\tau_+} && \text{and if } t = t^{pre} \text{ then } r_1 \rightarrow r_1 + 1, \\
\frac{dr_2(t)}{dt} &= -\frac{r_2(t)}{\tau_x} && \text{and if } t = t^{pre} \text{ then } r_2 \rightarrow r_2 + 1, \\
\frac{do_1(t)}{dt} &= -\frac{o_1(t)}{\tau_-} && \text{and if } t = t^{post} \text{ then } o_1 \rightarrow o_1 + 1, \\
\frac{do_2(t)}{dt} &= -\frac{o_2(t)}{\tau_y} && \text{and if } t = t^{post} \text{ then } o_2 \rightarrow o_2 + 1,
\end{aligned} \tag{1.3}$$

where τ_+ and τ_x are time constants for presynaptic events and τ_+ and τ_y are time constants for postsynaptic events. The change in the synaptic weight is then given by

$$\begin{aligned} w(t) &\rightarrow w(t) + o_1(t)\left[A_2^- + A_3^- r_2(t-\epsilon)\right] \qquad \text{if } t = t^{pre}, \\ w(t) &\rightarrow w(t) + r_1(t)\left[A_2^+ + A_3^+ o_2(t-\epsilon)\right] \qquad \text{if } t = t^{post}, \end{aligned} \tag{1.4}$$

where A_2^- and A_2^+ are the amplitudes of synaptic weight change for post-pre and pre-post events, respectively, and A_3^- and A_3^+ are the amplitudes of depression and potentiation, respectively.

Recent experimental observations have been inspiring new models of synaptic plasticity [González-Rueda et al., 2018]. In chapter 3, we propose a novel, phenomenological synaptic plasticity model. Based on observations from *in vivo* recordings of cortical neurons, we propose a synaptic plasticity model in which synaptic connections are depressed if presynaptic neurons fire alone but are unchanged if presynaptic action potentials are closely followed by postsynaptic spikes. We then investigate the functional implications of this new model of synaptic plasticity.

Finally, when using rate-based neuron models, we implement a synaptic plasticity rule that depends on the activity rate of pre- and postsynaptic neurons. In this form, the conventional STDP rule is rewritten as

$$\Delta w_{ij}(t) = \eta r_j r_i \quad ,$$

where η is the learning rate, w_{ij} is the synaptic weight from presynaptic neuron j to postsynaptic neuron i, r_j is the presynaptic activity rate, and r_i is the postsynaptic activity rate. Similarly to the spiking case, this synaptic plasticity rule is unstable

and requires further homeostatic mechanisms to control network activity. In our simulations, we include an extra homeostatic term that depends on the sum of all the incoming weights to a postsynaptic neuron such that the equation becomes

$$\Delta w_{ij}(t) = \eta r_j r_i - \xi \left(\sum_j w_{ij} - \theta \right) \quad ,$$

where xi is the homeostatic learning rate and θ is a target value for the sum of the weights. This plasticity rule can also be extended for multi-compartment models. In chapter 4, we consider only the postsynaptic dendritic activity to calculate the rate of change in synaptic weights. In chapter 5, we propose a novel form of excitatory plasticity in which the change in synaptic weight depends on the product of the dendritic and the somatic activity. this plasticity rule is inspired in recent experimental evidence suggesting that coincident dendritic regenerative events and somatic action potential can lead to a strong form of plasticity [Bittner et al., 2015, 2017].

1.4 Inhibitory synaptic plasticity

While excitatory plasticity has been widely studied over the past decades [Bienenstock et al., 1982; Clopath et al., 2010; Gerstner et al., 1996; Gjorgjieva et al., 2011], inhibitory plasticity is still lacking investigation. The most commonly used inhibitory synaptic plasticity model was introduced by Vogels et al. [Vogels et al., 2011]. Similarly to the standard excitatory synaptic plasticity model, this rule modulates inhibitory connections depending on the timing of pre- and postsynaptic spikes [Vogels et al., 2011]. Under this rule, inhibitory synaptic weights are potentiated for near-coincident pre- and postsynaptic spikes, independent of the order, and are

depressed for every presynaptic spike (figure 1.2):

$$\Delta w^I = \begin{array}{l} + \textit{ pre-post} \text{ or } \textit{post-pre} \\ - \textit{ pre} \end{array} ,$$

which in a rate-based version takes the form $\Delta w^I = pre \times (post - target)$. Therefore, the inhibitory weights will be modified unless either there is no presynaptic activity or the postsynaptic neuron is firing at the target firing rate (or both). In order to implement this rule, we define an inhibitory synaptic trace for every neuron x_i that is increased every time neuron i fires and decays exponentially otherwise, such that

$$\begin{array}{ll} x_i \rightarrow x_i + 1 & \text{if neuron } i \text{ fires and} \\ \tau_{inh} \frac{dx_i}{dt} = -x_i & \text{otherwise,} \end{array} \tag{1.5}$$

where τ_{inh} is the inhibitory plasticity time constant. The synaptic weight is then updated for every pre- or postsynaptic spike according to

$$w_{ij} \rightarrow w_{ij} + \eta_I (x_i - \alpha) \qquad \text{for a presynaptic spike and} \tag{1.6}$$

$$w_{ij} \rightarrow w_{ij} + \eta_I x_j \qquad \text{for a postsynaptic spike,} \tag{1.7}$$

where η_I is the inhibitory learning rate, $\alpha = 2 \times \rho_0 \times \tau_{inh}$ is a depression factor and ρ_0 is the target firing rate of the postsynaptic neuron. This learning rule results in a learning window defined by

$$\Delta W_{ij} = \eta_I \left[\exp\left(\frac{-|t_i^{(f)} - t_j^{(f)}|}{\tau_{inh}} \right) - \alpha \right] , \tag{1.8}$$

where $t_i^{(f)}$ denotes the postsynaptic firing time and $t_j^{(f)}$ denotes the presynaptic firing time.

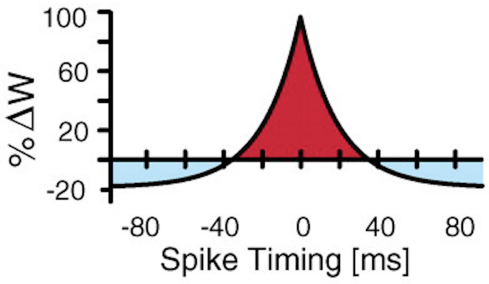

Figure 2. Inhibitory STDP learning window. Relative change in inhibitory synaptic weight as a function of the time window between pre- and postsynaptic spikes. Synaptic weights are potentiated for near-coincident pre- and postsynaptic spikes and depressed otherwise. This figure has been adapted from Vogels et al. [2011].

In chapter 6, we propose a new form of inhibitory synaptic plasticity which updates inhibitory synaptic weights as a function of presynaptic spiking time and postsynaptic membrane voltage. This plasticity rule acts as a homeostatic mechanism by forcing the postsynaptic membrane voltage to remain around a target value over a long time scale.

1.5 Aims

This thesis aims to investigate the role that excitation and inhibition play in learning. Furthermore, we explore how third factors such as neuromodulators can influence excitation and inhibition and thus shape learning.

In chapter 2, we review the effects of neuromodulators in neural networks and explore how those different effects can affect cortical plasticity. In particular, we explore the fact that neuromodulators can affect excitatory synaptic plasticity directly by

reshaping the excitatory learning window. Next, we explore another effect of neuromodulators in modulating neuronal activity. We then compare the neuromodulatory effects of upregulating the plasticity learning rate versus the effects of upregulating neuronal activity. We find that these seemingly similar mechanisms yield different outcomes: upregulating neuronal activity can lead to either a broadening or a sharpening of receptive field tuning, whereas upregulating learning rate only intensifies the sharpening of receptive field tuning.

In chapter 3, we present experimental data on a novel type of STDP observed in vivo and computational simulations investigating its functional implications. We observe that connections from L4 to L2/3 neurons in barrel cortex follow a network-state dependent plasticity. The network alternates between an Up and Down state, similarly to the cycles observed in mice during sleep. On Up states, presynaptic spikes lead to synaptic depression whereas pre- followed shortly by postsynaptic spikes prevents depression. We simulate a network imposing an excitatory plasticity rule based on our experimental findings. From our simulations, we conclude that this plasticity rule is a potential mechanism to refine representations.

In chapter 4, we investigate the role that different types of interneurons play in place field development and stabilization. Our simulations suggest that dendrite-targeting interneurons play a crucial role to place field development and consolidation whereas soma-targeting interneurons can quickly and transiently turn place cells into silent cells or the other way around.

In chapter 5, we present experimental data on interneuron-type-specific inhibitory plasticity and explore its functional consequences using computational simulations. We observe that connections from somatostatin-expressing interneurons exhibit pre-

dominantly long-term potentiation whereas connections from parvalbumin-expressing interneurons exhibit predominantly long-term depression. Using computational simulations, we suggest that this combination of plasticity rules leads to stable place field consolidation.

In chapter 6, inspired by the interneuron-type-specific inhibitory plasticity we presented in the previous chapter, we propose a voltage-based inhibitory synaptic plasticity model. We show that this model regulates network activity by setting a target value for the ratio between excitatory and inhibitory inputs onto the postsynaptic cell. Additionally, our voltage-based rule imposes a maximum postsynaptic firing rate without constricting it to a narrow range.

Overall, our goal is to combine experimental observations with computational modelling to understand how low scale observations affect network functionally. Ultimately, predictions from computational simulations can be fed back onto the design of new experiments to help to elucidate how the brain works.

Chapter 2

The role of neuromodulators in cortical plasticity. A computational perspective.

Neuromoculators are responsible for communicating behavioral context to other brain regions. In adult animals, they are essential for learning and adaptation. Neuromodulators are thought to regulate learning by gating synaptic plasticity, or by upregulating neuronal activity. Using a computational model, we investigate how these two mechanisms affect cortical plasticity. Firstly, we implement four different learning rules and demonstrate their effects on receptive field plasticity. Next, we compare the effects of increasing the plasticity learning rate versus the effects of upregulating neuronal activity. Although both mechanisms are similar, they lead to different outcomes. The increase in neuronal activity can lead to either the broadening or sharpening of the receptive field, depending on the neuron's initial excitatory input.

Contrastingly, the increase in learning rate leads to the sharpening of the neuron's place field independently of the level of excitatory inputs.

The layout of the work will be presented in an article format as it has been published on Frontiers in Synaptic Neuroscience. We would like to thank Claudia Clopath for supervising and guiding the work.

The role of neuromodulators in cortical plasticity. A computational perspective.

Abstract

Neuromodulators play a ubiquitous role across the brain in regulating plasticity. With recent advances in experimental techniques, it is possible to study the effects of diverse neuromodulatory states in specific brain regions. Neuromodulators are thought to impact plasticity through predominantly two mechanisms: the gating of plasticity, or the upregulation of neuronal activity. However, the consequences of these mechanisms are poorly understood and there is a need for both experimental and theoretical exploration. Here we illustrate how neuromodulatory state affects cortical plasticity through these two mechanisms. First, we explore the ability of neuromodulators to gate plasticity by reshaping the learning window for spike-timing-dependent plasticity. Using a simple computational model, we implement four different learning rules and demonstrate their effects on receptive field plasticity. We then compare the neuromodulatory effects of upregulating learning rate versus the effects of upregulating neuronal activity. We find that these seemingly similar mechanisms do not yield

the same outcome: upregulating neuronal activity can lead to either a broadening or a sharpening of receptive field tuning, whereas upregulating learning rate only intensifies the sharpening of receptive field tuning. This simple model demonstrates the need for further exploration of the rich landscape of neuromodulator-mediated plasticity. Future experiments, coupled with biologically detailed computational models, will elucidate the diversity of mechanisms by which neuromodulatory state regulates cortical plasticity.

Keywords:

neuromodulators; noradrenaline; acetylcholine; dopamine; synaptic plasticity; computational modeling;

2.1 Introduction

Cortical circuits are modified by experience. It is widely thought that such modifications enhance the representations of behaviorally important sensory stimuli, such as natural scenes for the visual cortex, or speech for the auditory cortex. These modifications can lead to the development or refinement of receptive fields in cortical neurons through synaptic plasticity. Across many species, the amount of cortical plasticity has been shown to depend on age. In juvenile mice, for example, tuning curves can shift from responding maximally to a preferred stimuli to responding maximally to a training stimulus (Dorrn et al. [2010]). This is not thought to require neuromodulation and, interestingly, is associated with a state of unbalanced excitation and inhibition. Conversely, experimental data from adults suggest that sensory stimulation is not sufficient to induce a change in receptive fields. Experiments in adult mice suggest that activation of neuromodulatory systems is also necessary for this change (Bakin and Weinberger [1996]; Bear and Singer [1985]; Chun et al. [2013]; Drever [2011]; Froemke et al. [2007]; Gu [2002]; Kilgard and Merzenich [1998]; Ma and Suga

[2005]; Martins and Froemke [2015]; Shulz et al. [2000]). In primary auditory cortex, Froemke et al. (Froemke et al. [2007]) observed that repeated exposure to a training sound frequency is not sufficient to evoke experience-dependent plasticity in adult rats. However, the tuning curve shifts to the training frequency if the stimulus is paired with cholinergic stimulation (from Nucleus Basalis). Interestingly, the stability of receptive fields is thought to be associated with the balance between excitation and inhibition, which is observed across many regions in the adult brain (Destexhe and Sejnowski [2003]; Froemke et al. [2013, 2007]; Graupner and Reyes [2013]; Haider et al. [2006]; Jia Xue [2014]; Okun and Lampl [2008]; Shu et al. [2003]; Wehr and Zador [2003]). Experiments indicate that some neuromodulators act to disrupt this balance (Froemke et al. [2013, 2007]; Letzkus et al. [2011]), enabling cortical plasticity. These neuromodulatory systems may be responsible for communicating the behavioral context of sensory stimuli to other brain regions (Gu [2002]; Shulz et al. [2000]).

Neuromodulators are observed to induce different effects in neural circuits. One main neuromodulatory effect is to gate plasticity by modifying the spike-timing-dependent plasticity (STDP) learning window (Bissière et al. [2003]; Caporale and Dan [2008]; Couey et al. [2007]; Lin et al. [2008]; Pawlak and Kerr [2008]; Pawlak et al. [2010]; Seol et al. [2007]; Shen et al. [2008]; Zhang et al. [2009]). For example, in lateral amygdala, activation of D2 dopamine receptors was shown to be necessary to induce long-term potentiation (LTP) (Bissière et al. [2003]). While in dorsal striatum, dopamine signaling via D1/D5 receptors is required for both long-term potentiation and long-term depression (LTD) (Pawlak and Kerr [2008]). In prefrontal cortex layer 5 pyramidal neurons, nicotine was shown to be able to reverse LTP into LTD (Couey et al. [2007]). In visual cortex, the combined action of acetylcholine and noradrenaline is necessary for standard STDP, whereas the action of noradrenaline alone was shown to reverse LTD into LTP, and acetylcholine alone allows only

LTD (Seol et al. [2007]). Therefore, depending on the brain region and, possibly, the stimulation protocol, neuromodulatory signaling can completely reshape STDP learning windows. Additionally, Dopamine has been shown to be important for reinforcement learning (Schultz [2002]). Unlike previous work on dopamine and reinforcement learning, we focus this perspective article on other less explored neuromodulatory effects in an unsupervised learning scheme.

Neuromodulators have also been shown to upregulate neuronal activity. For example, cholinergic stimulation is known to lower feedforward inhibition (Froemke et al. [2013, 2007]; Metherate et al. [1992]; Woody and Gruen [1987]; Xiang [1998]). Similarly, noradrenaline is known to trigger a disinhibitory effect (Kuo and Trussell [2011]). It has been shown that stimulation of Locus Coeruleus, the main source of noradrenaline, reduces tonic inhibition in auditory cortex (Martins and Froemke [2015]). These disinhibitory mechanisms are thought to be essential for adult cortical plasticity (Hensch [2005]; Kuhlman et al. [2013]; Letzkus et al. [2011]). Indeed, a computational study by Clopath et al. (Clopath et al. [2016]) demonstrated that a disinhibitory gate is required for adult cortical plasticity. These findings indicate that a disinhibited system promotes learning, consistent with recent experimental work (Kuhlman et al. [2013]; Letzkus et al. [2011]).

In this perspective article, we review the possible effects of neuromodulators by using a simple computational model of a plastic feedforward network. First, we hypothesize four different learning windows that would result from the action of different neuromodulators. Then we show the consequences of these rules on receptive field plasticity. We verify that an antisymmetric STDP rule allows for receptive field development, whereas a rule with more potentiation allows for a greater modification of sensory representation. This demonstrates the role of different neuromodulators in these situations. Finally, we compare the effect of upregulating the learning rate to the effect of upregulating activity and show that they are not necessarily equivalent.

Upregulating activity can lead to either a sharpening or a broadening of receptive field tuning. Upregulating the learning rate, however, only amplifies the existing structure.

2.2 Results

To illustrate the effect of neuromodulation on cortical plasticity, we use four possible STDP learning rules for excitatory synapses (fig **1**A). Each one of the STDP rules can be thought of as the action of a specific neuromodulatory state. The first rule is the standard antisymmetric STDP rule, in which a presynaptic spike preceding a postsynaptic action potential leads to potentiation of synaptic connections, whereas the reverse leads to depression. We refer to this rule as the Depression-Potentiation (DP) rule (fig **1**A, blue curve). Although widely observed in neocortical neurons of juvenile animals (Feldman [2000]; Markram et al. [1997]; Nevian and Sakmann [2006]; Sjöström et al. [2001]), the DP rule seems to be neuromodulator dependent in adults. This rule has been observed in visual cortex when both noradrenaline and acetylcholine are present (Seol et al. [2007]), whereas in dorsal striatum it can be observed under activation of D1/D5 (dopamine-specific) receptors (Pawlak and Kerr [2008]). The second rule is a symmetrical STDP rule, in which all pairs of pre- and postsynaptic spikes lead to potentiation, regardless of their order. As such, we refer to this as the Potentiation-Potentiation (PP) rule (fig **1**A, red curve). This rule can be observed in adult visual cortex under the activation of β-adrenergic (noradrenaline-specific) receptors (Seol et al. [2007]), and in hippocampal neurons under the effect of dopamine (Zhang et al. [2009]). For the third rule, only presynaptic spikes followed by postsynaptic action potentials elicit synaptic weight changes, leading to potentiation. Thus, we refer to this as the Unchanged-Potentiation (UP) rule (fig **1**A, green curve). This rule can be associated with dopaminergic action via D2 receptors in Lateral amygdala (Bissière et al. [2003]). Lastly, the fourth rule states that synaptic weights

are weakened every time a postsynaptic spike precedes presynaptic action potentials, and is unchanged otherwise and hence we refer to this as the Depression-Unchanged (DU) rule (fig **1**A, pink curve). This rule has been reported in prefrontal cortex under nicotinergic modulation (Couey et al. [2007]).

We simulate a feedforward network, in which a set of presynaptic input neurons project onto one postsynaptic neuron (fig **1**B). Input neurons fire with a time-varying firing rate with Poisson statistics. Neighboring input neurons have correlated activity, as for example neurons with similar frequency/orientation (sensory feature) preference in auditory/visual cortex (for more details, see methods and supplementary figure 1). Using this network, we illustrate the receptive field formation and adaptation under different learning rules, which are shaped by different neuromodulatory states.

Standard STDP leads to symmetry breaking

Hebbian learning rules, when associated with a competitive mechanism, are known to induce symmetry breaking of synaptic weights, i.e. some weights become strong and some weights become weak. However, it is well known that even without explicit competition, it is possible to induce symmetry breaking. This happens when the STDP rule is such that the depression component of the STDP learning window is larger than the potentiation component (i.e. the integral of the learning window is negative) (Song et al. [2000]). To illustrate the behavior of synaptic weights for the four different learning rules, we first simulate a network composed of 100 presynaptic neurons with all synaptic weights initially set at the same value. The DP rule can be modified to ensure that the amount of depression is slightly higher than the amount of potentiation (by increasing the amplitude of depression by 2%, as observed in several experiments (Bi and Poo [1998]; Feldman [2000])). We observe that, after some time, some of the weights get completely depressed whereas the remaining get completely potentiated, i.e. the weights go to their upper and lower bounds

(fig **1**C and D). This happens because inputs with strong connections can more easily induce a postsynaptic action potential. As a consequence, the spiking activities of strongly connected inputs are more correlated with the activity of the postsynaptic neuron, resulting in a further strengthening of weights. For those inputs with weak connections, there is almost no correlation between their activity and that of the postsynaptic neuron. These low correlations ensure the learning window is equally sampled so that the asymmetry of potentiation and depression results in depression of these weak synaptic weights. This effect was formally derived in several studies, e.g. Babadi and Abbott [2016]; Gilson et al. [2009]; Kempter et al. [1999]; Song et al. [2000]. For the remaining learning rules, synaptic weights are either all potentiated or all depressed (fig **1**E).

Taken together, the DP rule is the only one which allows for the emergence of receptive fields in this simple model. This rule can be associated with the combined action of noradrenaline and acetylcholine in visual cortex (Seol et al. [2007]). This model suggests that development of receptive fields in this region can be facilitated through the action of these neuromodulators. The first section of this perspective considered the neuromodulatory state for receptive field formation. Next, we will show that the neuromodulatory state for receptive field adaptation might be different.

The stronger the potentiation, the faster the receptive field plasticity

In order to demonstrate the effect of different neuromodulatory states on the stability of receptive fields, we first consider the case where all inputs have on average the same firing rate. We assume a network with 10 inputs in which the postsynaptic neuron is already tuned to a preferred stimulus, i.e. it has a stronger weight for input 7 than for other inputs. For the DP rule (standard STDP) we observe a small increase in all synaptic weights, even though the amounts of potentiation and depression are the same. Synaptic changes are larger for synapses that were initially stronger in these

simulations (fig **1**F, blue curve). The activity of presynaptic neurons increases the probability of postsynaptic action potentials. Therefore, events in which presynaptic neurons fire before the postsynaptic neuron (while close in time) are more likely to occur than the opposite, as shown previously (Gilson et al. [2009]; Kempter et al. [1999]; Song et al. [2000]). The PP rule, with the largest amount of potentiation, results in the largest change of receptive field (fig **1**F, red curve), whereas the UP rule generates an intermediate increase (fig **1**F, green curve). For the DU rule, we observe a small decrease of all synaptic weights (fig **1**F, pink curve). Therefore, we observe that the final receptive field remains tuned to the initial tuning frequency for all learning rules (fig **1**F).

It has been demonstrated that neuromodulation can facilitate plasticity in different systems (Bakin and Weinberger [1996]; Bear and Singer [1985]; Chun et al. [2013]; Froemke et al. [2007]; Gu [2002]; Martins and Froemke [2015]; Shulz et al. [2000]). In this section, we want to illustrate how different learning rules, mediated by different neuromodulatory states, affect receptive field plasticity. To do this, we over-represent one input (input 4), called the training input, by increasing the firing rate of one input neuron and its neighbors. This corresponds to stimulating one sensory feature excessively—e.g. by the repeated presentation of one tone (for auditory stimulus) or one orientation (for visual stimulus). We observe a shift in the receptive field towards the training input for learning the PP and UP rules (fig **1**G, red and green curves), which are potentiation-only rules. For the DP rule, we observe a small increase in the connection from the training input. After 40 s, the peak of the receptive field is still at the initially preferred input. As such, the receptive field did not shift to the training input (fig **1**G, blue curve). When applying the DU rule, the stronger activation of the training input leads to a stronger depression of the corresponding synapse (fig **1**G, pink curve). When we compare the strength of the synapse from the training input with the one from input 7 (the initially preferred input), we observe that the rules

with only potentiation lead to fast receptive field plasticity towards the new preferred stimulus. Since the weights are bounded, this shift in the preferred input is transient and the postsynaptic neuron is untuned at the end of the simulation (fig **1**H). The antisymmetric DP rule leads to a slower shift yet achieving, on average, the same value of input specificity as the PP and UP rules (figure **1**H). The DU rule forces all the weights to decrease until they reach the lower bound value. Therefore, the difference between the neuron's response to the training input and the initially preferred input slowly converges to zero (fig **1**H, pink curve). Not surprisingly, only rules with potentiation lead to a receptive field shift towards the training input. Additionally, rules with a larger amount of potentiation result in a faster receptive field shift.

In the model so far, there was no explicit competition mechanism between weights for any of the learning rules implemented until now. We now want to illustrate whether such a mechanism would facilitate or obstruct receptive field plasticity. To address this question, we use a normalization rule together with the STDP learning rules. Again, we first consider the case where all the inputs have on average the same firing rate. For rules DP, PP and UP, we observe a narrowing of the receptive field tuning, whereas rule DU leads to a flattening (fig **1**I). When one stimulus is stronger, the receptive field is shifted towards the strongest stimulus for rules DP, PP and UP, whereas rule DU results in a weakening of the connection associated with this stimulus until it reaches the lower bound (fig **1**J). This receptive field shift is slower than for the case without normalization but can lead to a strong receptive field tuned to the new stimulus (fig **1**K).

In summary, the learning rule with the largest amount of potentiation is more efficient for receptive field plasticity, both with and without normalization. This learning rule, rule PP, can be associated with the action of noradrenaline on visual cortex (Seol et al. [2007]). Therefore, our results suggest that noradrenaline is a good candidate for facilitating receptive field plasticity in this brain region.

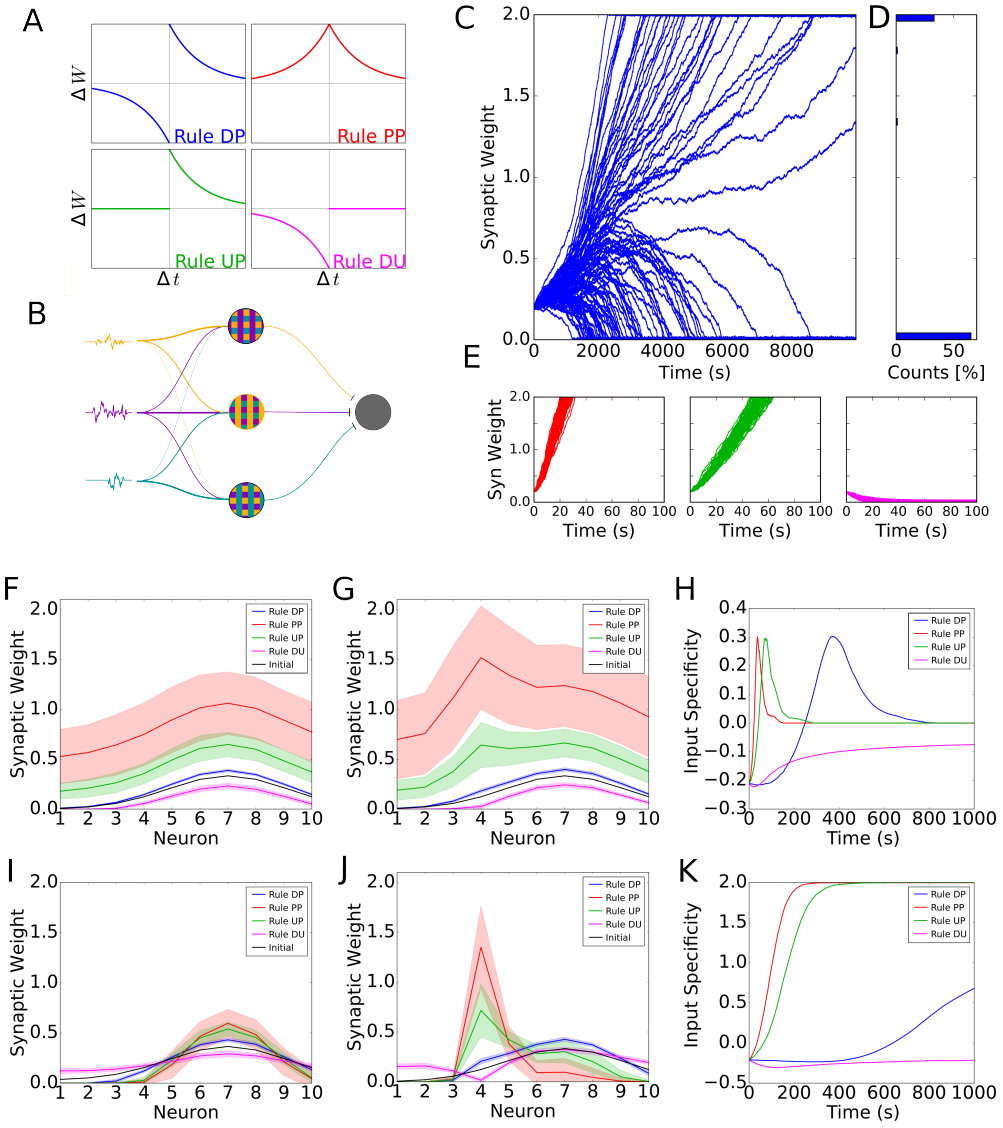

Figure 1: **Receptive field plasticity under the effect of neuromodulation.** **(A)** Diagram showing the four learning windows. Each learning window shows the change in synaptic strength (ΔW) as a function of the difference between the post- and presynaptic spike times $(\Delta t = t_{post} - t_{pre})$. Blue: rule DP (Depression-Potentiation); red: rule PP (Potentiation-Potentiation); green: rule UP (Unchanged-Potentiation); pink: rule DU (Depression-Unchanged). **(B)** Network diagram. Firing probabilities (signals, colored traces) are independently generated and each neuron's firing probability is determined by a weighted sum of these signals. Each signal can be understood as one specific sensory feature, such as one particular tone for auditory stimulation or one particular orientation for visual stimula-

tion. The input neurons project to one common postsynaptic neuron (gray circle). **(C)-(E)** Evolution of synaptic weights for the different learning rules. **(C)** Evolution of weights for a simulation with 100 presynaptic neurons projecting to one postsynaptic neuron. The excitatory weights follow the DP rule with the amplitude for depression slightly greater than the amplitude for potentiation. The small difference in amplitude is enough to generate bimodal distribution of weights. **(D)** Final distribution of weights in **C**. The synaptic weights are in the vertical axis and the counts of synaptic weights in each interval are in the horizontal axis. **(E)** First 10 seconds of the evolution of weights for plasticity rules PP, UP and DU (red, green and pink, respectively;). The weights quickly achieve the upper or lower bounds. **(F)-(K)** Simulation of a network with 10 presynaptic neurons. The excitatory connections follow the four STDP rules in **A**. **(F)** Final synaptic weights for each input neuron. All the inputs had the same intensity. **(G)** Final synaptic weights for each input neuron when stimulus 4 is 100% stronger than the other stimuli. **(H)** Difference between the synaptic weight from input neuron 4 (training input) and the weight from input neuron 7 (initial preferred input) as a function of time. We call this difference 'input specificity'. **(I)-(K)** Same as **F-H** but for a system in which the excitatory weights are also constrained by a normalization rule. In figures **F-K**, curves show the mean averaged over 100 trials and shaded areas represent one standard deviation from the mean.

Modulation of neuronal activity and learning rates have different effects in receptive field plasticity

Neuromodulation has been shown to affect many processes. Primarily, it has been shown to upregulate activity (e.g. by disinhibition—Froemke et al. [2007]; Martins and Froemke [2015]) or to gate plasticity (e.g. by changing the learning rule—Bissière et al. [2003]; Couey et al. [2007]; Pawlak and Kerr [2008]; Seol et al. [2007]). Intuitively, these two effects seem to be equivalent, since synaptic weight changes from Hebbian learning can be modeled as a product of the learning rate and neuronal activity. But is this really the case? Here we demonstrate in our simple computational model that upregulating either the learning rate or neuronal activity leads to different synaptic weight changes. To this end, we model a feedforward network with only one presynaptic and one postsynaptic neuron. The synaptic weights are updated according to learning rule DP (fig **1**A) with a learning rate amplitude α, and the presynaptic neuron fires with firing rate ν. We add an extra noise current to the

postsynaptic neuron in order to ensure postsynaptic firing at 10 Hz when the input neuron is kept silent.

First, we ask how plasticity depends on the synaptic weight, and whether the modulation of learning amplitude can alter this dependence (figures **2**A-C). We calculate the ratio between the synaptic weight change, Δw, and the synaptic weight, w, as a function of the weight. If the change is proportional to the weight, the ratio is constant. However, for small values of presynaptic activity, ν, strong weights increase relatively faster compared with weak weights, regardless of the value of the learning amplitude, α (fig **2**A). We observe that $\Delta w/w$ is proportional to the learning amplitude ($\Delta w/w = k\alpha$) and the proportionality constant, k, is higher for strong weights (fig **2**B). As such, strong weights change relatively faster than weak weights and the modulation of learning can only amplify or reduce this difference, but not reverse it.

Having shown how plasticity depends on the learning rate, we now ask if there is a similar dependence on neural activity (figures **2**D-F). We observe that, for large values of ν, the relative weight increase ($\Delta w/w$) does not increase with weight. Instead, small weights can grow faster than large weights for large enough values of ν (fig **2**C). For large weights, the modulation of neuronal activity has a similar effect to the modulation of learning rate. However, for weak weights, the modulation of neuronal activity can have a stronger effect (fig **2**D). Therefore, by controlling the activity of the presynaptic neuron, it is possible to shift from a scenario where strong weights learn faster to a scenario in which weak weights learn faster.

In summary, regulation of activity can lead to a scenario where weak weights learn relatively faster than strong weights. In other words, the regulation of activity can control whether the receptive field of a neuron is either sharpened of broadened. To demonstrate this, we simulate a feedforward network with 10 presynaptic neurons for two levels of presynaptic activity. For low activity, we observe a sharpening,

whereas high activity leads to a broadening of the receptive field (figure **2**F, supplementary figure 2). The upregulation of learning rate, on the other hand, can only amplify receptive field changes in our model. Therefore, for low firing rates, the regulation of learning rate will always lead to a sharpening of the receptive field tuning, regardless of the learning rate amplitude (figure **2**C, supplementary figure 2). These two modulation mechanisms act independently and do not disturb each other in our model (supplementary figure 2). The same behavior is observed when we use a more realistic, non-linear STDP model such as the triplet model (Pfister and Gerstner [2006]) (supplementary figure 3). Due to this large qualitative difference, more experiments are needed in order to identify how much, in which proportion, and when neuromodulation affects either learning, neural activity, or a combination of both.

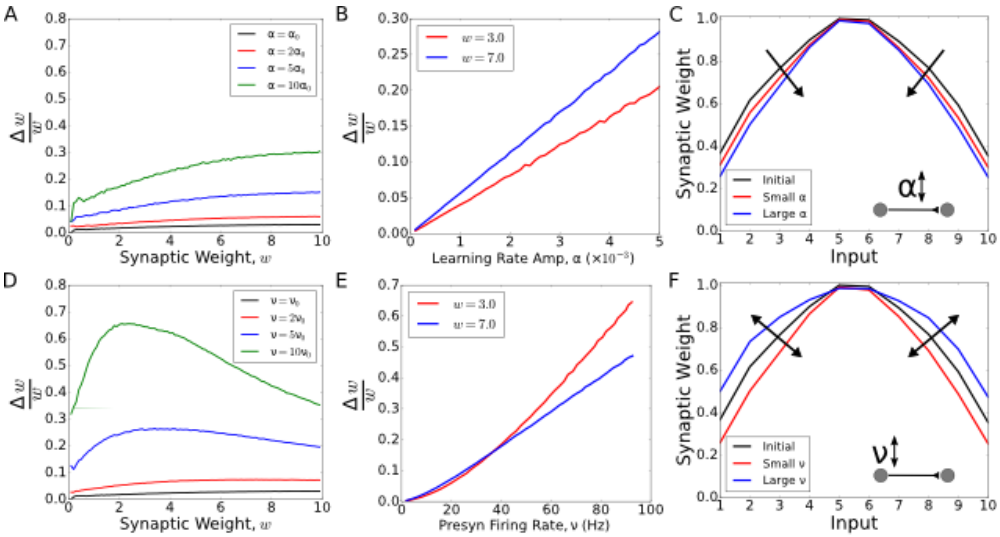

Figure 2: **Modulation of activity vs modulation of learning rate.** A network with one pre- and one postsynaptic neuron was simulated (in A, B, D and E). The synaptic weight changed following a standard STDP rule with amplitude α and the presynaptic neuron fired with firing rate ν. For synaptic weight $w = 0$, the postsynaptic neuron fired with firing rate $\sim$10 Hz. **(A)** Ratio between the synaptic change and the synaptic weight as a function of the weight for different values of α, with $\alpha_0 = 0.0005$ and presynaptic firing rate $\nu = 10$ Hz.

(B) Ratio between the synaptic change and the synaptic weight as a function of the amplitude of learning for $w = 3.0$ (red) and $w = 7.0$. In both cases, the presynaptic firing rate was set to $\nu = 10$ Hz. **(C)** Synaptic weights for a feedforward network with 10 presynaptic neurons and one postsynaptic neuron. The final synaptic weights were calculated for low presynaptic neuronal activity ($\nu = 1$ Hz) and two values of learning rate: $\alpha = 0.01$ (small α, red curve) and $\alpha = 0.02$ (large α, blue curve). The initial and final tuning curves were re-scaled by dividing all the tuning curves by their respective maximum weights. The increase in α always sharpens the receptive field tuning (for low presynaptic activity). **(D)** Ratio between the synaptic change and the synaptic weight as a function of the weight for different values of ν, with $\nu_0 = 10$ Hz and the amplitude of learning $\alpha = 0.0005$. **(E)** Ratio between the synaptic change and the synaptic weight as a function of the presynaptic neuronal firing rate for $w = 3.0$ (red) and $w = 7.0$. In both cases, the amplitude of learning was set to $\alpha = 0.0005$. In figures A, B, D and E, the curves are averages over 200 trials. In figures C and F, the curves are averages over 50 trials. **(F)** Synaptic weights for a feedforward network with 10 presynaptic neurons and one postsynaptic neuron. The final synaptic weights were calculated for learning rate $\alpha = 0.02$ and two values of presynaptic activity: $\nu = 1$ Hz (small ν, red curve) and $\nu = 10$ Hz (large ν, blue curve). The initial and final receptive fields were re-scaled by dividing all the tuning curves by their respective maximum weights. The modulation of neuronal activity, ν, can lead to either a sharpening or a flattening of receptive field tuning, depending on the value of ν.

2.3 Discussion

In this perspective article, we used four different learning rules, each associated with one or more neuromodulatory states, to illustrate how neuromodulation can affect receptive field plasticity. In order to explore the effects of different neuromodulatory states, we implemented these four learning rules in a feedforward network. As expected (Song et al. [2000]), we observed that receptive field development was only possible for one of these rules. This learning rule (DP) can be associated with the combined action of noradrenaline and acetylcholine in visual cortex, or the action of dopamine via D1/D5 receptors in dorsal striatum. It suggests that these neuromodulators can be important to the development of receptive fields in these brain regions, under the assumption that STDP is the dominant player in cortical plasticity. In our analysis, we also asked what would be the best rule to change a receptive field once it is formed. To this end, we combined each learning rule with

trained input. This simulates the association of a neuromodulatory state paired with a stimulus (e.g. a tone frequency, or an oriented bar). We observed that the rule with the largest amount of potentiation leads to faster receptive field plasticity. This rule can be associated with the action of noradrenaline on visual cortex, for example. This provides a mechanistic understanding of why noradrenaline can be important to receptive field plasticity in cortical areas, as seen in Martins and Froemke (Martins and Froemke [2015]).

Finally, we asked whether the modulation of presynaptic activity is equivalent to the modulation of plasticity. Our analysis suggests that the upregulation of learning rates can lead to faster learning. However, for low presynaptic activity, strong synaptic weights learn relatively faster than weak weights, regardless of the learning rate amplitude. Since strong weights become stronger, we see a sharpening of receptive field tuning. Upregulating activity, on the other hand, can lead to a scenario in which weak weights learn relatively faster than strong weights. This indicates that modulation of presynaptic activity could lead to a weakening of receptive fields by broadening their tuning.

In this perspective article, we illustrate some of the potential effects that neuromodulators can have in cortical plasticity. By assuming simple neuromodulator-meditated modifications of learning rules, we see interesting differences in the outcomes of receptive field development and adaptation. In all our simulations, we have only used pair-based spike-timing dependent plasticity rules (Abbott and Blum [1996]; Abbott and Nelson [2000]; Bi and Poo [1998]; Caporale and Dan [2008]; Gerstner et al. [1996, 1993]; Mehta et al. [2000]; Roberts [1999]; Sjöström et al. [2001]; Song et al. [2000]; Zhang et al. [1998]). This allowed us to explore a wide range of different possibilities within a frequently explored and well described framework. Some of the behaviors shown in this perspective article can also be explored analytically, using established techniques of plasticity in feedforward network (Babadi and Abbott

[2016]; Burkitt et al. [2007]; Câteau and Fukai [2003]; Gabriel Koch Ocker [2015]; Gilson et al. [2010, 2009]; Gjorgjieva et al. [2011]; Izhikevich and Desai [2003]; Kempter et al. [1999, 2001]; Rubin et al. [2001]; Song et al. [2000]; van Rossum et al. [2000]; Zhu et al. [2006]).

Experimental exploration of the effects of neuromodulation in cortical plasticity is a rapidly growing topic of interest. However, the precise effects of neuromodulators in neuronal networks remain unclear, and further experimental data is required. More biologically detailed rules can be explored as descriptions of the effect of neuromodulation on cortical plasticity come to light. Previous voltage-dependent or calcium-dependent models of synaptic plasticity may be modified in this regard (Clopath et al. [2010]; Graupner and Brunel [2012]; Pfister and Gerstner [2006]; Senn et al. [2001]; Shouval et al. [2002]). The effects of neuromodulators under these complex learning rules could be even vaster than for those studied in this perspective article. Moreover, we limited our perspective to a qualitative analysis. With more experimental data and more detailed models, it would be possible to extend this study to a quantitative description.

Synaptic connections in young animals are thought to be highly plastic and are associated with a state of unbalanced excitation and inhibition. In this case, neuromodulation might not be needed for plasticity. However, in adults, experiments indicate that neuromodulation is necessary to open a window of plasticity. We illustrate here that this can be done either by modulating the learning rule (by gating learning) or by modulating neuronal activity (e.g. by disinhibition—Clopath et al. [2016]). However, these two scenarios do not yield similar plasticity outcomes in our computational model. In the future, it would be interesting to have more experimental data on how behavior - mediated by neuromodulation - affects both the learning rule and neuronal activity. These insights can then be fed back to computational models to further understand their functional implications.

Bibliography

Abbott, L. F. and Blum, K. I. (1996). Functional significance of long-term potentiation for sequence learning and prediction. *Cerebral cortex (New York, N.Y. : 1991)*, 6(3):406–16.

Abbott, L. F. and Nelson, S. B. (2000). Synaptic plasticity: taming the beast. *Nature Neuroscience*, 3(Supp):1178–1183.

Babadi, B. and Abbott, L. F. (2016). Stability and Competition in Multi-spike Models of Spike-Timing Dependent Plasticity. *PLoS computational biology*, 12(3):e1004750.

Bakin, J. S. and Weinberger, N. M. (1996). Induction of a physiological memory in the cerebral cortex by stimulation of the nucleus basalis. *Proceedings of the National Academy of Sciences of the United States of America*, 93(20):11219–24.

Bear, M. F. and Singer, W. (1985). Modulation of visual cortical plasticity by acetylcholine and noradrenaline. *Nature*, 320(6058):172–176.

Bi, G. Q. and Poo, M. M. (1998). Synaptic modifications in cultured hippocampal neurons: dependence on spike timing, synaptic strength, and postsynaptic cell type. *The Journal of neuroscience : the official journal of the Society for Neuroscience*, 18(24):10464–10472.

Bissière, S., Humeau, Y., and Lüthi, A. (2003). Dopamine gates LTP induction in lateral amygdala by suppressing feedforward inhibition. *Nature neuroscience*, 6(6):587–592.

Burkitt, A. N., Gilson, M., and van Hemmen, J. L. (2007). Spike-timing-dependent plasticity for neurons with recurrent connections. *Biological cybernetics*, 96(5):533–46.

Caporale, N. and Dan, Y. (2008). Spike timing-dependent plasticity: a Hebbian learning rule. *Annual review of neuroscience*, 31:25–46.

Câteau, H. and Fukai, T. (2003). A stochastic method to predict the consequence of arbitrary forms of spike-timing-dependent plasticity. *Neural computation*, 15(3):597–620.

Chun, S., Bayazitov, I. T., Blundon, J. A., and Zakharenko, S. S. (2013). Thalamocortical long-term potentiation becomes gated after the early critical period in the auditory cortex. *The Journal of neuroscience : the official journal of the Society for Neuroscience*, 33(17):7345–57.

Clopath, C., Büsing, L., Vasilaki, E., and Gerstner, W. (2010). Connectivity reflects coding: a model of voltage-based STDP with homeostasis. *Nature Neuroscience*, 13(3):344–352.

Clopath, C., Vogels, T. P., Froemke, R. C., and Sprekeler, H. (2016). Receptive field formation by interacting excitatory and inhibitory synaptic plasticity. *bioRxiv*, (6):066589.

Couey, J. J., Meredith, R. M., Spijker, S., Poorthuis, R. B., Smit, A. B., Brussaard, A. B., and Mansvelder, H. D. (2007). Distributed Network Actions by Nicotine Increase the Threshold for Spike-Timing-Dependent Plasticity in Prefrontal Cortex. *Neuron*, 54(1):73–87.

Destexhe, A. and Sejnowski, T. J. (2003). Interactions between membrane conductances underlying thalamocortical slow-wave oscillations. *Physiological reviews*, 83(4):1401–53.

Dorrn, A. L., Yuan, K., Barker, A. J., Schreiner, C. E., and Froemke, R. C. (2010). Developmental sensory experience balances cortical excitation and inhibition. *Nature*, 465(7300):932–6.

Drever, B. D. (2011). The cholinergic system and hippocampal plasticity. *Behavioural Brain Research*, 221(2):505–514.

Feldman, D. E. (2000). Timing-Based LTP and LTD at Vertical Inputs to Layer II/III Pyramidal Cells in Rat Barrel Cortex. *Neuron*, 27(1):45–56.

Froemke, R. C., Carcea, I., Barker, A. J., Yuan, K., Seybold, B. A., Martins, A. R. O., Zaika, N., Bernstein, H., Wachs, M., Levis, P. A., Polley, D. B., Merzenich, M. M., and Schreiner, C. E. (2013). Long-term modification of cortical synapses improves sensory perception. *Nat Neurosci*, 16(1):79–88.

Froemke, R. C., Merzenich, M. M., and Schreiner, C. E. (2007). A synaptic memory trace for cortical receptive field plasticity. *Nature*, 450(7168):425–429.

Gabriel Koch Ocker, Ashok Litwin-Kumar, B. D. (2015). Self-Organization of Microcircuits in Networks of Spiking Neurons with Plastic Synapses. *PLOS Computational Biology*, 11:e1004458.

Gerstner, W., Kempter, R., van Hemmen, J. L., and Wagner, H. (1996). A neuronal learning rule for sub-millisecond temporal coding. *Nature*, 383(6595):76–78.

Gerstner, W., Ritz, R., and van Hemmen, J. L. (1993). Why spikes? Hebbian learning and retrieval of time-resolved excitation patterns. *Biological cybernetics*, 69(5-6):503–15.

Gilson, M., Burkitt, A., and van Hemmen, L. J. (2010). STDP in Recurrent Neuronal Networks. *Frontiers in computational neuroscience*, 4.

Gilson, M., Burkitt, A. N., Grayden, D. B., Thomas, D. A., and Van Hemmen, J. L. (2009). Emergence of network structure due to spike-timing-dependent plasticity in recurrent neuronal networks. II. Input selectivity-symmetry breaking. *Biological Cybernetics*, 101(2):103–114.

Gjorgjieva, J., Clopath, C., Audet, J., and Pfister, J.-P. (2011). A triplet spike-timing-dependent plasticity model generalizes the Bienenstock-Cooper-Munro rule to higher-order spatiotemporal correlations. *Proceedings of the National Academy of Sciences of the United States of America*, 108(48):19383–8.

Graupner, M. and Brunel, N. (2012). Calcium-based plasticity model explains sensitivity of synaptic changes to spike pattern, rate, and dendritic location. *Proceedings of the National Academy of Sciences of the United States of America*, 109(10):3991–6.

Graupner, M. and Reyes, A. D. (2013). Synaptic input correlations leading to membrane potential decorrelation of spontaneous activity in cortex. *The Journal of neuroscience : the official journal of the Society for Neuroscience*, 33(38):15075–85.

Gu, Q. (2002). Neuromodulatory transmitter systems in the cortex and their role in cortical plasticity. *Neuroscience*, 111(4):815–835.

Haider, B., Duque, A., Hasenstaub, A. R., and McCormick, D. A. (2006). Neocortical network activity in vivo is generated through a dynamic balance of excitation and inhibition. *The Journal of neuroscience : the official journal of the Society for Neuroscience*, 26(17):4535–45.

Hensch, T. K. (2005). Critical period plasticity in local cortical circuits. *Nature reviews. Neuroscience*, 6(11):877–88.

Izhikevich, E. M. and Desai, N. S. (2003). Relating STDP to BCM. *Neural computation*, 15(7):1511–23.

Jia Xue, Susanne V. Schmidt, J. S. A. D. W. K. I. Q. D. D. N. T. D. G. M. E. L. S. H. G. A. N.-C. M. R. M. L. L. H. T. M. K. M. B. E. L. T. C. F. T. U. J. L. S. (2014). Transcriptome-Based Network Analysis Reveals a Spectrum Model of Human Macrophage Activation. *Immunity*, 40:274–288.

Kempter, R., Gerstner, W., and Van Hemmen, J. (1999). Hebbian learning and spiking neurons. *Physical Review E*, 59(4):4498–4514.

Kempter, R., Gerstner, W., and van Hemmen, J. L. (2001). Intrinsic stabilization of output rates by spike-based Hebbian learning. *Neural computation*, 13(12):2709–41.

Kilgard, M. P. and Merzenich, M. M. (1998). Cortical Map Reorganization Enabled by Nucleus Basalis Activity. *Science*, 279(5357).

Kuhlman, S. J., Olivas, N. D., Tring, E., Ikrar, T., Xu, X., and Trachtenberg, J. T. (2013). A disinhibitory microcircuit initiates critical-period plasticity in the visual cortex. *Nature*, 501(7468):543–6.

Kuo, S. P. and Trussell, L. O. (2011). Spontaneous Spiking and Synaptic Depression Underlie Noradrenergic Control of Feed-Forward Inhibition. *Neuron*, 71(2):306–318.

Letzkus, J. J., Wolff, S. B. E., Meyer, E. M. M., Tovote, P., Courtin, J., Herry, C., and Lüthi, A. (2011). A disinhibitory microcircuit for associative fear learning in the auditory cortex. *Nature*, 480(7377):331–335.

Lin, Y.-W., Yang, H.-W., Min, M.-Y., and Chiu, T.-H. (2008). Inhibition of associative long-term depression by activation of β-adrenergic receptors in rat hippocampal CA1 synapses. *Journal of Biomedical Science*, 15(1):123–131.

Ma, X. and Suga, N. (2005). Long-term cortical plasticity evoked by electric stimulation and acetylcholine applied to the auditory cortex. *Proceedings of the National Academy of Sciences of the United States of America*, 102(26):9335–40.

Markram, H., Lubke, J., Frotscher, M., and Sakmann, B. (1997). Regulation of synaptic efficacy by coincidence of postsynaptic APs and EPSPs. *Science*, 275(5297):213–215.

Martins, A. R. O. and Froemke, R. C. (2015). Coordinated forms of noradrenergic plasticity in the locus coeruleus and primary auditory cortex. *Nature neuroscience*, 18(August):1–12.

Mehta, M. R., Quirk, M. C., and Wilson, M. A. (2000). Experience-Dependent Asymmetric Shape of Hippocampal Receptive Fields. *Neuron*, 25(3):707–715.

Metherate, R., Cox, C. L., and Ashe, J. H. (1992). Cellular bases of neocortical activation: modulation of neural oscillations by the nucleus basalis and endogenous acetylcholine. *The Journal of neuroscience : the official journal of the Society for Neuroscience*, 12(12):4701–11.

Nevian, T. and Sakmann, B. (2006). Spine Ca2+ Signaling in Spike-Timing-Dependent Plasticity. *Journal of Neuroscience*, 26(43):11001–11013.

Okun, M. and Lampl, I. (2008). Instantaneous correlation of excitation and inhibition during ongoing and sensory-evoked activities. *Nature Neuroscience*, 11(5):535–537.

Pawlak, V. and Kerr, J. N. D. (2008). Dopamine receptor activation is required for corticostriatal spike-timing-dependent plasticity. *Journal of Neuroscience*, 28(10):2435–2446.

Pawlak, V., Wickens, J. R., Kirkwood, A., and Kerr, J. N. D. (2010). Timing is not everything: Neuromodulation opens the STDP gate.

Pfister, J.-P. and Gerstner, W. (2006). Triplets of spikes in a model of spike timing-dependent plasticity. *The Journal of neuroscience : the official journal of the Society for Neuroscience*, 26(38):9673–82.

Roberts, P. D. (1999). Computational Consequences of Temporally Asymmetric Learning Rules: I. Differential Hebbian Learning. *Journal of Computational Neuroscience*, 7(3):235–246.

Rubin, J., Lee, D. D., and Sompolinsky, H. (2001). Equilibrium properties of temporally asymmetric Hebbian plasticity. *Physical review letters*, 86(2):364–7.

Schultz, W. (2002). Getting Formal with Dopamine and Reward. *Neuron*, 36(2):241–263.

Senn, W., Markram, H., and Tsodyks, M. (2001). An Algorithm for Modifying Neurotransmitter Release Probability Based on Pre- and Postsynaptic Spike Timing. *Neural Computation*, 13(1):35–67.

Seol, G. H., Ziburkus, J., Huang, S., Song, L., Kim, I. T., Takamiya, K., Huganir, R. L., Lee, H. K., and Kirkwood, A. (2007). Neuromodulators Control the Polarity of Spike-Timing-Dependent Synaptic Plasticity. *Neuron*, 55(6):919–929.

Shen, W., Flajolet, M., Greengard, P., and Surmeier, D. J. (2008). Dichotomous Dopaminergic Control of Striatal Synaptic Plasticity. *Science*, 321(5890).

Shouval, H. Z., Bear, M. F., and Cooper, L. N. (2002). A unified model of NMDA receptor-dependent bidirectional synaptic plasticity. *Proceedings of the National Academy of Sciences of the United States of America*, 99(16):10831–6.

Shu, Y., Hasenstaub, A., and McCormick, D. A. (2003). Turning on and off recurrent balanced cortical activity. *Nature*, 423(6937):288–293.

Shulz, D. E., Sosnik, R., Ego, V., Haidarliu, S., and Ahissar, E. (2000). A neuronal analogue of state-dependent learning. *Nature*, 403(6769):549–553.

Sjöström, P. J., Turrigiano, G. G., and Nelson, S. B. (2001). Rate, timing, and cooperativity jointly determine cortical synaptic plasticity. *Neuron*, 32(6):1149–1164.

Song, S., Miller, K. D., and Abbott, L. F. (2000). Competitive Hebbian learning through spike-timing-dependent synaptic plasticity. *Nature neuroscience*, 3(9):919–926.

van Rossum, M. C., Bi, G. Q., and Turrigiano, G. G. (2000). Stable Hebbian learning from spike timing-dependent plasticity. *The Journal of neuroscience : the official journal of the Society for Neuroscience*, 20(23):8812–21.

Wehr, M. and Zador, A. M. (2003). Balanced inhibition underlies tuning and sharpens spike timing in auditory cortex. *Nature*, 426(6965):442–446.

Woody, C. D. and Gruen, E. (1987). Acetylcholine reduces net outward currents measured in vivo with single electrode voltage clamp techniques in neurons of the motor cortex of cats.

Xiang, Z. (1998). Cholinergic Switching Within Neocortical Inhibitory Networks. *Science*, 281(5379):985–988.

Zhang, J.-C., Lau, P.-M., and Bi, G.-Q. (2009). Gain in sensitivity and loss in temporal contrast of STDP by dopaminergic modulation at hippocampal synapses. *Proceedings of the National Academy of Sciences of the United States of America*, 106(31):13028–33.

Zhang, L. I., Tao, H. W., Holt, C. E., Harris, W. a., and Poo, M.-m. (1998). and Competition Among Developing. *Metrologia*, 395(September):37–44.

Zhu, L., Lai, Y.-C., Hoppensteadt, F. C., and He, J. (2006). Cooperation of spike timing-dependent and heterosynaptic plasticities in neural networks: A Fokker-Planck approach. *Chaos: An Interdisciplinary Journal of Nonlinear Science*, 16(2):023105.

2.5 Methods

Neuron model

For all our simulations we use the leaky integrate-and-fire neuron model (Gerstner and Kistler [2002]; Stein [1967]). In this model, the membrane potential of a neuron is described by

$$\tau_m \frac{du}{dt} = -(u - u_{rest}) + RI(t) \,, \tag{2.1}$$

where u_{rest} denotes the membrane voltage at rest, R denotes the membrane resistance, $I(t)$ denotes the external current and τ_m denotes the membrane time constant. If the membrane potential reaches a threshold u_{th} at time $t^{(f)}$, the membrane potential is reset to u_{reset} and we call $t^{(f)}$ the firing time. After being reset, the membrane potential follows equation 2.1 again.

The term $I(t)$ takes into account all of the current being injected into a neuron; these can be from an external source (e.g. an electrode) or from other neurons. When a neuron fires, it propagates a current to all other connected neurons. In order to model this current, we assume that the conductance between a presynaptic neuron j and a postsynaptic neuron i increases instantaneously every time the presynaptic neuron fires, and decays exponentially otherwise:

$$g_j \to g_j + \bar{g}_E \qquad \text{if } j \text{ fires and} \tag{2.2}$$

$$\frac{dg_j}{dt} = -g_j/\tau_{syn} \qquad \text{otherwise,} \tag{2.3}$$

where τ_{syn} is the synaptic time constant and $\bar{g}_E$ is a constant. The synaptic current is then calculated through

$$I^{syn}(t) = -w_{ij} g_j (u - E^{syn}) \,, \tag{2.4}$$

where w_{ij} is the synaptic weight from neuron j to neuron i and E^{syn} is the synaptic reversal potential.

Input signals

Each stimulus is represented by a filtered gaussian noise, with a time constant of $\tau_{filt} = 50$ ms, from which we subtract a constant c, then rectify all negative values to zero and multiply by a constant ν_j (to control the mean), resulting in a function $s_j(t)$ (a signal, or stimulus). In summary,

$$s_j(t) = \nu_j[f_j(t) - c]_+ \,, \tag{2.5}$$

$$\tau_{filt}\frac{df_j(t)}{dt} = f_j(t) - \xi_j(t) \,, \tag{2.6}$$

where $\xi_j(t)$ is a Gaussian white noise. The constant c controls the lifetime sparseness of the signals (Franco et al. [2007]), controlling how well the postsynaptic neuron can differentiate between two presynaptic neurons. When all the stimuli are equally represented, $\nu_j = m$ for all j. When one of the stimuli is over-represented, the corresponding value of ν_j is increased.

We assume that all input neurons received contributions from all stimuli with different intensities. For each neuron, we associated a weighted sum of the stimuli, $p_i(t) = \sum_j T_{ij}s_j(t)$, where T_{ij} is a tuning strength defined from a Gaussian distribution: $T_{ij} \propto \exp\left(-(i-j)^2/2\sigma^2\right)$ and it is normalized such that $\sum_j T_{ij} = 1$. The parameter $\sigma = 1$ is the tuning width. The function $p_i(t)$ is then defined as the firing probability of input neuron i.

See diagram in supplementary figure 2.1.

Synaptic plasticity model (pair-based)

According to the STDP rule we use, the synaptic weight between a presynaptic neuron j and a postsynaptic neuron i evolves following (Gerstner and Kistler [2002]; Kistler and van Hemmen [2000])

$$\frac{d}{dt}w_{ij}(t) = A_- S_j(t) \int_0^\infty \mathrm{e}^{-s/\tau_-} S_i(t-s)ds + A_+ S_i(t) \int_0^\infty \mathrm{e}^{-s/\tau_+} S_j(t-s)ds \,, \tag{2.7}$$

where $S_j = \sum_f \delta\left(t - t_j^{(f)}\right)$ and $S_i = \sum_f \delta\left(t - t_i^{(f)}\right)$ are pre- and postsynaptic spike trains, respectively, A_- is the depression amplitude, A_+ is the potentiation amplitude, τ_- is the depression time constant and τ_+ is the potentiation time constant. This rule takes into account only pairs of pre-post or post-pre activity and therefore can be summarized by the effect of only one pair (known as a learning window),

$$\Delta w_{ij}(t) = \begin{cases} A_+ \exp(-t/\tau_+) & \text{if } t < 0 \\ A_- \exp(-t/\tau_-) & \text{if } t > 0 \end{cases}, \tag{2.8}$$

where $t = t_j^{(f)} - t_i^{(f)}$ is the difference between the postsynaptic and the presynaptic firing times. In order to implement this rule, we define a presynaptic trace $\bar{x}_j$ and a postsynaptic trace $\bar{y}_i$ that is incremented by 1 for each pre or postsynaptic spike, respectively, and decay otherwise following

$$\begin{aligned} &\bar{x}_j \to \bar{x}_j + 1 && \text{if presynaptic neuron } j \text{ fires and} \\ &\tau_+ \tfrac{d\bar{x}_j}{dt} = -\bar{x}_j && \text{otherwise,} \end{aligned} \tag{2.9}$$

and

$$\begin{aligned} &\bar{y}_i \to \bar{y}_i + 1 && \text{if postsynaptic neuron } i \text{ fires and} \\ &\tau_- \tfrac{d\bar{y}_i}{dt} = -\bar{y}_i && \text{otherwise.} \end{aligned} \tag{2.10}$$

The synaptic weight w_{ij} is then updated by the following:

$$\begin{aligned} w_{ij}(t) &\to w_{ij}(t) + A_{-}\bar{y}(t) \qquad \text{if } t = t^{pre}, \\ w_{ij}(t) &\to w_{ij}(t) + A_{+}\bar{x}(t) \qquad \text{if } t = t^{post}. \end{aligned} \tag{2.11}$$

Synaptic weights were also bounded between 0 and 2: $0 < w < 2$.

Synaptic plasticity model (triplet)

In supplementary figure 3, we use the triplet model (Pfister and Gerstner [2006]) to update the synaptic weights. We first consider two detectors of presynaptic events, r_1 and r_2, and two detectors of postsynaptic events, o_1 and o_2. These variables evolve according to the following:

$$\begin{aligned} \tfrac{dr_1(t)}{dt} &= -\tfrac{r_1(t)}{\tau_+} \qquad \text{and if } t = t^{pre} \text{ then } r_1 \to r_1 + 1, \\ \tfrac{dr_2(t)}{dt} &= -\tfrac{r_2(t)}{\tau_x} \qquad \text{and if } t = t^{pre} \text{ then } r_2 \to r_2 + 1, \\ \tfrac{do_1(t)}{dt} &= -\tfrac{o_1(t)}{\tau_-} \qquad \text{and if } t = t^{post} \text{ then } o_1 \to o_1 + 1, \\ \tfrac{do_2(t)}{dt} &= -\tfrac{o_2(t)}{\tau_y} \qquad \text{and if } t = t^{post} \text{ then } o_2 \to o_2 + 1, \end{aligned} \tag{2.12}$$

where τ_+ and τ_x are time constants for presynaptic events and τ_+ and τ_y are time constants for postsynaptic events. The change in the synaptic weight w_{ij} is then calculated through

$$\begin{aligned} w_{ij}(t) &\to w_{ij}(t) + o_1(t)\left[A_2^- + A_3^- r_2(t-\epsilon)\right] \qquad \text{if } t = t^{pre}, \\ w_{ij}(t) &\to w_{ij}(t) + r_1(t)\left[A_2^+ + A_3^+ o_2(t-\epsilon)\right] \qquad \text{if } t = t^{post}, \end{aligned} \tag{2.13}$$

where A_2^- and A_2^+ denote the amplitude of synaptic weight change for post-pre and pre-post events, respectively. A_3^- and A_3^+ denote the amplitude of depression and potentiation, respectively, for the triplet term.

Parameters and simulations

Figures 1C - 1E

Our feedforward network consisted of 100 presynaptic neurons and one postsynaptic neuron. All the weights were initialized to 0.2 and the network was run for 1000 s with a time step of 1 ms. All the numerical parameters can be seen in supplementary table 1. In figure 1C, rule 1 was modified by increasing the amplitude for depression by 2%.

Figures 1F - 1K

The feedforward network consisted of 10 presynaptic neurons and one postsynaptic neuron. The weights were initialized by assuming an initial receptive field tuned to input 7. All the curves are calculated from an average over 200 trials. The shading areas represent one standard deviation from the mean. For figures 1F and 1G, the network runs for 20 s. For figures 1I and 1J, the network runs for 80 s. All other numerical parameters can be found in supplementary table 1.

Figures 2A, 2B, 2D and 2E

The feedforward network consisted of one presynaptic neuron and one postsynaptic neuron. All the parameters used in these simulations can be found in supplementary table 2. Note that some of the values for the neuron model are different from the values used for figure 1. In particular, the membrane time constant and the increment in synaptic conductance for each presynaptic spike are lower. The faster membrane time constant leads to a faster relaxation and increased effect of presynaptic spikes whereas the lower increment in synaptic conductance decreases the effect of presynaptic spikes. Taken together, both modifications lead to a faster membrane voltage dynamics and a lower effect of presynaptic spikes. Whilst this aids with computational simulation time, it has no influence on the qualitative results discussed throughout this text. The

network was simulated for 100 s. For each value of the synaptic weight, w, the total change in synaptic weight was calculated as the sum of synaptic weight changes in each time step (1 ms). However, the changes were not applied to the weights to ensure that the calculated synaptic change was specific to each value of w. Therefore, the calculated value of Δw is the effective change in synaptic weight. The curves show an average over 200 trials.

Figure 2C

The feedforward network consisted of 10 presynaptic neurons and one postsynaptic neuron. All the parameters used in these simulations can be found in supplementary table 2. Weights were initialized assuming an initial receptive field tuned to inputs 5 and 6. The final receptive field was calculated for $\nu = 1$ Hz and two values of the learning rate: $\alpha = 0.02$ (large) and $\alpha = 0.01$ (small). The initial and final receptive fields were re-scaled by dividing all the tuning curves by their respective maximum weights. Curves show an average over 50 trials.

Figure 2F

The feedforward network consisted of 10 presynaptic neurons and one postsynaptic neuron. All the parameters used in these simulations can be found in supplementary table 2. Weights were initialized assuming an initial receptive field tuned to inputs 5 and 6. The final receptive field was calculated for $\alpha = 0.02$ Hz and two values of presynaptic activity: $\nu = 10$ Hz (large) and $\nu = 1$ Hz (small). The initial and final receptive fields were re-scaled by dividing all the tuning curves by their respective maximum weights. Curves show an average over 50 trials.

Supplementary figure 2

The feedforward network consisted of 10 presynaptic neurons and one postsynaptic neuron. All the parameters used in these simulations can be found in supplementary table 2. Weights were initialized assuming an initial receptive field tuned to inputs 5

and 6. The final receptive field was calculated for the following values of learning rate (α) and presynaptic activity (ν): $\alpha \downarrow = 0.01$, $\alpha \uparrow = 0.02$, $\nu \downarrow = 1$ Hz, $\nu \uparrow = 10$ Hz. The initial and final receptive fields were re-scaled by dividing all the tuning curves by their respective maximum weights. Curves show an average over 50 trials.

Supplementary figure 3A

The synaptic weights were updated following a triplet rule. The feedforward network consisted of 10 presynaptic neurons and one postsynaptic neuron. All the parameters used in these simulations can be found in supplementary table 2. Weights were initialized assuming an initial receptive field tuned to inputs 5 and 6. The final receptive field was calculated for $\nu = 1$ Hz and two values of the learning rate: $\alpha = 0.02$ (large) and $\alpha = 0.01$ (small). The initial and final receptive fields were re-scaled by dividing all the tuning curves by their respective maximum weights. Curves show an average over 50 trials.

Supplementary figure 3B

The synaptic weights were updated following a triplet rule. The feedforward network consisted of 10 presynaptic neurons and one postsynaptic neuron. All the parameters used in these simulations can be found in supplementary table 2. Weights were initialized assuming an initial receptive field tuned to inputs 5 and 6. The final receptive field was calculated for $\alpha = 0.02$ Hz and two values of presynaptic activity: $\nu = 5$ Hz (large) and $\nu = 1$ Hz (small). The initial and final receptive fields were re-scaled by dividing all the tuning curves by their respective maximum weights. Curves show an average over 50 trials.

2.6 Supplementary Tables and Figures

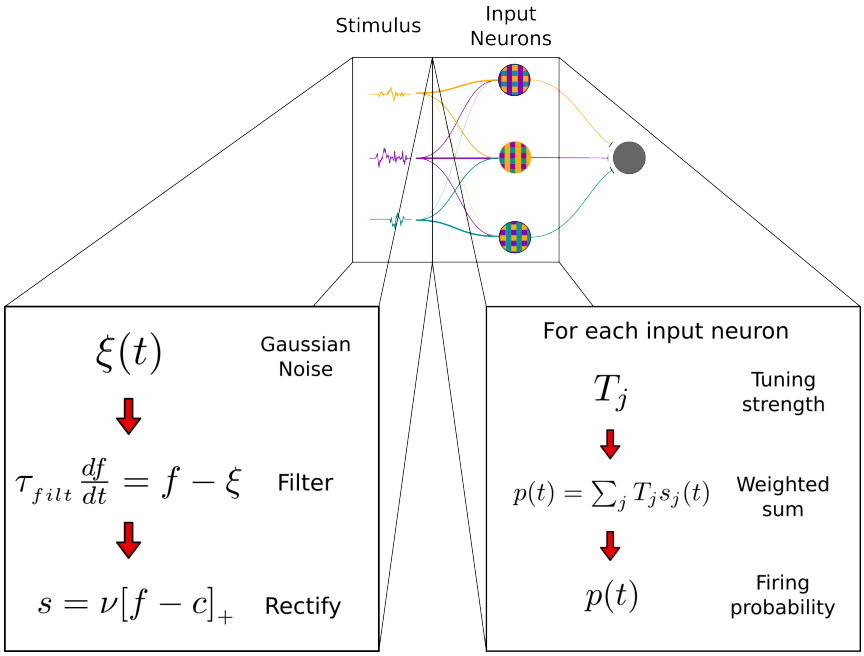

Supplementary Figure 1. Generation of presynaptic spike trains. The procedure used to generate the firing probability of each input neuron can be split into two steps: (i) generation of N independent rectified time-filtered Gaussian white noise (left box); (ii) weighted sum of the N signals generated in the first step (right box). The set of tuning strengths for each neuron is defined such that input neuron i is tuned to signal i.

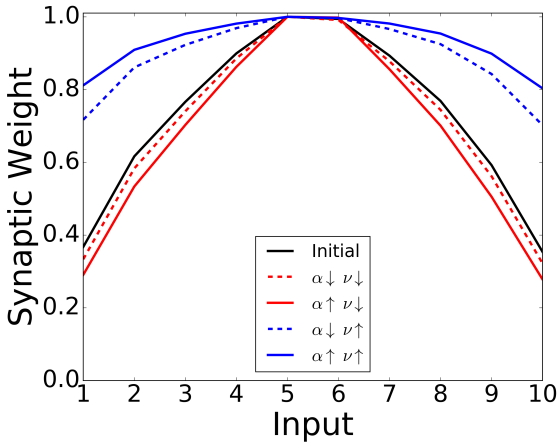

Supplementary Figure 2. Receptive field plasticity under neuronal activity and/or learning rate modulation. Synaptic weights for a feedforward network with 10 presynaptic neurons and one postsynaptic neuron. The final synaptic weights were calculated for the following values of learning rate (α) and presynaptic activity (ν): $\alpha \downarrow = 0.01$ (dashed lines), $\alpha \uparrow = 0.02$ (solid lines), $\nu \downarrow = 1$ Hz (red curves), $\nu \uparrow = 10$ Hz (blue curves). The initial and final receptive fields were rescaled by dividing all the tuning curves by their respective maximum weights. The effects of both types of modulations are independent.

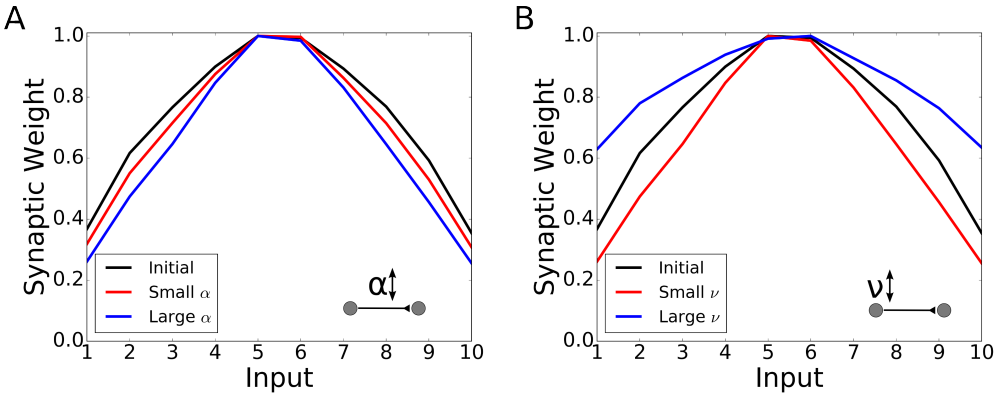

Supplementary Figure 3. Modulation of activity vs modulation of learning rate, using the triplet model (Pfister and Gerstner [2006]). Synaptic weights for a feedforward network with 10 presynaptic neurons and one postsynaptic neuron. The final synaptic weights were simulated for the following values of learning rate (α) and presynaptic activity (ν): **A** $\nu = 1$ Hz, small $\alpha = 0.01$ (red curve), large $\alpha = 0.02$ (blue curve); **B** $\alpha = 0.01$, small $\nu = 1$ Hz (red curve), large $\nu = 5$ Hz (blue curve). In all the figures, the initial and final receptive fields were rescaled by dividing all the tuning curves by their respective maximum weights. The results observed with the triplet model are qualitatively identical to the results observed with the standard pair-based STDP model.

Supplementary Table 1. Parameter summary for simulations in figure 1.

Neuron Model		
Name	**Value**	**Description**
τ_m	50 ms	Membrane time constant
u_{th}	10 mV	Spiking threshold
u_{rest}	0 mV	Resting potential
E^{syn}	30 mV	Synaptic reversal potential
u_{reset}	0 mV	Value at which the potential is reset after a spike

Network and Synapse Model		
Name	**Value**	**Description**
N_E (C-E)	100	Size of presynaptic population for figure 1C-E
N_E (F-K)	10	Size of presynaptic population for figure 1F-K
τ_E	15 ms	Decay constant of excitatory conductance
$\bar{g}_E$	1 nS	Maximum increment in synaptic conductance

Plasticity Model		
Name	**Value**	**Description**
τ_{STDP}	8 ms	Decay constant of pre- and post synaptic traces
A_+	$\gamma_+ 3 \times 10^{-4}$	Amplitude of learning rate for pre-post events
A_-	$\gamma_- 3 \times 10^{-4}$	Amplitude of learning rate for post-pre events
γ_+	1, 1, 1, 0	For rules 1, 2, 3 and 4, respectively
γ_-	-1, 1, 0, -1	For rules 1, 2, 3 and 4, respectively

Supplementary Table 2. Parameter summary for simulations in figure 2.

Neuron Model		
Name	**Value**	**Description**
τ_m	10 ms	Membrane time constant
u_{th}	10 mV	Spiking threshold
u_{rest}	0 mV	Resting potential
E^{syn}	30 mV	Synaptic reversal potential
u_{reset}	0 mV	Value at which the potential is reset after a spike

Network and Synapse Model		
Name	**Value**	**Description**
N_E	1	Size of presynaptic population for figure 2
N_E	10	Size of presynaptic population for figure 2
τ_E	10 ms	Decay constant of excitatory conductance
$\bar{g}_E$	0.1 nS	Maximum increment in synaptic conductance
ν	ν	Presynaptic firing rate ($\nu_0 = 10$ Hz)

Plasticity Model (pair-based)		
Name	**Value**	**Description**
τ_{STDP}	8 ms	Decay constant of pre- and post synaptic traces
A_+	$+\alpha$	Amplitude of learning rate for pre-post events ($\alpha_0 = 5 \times 10^{-4}$)
A_-	$-\alpha$	Amplitude of learning rate for post-pre events ($\alpha_0 = 5 \times 10^{-4}$)

Plasticity Model (triplet)		
Name	**Value**	**Description**
$\tau_{+/-}$	8 ms	Decay constant of pre- and post synaptic traces (r_1 and o_1)
$\tau_{x/y}$	10 ms	Decay constant of pre- and post synaptic traces (r_2 and o_2)
A_2^+	$+\alpha$	Amplitude of learning rate for pre-post events
A_2^-	$-\alpha$	Amplitude of learning rate for post-pre events
A_3^+	$+\alpha$	Amplitude of the triplet term for potentiation
A_3^-	$-\alpha$	Amplitude of the triplet term for depression

Bibliography

Franco, L., Rolls, E. T., Aggelopoulos, N. C., and Jerez, J. M. (2007). Neuronal selectivity, population sparseness, and ergodicity in the inferior temporal visual cortex. *Biological Cybernetics*, 96(6):547–560.

Gerstner, W. and Kistler, W. (2002). *Spiking Neuron models*. Cambridge University Press.

Kistler, W. M. and van Hemmen, J. L. (2000). Modeling synaptic plasticity in conjuction with the timing of pre- and postsynaptic action potentials. *Neural computation*, 12(2):385–405.

Pfister, J.-P. and Gerstner, W. (2006). Triplets of spikes in a model of spike timing-dependent plasticity. *The Journal of neuroscience : the official journal of the Society for Neuroscience*, 26(38):9673–82.

Stein, R. B. (1967). Some Models of Neuronal Variability. *Biophysical Journal*, 7(1):37–68.

Chapter 3

Activity-dependent downscaling of subthreshold synaptic inputs during slow wave sleep-like activity in vivo

Besides being regulated by neuromodulators, excitatory synaptic plasticity may also be regulated by network state. Here, we investigate the synaptic plasticity rules governing connections from L4 to L2/3 neurons in barrel cortex in vivo. We observed that those synapses follow a network-state dependent plasticity rule. In anaesthetised mice, the brain network alternates between Up and Down states, similarly to the cycles observed in mice during sleep. During Up states, isolated presynaptic spikes lead to synaptic depression whereas pre- followed shortly by postsynaptic spikes conserves synaptic weights. During Down states, synaptic weights follow the conventional spike-timing-dependent plasticity rule. Using computational modelling, we then simulate a network following a plasticity rule inspired by our experimental observations. Our

simulations suggest that this plasticity rule provides a potential mechanism for the refinement of sensory representations.

The layout of the work will be presented in an article format as it has been published on Neuron. We would like to thank Ana Gonzalez-Rueda, Rachael Feord and Ole Paulsen for the experimental results and insightful discussions and idea, and Claudia Clopath for supervising and guiding the project.

Activity-dependent downscaling of subthreshold synaptic inputs during slow wave sleep-like activity *in vivo*

SUMMARY

Activity-dependent synaptic plasticity is critical for cortical circuit refinement. The synaptic homeostasis hypothesis suggests that synaptic connections are strengthened during wake and downscaled during sleep; however, it is not obvious how the same plasticity rules could explain both outcomes. Using whole-cell recordings and optogenetic stimulation of presynaptic input in urethane-anesthetized mice, which exhibit slow-wave-sleep (SWS)-like activity, we show that synaptic plasticity rules are gated by cortical dynamics *in vivo*. Whilst Down states support conventional spike timing-dependent plasticity, Up states are biased towards depression such that presynaptic stimulation alone leads to synaptic depression, while connections contributing to postsynaptic spiking are protected against this synaptic weakening. We find that this novel activity-dependent and input-specific downscaling mechanism has two important computational advantages: 1) improved signal-to-noise ratio, and 2) preservation of stored information. Thus, these synaptic plasticity rules provide an attractive mechanism for SWS-related synaptic downscaling and circuit refinement.

INTRODUCTION

During development synaptic connections are formed, pruned and refined following synaptic plasticity rules, the most prominent candidate of which is Hebbian plasticity. Hebb postulated that synapse modifications occur when presynaptic activity leads to, or correlates with, postsynaptic action potentials (spikes; Hebb, 1949). Hebbian forms of plasticity, including spike-timing-dependent plasticity (STDP), have since been extensively studied *in vitro* (Bi and Poo, 1998; Feldman, 2000) and incorporated in many computational models of circuit refinement during development (Song and Abbott, 2001; Clopath et al., 2010a,b; van Ooyen, 2011). However, to what extent these rules apply in the intact mammalian brain is not known.

The synaptic homeostasis hypothesis (Tononi and Cirelli, 2003) proposes that, whereas sensory experience at wake leads to strengthening of the associated neocortical synapses, slow-wave sleep (SWS) leads to a net depression of synaptic weights (Vyazovskiy et al., 2008; Liu et al., 2010). While Hebbian plasticity, such as STDP, could explain the sensory-dependent strengthening of synapses and underlie the emergence of neuronal assemblies during wake, it is not obvious how the same synaptic plasticity rules could also explain synaptic weakening during sleep. Indeed, it is not known whether the SWS-related downscaling of synaptic weights is due to synapse-specific mechanisms or more global, neuron-wide downscaling of synaptic weights (Turrigiano et al., 1998).

During SWS cortical networks fluctuate at low frequency (<1 Hz) between periods of high activity, known as Up states, and more quiescent periods, known as Down states (Steriade et al., 1993). Up and Down states (UDS) are observed in single cells as subthreshold oscillations of up to 20 mV leading to occasional firing exclusively during Up states. In contrast, during awake attention and rapid eye movement

(REM) sleep the cortex is characterized by asynchronous and irregular activity. Thus, it is possible that one role of UDS during SWS is to modulate synaptic plasticity rules in order to promote the appropriate downscaling of synapses during sleep.

Here we compared synaptic plasticity rules during Up and Down states in the developing barrel cortex of urethane-anesthetized mice showing SWS-like dynamics (Contreras and Steriade, 1997). We studied layer (L)4-L2/3 connections at postnatal day (P)16-P21 corresponding to the end of the critical period of development of this synapse, when maximal circuit refinement and sparsification of inputs are seen (Stern et al., 2001; Itami and Kimura, 2012; van der Bourg et al., 2017). We discovered that plasticity rules are modulated by Up states: spike-timing-dependent potentiation (t-LTP) is absent and active synapses failing to contribute to postsynaptic spiking are selectively depressed. We show in a computational model that this synaptic downscaling mechanism promotes the elimination of weak and preservation of strong synapses, thus enhancing signal-to-noise ratio (S/N).

RESULTS

Study of synaptic plasticity *in vivo*

STDP-like synaptic changes *in vivo* have been previously described using sensory-evoked postsynaptic responses (Meliza and Dan, 2006; Jacob et al., 2007; Gambino and Holtmaat, 2012; Pawlak et al., 2013). While such studies are important to understand sensory coding, the specific inputs involved in each trial are unknown. To study synapse-specific plasticity *in vivo*, we used an LED for optogenetic activation of presynaptic afferents during whole-cell recording of L2/3 regular

spiking neurons (**Figure 1A and S1**) in the barrel cortex of Six3-cre/Ai32 urethane-anesthetized mice expressing channelrhodopsin-2 (ChR2) selectively in L4 neurons (**Figure 1B**). The resting membrane potential of every L2/3 neuron recorded presented low frequency (0.7 ± 0.06 Hz, n = 92) fluctuations between Up and Down states (-55 mV *vs.* -69 mV, **Figure 1C**). Occasional REM-like activity was observed, characterized as long-lasting activated states (>5 seconds) (**Figure S2**). Firing of L2/3 neurons was sparse (0.25 Hz *vs* 1.06 Hz in L4, **Figure S2**) and restricted to activated states, with only few highly active neurons (7 out of 92; **Figure 1C**; de Kock and Sakmann, 2009). Excitatory postsynaptic potentials (EPSPs) were recorded in postsynaptic L2/3 neurons following light-stimulation of L4 fibers. To monitor EPSPs, we stimulated L4 at 0.1 Hz only during Down states using a closed-loop circuit to prevent stimulation during activated states (**Figure 1C, 1D and 1E**). To assess synaptic plasticity, a pairing protocol (100 repetitions at <0.2 Hz) was applied following a 10-minute stable baseline. At the end of the plasticity protocol, the Down state stimulation was resumed for a further 20 to 30 minutes (**Figure 1F**). Continued low-frequency light-stimulation of L4 input during Down states over 50 minutes did not produce any significant change in synaptic weight (98 ± 6%, n = 13, one sample Student's *t*-test p = 0.77, **Figure 2A-D**), allowing us to use this method to study synaptic plasticity *in vivo*.

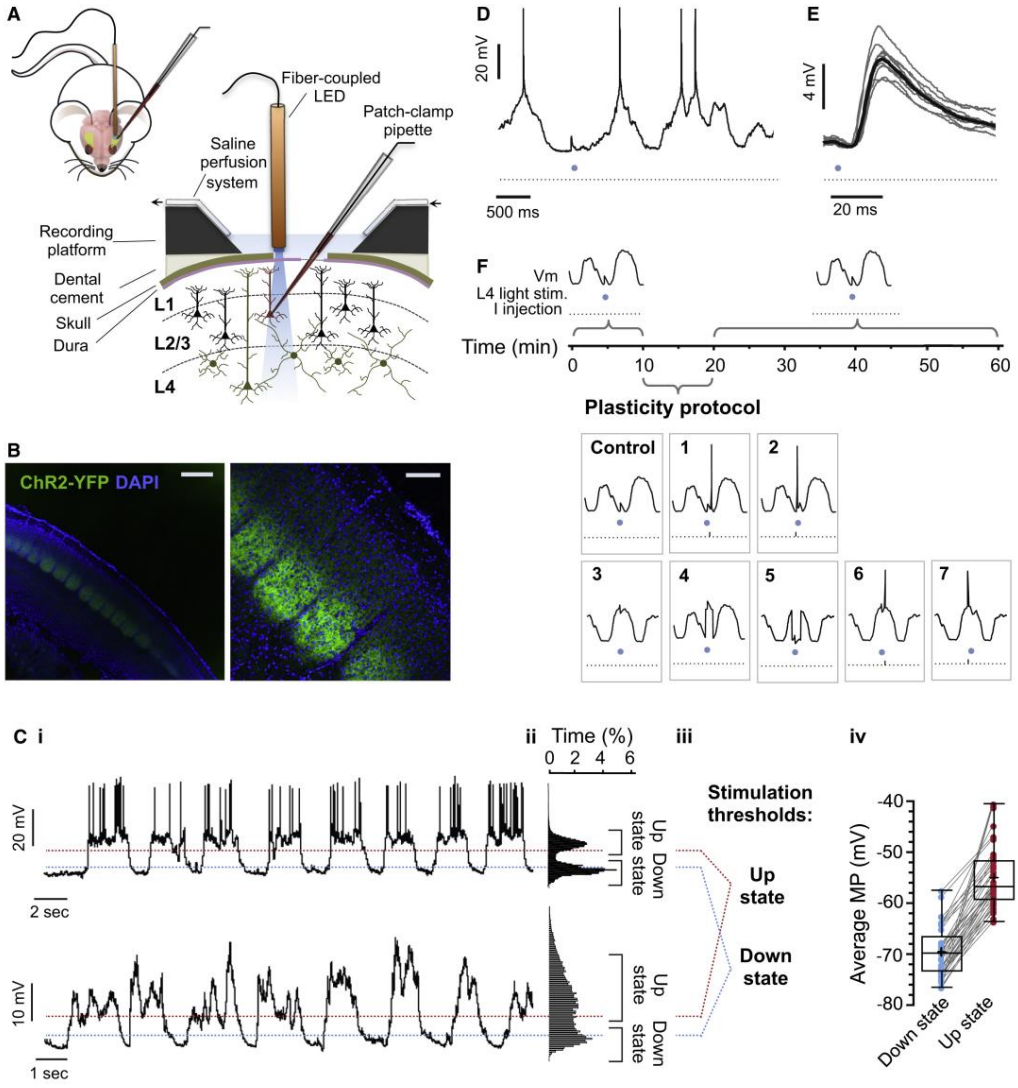

Figure 1: Monitoring L4 to L2/3 synaptic strength in vivo. (**A**) Schematic of the technical approach. L2/3 neurons of urethane-anesthetized Six3-cre/Ai32 mice were recorded in whole-cell mode and ChR2-expressing L4 afferent fibers were activated using a fiber-coupled LED. (**B**) Pattern of expression of ChR2 in the barrel cortex (scale bars: left, 500 µm, right, 200 µm). (**C**) (i) Example trace of highly active L2/3 neuron (top) and sparsely spiking L2/3 neuron (bottom). (ii) Bimodal distribution of membrane potential (MP). (iii) Thresholds for stimulation during Up states and Down states were 0.5 mV negative to the mean Up state MP (red dotted line) and 0.5 mV positive to the mean Down state MP (blue dotted line), respectively. (iv) Mean MP at Up states and Down states for all cells recorded (n = 92 neurons in N = 81 mice). Box-and-whisker plots represent

maximum, upper quartile, mean (cross), median, lower quartile and minimum values. (**D**) Example trace of light-evoked EPSP during Down state. A closed-loop was used to elicit EPSPs only at MP negative to Down-state-threshold. Spikes are truncated for clarity. See also Figures S1 and S2. (**E**) Ten overlaid traces of light-evoked EPSPs during Down states (gray) and their mean (black). (**F**) Diagram of the experimental design. EPSPs were monitored for 10 minutes using a 2-ms light-pulse only during Down states (<0.1 Hz). Subsequently, one of eight protocols was applied (100 repetitions at <0.2 Hz): light-stimulation at Down states only (control); light-stimulation at Down states followed (1) or preceded (2) by postsynaptic spike; light-pulse during Up states only (3); light-pulse during Down states paired with postsynaptic depolarization (4); light-pulse during Up states paired with postsynaptic hyperpolarization (5); and presynaptic light-stimulation during Up states followed (6) or preceded (7) by a postsynaptic spike. Following the plasticity protocol, EPSP was monitored by light-stimulation during Down states (<0.1 Hz) for 20 to 30 minutes.

Conventional STDP during Down states

We first asked whether STDP can be induced during Down states *in vivo* by protocols similar to those described *ex vivo* in the absence of network activity (Feldman, 2000; Rodríguez-Moreno and Paulsen, 2008). When L4 light-stimulation was followed within 10 ms by a single postsynaptic spike during Down states, t-LTP was induced (129 ± 15%, n = 8, *vs.* 98 ± 6% interleaved controls, n = 13; two sample Student's *t*-test p = 0.038; **Figure 2A-D**). Conversely, when light-stimulation was preceded within 10 ms by a single postsynaptic spike, significant timing-dependent long-term depression (t-LTD) was induced (48 ± 11%, n = 5 *vs.* 98 ± 6%, n = 13; two-sample Student's *t*-test p = 0.0012; **Figure 2A-D**). Thus, spike pairing during Down states induces conventional STDP *in vivo*, validating previous *ex vivo* results. However, neurons rarely spike during Down states (**Figure 1C**) implying that pairings of single pre- and postsynaptic spikes would not naturally occur during these periods. Thus, we next asked whether the same plasticity rules apply during Up states.

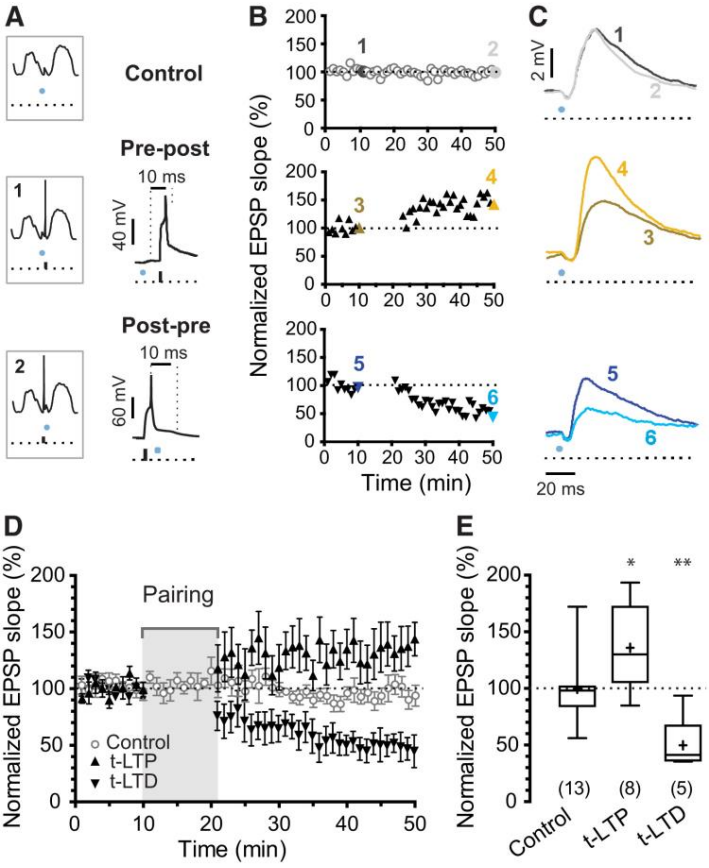

Figure 2: Synapse-specific STDP induced using light-stimulation during Down states *in vivo*. (**A**) Diagram of the protocols applied: top, control; middle, protocol 1 (pre-post); bottom, protocol 2 (post-pre). (**B**) Examples of each of the three experiments in **A**. Symbols show one-minute means of the EPSP slopes normalized to the 10-minute base-line. (**C**) Representative mean traces from the 10th (1, 3 and 5) and 50th minute (2, 4 and 6) of recording. (**D**) Evoked EPSPs were stable over 50 minutes (<0.1 Hz, control; n = 13 cells in N = 10 mice, mean ± SEM). A pre-post pairing protocol applied during Down states led to t-LTP (n = 8 neurons in N = 8 mice, mean ± SEM), while a post-pre pairing protocol led to t-LTD (n = 5 neurons in N = 5 mice, mean ± SEM). (**E**) Summary of the results in **D**. Number of recordings indicated in parentheses. Mean EPSP slope from last five minutes of recording was normalized to mean EPSP slope of the last five minutes of the baseline. The box and whisker plots represent maximum, upper quartile, mean (cross), median, lower quartile and minimum values. One way ANOVA and Dunnett's post-hoc test, * $p < 0.05$, ** $p < 0.01$.

Synaptic depression during Up states

In order to investigate how Up states influence synaptic plasticity, we first modified the closed-loop procedure to stimulate L4 afferents only during Up states in the plasticity protocol (100 repetitions at <0.2 Hz, protocol 3 in **Figure 1F;** fewer than 10% of stimulations occurred during activated states lasting >5 seconds, which might correspond to REM-like episodes, **Figure S2**). Surprisingly, we observed significant synaptic depression (63 ± 6%, n = 10, one sample Student's *t*-test p = 0.0002; **Figure 3A**), which was confirmed in Scnn1a-cre/Ai32 mice expressing ChR2 only in excitatory L4 neurons (51 ± 8 %, n = 6, one sample Student's *t*-test p = 0.001; **Figure S3**).

Both experiments and computational models suggest that the membrane potential of the postsynaptic neuron can modify STDP induction (Sjöström et al., 2004; Clopath et al., 2010a,b). To test whether pairing of presynaptic spiking and subthreshold depolarization of L2/3 neurons was sufficient to induce synaptic plasticity, we paired presynaptic stimulation during Down state with a 500 ms positive current step, starting 250 ms before L4 stimulation (protocol 4 in **Figure 1F**), yielding a somatic depolarization equivalent to the mean potential during Up states for that neuron. This protocol did not induce plasticity (103 ± 13%, n = 6, one sample Student's *t*-test p = 0.83; **Figure 3B**). Conversely, pairing L4 stimulation during Up states with hyperpolarization to Down state level (protocol 5 in **Figure 1F**) did not prevent the induction of LTD (48 ± 8%, n = 6, one sample Student's *t*-test p = 0. 0011; **Figure 3B**), suggesting that postsynaptic membrane voltage does not control Up state-associated synaptic depression.

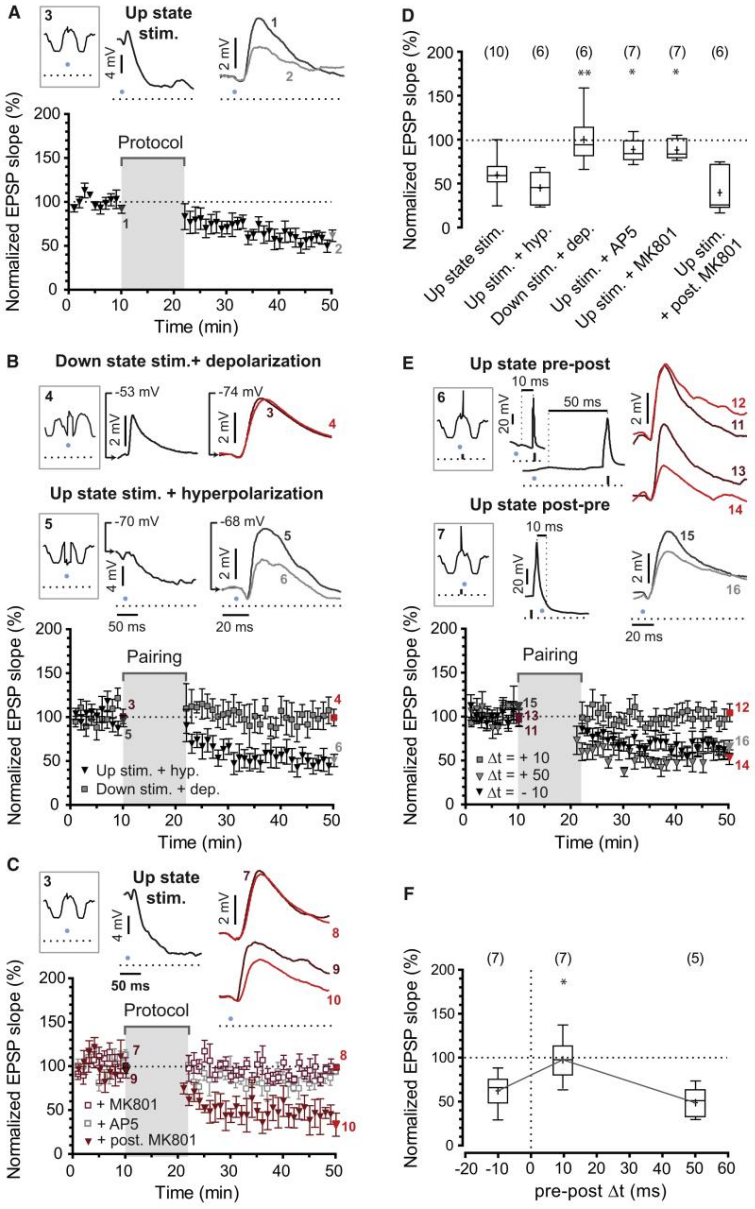

Figure 3: Up states modulate the indu-ction of synaptic plasticity. (**A**) Presynaptic stimulation during Up states led to significant LTD (n = 10 cells in N = 10 mice, mean ± SEM). Schematic of the stimulation protocol (protocol 3, top left), representative traces of the plasticity protocol (black trace, top middle) and mean traces from the 10th (1) and 50th minute (2) of exam-ple experiment are shown (see also Figure S3). (**B**) Pairing of presynaptic stimulation during Down state and postsy-naptic depolarization to Up state level (-53 mV in the example, protocol 4, top left and middle) failed to induce LTD (n = 6 neurons in N = 5 mice); while LTD was still induced when presynaptic stimulation during Up states was paired with postsynaptic hyperpolarization to Down state level (-70 mV in the example, protocol 5, n = 6 cells in N = 6 mice). Mean traces before (3 and 5) and after (4 and 6) plasticity protocol are shown. (**C**) Up state-mediated LTD was prevented by AP5 (n = 7 cells in N = 7 mice) and MK801 (n = 7 neurons in N = 6 mice). Postsynaptic loading of

MK801 failed to prevent LTD (n = 6 cells in N = 6 mice). Schematic of the stimulation protocol (protocol 3, top left), representative traces of the plasticity protocol (black trace, top middle) and the average traces from the 10th (7) and 50th minute (8) of one of the experiments after MK801 application and with MK801 in the recording pipette (9 and 10 respectively) are shown. (**D**) Summary of the results in **A**, **B** and **C.** Number of cells are indicated in parentheses. Mean EPSP slope from the last five minutes of recording was normalized to mean EPSP slope of the last five minutes of the baseline. Box-and-whisker plots represent maximum, upper quartile, mean (cross), median, lower quartile and minimum values. One way ANOVA and Dunnett's post-hoc test * $p < 0.05$, ** $p < 0.01$. (**E**) LTD was prevented by postsynaptic spikes when preceding presynaptic stimulation within 10 ms (Up state pre-post pairing, $\Delta t = +10$, gray squares, n = 7 neurons in N = 7 mice), while LTD was still present if the pre-post time-window was widened to 50 ms (Up state pre-post pairing, $\Delta t = +50$, gray triangles, n = 5 cells in N = 5 mice) or reversed (Up state post-pre pairing, $\Delta t = -10$, black triangles, n = 7 neurons in N = 7 mice). (**F**) Summary of results in **E** represented as in **D**.

Presynaptic *N*-methyl-D-aspartate receptor (NMDAR) activation is required for the induction of t-LTD at L4-L2/3 synapses of the barrel cortex (Bender et al., 2006; Rodríguez-Moreno and Paulsen, 2008). To investigate whether NMDARs are necessary also for *in vivo* Up state-associated LTD, we applied the NMDAR antagonist 2-amino-5-phosphonopentanoate (AP5; 0.2 mM) to the surface of the cortex. AP5 blocked depression (92 ± 5%, n = 7, one sample Student's *t*-test p = 0.17; **Figure 3C**). Equivalent results were obtained with extracellular application of the NMDAR channel blocker MK801 (30 µM) (91 ± 4%, n = 7, one sample Student's *t*-test p = 0.09; **Figure 3C**). However, MK801 loaded in the postsynaptic cell did not prevent Up state-mediated depression (44 ± 11%, n = 6, one sample Student's *t*-test p = 0.0033; **Figure 3C**). These results demonstrate that non-postsynaptic ionotropic NMDARs are required for Up state-associated LTD and that plasticity rules distinct from conventional STDP operate during Up states.

To test whether postsynaptic spikes following presynaptic activity during Up states

(protocol 6 in **Figure 1F**) induces potentiation, as seen during Down states, we elicited a single spike in the postsynaptic L2/3 neuron 10 ms after presynaptic L4 light-stimulation during Up states. While no significant potentiation was observed, synapses were protected from depression (100 ± 9%, n = 7, one sample Student's *t*-test p = 0. 87; **Figure 3E**). This protection was not effective when a postsynaptic spike was evoked 50 ms following presynaptic stimulation (53 ± 8%, n = 5, one sample Student's *t*-test p = 0.0038; **Figure 3E**) or 10 ms prior to L4 stimulation during Up states (66 ± 7%, n = 7, one sample Student's *t*-test p = 0.0041; **Figure 3E**), indicating a relatively narrow time-window for protection against depression (**Figure 3F**).

Up state-mediated depression could explain input-specific downscaling during SWS

The Up state-specific synaptic plasticity rule uncovered here would be consistent with the synaptic homeostasis hypothesis, which implies that synapses are selectively downscaled during SWS. However, in contrast to a global rescaling mechanism (Turrigiano et al., 1998), the rule uncovered here requires presynaptic activity during Up states. To test the implications of this plasticity rule, we developed a network model of 100 independently driven leaky integrate-and-fire presynaptic L4 neurons, projecting onto a single postsynaptic L2/3 neuron (**Figure 4A**). Synaptic weights were initially set at comparable values (0.2 ± 0.02, **Figure 4B and C**). To model synaptic weight changes during wake and successive sleep, the simulation was divided into two phases: 'wake' and 'sleep'. To create a wake representation in L4-L2/3 connections ('sensory experience'), during the first half of the simulation, 5 of the L4 neurons received a 50% stronger external drive, and synaptic weights were updated according a conventional STDP rule (**Figure 4B**).

This resulted in an overall potentiation of synaptic weights with stronger potentiation of connections from L4 neurons that received stronger input, due to the boosted coincidence of pre-postsynaptic pairings (**Figure 4C**), and to an increase in S/N (from 1.1 to 2.5, **Figure 4D**). To mimic synaptic weight changes during SWS in the subsequent sleep simulation all L4 neurons received a comparable input drive and synaptic weights were updated with the Up state-specific synaptic plasticity rule uncovered here, such that L4 spikes alone led to depression unless followed within 10 ms by a L2/3 spike (**Figure 4B**). This SWS-like period resulted in the preservation of the highest synaptic weights, corresponding to the representation created during 'wake', the depression of all other synaptic weights (**Figure 4C**), and a further increase in S/N (to 11.2, **Figure 4D**). The depression or maintenance of synaptic weights was independent of the synaptic plasticity rules during 'wake' and only depended on the synaptic weights before 'sleep' and the consequential probability of L4-L2/3 coincidence, which correlated to their firing rates (**Figure S4**).

To test the impact of the initial synaptic weight on the amount of synaptic weakening endured during SWS in our model, the initial synaptic weights were first set between 0.1 and 1 and the 'sleep' simulation was run. Weak synapses were strongly depressed while stronger synapses remained unchanged (**Figure 4E**), consistent with theoretical predictions (Hashmi et al., 2013; Nere et al., 2013) and ultrastructural data (de Vivo et al., 2017).

Intuitively, the requirement of input activity for synaptic depression, combined with the protection against depression by postsynaptic spikes, would preserve previously stored synaptic representations despite presentation of new input patterns. Thus, we tested whether the new learning rule would retain previously stored input patterns while increasing the S/N for a new set of inputs by repeating the 'wake' and 'sleep'

phases over five days. A first set of inputs was strengthened at day 0 (pattern 1, **Figure 4F**). During the following 'sleep' phase all weights were updated either according the Up state-specific plasticity rule or an homogeneous global downscaling rule. As expected, the S/N increased and the amplitude of the pattern was conserved only following Up state-specific plasticity (**Figure 4F**). At day 1, a different set of inputs was strengthened (pattern 2). We observed that both patterns were preserved with increased S/N even after several subsequent wake/sleep cycles. In contrast, both S/N and pattern amplitude gradually decayed when a global scaling rule was used (**Figure 4F**). Thus, compared to global downscaling, this new plasticity rule promotes an increase in S/N and the retention of previously stored input patterns.

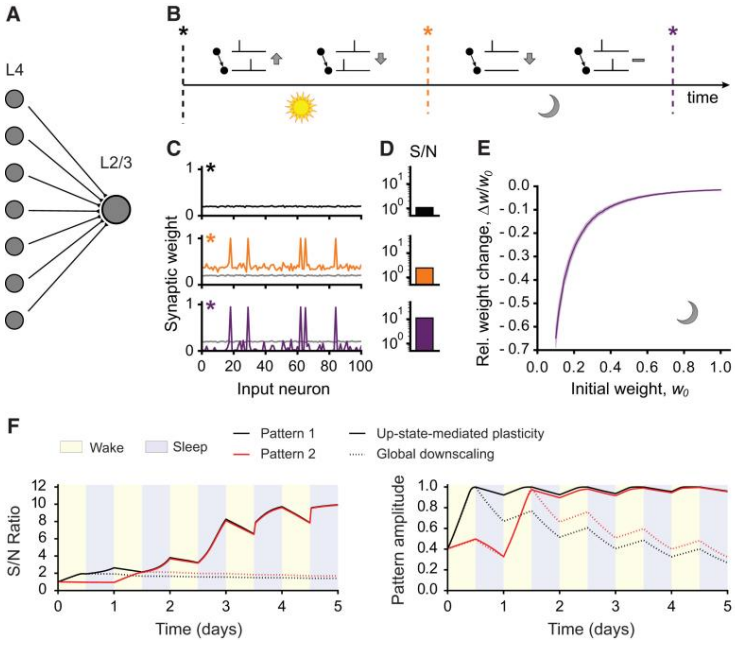

Figure 4: Up state-mediated depression leads to circuit refinement in model network following simulated wake and sleep. (**A**) Model of a feedforward network with 100 presynaptic neurons L4 neurons projecting onto one single postsynaptic L2/3 neuron. (**B**) Simulation protocol. Synaptic weights from all connections were initiated with compara-ble amplitude (black star). For the first half of the simulation ('wake', sun symbol, 800 seconds), synaptic weights were updated according a conventional STDP rule. All presynaptic neurons received an external input to promote spiking and five of them received a 50% stronger input. During the second half ('sleep',

moon symbol, 800 seconds), synaptic weights were updated with the Up state-mediated synaptic plasticity rule. (**C**) Synaptic weights for three stages of the simulation. Top, black: start (black star in **B**). Middle, orange: after 'wake' (orange star in **B**). Bottom, purple: end (purple star in **B**). (**D**) Signal to noise ratio (S/N) for the three stages in **C**. (**E**) Relative weight change, $\Delta w/w_0$, plotted as a function of the initial synaptic weight, w_0, after Up state-mediated (sleep) plasticity. 200 simulations were averaged and the shaded area represents the SD. (**F**) Simulated Up state-mediated plasticity preserves and enhances previously stored patterns. At day 0, five presynaptic neurons received 50% stronger input (pattern 1). At day 1, neurons from pattern 1 did not receive any extra external input, but another set of five neurons did (pattern 2). All presynaptic neurons received comparable external input and fired at the same rate from day 2. Left: evolution of S/N for both patterns (1, black; 2, red). Right: evolution of both pattern amplitudes. During 'wake' (yellow), synaptic weights were updated according STDP. During 'sleep' (purple), synaptic weights were updated according either Up state-modulated plasticity (solid lines) or homogeneous synaptic scaling rule (dotted lines). Curves show a mean over 50 trials. See also Figure S4.

DISCUSSION

Our study shows that cortical network activity influences synaptic plasticity rules. Specifically, conventional STDP applies during slow wave sleep-like activity *in vivo* only during Down states. Synaptic stimulation during Up states invariably led to NMDAR-dependent synaptic depression unless the postsynaptic neuron spiked within a narrow time-window following presynaptic stimulation, which protected against synaptic weakening. Incorporated into a computational network model, two important advantages of this new plasticity rule compared to conventional global rescaling were demonstrated: 1) improved S/N, 2) preservation of previously stored input patterns.

The induction of STDP during Down states is consistent with a huge body of experimental work in brain slices (e.g. Feldman, 2000; Rodríguez-Moreno and

Paulsen, 2008). However, the physiological relevance of such STDP could be questioned, since cortical networks are relatively quiescent during Down states. Fewer and divergent studies have investigated synaptic plasticity following the pairing of presynaptic inputs and spontaneous or electrically evoked persistent activity in acute brain slices (Kruskal et al., 2013; Bartram et al., 2017), highlighting the importance of studying synaptic plasticity during activated states *in vivo*. During *in vivo* Up states, when spikes are more likely to occur, presynaptic-postsynaptic spike correlations were not required for synaptic plasticity, as subthreshold synaptic input was sufficient to induce NMDAR-dependent LTD. This may be a prominent form of plasticity *in vivo* owing to the low firing rate in L2/3 (**Figure S2**). LTD independent of postsynaptic spikes has previously been reported in slice preparations from neocortex, when presynaptic stimulation was paired with subthreshold postsynaptic depolarization (Sjöström et al., 2004), and even without any postsynaptic activity (Rodríguez-Moreno et al., 2013). Although our evidence suggests that postsynaptic depolarization is not required for Up state-associated LTD *in vivo*, we cannot exclude the possibility that local dendritic depolarization during Up states might be involved. Alternatively, the conditions for activation of presynaptic NMDARs might be met during Up state activity without the need for postsynaptic activity (Rodríguez-Moreno et al., 2013).

Our results highlight the importance of network activity in gating synaptic plasticity and indicate a bias towards synaptic depression during cortical slow oscillations. The plasticity rule uncovered here provides a mechanism by which connections that are strengthened during wake would be protected from depression, rather than further strengthened. This could be especially important during development as studied here, when neuronal connections are expected to depress (Feldman et al.,

2000; Itami and Kimura, 2012; Banerjee et al., 2014). Interestingly, however, Up-state-associated synaptic depression was also seen in adult mice (P30-P50, 71 ± 9%, n = 8 vs. control 99 ± 9%, n = 6; **Figure S3**), suggesting this form of plasticity could also contribute to circuit reshaping in mature cortex.

Network activity under urethane anesthesia resembles that during natural sleep (Contreras and Steriade, 1997; Clement et al., 2008). To what extent changes in neuromodulators are preserved during urethane anesthesia is not well studied; however, it has been reported that cholinergic modulation is comparable between urethane anesthesia sleep-like transitions and natural sleep (Steriade 1993; Manns et al., 2000). Nevertheless, we cannot exclude the possibility that neuromodulatory systems are differentially regulated and it will be important to confirm our findings during natural sleep in future experiments. Although the vast majority of stimulations in the Up state plasticity protocols happened during SWS-associated Up states of short duration, a few stimulations occurred during REM-sleep-like episodes, and, although we find it unlikely, we cannot rule out that stimulations during REM-like episodes could have a disproportionate effect on synaptic weights. Still, our results offer a possible mechanism for the finding that sleep favors synaptic depression.

The Up-state-associated plasticity studied here only takes account of pre- and postsynaptic spikes. Intuitively, if spiking activity was the only determinant of plasticity, the higher firing rate of L4 neurons compared to that of L2/3 neurons (**Figure S2**) would promote depression on its own. However, other mechanisms, such as subthreshold input cooperation within dendritic segments (Golding et al.,

2002; Losonczy et al., 2008; Lee et al., 2016) could also promote the protection of synaptic connections even in the absence of postsynaptic spikes. Similarly, mechanisms other than those uncovered here could allow for the depression of highly efficacious synapses that would otherwise be permanently protected.

In our computational model the Up state-associated synaptic plasticity rule effectively refined a previously acquired representation via the selective downscaling of synapses with lower synaptic weights which is attractive as a mechanism for activity-dependent synaptic downscaling during sleep. Our data could explain how the occurrence of UDS during SWS induces selective downscaling of synaptic weights in an NMDAR-dependent manner without the need for any additional external input. The protection against depression by postsynaptic spikes suggests a mechanism by which spiking Hebbian assemblies maintain their synaptic weights ('neurons that fire together wire together'), whilst non-participating connections are depressed. This would also result in the sparsification of neuronal activity, which is seen during critical periods of development (van der Bourg et al., 2017). This mechanism also allows consolidation of new neuronal representations while conserving previously stored ones. In conclusion, we suggest that Up state-associated synaptic depression is a strong candidate for a mechanism to contribute to activity-dependent synaptic downscaling during SWS.

REFERENCES

Banerjee, A., González-Rueda, A., Sampaio-Baptista, C., Paulsen, O. and Rodríguez-Moreno, A. (2014). Distinct mechanisms of spike timing-dependent LTD at vertical and horizontal inputs onto L2/3 pyramidal neurons in mouse barrel cortex. Physiol. Rep. *27*, e00271.

Bartram, J., Kahn, M. C., Tuohy, S., Paulsen, O., Wilson, T. and Mann, E. O. (2017) Cortical Up states induce the selective weakening of subthreshold synaptic inputs. Nat. Commun. *8,* 665.

Bender, V.A., Bender, K.J., Brasier, D.J. and Feldman, D.E. (2006). Two coincidence detectors for spike timing-dependent plasticity in somatosensory cortex. J. Neurosci. *26*, 4166–4177.

Bi, G.Q. and Poo, M.-m. (1998). Synaptic modifications in cultured hippocampal neurons: dependence on spike timing, synaptic strength, and postsynaptic cell type. J. Neurosci. *18*, 10464–10472.

Clement, E.A., Richard, A., Thwaites, M., Ailon, J., Peters, S. and Dickson, C.T. (2008). Cyclic and sleep-like spontaneous alternations of brain state under urethane anaesthesia. PLoS One *16*, e2004.

Clopath, C. and Gerstner, W. (2010a) Voltage and spike timing interact in STDP – a unified model. Front. Synaptic Neurosci. 21, 2-25.

Clopath, C., Büsing, L., Vasilaki E. and Gerstner W. (2010b). Connectivity reflects coding: a model of voltage-based STDP with homeostasis. Nat. Neurosci. *13*, 344-352.

Contreras, D. and Steriade, M. (1997). State-dependent fluctuations of low-frequency rhythms in corticothalamic networks. Neuroscience *76*, 25–38.

Craig, M. T., Mayne, E. W., Bettler, B., Paulsen, O. and McBain, C. J. (2013). Distinc roles of GABA1a- and GABA1b-containing GABAB receptors in spontaneous and evoked termination of persistent cortical activity. J. Physiol. *591*, 835-843.

de Kock, C.P. and Sakmann, B. (2009). Spiking in primary somatosensory cortex during natural whisking in awake head-restrained rats is cell-type specific. Proc. Natl. Acad. Sci. USA *106*, 16446-16450.

de Vivo, L., Bellesi, M., Marshall, W., Bushong, E.A., Ellisman, M.H., Tononi, G. and Cirelli, C. (2017). Ultrastructural evidence for synaptic scaling across the wake/sleep cycle. Science. *6324*, 507-510.

Feldman, D.E. (2000). Timing-based LTP and LTD at vertical inputs to layer II/III pyramidal cells in rat barrel cortex. Neuron *27*, 45–56.

Furuta, Y., Lagutin, O., Hogan, B.L. and Oliver, G.C. (2000). Retina- and ventral forebrain-specific Cre recombinase activity in transgenic mice. Genesis *26*, 130-132.

Gambino, F. and Holtmaat, A. (2012). Spike-timing-dependent potentiation of sensory surround in the somatosensory cortex is facilitated by deprivation-mediated disinhibition. Neuron *75*, 490–502.

Golding, N. L., Staff, N. P. and Spruston, N. (2002). Dendritic spikes as a mechanism for cooperative long-term potentiation. Nature *418,* 326-331.

Hashmi, A., Nere, A. and Tononi, G. (2013). Sleep-dependent synaptic down-selection (I): single-neuron level benefits for matching, selectivity, and specificity. Front. Neurol. *4*, 148.

Hebb, D.O. (1949). The organization of behavior. (Wiley, New York).

Itami, C. and Kimura, F. (2012). Developmental switch in spike timing-dependent plasticity at layer4-2/3 in the rodent barrel cortex. J. Neurosci. *32,* 15000-15011.

Jacob, V., Brasier D.J., Erchova, I., Feldman, D.E. and Shulz D.E. (2007). Spike timing-dependent synaptic depression in the in vivo barrel cortex of the rat. J. Neurosci. *27*, 1271–1284.

Kruskal, P. B., Li, L. and MacLean, L. N. (2013) Circuit reactivation dynamically regulates synaptic plasticity in neocortex. Nat. Commun. *4,* 2574.

Lee, K. F., Soares, C., Thivierge, J. P. and Béïque, J. C. (2016). Correlated synaptic inputs drive dendritic calcium amplification and cooperative plasticity during clustered synapse development. Neuron *89,* 784-799.

Liu, Z.-W., Faraguna, U., Chiara Cirelli, C., Tononi, G. and Xiao-Bing Gao, X.-B. (2010). Direct evidence for wake-related increases and sleep-related decreases in synaptic strength in rodent cortex. J. Neurosci. *30*, 8671-8675.

Losonczy, A., Makara, J. K. and Magee, J. C. (2008). Compartmentalized dendritic plasticity and input feature storage in neurons. Nature *452,* 436-441.

Manns, I. D., Alonso, A. and Jones, B. E. (2000). Discharge properties of juxtacellularly labelled and immunohistochemically identified cholinergic basal forebrain neurons recorded in association with the electroencephalogram in anesthetized rats. J. Neurosci. *20,* 1505-1518.

Meliza, C.D. and Dan, Y. (2006). Receptive-field modification in rat visual cortex induced by paired visual stimulation and single-cell spiking. Neuron *49*, 183-189.

Nere, A., Hashmi, A., Cirelli, C. and Tononi, G. (2013). Sleep-dependent synaptic down-selection (II): modeling the benefits of sleep on memory consolidation and integration. Front. Neurol. *4*, 143.

Pawlak, V., Greenberg, D.S., Sprekeler ,H., Gerstner, W. and Kerr, J.N.D. (2013). Changing the responses of cortical neurons from sub- to suprathreshold using single spikes in vivo. Elife 2, e00012.

Rema, V., Armstrong-James, M. and Ebner, F.F. (1998). Experience-dependent plasticity of adult rat S1 cortex requires local NMDA receptor activation. J. Neurosci. *18*, 10196-10206.

Rodríguez-Moreno, A. and Paulsen, O. (2008). Spike timing-dependent long-term depression requires presynaptic NMDA receptors. Nat. Neurosci. *11*, 744–745.

Rodríguez-Moreno, A., González-Rueda, A., Banerjee, A., Upton, A.L., Craig, M.T. and Paulsen, O. (2013). Presynaptic self-depression at developing neocortical synapses. Neuron *77*, 35-42.

Sjöström, P.J., Turrigiano, G.G. and Nelson, S.B. (2004) Endocannabinoid-dependent neocortical layer-5 LTD in the absence of postsynaptic spiking. J. Neurophysiol. *92*, 3338-3343.

Song, S. and Abbott, L.F. (2001). Cortical development and remapping through spike timing-dependent plasticity. Neuron *32*, 339-350.

Steriade, M., Nunez, A. and Amzica, F. (1993). Intracellular analysis of relations between the slow (<1 Hz) neocortical oscillation and other sleep rhythms of the electroencephalogram. J. Neurosci. *13*, 3252–3265.

Stern, E. A., Maravall, M. and Svoboda, K. (2001). Rapid development and plasticity of layer 2/3 maps in rat barrel cortex in vivo. Neuron *31,* 305-315.

Tononi G. and Cirelli C. (2003). Sleep and synaptic homeostasis: a hypothesis. Brain. Res. Bull. *62*, 143-150.

Turrigiano, G.G., Leslie, K.R., Desai, N.S., Rutherford, L.C. and Nelson, S.B. (1998). Activity-dependent scaling of quantal amplitude in neocortical neurons. Nature *391*, 892-896.

van der Bourg, A., Yang, J. W., Reyes-Puerta, V., Laurenczy, B., Wieckhorst, M., Stüttgen, M. C., Luhmann, H. J. and Helmchen, F. (2017). Layer-specific refinement of sensory coding in developing mouse barrel cortex. Cereb. Cortex. *27,* 4835-4850.

van Ooyen, A. (2011). Using theoretical models to analyse neural development. Nat. Rev. Neurosci. *12*, 311-326.

Vyazovskiy, V.V., Cirelli, C., Pfister-Genskow, M., Faraguna, U. and Tononi, G. (2008). Molecular and electrophysiological evidence for net synaptic potentiation in wake and depression in sleep. Nat. Neurosci. *11*, 200–208.

STAR METHODS

Contact for reagent and resource sharing

For further information contact Prof. Ole Paulsen (op210@cam.ac.uk) or Dr. Ana González-Rueda (arueda@mrc-lmb.cam.ac.uk). Any requests for resources should be directed to and will be fulfilled by Prof. Ole Paulsen.

Experimental model and subject details

Tg(Six3-Cre)69Frty/GcoJ (Six3-cre) mice were crossed with B6;129S-Gt(ROSA)26Sortm32(CAG–COP4*H134R/eYFP)Hze/J mice (Ai32; Jackson Laboratory, Maine, USA) in order to express ChR2(H134R)-YFP in L4 neurons of the somatosensory cortex (Furuta et al., 2000). For a subset of experiments Ai32 mice were crossed with B6;C3-Tg(Scnn1a-cre)3Aibs/J (Scnn1a-Cre; Jackson Laboratory, Maine, USA). Unless otherwise stated, only Six3-cre/Ai32 mice ranging from P15 to P21 were used for experiments. Animals were housed on a 12-hour light/dark cycle and the mother was fed *ad libitum*. The research was performed under the Animals (Scientific Procedures) Act 1986 Amendment Regulations 2012 following ethical review by the University of Cambridge Animal Welfare and Ethical Review Body (AWERB).

Method details

Surgery. Mice were anesthetized with an intraperitoneal injection of urethane (1 g per kg of body weight). Upon cessation of reflexes, the top of the head of the animal

was shaved and the skin covering the right hemisphere was removed. A blue LED light was used to identify and mark over the skull the YFP-fluorescent barrel field. A head-restraining platform was cemented (Super-Bond C & B; Prestige Dental Ltd., Bradford, UK) to the skull around the mark indicating the barrel cortex location. The animal was placed on the recording frame over a low-noise heating pad (FHC inc., Termobit Prod. srl., Bucharest, Romania) to aid body temperature maintenance. A 200-500 μm craniotomy was performed at the marked spot and the dura mater was carefully removed from a small area of the craniotomy (20-100 μm). Care was taken to avoid bleeding or drying of the meninges and brain tissue. Saline (0.9 % NaCl) was superfused constantly with a 2 mL/minute laminar flow using a peristaltic pump.

Electrophysiology. Whole-cell current-clamp recordings were obtained from L2/3 neurons of the primary somatosensory cortex of urethane-anesthetized mice using 6-9 MΩ pipettes pulled from borosilicate glass capillaries (1B120F-4, World Precision Instruments, Stevenage, UK). Pipettes were filled with artificial intracellular solution containing (in mM): K-gluconate 150, HEPES 10, NaCl 4, ATP-Mg 4, GTP-Na 0.3 and EGTA 0.2; adjusted to pH 7.2 and osmolarity 270-290 mOsm/L. Data were recorded using an Axon Multiclamp 700B amplifier (Molecular Devices, Union City, CA, USA). Signals were low-pass filtered at 2 kH and acquired at 5 kHz using a data interface ITC-18 AD board (Instrutech, Port Washington, NY, USA) on a PC running Igor Pro (Wavemetrics, Lake Oswego, OR, USA). A reference silver pellet electrode (A-M Systems, Carlsborg, WA, USA) was placed in the saline bath covering the craniotomy. The recording pipette was controlled using a micromanipulator at a 50° inclination. High positive pressure (>500 mbar) was applied and the pipette was lowered to the surface of the brain. A

5-ms-long square pulse of voltage of 4 to 8 mV at 100 Hz was delivered via the recording electrode. The pipette was quickly advanced 100 μm to L2 of the barrel cortex. The pressure was lowered to 60 mbar and the pipette was advanced in 2 μm steps. Cell contact produced a small reduction (around 10%) in resistance of the pipette, which could be seen as a proportional decrease in the size of the step of current in the oscilloscope. Cell contact also produced a pulsation artefact or flickering in the positive values of the current recorded. If no cell contact was detected after 250 steps of 2 μm, the pipette was retracted and a new pipette was used to record a new cell. Recordings were discarded if the access resistance was >25 MΩ or changed >10% along the recording. For a subset of experiments, single unit recordings of L2/3 and L4 neurons were done using 3-4 MΩ tungsten electrodes (Microelectrodes Ltd., Cambridge, UK) paired with 1 MΩ tungsten electrodes for L2/3 LFP recording.

Thalamocortical slices. Thalamocortical slices of 350 μm thickness containing the barrel subfield of somatosensory cortex were prepared as previously described (Rodríguez-Moreno et al., 2013; Banerjee et al., 2014) Briefly, mice were decapitated under isoflurane anesthesia and the brain was rapidly removed and placed in ice-cold artificial cerebrospinal fluid (aCSF) with the following composition (in mM): NaCl 126, KCl 3, NaH_2PO_4 1.25, $MgSO_4$ 2, $CaCl_2$ 2, $NaHCO_3$ 26, glucose 10, pH 7.2-7.4; bubbled with carbogen gas (95% O_2 / 5% CO_2) and with an osmolarity adjusted to 280-300 mOsm/L. The brain was placed on a 10° ramp rostral side down and a vertical cut was made through the tissue at an angle of 55° to the anteroposterior axis of the brain. Slices from the right somatosensory cortex were cut using a vibratome (VT 1200S, Leica, Wetzlar,

Germany) and maintained in a submerged-style chamber at room temperature until used. The flow rate of aCSF in the recording chamber was 2 ml/min.

Optogenetics and plasticity experiments. L4 neurons were excited using a 470 nm fibre-coupled LED system (150 µm, Thorlabs LTD, Ely, UK). The LED fibre was positioned centrally above the recorded cell on top of the dura mater. Light intensity was adjusted to produce 3-6 mV EPSPs at Down states. The average membrane potential during Down states and Up states was measured over 10 seconds prior to the start of the plasticity protocol. The average membrane potential at Down states plus 0.5 mV was used as the Down state threshold, whereas the average membrane potential at Up states minus 0.5 mV was used as threshold for Up states. In order to trigger a light-pulse only at Down states and at <0.1 Hz, the membrane potential was scanned in 10-ms time bins using a closed-loop. When the membrane potential crossed the threshold for Down states a 10 seconds recording was triggered and a 2-ms light-pulse was delivered 10 ms into the recording. At the end of the 10-second-recording the closed-loop scanning was resumed in order to detect the next Down state. Each light stimulus was time stamped in order to obtain minute-averages of the EPSP slope. Following a 10-minute baseline recording, a plasticity protocol was applied at <0.2 Hz for 100 repeats. Following the plasticity protocol, the stimulus during Down states were resumed in order to assess changes in the EPSP slope.

For the experiments performed in acute brain slices, a monopolar stainless steel stimulation electrode was used to elicit EPSPs in L2/3 as control. Electrical stimulation was delivered with 2 seconds delay from the light-pulse.

Pharmacology. In a subset of experiments, NMDA receptors were blocked by epidural administration of 0.2 mM AP5 or 30 μM MK801 (Tocris Bioscience, Bristol, UK) via the superfusate, as previously described (Rema et al., 1998). In order to determine the reversal potential of the inhibitory component of ChR2 stimulation, 0.2 mM AP5 and 20 μM DNQX (Tocris Bioscience, Bristol, UK) were added to the superfusate.

Immunohistochemistry. Images from the barrel cortex of Six3-Cre/Ai32 mice and Scnn1a-Cre/Ai32 were taken to assess the level and location of ChR2 expression. Moreover, post-hoc reconstruction of a subset of the neurons recorded *in vivo* was possible after biocytin (Sigma-Aldrich, Dorset, UK) staining. Biocytin was diluted at 5 mg/ml in the internal solution used for whole-cell recordings. At the end of the recordings, the brain was cut in 200 μm thalamocortical slices as previously described. Slices containing the barrel cortex were washed once in PBS and were left overnight in fixing solution containing 4% (w/v) PFA in PBS at 4 °C. Slices were incubated in Alexa 633 Fluor-conjugated streptavidin (1:1000; Molecular Probes, Eugene, OR) in PBS and 0.3% Triton X-100 (Sigma-Aldrich, Dorset, UK) overnight at 4 °C. Before mounting, slices were incubated for 2 minutes in DAPI in PBS. Images were taken with a confocal microscope (SP8, Leica, Wetzlar, Germany) and a 25X and a 40X objective and color intensity was adjusted using Image J.

Analysis of synaptic plasticity. To assess plasticity, EPSP slopes were used as a measure of synaptic strength. Slope measurements were made on the rising phase of the EPSP as a linear fit between time points corresponding to 25-30% and 70-

75% of peak amplitude of the EPSP, or of the first slope in the case of polysynaptic EPSPs. EPSP slopes were averaged over 1-minute time bins. The change in EPSP slope after the plasticity protocol was expressed relative to EPSP slopes during the baseline recording. EPSP slopes were averaged over the last 5 minutes of the initial baseline and the last 5 minutes of recording, generally corresponding to minutes 25-30 after the plasticity induction protocol. For off-line UDS analysis, the membrane potential noise level was used as previously described (Craig et al., 2013).

Computational model. We simulated a feedforward network composed of 100 presynaptic neurons projecting onto one postsynaptic neuron. We used the leaky integrate-and-fire neuron model. In this model, the membrane potential of a neuron is described by

$$\tau_m \frac{du}{dt} = -(u - u_{rest}) + RI(t)\,,$$

where u_{rest} denotes the membrane voltage at rest, R denotes the membrane resistance, $I(t)$ denotes the external current and τ_m denotes the membrane time constant. If the membrane potential reaches a threshold u_{th} at time $t^{(f)}$, the membrane potential is reset to u_{reset} and we call $t^{(f)}$ the firing time. After being reset, the membrane potential follows the same equation again.

The term $I(t)$ takes into account all of the current being injected into a neuron; these can be from an external source or from other neurons. When a neuron fires it propagates a current to all other connected neurons. In order to model this current, we assumed that the conductance between a presynaptic neuron j and a postsynaptic

neuron i increases instantaneously every time the presynaptic neuron fires, and decays exponentially otherwise:

$$\begin{aligned} g_j &\rightarrow g_j + 1 && \text{if j fires and} \\ \frac{dg_j}{dt} &= -g_j/\tau_{syn} && \text{otherwise,} \end{aligned}$$

where τ_{syn} is the synaptic time constant. The synaptic current was then calculated through

$$I^{syn}(t) = -w_{ij} g_j (u - E^{syn}) ,$$

where w_{ij} is the synaptic weight from neuron j to neuron i and E^{syn} is the synaptic reversal potential.

Each presynaptic neuron received an independent external current whose amplitude varied in time and was determined by a filtered gaussian noise, with filtering time constant 20 ms. The postsynaptic neuron also received a constant external current.

For the wake phases of the simulations, the synaptic weights were updated by the conventional STDP rule, in which pre-post events lead to potentiation and post-pre events lead to depression. In order to implement this rule, we defined a presynaptic trace $\bar{x}_j$ (for each presynaptic neuron j) and a postsynaptic trace $\bar{y}$ that was incremented by 1 for each pre or postsynaptic spike, respectively, and decayed otherwise:

$$\begin{aligned} \bar{x}_j &\rightarrow \bar{x}_j + 1 && \text{if presynaptic neuron j fires and} \\ \tau_+ \frac{d\bar{x}_j}{dt} &= -\bar{x}_j && \text{otherwise,} \end{aligned}$$

and

$$\begin{aligned} &\bar{y} \to \bar{y} + 1 && \text{if the postsynaptic neuron fires and} \\ &\tau_- \frac{d\bar{y}}{dt} = -\bar{y}_i && \text{otherwise,} \end{aligned}$$

where τ_- is the depression time constant and τ_+ the potentiation time constant.

The synaptic weight w_j was then updated by the following:

$$\begin{aligned} &w_j(t) \to w_j(t) - A_-\bar{y}(t) && \text{if } t = t^{pre}, \\ &w_j(t) \to w_j(t) + A_+\bar{x}_j(t) && \text{if } t = t^{post}. \end{aligned}$$

where A_- is the depression amplitude and A_+ is the potentiation amplitude. Synaptic weights were also bounded between 0 and 1: $0 < w < 1$.

During the sleep phases of our simulations, the synaptic weights were updated following either an Up state-mediated plasticity or an homogeneous synaptic scaling. For the Up state-mediated plasticity, synaptic weights were updated such that presynaptic spikes alone led to depression whereas presynaptic spikes followed within 10 ms by a postsynaptic action potential led to no change. In order to implement this rule, we defined a presynaptic trace $\bar{x}_j$ (for each presynaptic neuron j) that was reset to 10 for every presynaptic spike and decayed linearly otherwise obeying

$$\begin{aligned} &\bar{x}_j \to 10 && \text{if presynaptic neuron j fires and} \\ &\tau \frac{d\bar{x}_j}{dt} = -1 && \text{otherwise,} \end{aligned}$$

where $\tau = 1$ ms. The synaptic weight w_j was then updated by the following:

$$\begin{aligned} &w_j(t) \to w_j(t) - A && \text{if } t = t^{pre}, \\ &w_j(t) \to w_j(t) + AH\big(\bar{x}_j(t)\big) && \text{if } t = t^{post}. \end{aligned}$$

where A is the depression amplitude and $H(x)$ is the Heaviside step function defined by $H(x) = 1$ if $x > 0$ and $H(x) = 0$ if $x < 0$. Therefore, a presynaptic

spike leads to depression with amplitude A and a postsynaptic spike within 10 ms of the presynaptic spike protects against this depression (increases the synaptic weight be the same amount A). Synaptic weights were also bounded between 0 and 1: $0 < w < 1$.

The homogeneous synaptic scaling was implemented by downscaling all synaptic weights by the same amount. The weights were downscaled such that they would be reduced by 33% at the end of each sleep phase.

Signal-noise analysis. The S/N was measured as the mean amplitude of the synaptic weights from the neurons relative to a specific pattern divided by the average of all synaptic weights.

Quantification and statistical analysis

A two-tailed one sample Student's t-test was used to assess long-term plasticity. In order to compare the magnitude of plasticity to a control condition a two-tailed two sample Student's t-test was used. For multiple comparisons to a single group, a one way ANOVA followed by a Dunnett's test was performed.

Table 1. *Parameter summary for simulations in figure 4.*

Neuron Model		
Name	**Value**	**Description**
τ_m	10 ms	Membrane time constant
u_{th}	10 mV	Spiking threshold
u_{rest}	0 mV	Resting potential
E^{syn}	30 mV	Synaptic reversal potential
u_{reset}	0 mV	Value at which the potential is reset after a spike
T_{ref}	3 ms	Refractory time
Network and Synapse Model		
Name	**Value**	**Description**
N_E	100	Size of presynaptic population
τ_E	10 ms	Decay constant of excitatory conductance
$\overline{g}_E$	1 nS	Peak synaptic conductance
Plasticity Model		
Name	**Value**	**Description**
τ_{STDP}	20 ms	Decay constant of pre- and postsynaptic traces
A_+ (C-D)	1×10^{-3}	Amplitude of learning rate for pre-post events (conventional STDP) - fig 4C-D.
A_- (C-D)	1×10^{-3}	Amplitude of learning rate for post-pre events (conventional STDP) - fig 4C-D.
A (C-D and F)	1×10^{-3}	Amplitude of learning rate for presynaptic events (sleep plasticity) - fig 4C-D and F.
A (e)	2×10^{-4}	Amplitude of learning rate for presynaptic events (sleep plasticity) - fig 4E.
A_+ (F)	2×10^{-5}	Amplitude of learning rate for pre-post events (conventional STDP) - fig 4F.
A_- (F)	2×10^{-5}	Amplitude of learning rate for post-pre events (conventional STDP) - fig 4F.
A (S4 C-D)	5×10^{-3}	Amplitude of learning rate for presynaptic events (sleep plasticity) - fig S4C-D.

Key resources table

REAGENT or RESOURCE	SOURCE	IDENTIFIER
Chemicals, Peptides, and Recombinant Proteins		
AP5	Tocris Bioscience	Cat.# 0106
MK801	Tocris Bioscience	Cat.# 0924
DNQX	Tocris Bioscience	Cat.# 0189
Biocytin	Sigma-Aldrich	Cat.# B4261
Streptavidin, Alexa 633 Fluor-conjugated	Thermo Fisher Scientific, Molecular Probes	Cat.# S21375
Experimental Models: Organisms/Strains		
Mouse: B6;129S-Gt(ROSA)26Sortm32(CAG−COP4*H134R/eYFP)Hze/J mice (Ai32)	The Jackson Laboratory	JAX: 012569
Mouse: Tg(Six3-Cre)69Frty/GcoJ (Six3-cre)	Furuta et al., 2000	N/A
Mouse: B6;C3-Tg(Scnn1a-cre)3Aibs/J	The Jackson Laboratory	JAX: 009613
Software and Algorithms		
Igor Pro	Wavemetrics	https://www.wavemetrics.com/products/igorpro/igorpro.htm
Python		The code for all the simulations will be submitted to ModelDB after publication

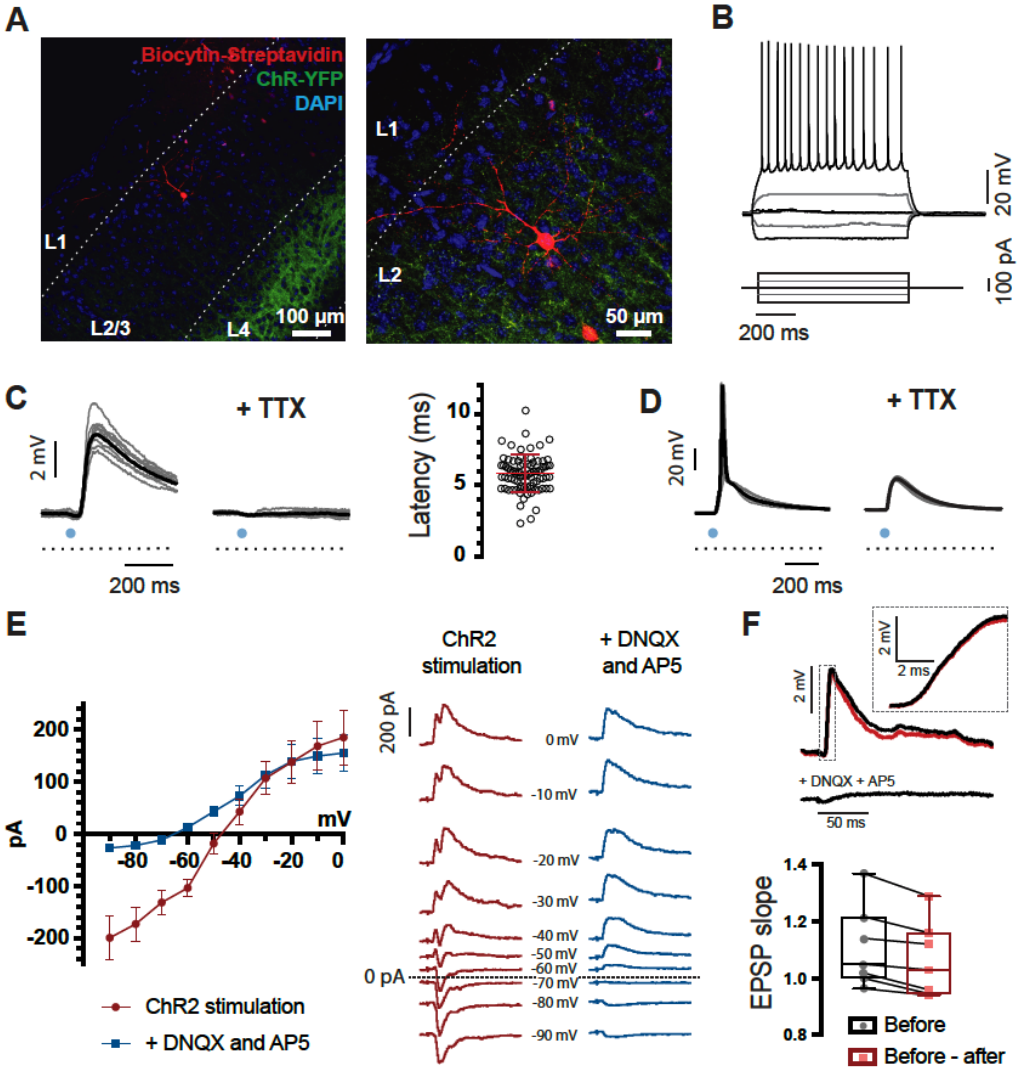

Figure S1 (related to Figure 1): Whole-cell patch clamp of L2/3 neurons in Six3-cre/Ai32 mice.

(A) Example L2/3 neuron recorded in vivo and filled with biocytin.

(B) Example response of the membrane potential of a regular spiking neuron recorded in vivo (top) to different steps of current (bottom).

(C) Light-evoked EPSPs recorded in L2/3 are completely eliminated when tetrodotoxin (TTX) is added to the superfusate. The average EPSP latency of all recordings is shown (n = 92, mean ± SD).

(D) Subthreshold depolarization by direct activation of ChR2 in L4 neurons is unaffected by TTX.

(E) Light-evoked EPSC current-voltage curve before (red) and after (blue) DNQX and AP5 application in acute brain slices. Light intensity was previously adjusted to produce a 4 mV EPSP at resting potential in current clamp. The reversal potential of the ChR2-mediated EPSC could be extrapolated at -47 mV and the inhibitory component at -66 mV. n = 7 cells in N = 3 mice.

(F) Example light-evoked EPSP before (black top) and after (black bottom) DNQX and AP5 application in acute brain slices. The subtracted trace (before minus after) is shown in red. n = 7 cells in N = 3 mice. The box-and-whisker plots represent the maximum, upper quartile, mean (cross), median, lower quartile and minimum values and the values for individual neurons are overlaid. The GABA-mediated component of the EPSP could only account for 4% of the measured slope.

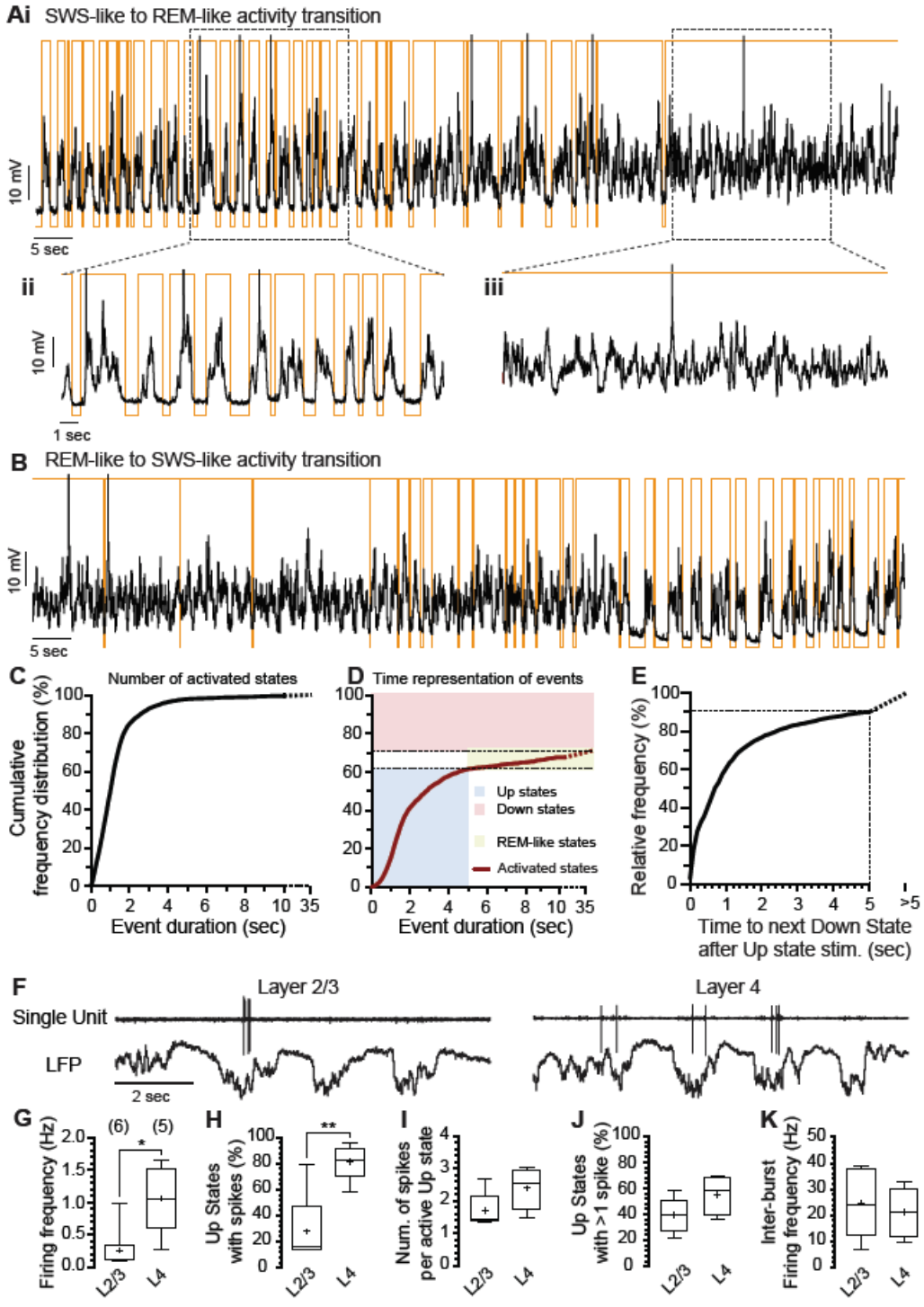
Ai SWS-like to REM-like activity transition
10 mV
5 sec
ii
iii
10 mV
1 sec
B REM-like to SWS-like activity transition
10 mV
5 sec
C Number of activated states
Cumulative frequency distribution (%)
Event duration (sec)
D Time representation of events
Up states
Down states
REM-like states
Activated states
Event duration (sec)
E
Relative frequency (%)
Time to next Down State after Up state stim. (sec)
F
Layer 2/3
Layer 4
Single Unit
LFP
2 sec
G
Firing frequency (Hz)
(6)
(5)
*
L2/3
L4
H
Up States with spikes (%)
**
I
Num. of spikes per active Up state
J
Up States with >1 spike (%)
K
Inter-burst Firing frequency (Hz)

Figure S2 (related to Figure 1): Spontaneous activity in P16-P21 Six3-Cre/Ai32 mice under urethane anaesthesia.

(**A**) Example of slow-wave-sleep (SWS)-like to rapid eye movement (REM)-like activity transition (**i**). The Up and Down state transitions are overlaid in orange and a close up of a SWS-like period (**ii**) and REM-like period (**iii**) are shown. Spikes were cut for display.

(**B**) Example of REM-like to SWS-like transition.

(**C**) Cumulative distribution of the number of activated states (Up states and REM-like states) of different durations. The majority of activated events (84.5%) correspond to Up states lasting < 2 seconds and only 2.2% of the events corresponded to putative REM-like states lasting > 5 seconds. Data obtained from 30 minute recordings in n = 5 neurons in N = 4 mice.

(**D**) Time representation of Up states, putative REM-like states (lasting > 5 seconds) and Down states (as analysed for **C**). Neurons spent 10.1% of the total time in REM-like states.

(**E**) Time to next Down state following Up state stimulation during Up state stimulation protocols (protocols 3, 5, 6 and 7). Only 9% of stimulations were done during putative REM-like states.

(**F**) Example traces of Layer (L)2/3 and L4 single unit recordings paired with LFP recordings in L2/3. n = 6 L2/3 and n = 5 L4 neurons recorded in N = 4 mice.

(**G**) Firing frequency (in Hz) of L2/3 and L4 neurons.

(**H**) Percentage of Up states in which L2/3 and L4 were active.

(**I**) Number of spikes per Up state in which L2/3 or L4 were active (respectively).

(**J**) Percentage of Up states in which neurons spiked and produced more than 1 action potential.

(**K**) Inter-burst frequency when neurons were activated more than once in an Up state.

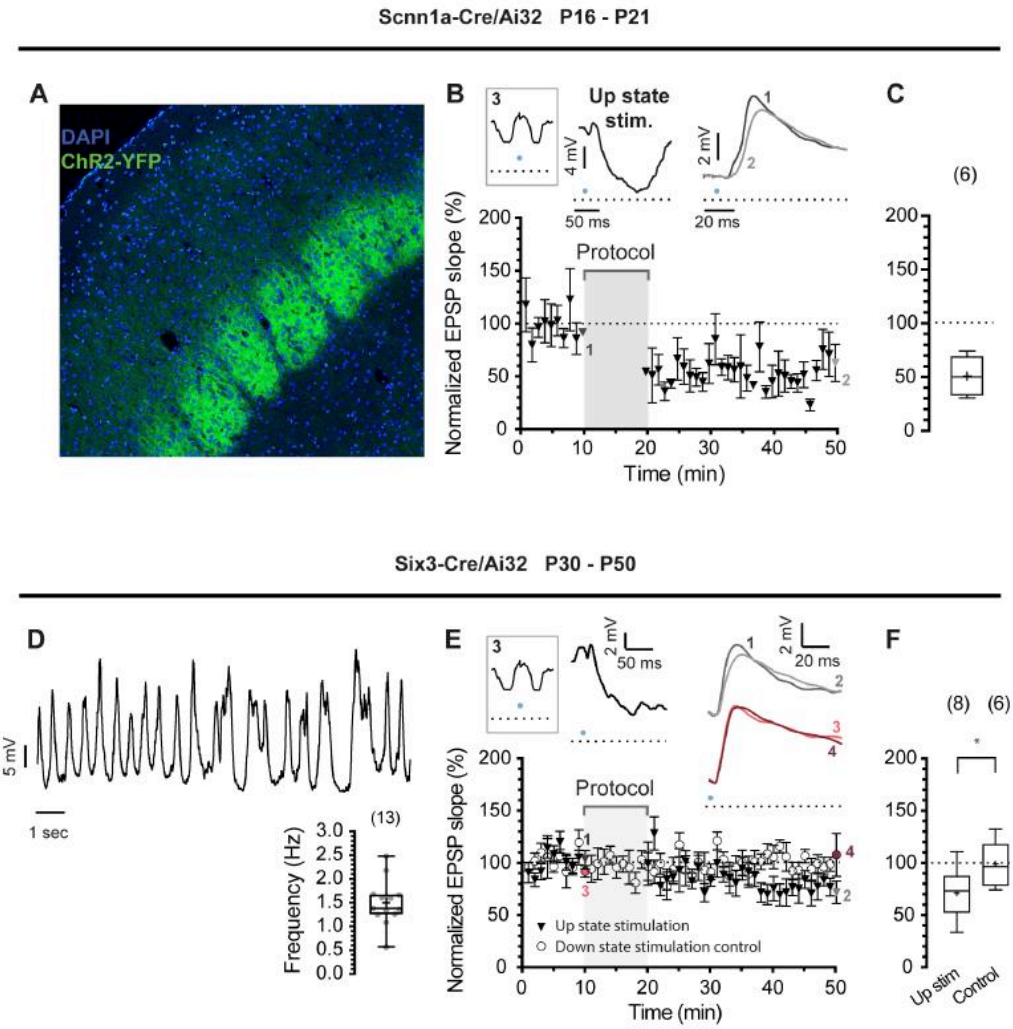

Figure S3 (related to Figure 3): Up state stimulation leads to L4 to L2/3 depression in a different mouse line and at a different age.

(**A**) ChR2 expression pattern in Scnn1a-cre/Ai32 mice.

(**B**) L4 light-stimulation during Up states leads to LTD in Scnn1a-cre/Ai32 mice. Schematic of the stimulation protocol (protocol 3, gray rectangle, top left), representative traces of the plasticity protocol (black trace, top middle) and the

average traces from the 10th and 50th minute of an example experiment (1 and 2 respectively) are shown.

(**C**) Summary of result in B. The box-and-whisker plots represent the maximum, upper quartile, mean (cross), median, lower quartile and minimum values (n = 6 cells in N = 6 mice).

(**D**) Example of spontaneous Up and Down state (UDS) activity in P30-P50 Six3-cre/Ai32 mice under urethane anaesthesia. The UDS frequency for all neurons recorded at this age is shown (n = 13 neurons in N = 10 mice).

(**E**) L4 light-stimulation during Up states leads to depression (black triangles, n = 8 neurons in N = 8 mice) while no changes in synaptic weight are observed when presynaptic stimulation is performed during Down states (control, circles, n = 6 neurons in N = 5 mice).

(**F**) Summary of results in E. Two-tailed Student's t test. * $p < 0.05$.

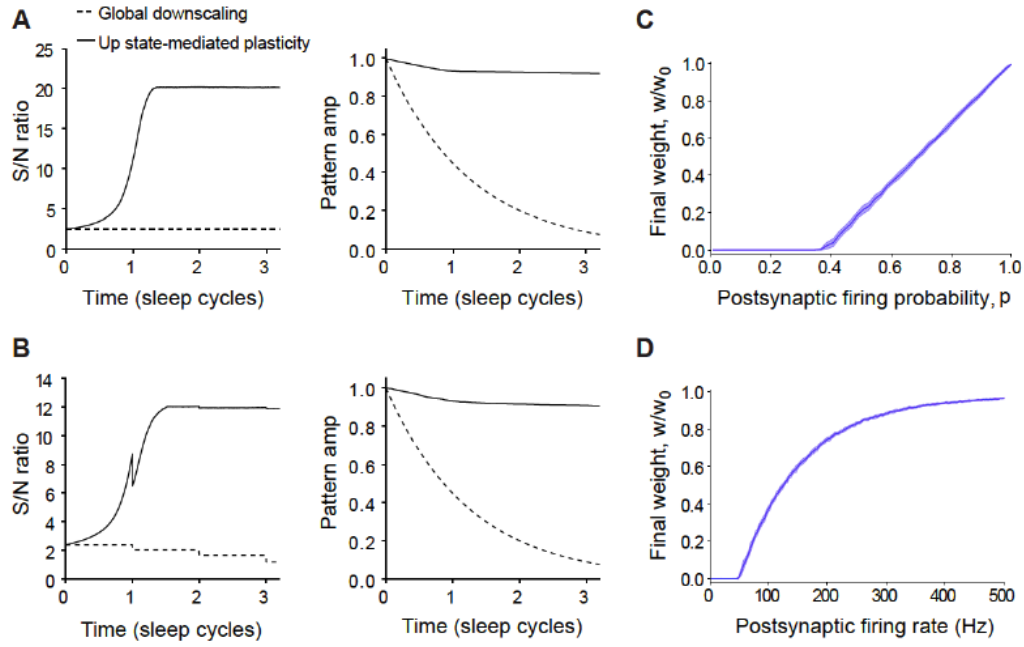

Figure S4 (related to Figure 4): Circuit refinement is independent of specific awake learning rule and synaptic depression can be prevented by postsynaptic activity.

(**A-B**) Simulation of a feedforward network composed of 100 presynaptic neurons (representing L4 neurons) projecting onto one single postsynaptic neuron (representing a L2/3 neuron), analogous to simulations in Figure 4. One 'wake' phase of learning was simulated. During this phase, 5 presynaptic neurons received 50% stronger inputs. The synaptic weights at the end of this simulation were used as the initial weight for the sleep phase. These simulations are analogous to the simulations performed in Figure 4F, but with different awake learning rules.

(**A**) Simulated Up state-mediated plasticity preserves and enhances previously stored patterns without learning between sleep cycles. During sleep cycles, all presynaptic neurons received comparable external input and fired at the same rate, on average. Left: evolution of S/N ratio over three sleep cycles. Right: evolution of pattern amplitudes. During sleep cycles, synaptic weights were updated following either the Up state-modulated plasticity (solid lines) or a homogeneous synaptic scaling rule (dashed lines). Between sleep cycles, synaptic weights were kept fixed. Curves show an average over 50 trials.

(**B**) Simulated Up state-mediated plasticity preserves and enhances previously stored patterns when a second pattern is strengthened between sleep cycles. The simulation was performed in the same way as in A but a second pattern was strengthened between sleep cycles. During sleep cycles, all presynaptic neurons received comparable external input and fired at the same rate, on average. Left: evolution of S/N ratio over three sleep cycles. Right: evolution of pattern amplitudes. During sleep cycles, synaptic weights were updated following either the Up state-modulated plasticity (solid lines) or a homogeneous synaptic scaling rule (dashed lines). Between sleep cycles, the synaptic weights of a second set of presynaptic neurons (pattern 2) were reset to their maximum values. Curves show an average over 50 trials. Our simulations indicate that the Up state-mediated depression leads to circuit refinement independent of the specific rule underlying awake learning.

(**C**-**D**) We simulated a very simple feedforward network, with only one pre- and one postsynaptic neuron. The presynaptic neuron fired at 10 Hz and we assumed

that the connection between the neurons was weak enough such that, at this rate, presynaptic spikes would not elicit postsynaptic action potentials.

(**C**) Ratio between final synaptic weight and initial synaptic weight as a function of p, where p is the probability of the postsynaptic neuron to fire within 10 ms after a presynaptic spike (and then prevent synaptic depression). The synapse was updated following the Up state-mediated plasticity. Curves show an average over 50 trials. Shaded areas represent one standard deviation from average.

(**D**) Ratio between final synaptic weight and initial synaptic weight as a function of the postsynaptic firing rate. Both neurons fired independently following a Poisson process. The synapse was updated following the Up state-mediated plasticity. Curves show an average over 50 trials. Shaded areas represent one standard deviation from average.

Chapter 4

The interplay between somatic and dendritic inhibition promotes the emergence and stabilization of place fields

In the previous chapters, we explored the role of excitation and excitatory plasticity in the development and refinement of sensory representations. We next wonder whether inhibitory neurons play a role in the development excitatory receptive fields. To further explore this question, we focus on the hippocampal CA1 region as a model network. We analyse the emergence and stabilization of place fields in hippocampal CA1 pyramidal cells. When an animal enters a novel environments, the interneuron activity is modulated. More specifically, parvalbumin-expressing (PV) interneuron activity is upregulated whereas somatostatin-expressing (SST) interneuron activity

is suppressed. We investigate how this modulation of interneuron activity in novel environments promotes the emergence of new receptive fields. Our simulations suggest that dendrite-targeting interneurons—thought of as SST interneurons—play a crucial role in place field development and stabilization, whereas soma-targeting interneurons—thought of as PV interneurons—can quickly and reversibly turn silent cells into place cells.

The layout of the work will be presented in an article format as it has been submitted for publication. We would like to thank Claudia Clopath for supervising and guiding the project.

The interplay between somatic and dendritic inhibition promotes the emergence and stabilization of place fields

Abstract

During the exploration of novel environments, place fields are rapidly formed in hippocampal CA1 neurons. Place cell firing rate increases in early stages of exploration of novel environments but returns to baseline levels in familiar environments. Although similar in amplitude and width, place fields in familiar environments are more stable than in novel environments. We propose a computational model of the hippocampal CA1 network, which describes the formation, dynamics and stabilization of place fields. We show that although somatic disinhibition is sufficient to form place cells, dendritic inhibition along with synaptic plasticity is necessary for place field stabilization. Our model suggests that place cell stability can be attributed to large excitatory synaptic weights and large dendritic inhibition. We show that the interplay between somatic and dendritic inhibition balances the increased excitatory

weights, so that place cells return to their baseline firing rate after exploration. Our model suggests that different types of interneurons are essential to unravel the mechanisms underlying place field plasticity. Finally, we predict that artificially induced dendritic events can shift place fields even after place field stabilization.

Keywords: hippocampus, CA1, synaptic plasticity, computational model, place cells, place fields.

4.1 Introduction

The hippocampus encodes spatial information through a subset of pyramidal cells—the place cells—that fires action potentials when the animal is in a specific location within the environment—the place fields [O'Keefe, 1976; O'Keefe and Dostrovsky, 1971; O'Keefe and Nadel, 1978; Wilson and McNaughton, 1993]. These neurons are thought to encode and store new memories by taking part in activity-dependent synaptic plasticity [Bliss and Collingridge, 1993; Golding et al., 2002; Magee and Johnston, 1997; Schiller et al., 1998; Sheffield and Dombeck, 2019]. How these place fields are formed is not clear and recent experimental data, while unravelling specific parts of the mechanisms underlying place cell dynamics, have also opened up some puzzling questions, especially when put together [Bittner et al., 2017; Cohen et al., 2017; Epsztein et al., 2011; Frank et al., 2004; Grienberger et al., 2017; Lee et al., 2012; Sheffield et al., 2017; Sheffield and Dombeck, 2019]. Although here we focus on the role of hippocampal cells in spatial memory development, the hippocampus is also associated with other types of memories [Fanselow, 2000; Mayford, 2013], and the principles governing place field dynamics are likely to be common across several types of hippocampal memory formation.

Subthreshold responses of silent cells, when recorded at the soma, are not place-tuned [Epsztein et al., 2011]. If a spatially uniform current is applied to a silent

cell, however, this cell starts to produce place-tuned activity [Lee et al., 2012]. This transition from silent to place cell is abrupt and once the silent cell is turned into a place cell, the amplitude of the place field is fairly independent of the amplitude of the applied current [Lee et al., 2012]. These results suggest that silent cells receive place-tuned inputs even though there is no signature of those inputs at the soma. Therefore, inputs from dendrites are thought to be nonlinearly propagated to the soma with the somatic depolarization acting as a gate for this propagation [Lee et al., 2012]. The functional consequences of this gating for the hippocampal network have not been fully explored. For instance, it is not clear which elements of the network are responsible for modulating this dendrite-to-soma propagation.

There is increasing evidence suggesting that place fields are not formed from scratch [Cacucci et al., 2007; Cohen et al., 2017; Dragoi and Tonegawa, 2011, 2013, 2014; Epsztein et al., 2011; Frank et al., 2004; Fyhn et al., 2007; Hill, 1978; Kentros et al., 1998; Leutgeb et al., 2005, 2004; McHugh et al., 1996; Sheffield et al., 2017]. Instead, spatial representation might be built from the selection of already strong connections, without the need for synaptic plasticity [Dragoi and Tonegawa, 2011, 2013, 2014; Lee et al., 2012]. For instance, many place fields, although not stable, are present from the animal's first traversal of a novel environment [Epsztein et al., 2011; Frank et al., 2004; Hill, 1978; Sheffield et al., 2017]. Furthermore, additional place cells are formed mainly during the first few laps of exploration [Sheffield et al., 2017]. This poses a question for the role of synaptic plasticity in place field development.

During exploration of a novel linear track, new place fields are formed over several laps [Sheffield et al., 2017]. The development of these new place fields has been shown to be preceded by dendritic regenerative events—back propagating action potentials or dendritically generated spikes [Sheffield et al., 2017; Sheffield and Dombeck, 2015]—which are promoted by a reduction in dendritic inhibition through the suppression of somatostatin-expressing (SST) interneuron activity [Sheffield

et al., 2017]. These dendritic events can be associated with a myriad of factors such as dendritic disinhibition [Doron et al., 2017; Grienberger et al., 2017; Müller et al., 2012], back-propagating action potentials [Hill et al., 2013; Magee and Johnston, 1997; Spruston et al., 1995; Zhou et al., 2008], NMDA spikes [Brandalise et al., 2016; Gasparini et al., 2004; Palmer et al., 2014], or plateau potentials [Bittner et al., 2015; Grienberger et al., 2014; Takahashi and Magee, 2009]. More recently, the conjunctive activation of presynaptic inputs and postsynaptic calcium plateau potentials have been applied to artificially induce new place fields [Bittner et al., 2015, 2017]. Additionally, place fields have also been induced following juxtacellular stimulation of CA1 silent cells [Diamantaki et al., 2018]. Although dendritic disinhibition has been implicated in place field development [Sheffield et al., 2017], it is still not clear which role the different types of interneuron play in place field formation and stabilization.

Overall CA1 pyramidal cell depolarization is initially low but rapidly increases during exploration of novel environments [Cohen et al., 2017], which might be linked to a quick increase in place cell firing rate in early stages of exploration [Cohen et al., 2017; Frank et al., 2004]. Surprisingly, in familiar environments, subthreshold hill of depolarization associated with place field firing returns to a lower level, comparable to the level observed during initial exploration of novel environments [Cohen et al., 2017]. Remarkably, although the level of CA1 pyramidal cell depolarization is similar in the first stages of exploration of novel environments and in familiar environments, place fields in familiar environments have been shown to be considerably more stable [Cacucci et al., 2007; Cohen et al., 2017; Leutgeb et al., 2004; Wilson and McNaughton, 1993]. Synaptic plasticity has been suggested to be involved in this stabilization [Cohen et al., 2017]. Moreover, the blockage of NMDA receptors in CA1 neurons has been shown to significantly decrease the number of new place fields being formed across the network [Sheffield et al., 2017]. These results suggest that synaptic plasticity is not required for the formation of place fields but is involved

in the development of new place cells and stabilization of spatial representations. Therefore, these results lead to the question of what role synaptic plasticity plays in place field stabilization.

Several computational models have been proposed to account for place field development [Barry et al., 2006; Battaglia and Treves, 1998; Blair et al., 2008; Burgess and O'Keefe, 2011; Conklin and Eliasmith, 2005; Franzius et al., 2007; Grienberger et al., 2017; Hartley et al., 2000; Knierim and Zhang, 2012; Levy, 1996; Samsonovich and McNaughton, 1997; Soman et al., 2018; Treves and Rolls, 1994; Tsodyks, 1999; Weber and Sprekeler, 2018]. The interaction between excitatory and inhibitory plasticity has been shown to lead to the development of place fields in initially untuned pyramidal cells [Weber and Sprekeler, 2018]. Alternatively, attractor network models have been proposed as more abstract models of hippocampal circuit dynamics [Battaglia and Treves, 1998; Conklin and Eliasmith, 2005; Knierim and Zhang, 2012; Levy, 1996; Samsonovich and McNaughton, 1997; Treves and Rolls, 1994; Tsodyks, 1999] and some models have even been extended to more than two dimensions [Soman et al., 2018]. All these models, however, do not take into account individual interneuron types and their modulation during exploration of novel environments.

All these questions call for a simplified computational model that can account for place field formation and stabilization in order to understand the mechanisms underlying these processes. We therefore develop a data-driven model of the hippocampal CA1 network. We show that somatic disinhibition is sufficient to form place cells. However, dendritic inhibition and synaptic plasticity allows for silent cells to turn into stable place cells. We show that the combined action of somatic and dendritic inhibition balances an increase in excitatory weights due to synaptic plasticity, so that place cells after exploration return to their baseline firing rate. Our model suggests that place cell stability is due to large excitatory synaptic weights and large dendritic inhibition. Therefore, our model suggests that different types of interneurons are

essential to unravel the mechanisms underlying place field plasticity. Finally, we use our model to predict how to perturb place fields. Artificially induced dendritic events in place cells can shift place field location even after place field stabilization. Our model reproduces a wide range of observations from the hippocampal CA1 network, provides a circuit level understanding, and finally makes predictions that can be tested in future experiments. Importantly, our model suggests that interneuron diversity is crucial for the emergence of place fields and their consolidation.

4.2 Results

In all simulations, we model CA1 pyramidal neurons as two-compartment, rate-based neurons (figure **1**A). The neurons are composed of a non-linear dendritic unit, that accounts for dendritic spikes, and a perisomatic unit (figure **1**A). Place cells can be observed even during the first stages of exploration of novel environments [Cacucci et al., 2007; Cohen et al., 2017; Dragoi and Tonegawa, 2011, 2013, 2014; Epsztein et al., 2011; Frank et al., 2004; Fyhn et al., 2007; Hill, 1978; Kentros et al., 1998; Leutgeb et al., 2005, 2004; McHugh et al., 1996; Sheffield et al., 2017] and silent cells can be quickly turned into place cells upon the injection of a spatially uniform current [Lee et al., 2012]. Therefore, we assume that all CA1 cells—both active and silent cells—receive place-tuned inputs which are projected onto their dendrites when the animal enters a new environment. Additionally, the propagation of dendritic activity to the soma is not uniform and, in particular, can be modulated by somatic depolarization [Jarsky et al., 2005; Lee et al., 2012]. In our model, the propagation of inputs from dendrites to soma is gated by the somatic "potential" which is determined by the total input projected directly onto the perisomatic unit (figure **1**A, see methods). To account for changes in synaptic connections, we implement an activity-dependent synaptic plasticity rule. Synaptic potentiation has been shown to be dependent on the activation of presynaptic terminals paired with strong postsynaptic dendritic

depolarization [Bittner et al., 2017; Brandalise et al., 2016; Magee and Johnston, 1997; Sheffield and Dombeck, 2019; Spruston et al., 1995; Takahashi and Magee, 2009]. For the sake of simplicity, we assume that synaptic plasticity depends on presynaptic activity and the postsynaptic dendritic activation only (figure **1**A, see methods for details). Moreover, the simulated CA1 pyramidal cells receive inhibitory inputs from two types of interneurons: dendrite-targeting interneurons (thought of as a subset of SST cells) and soma-targeting interneurons (thought of as a subset of parvalbumin-expressing cells) (figure 1A). The interneuron activity is assumed to be spatially uniform [Grienberger et al., 2017]. Finally, Sheffield et al. [Sheffield et al., 2017] have shown that the exploration of novel environments modulates CA1 interneuron activity in an interneuron-type-specific manner [Sheffield et al., 2017]. They observed a decrease in SST interneuron activity accompanied by an increase in parvalbumin-expressing (PV) interneuron activity that lasts for tens of seconds when the animal enters a novel environment [Sheffield et al., 2017]. In our model, we hypothesize the existence of a novelty signal responsible for modulating interneuron activity once the animal enters a new environment (figure **2**A, see methods). This novelty signal increases instantly once the animal enters the environment and decays exponentially with a time constant of 100 s (see methods). This novelty signal leads to the suppression of dendrite-targeting inhibition and the amplification of soma-targeting inhibition (figure **2**A). Both interneuron activities slowly return to baseline levels as the novelty signal fades away.

Somatic disinhibition is sufficient to turn silent cells into place cells

We first investigate how silent cells can be transiently turned into place cells through the injection of a spatially uniform current [Lee et al., 2012]. We simulate 10 input neurons, which could be thought of as part of CA3, projecting onto one postsynaptic CA1 neuron. Here, we assume that the animal is running through a familiar envi-

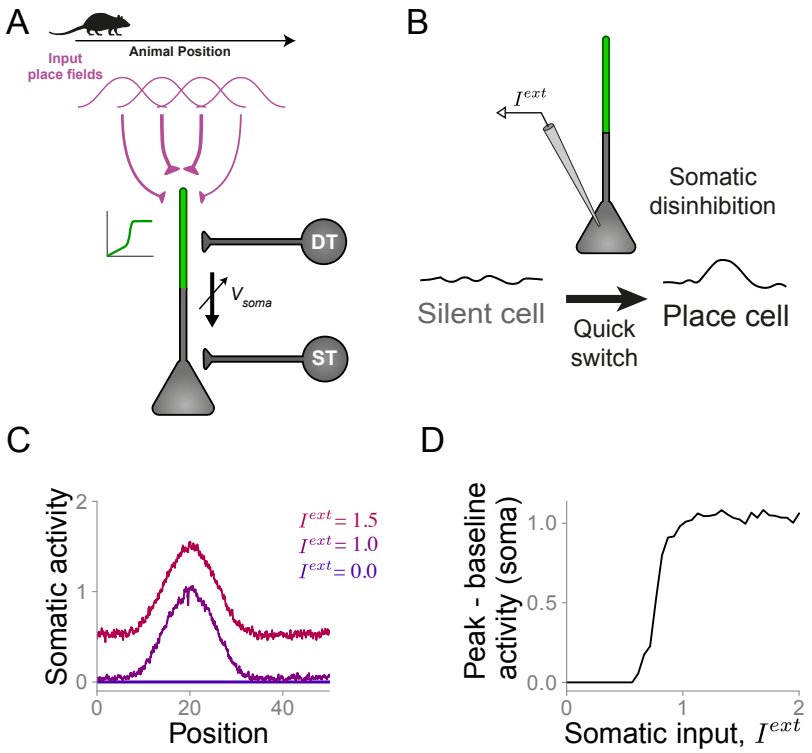

Figure 1: **Somatic disinhibition is sufficient to turn silents cells into place cells. (A)** Network diagram. Pyramidal neurons receive place-tuned, excitatory input and inputs from two types of interneurons: dendrite-targeting (DT), representing somatostatin-expressing interneurons, and soma-targeting (ST), representing parvalbumin-expressing interneurons. The propagation of inputs from dendrites to soma is gated by the somatic "potential" (see methods). The CA1 pyramidal cell is modelled as a two-compartment neuron model with a nonlinear dendritic unit and a perisomatic unit. **(B)** Diagram of a silent cell being turned into a place cell following spatially uniform somatic depolarization. **(C)** Pyramidal cell firing rate as a function of the animal position for three different amplitudes of external injected current: zero, 1.0 and 1.5. **(D)** Difference between peak and baseline firing rate as a function of the external somatic input. Because of the gated propagation of inputs from dendrites to soma, there is an abrupt transition from silent to place cell.

ronment and, therefore, there is no novelty signal and the interneuron activity is constant throughout these simulations. For simplicity, all presynaptic neurons are assumed to have time-invariant, uniformly distributed place fields, spanning over the entire track. These presynaptic neurons project onto one postsynaptic CA1 neuron through non-uniform connections. Although not uniform, the initial synaptic weights

are such that the postsynaptic CA1 cell is silent during the first lap of exploration. During the second lap of exploration, an external depolarizing current is applied to the somatic compartment. Since plasticity is slow, synaptic weights are not significantly changed from the first to the second lap. However, because the propagation of inputs from dendrites to soma is gated by somatic depolarization, silent cells are rapidly turned into place cells in an all-or-nothing manner (figure 1B-D). For weak external currents, silent cells remain silent (figure 1C, $I^{ext} = 0$). For sufficiently strong external currents, however, silent cells are turned into place cells (figure 1C, $I^{ext} = 1.0$ and $I^{ext} = 1.5$). Furthermore, the transition from silent to place cell is abrupt. Given that the amplitude of the injected current is above a certain threshold, the neuron is turned into a place cell and the amplitude of the place field does not depend on the amplitude of the injected current (figure 1D). If the external current is removed, the neuron becomes silent again. Therefore, our model indicates that silent cells can be transiently turned into place cells due to a combination of two features: silent cells receive place-tuned input and the propagation of these inputs from dendrites to soma is gated by somatic depolarization. Since the somatic input is also controlled by soma-targeting inhibitory neurons, these cells could also act as a gate for the propagation of inputs from dendrites to soma.

Dendritic disinhibition and synaptic plasticity promote the development of place cells

Using our model, we next investigate whether there is an alternative mechanism underlying place field formation from originally silent cells (figure 2A-B). As before, we simulate 10 input neurons projecting onto one postsynaptic CA1 neuron. Synaptic connections from input neurons to the postsynaptic neuron are plastic and their change depends on the activity of the postsynaptic dendritic compartment. Here, the animal explores a novel environment for several laps. Inspired by the experiments

from Sheffield et al. [Sheffield et al., 2017], we simulate a "novelty signal", so that the activity of dendrite-targeting interneurons is initially low in novel environments and increases gradually while the environment is becoming familiar, whereas the activity of soma-targeting interneurons is initially high and gradually decreases (figure 2A). Simulating our model reveals that the reduction in dendrite-targeting inhibition increases dendritic activity in the pyramidal cells, regardless of the somatic activity (figure 2C). This dendritic activation leads to a quick strengthening in synaptic weights (figure 2E-G). The combination of stronger synaptic weights and a later decrease in soma-targeting inhibition finally leads to the development of place-tuned somatic activity (figure 2C-D). Therefore, our model suggests that the combination of dendritic-activity-dependent synaptic plasticity and novelty-modulated interneuron activity can turn silent cells into place cells. Interestingly, dendritic activity in simulated CA1 neurons precedes and predicts place field development in silent cells in our model, consistent with the experimental findings from Sheffield et al. [Sheffield et al., 2017].

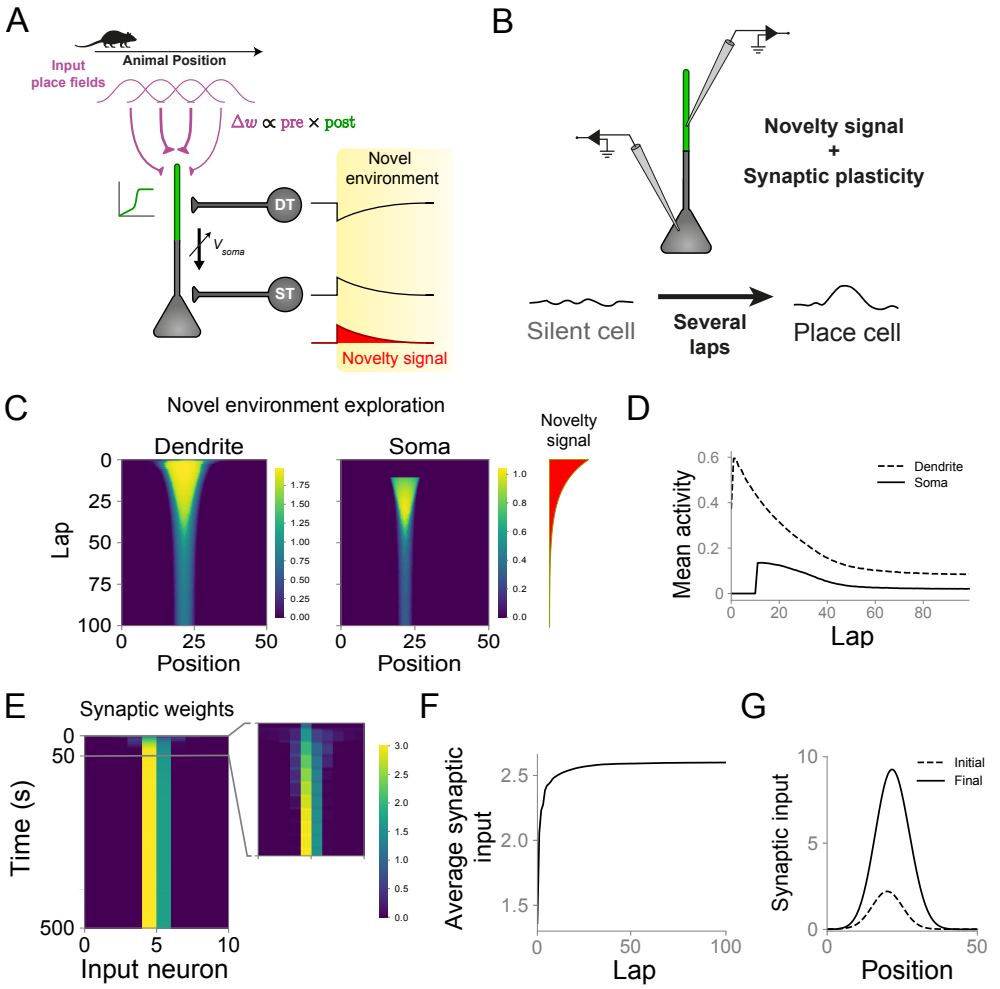

Figure 2: **Dendritic disinhibition and synaptic plasticity promote the development of place cells. (A)** Network diagram similar to figure 1A. The activity of interneurons is modulated during the exploration of novel environments. DT interneuron activity (top black curve) decreases, whereas ST interneuron activity (bottom black curve) increases in novel environments. Both interneuron activities gradually return to baseline levels with a timescale defined by the hypothesized novelty signal (red curve, see methods and main text for details). Synaptic connections from input neurons to CA1 pyramidal cells are updated following a Hebbian-type learning rule dependent on presynaptic activity and postsynaptic dendritic activation. **(B)** Diagram of a silent cell being turned into a place cell after several laps of exploration of a novel environment (see methods). **(C)** Silent cell turns into place cell following exploration of a novel environment. Evolution of dendritic (left) and somatic (middle) activity during exploration of a novel environment for an initially silent cell. Amplitude of novelty signal over laps (right, red). Dendritic activity precedes somatic activation, in agreement

with experiments [Sheffield et al., 2017]. Somatic activity increases abruptly due to the gated propagation of dendritic inputs (see methods). **(D)** Evolution of mean dendritic and somatic activity for one example neuron. The neuron is initially silent (no somatic activity) and is turned into a place cell after several laps of exploration. **(E)** Evolution of synaptic weights for the same example cell shown in C. Inset: first 10% (50 s) of exploration. **(F)** Evolution of average synaptic input over laps for the same example cell as in C. **(G)** Initial (dashed) and final (solid) synaptic inputs as a function of the animal position for the same example cell as in C. The synaptic input was measured as the convolution between initial/final synaptic weights and the input neuron activities.

The interplay between somatic and dendritic inhibition balances increased excitatory synaptic weights so that place cell firing returns to baseline

Next, we use our model to study neurons that are initially active when the animal enters a new environment (figure 3A). We aim to understand the mechanisms that could lead to place field stabilization and that underlie place field dynamics. As before, our model consists of a CA1 cell receiving place-tuned inputs. But here, the synaptic weights are such that the neuron is active since the first lap of exploration (figure **3**B-E, blue traces). The initial low dendritic inhibition in our model leads to the activation of dendritic compartments and thus the strengthening of synaptic weights. Stronger synaptic weights produce a stronger neuronal response (figure **3**B-E, purple traces). However, as the animal explores the environment, the novelty signal gradually dissipates, resulting in the increase in dendritic inhibition and thus in a lower activation of the dendritic compartment (figure **3**C, orange trace). The lower level of somatic inhibition in familiar environments allows the neuron to exhibit the same level of activity as is exhibited during the first stages of exploration, even under reduced dendritic activation (figure **3**E, orange trace, and figure **3**F). Our model is therefore consistent with the experimental data showing that overall CA1 pyramidal cell depolarization increases in early stages of novel environment exploration and later

returns to initial levels in familiar environments [Cohen et al., 2017]. Importantly, although the neuronal firing on the first and last laps are indistinguishable, the network states are completely different. During the first lap, the neuron receives weak excitatory input, weak dendritic inhibition, and strong somatic inhibition (figure 3G). Synaptic plasticity then leads to the strengthening of synaptic weights, forming strongly-tuned connections (figure 3F-G). Finally, the decay of the novelty signal leads to a slow shift in soma- and dendrite-targeting inhibition. During the last lap—when the environment is familiar—the neuron receives strong excitatory input, strong dendritic inhibition, and weak somatic inhibition (figure **3**G). Therefore, the intricate interplay between excitatory plasticity and somatic and dendritic inhibition leads to the development of a new network structure. Although this new state presents the same network output, it might have different stability properties.

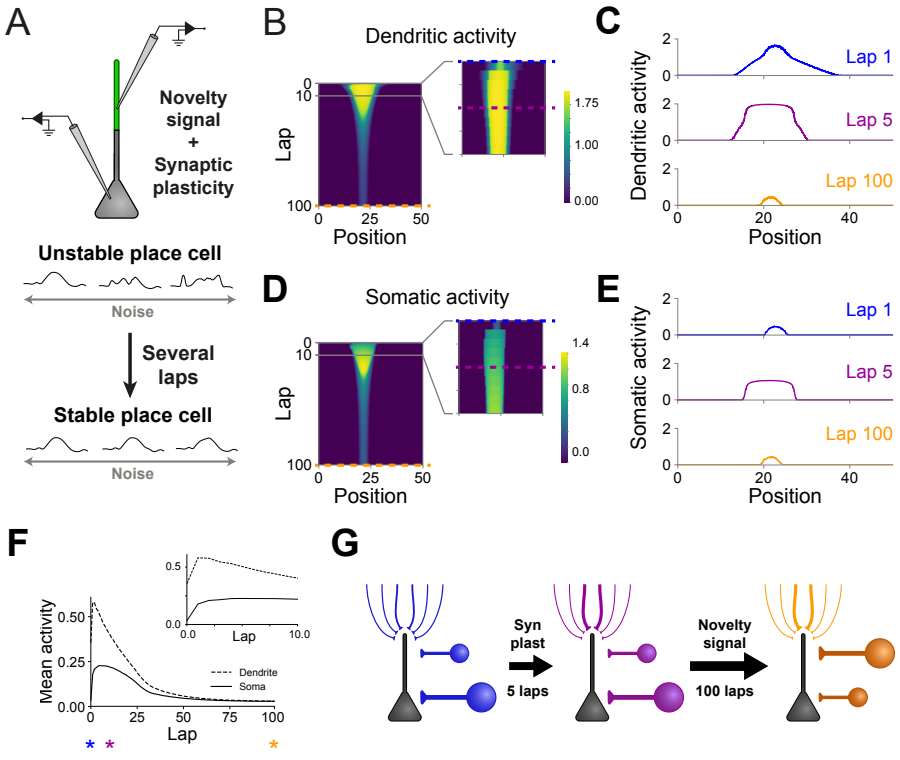

Figure 3: **The interplay between somatic and dendritic inhibition balances increased excitatory synaptic weights so that place cell firing returns to baseline.** **(A)** Diagram of an unstable place cell becoming stable after several laps of exploration of a novel environment (see methods). Place cells are assumed to be unstable due to their sensitivity to noise. **(B)** Evolution of dendritic activity for an example place cell. Inset: first 10 laps of exploration. **(C)** Dendritic activity as a function of the animal's position for three stages of the simulation: lap 1 (top, blue; blue dashed line in (B)), lap 5 (middle, purple; purple dashed line in (B)), and lap 100 (bottom, orange; orange dashed line in (B)). **(D)** Evolution of somatic activity for the same cell as in (B). Inset: first 10 laps of exploration. **(E)** Somatic activity as a function of the animal's position for three stages of the simulation: lap 1 (top, blue; blue dashed line in (D)), lap 5 (middle, purple; purple dashed line in (D)), and lap 100 (bottom, orange; orange dashed line in (D)). **(F)** Evolution of mean dendritic (dashed line) and somatic (solid line) activity for the same example cell as in (B) and (D). Stars indicate laps 1 (blue), 5 (purple) and 100 (orange). Both somatic and dendritic activities increase sharply during the first laps of exploration due to synaptic plasticity. Inset: first 10 laps of exploration. **(F)** Diagram showing the changes in the network from the first to the last lap of exploration. Initially (left, blue), input synaptic weights are weak, dendritic inhibition is low and somatic inhibition is high. Next, synaptic weights are quickly strengthened through activity-dependent synaptic plasticity (middle, purple). During the final lap (right, orange), some input synaptic weights are strong, dendritic inhibition is high and somatic inhibition is low. Therefore, although place field amplitude and width are the same in the first and last lap (D blue and orange), the network is in a different state.

Large excitatory synaptic weights and large dendritic inhibition provide place cell stability

We next investigate whether place fields in familiar environments are more stable than at the beginning of the exploration phase in novel environments—despite being similar in amplitude and width. Place fields have been shown to be unreliable and to change abruptly from lap to lap in novel environments [Cohen et al., 2017]. We speculate that this variability is caused by the place field's sensitivity to noise rather than synaptic plasticity processes. We assume that the place field can be affected by three sources of noise: (i) noise on the place fields of presynaptic neurons, (ii) noise on the firing rates of presynaptic neurons, or (iii) noise on synaptic weights, accounting, for example, for synaptic turnover or synaptic failure (figure **4**). In all three cases, we

compare the effect of noise on place fields at the beginning of exploration (figure **4**, blue curves) to its effect on place fields at the end of exploration (figure **4**, orange curves; see methods). In case (i), we assume that the amplitudes of presynaptic place fields are not all the same. Instead, we multiply each place field by a random number whose variance increases with the noise amplitude (see methods). As expected, the more noise we impose, the less stable place cells are (figure **4**A). However, the noise on presynaptic place fields is more effective at destabilizing place cells in the first lap of exploration than at the end of exploration (figure **4**A), suggesting that place cells become more stable. In case (ii), we assume that all presynaptic place fields have the same amplitude but input neurons can also fire at any time with probability p. This probability increases linearly with noise amplitude. Again, place fields at the final lap are more stable than initial place fields (figure **4**B). In case (iii), we change synaptic weights by random amounts drawn from a normal distribution whose variance is proportional to the noise amplitude. This source of noise also affects initial place fields more than it does to final place fields (figure **4**C). In all three cases, the stabilization of place fields results from increased synaptic weights and higher dendritic inhibition (figure **3**G). Therefore, place fields in familiar environments are more stable to noise than place fields at the beginning of exploration of novel environments, consistent with experimental observations [Cohen et al., 2017].

In order to investigate the role of each component of the network in stabilizing place fields, we artificially modify the final state of the network while keeping the neuron's place field unchanged. We first reduce the amplitude of both excitatory weights and dendritic inhibition (figure S1A). The reduced synaptic weights decrease place field stability when noise is added on the synaptic weights (figure S1B). Next, we reduce dendritic inhibition and increase somatic inhibitory input (figure S1C). Since synaptic weights are strong and dendritic inhibition is low, the postsynaptic neuron is more susceptible to presynaptic inputs. Thus, noise on presynaptic neurons is

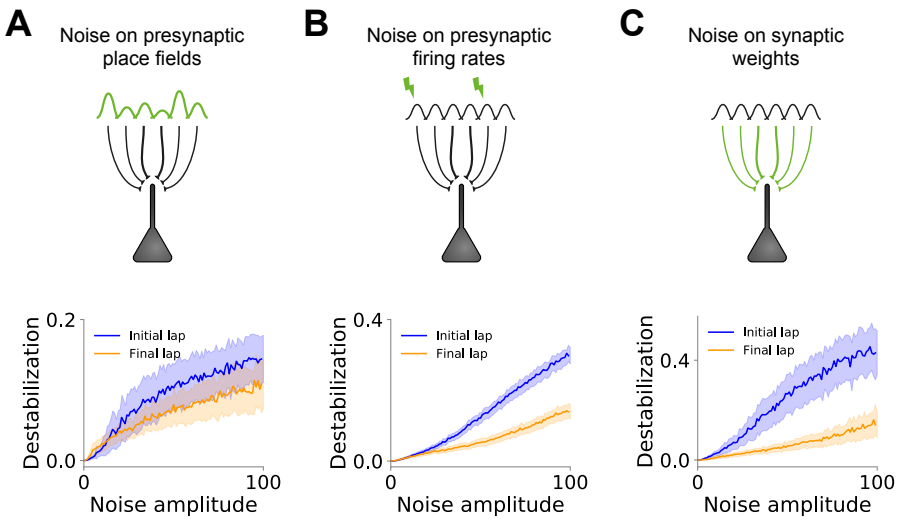

Figure 4: **Large excitatory synaptic weights and large dendritic inhibition provide place cell stability. (A-C)** Effect of noise on place fields for the first (blue) and last (orange) laps of exploration. **(A)** Destabilization of place fields by noise on presynaptic place fields. We measure the change on postsynaptic place field following changes on presynaptic place field amplitudes (see methods). **(B)** Destabilization of place fields by noise on presynaptic firing rates. We measure the change on postsynaptic place field following the addition of a noisy input to presynaptic neurons (see methods). **(C)** Destabilization of place fields by noise on synaptic weights. We measure the change in postsynaptic place field following changes on synaptic weights (see methods). For all three sources of noise (A-C), the effect of the noise over place fields is higher in the first lap than in the last lap.

carried on to postsynaptic place fields, destabilizing them (figure S1D). In summary, strong synaptic connections are relatively less affected by noise on synaptic weights, whereas higher dendritic inhibition cancels out-of-field fluctuations being transmitted from presynaptic neurons.

We next investigate whether dendritic nonlinearity can contribute to stable place field development. While our model has indicated that dendritic disinhibition opens a window for synaptic plasticity and promotes place cell development, we hypothesize that dendritic nonlinearities might promote place cell stability by ensuring that the location of a place field does not change once the place field is developed. In our model, when inputs are strong enough, they can induce dendritic spikes, which in

turn lead to strong potentiation. Because of competition mechanisms such as synaptic normalization, the remaining inputs are depressed, pushing them further away from the threshold for dendritic events. Without dendritic nonlinearities, the noise could be enough to counter-balance this competition, leading to unstable place fields. As such, dendritic spikes—or dendritic nonlinearities—might form a mechanism for reliably selecting presynaptic inputs. To test this hypothesis, we simulate our model with initially uniform synaptic weights and no novelty signal. We then compare it with an alternative model where dendrites do not have an amplifying nonlinearity but can reach the same maximum level of activity (linear dendrites, figure S2A-B). Neurons with a dendritic nonlinearity develop place fields faster and, importantly, more reliably (figure S2C). In several cases, neurons with linear dendrites do not develop place fields and their activities vary from lap to lap (figure S2D). Contrarily, neurons with a dendritic nonlinearity consistently develop stable place fields. Therefore, our model suggests that dendritic nonlinearities might contribute to place field development and stability by promoting a reliable selection of inputs.

Artificially induced dendritic events induce place field plasticity

Using our model, we next explore whether it is possible to perturb or change single CA1 place fields [Bittner et al., 2015, 2017; Diamantaki et al., 2018; Takahashi and Magee, 2009]. We simulate a single neuron receiving place-tuned input such that one of its input synapses is stronger than the remaining connections. We assume that the animal is exploring a novel environment. As such, interneuron activity is modulated by a novelty signal that decays over time. The stronger synaptic weight leads to the activation of the postsynaptic neuron, which leads to the strengthening of that synaptic weight (figure **5**A-B, see methods). This positive feedback loop leads to the development of a strong place field when the environment becomes familiar (figure **5**B).

We then test whether we can shift the tuning of the place field towards a new location by artificially activating CA1 neurons. In order to do that, we simulate the network until the novelty signal is negligible—the environment is hence considered familiar—and the postsynaptic place field is stable. At this stage, we inject an extra current in the dendritic compartment of the simulated neuron to induce a strong dendritic activity. The current is injected in the dendritic compartment because, in our model, the synaptic plasticity is assumed to depend on dendritic activation only. This current is induced only in a small region within the track, far from the peak of the postsynaptic place field (figure **5**, see methods). The induction of extra dendritic activity over one lap does not alter the postsynaptic place field (figure **5**B). We next induce the extra dendritic activity over several (15) laps. In this case, the position of the place field is shifted towards the new location (figure **5**D). For an intermediate number of induction laps, the initial place field is removed without the formation of a new place field, thus turning the place cell into a silent cell (figure **5**C, figure S3C). Note that this newly formed silent cell can potentially redevelop a place field in case there is remaining dendritic activity. This dendritic activity allows for plasticity, and therefore for the re-emergence of a place field (figure S3B). Altogether, our model predicts that, if induced over enough laps, artificial dendritic activity can shift place field location.

The size of the induction region might affect the efficacy to shift place field location. We hypothesized that shifting place fields would be easier with a larger induction region. To investigate this, we increase the induction area to three times its original size. In this case, the induction over one lap is enough to remove the initial place field, but not enough to induce the formation of a new one (figure **5**E). In contrary to what we hypothesized, the induction over 15 laps—which is enough to induce the development of a new place field for a small induction area—is not enough to promote the development of a new place field (figure **5**F). The larger the induction area, the easier it is to remove the initial place tuning (figure **5**G). Nevertheless, a

large induction area leads to a competition between inputs within that area. Because of that, our model predicts that, surprisingly, the larger the induction region, the more induction laps are needed to induce the development of new receptive fields (figure **5**H).

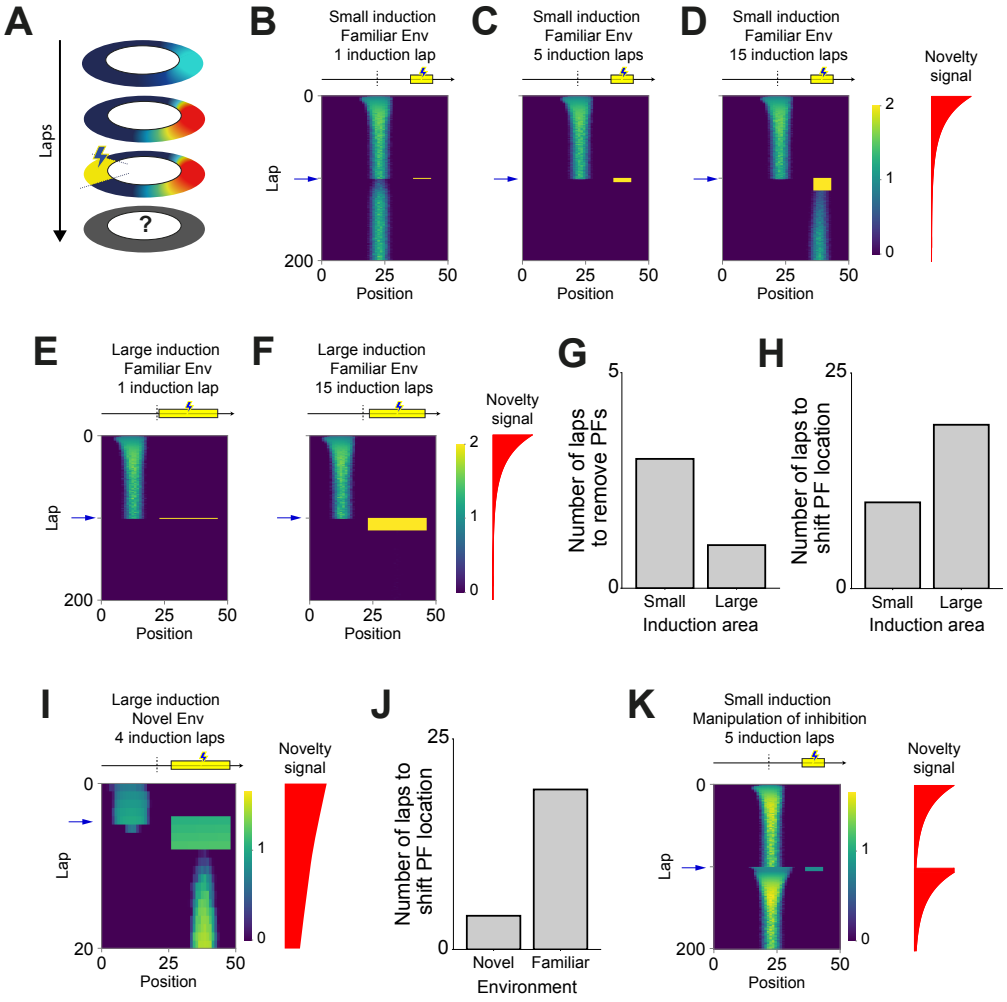

Figure 5: **Artificially induced dendritic events induce place field plasticity. (A)** Single-cell diagram. **(B-D)** Evolution of place fields for the case in which an extra current is applied to the postsynaptic neuron while the animal traverses a small section (15%) of the track. Yellow bar indicates the induction region in which the extra current is applied. Dashed line indicates the position of the peak of the initial place field. Blue arrow indicates the

first induction lap (lap 100). Red curve shows the evolution of the novelty signal over laps. **(B)** Place field evolution for 1 induction lap. Place fields are not disturbed following the application of extra current. **(C)** Place field evolution for 5 induction laps. Place fields are removed by the application of extra current. **(D)** Place field evolution for 15 induction laps. Place fields are shifted towards a new position determined by the region of extra current application. **(E-F)** Evolution of place fields for the case in which an extra current is applied to the postsynaptic neuron while the animal traverses a large section (45%) of the track. Yellow bar indicates the induction region in which the extra current is applied. Dashed line indicates the position of the peak of the initial place field. Blue arrow indicates the first induction lap (lap 100). Red curve shows the evolution of the novelty signal over laps. **(E)** Place field evolution for 1 induction laps. Place fields are removed by the application of extra current. **(F)** Place field evolution for 15 induction laps. Place fields are removed by the application of extra current. **(G)** Number of induction laps required to remove stable place field for small and large induction areas. **(H)** Number of induction laps required to shift place field location for small and large induction areas. **(I)** Evolution of place fields for the case in which an extra current is applied during exploration of a novel environment (lap 5). The extra current is applied to the postsynaptic neuron while the animal traverses a large section (45%) of the track. Yellow bar indicates the induction region in which the extra current is applied. Dashed line indicates the position of the peak of the initial place field. Blue arrow indicates the first induction lap (lap 5). Red curve shows the evolution of the novelty signal over laps. **(J)** Number of induction laps required to shift place field location for novel and familiar environments. **(K)** Evolution of place fields for the case in which the application of an extra current is paired with the resetting of the novelty signal. The extra current is applied to the postsynaptic neuron while the animal traverses a small section (15%) of the track. Yellow bar indicates the induction region in which the extra current is applied. Dashed line indicates the position of the peak of the initial place field. Blue arrow indicates the first induction lap (lap 100). Red curve shows the evolution of the novelty signal over laps. Re-setting the novelty signal leads to a reduction in dendritic inhibition across the whole track. Therefore, the in-field activity increases, leading to the reinforcement of the initial place field.

We next compare the induction of place field shift in novel and familiar environments. We hypothesize that in novel environments, place fields should be more plastic and, therefore, it should be easier to induce a shift in place field location. In order to test this, we induce dendritic activity on lap 5 instead of 100. As shown above, the induction protocol in familiar environments has to be applied over several laps to successfully induce place field shift. In novel environments, conversely, applying the induction protocol over a few laps is enough to induce the development of a new place field. Indeed, the induction of dendritic activity over 4 laps is sufficient to shift

place field location (figure **5**I-J). As initially hypothesized, our model indicates that we need fewer induction laps to induce place field shift in novel environments than in familiar ones. This extra plasticity of place fields in novel environments is due to two factors: synaptic weights are not yet strongly tuned in the first laps, and the novelty signal induces an increase in postsynaptic dendritic activity.

Finally, we investigate whether we can artificially manipulate the interneuron activity in familiar environments so that the model returns to the state it is found in novel environments. In particular, place fields could become more plastic following the manipulation of interneuron activity. To test that, we run the simulations for 100 laps—until the environment becomes familiar. At lap 100, we decrease dendrite-targeting inhibition and increase soma-targeting inhibition, resetting them to the level of novel environment exploration. Simultaneously, at lap 100, we induce dendritic activity within a region far from the peak of the neuron's place field. Since the modulation of inhibition is applied over the entire environment, there is an increase in both within-field and out-of-field firing rate. Accordingly, the shift in place field location is harder than in the case without manipulation of inhibition (figure **5**K). We conclude that, surprisingly, re-setting inhibition to novel environment levels is not enough to make place fields plastic again. Indeed, overall manipulation of inhibition reinforces stable place fields by increasing within-field activity.

In summary, our model suggests that single-cell place fields can be shifted under the induction of dendritic activity. Our model predicts that small induction areas are more effective at inducing the development of new place fields. Induction in novel environments is also more efficient than in familiar ones. Counter-intuitively, resetting novel environment level of inhibition represses place field plasticity.

4.3 Discussion

We propose a model of hippocampal CA1 place cells in which interneuron activity is modulated by novelty in an interneuron-type-dependent manner. Using our simulations, we identify the potential mechanisms underlying the evolution of place fields and the transition from silent to place cells in novel environments. During the initial stages of exploration of novel environments, dendrite-targeting inhibition is reduced whereas soma-targeting inhibition is increased. The reduction in dendritic inhibition opens a window for plasticity, leading to the formation and stabilization of receptive fields. We then show that place fields are more stable in familiar environments than in novel environments. Our simulations suggest that this extra stability is due to stronger synaptic weights and increased dendritic inhibition. Our model makes predictions on how to perturb place fields by dendritic activation. In our model, dendritic activation can shift place field location. We predict that this shift is easier if the dendritic activity is induced only within a small region of the environment, in the order of the size of presynaptic place field widths. We also predict that it is easier to induce place field shift in novel than in familiar environments. Our model, albeit simple, provides a mechanism for several features of the CA1 network and provides testable predictions.

The modulation of interneuron activity during exploration of novel environments is thought to be important for place field development and stabilization. Dendritic events, such as NMDA spikes and Ca^{2+} plateau potentials [Bittner et al., 2017; Sheffield et al., 2017; Sheffield and Dombeck, 2015], have been implicated in the development of new place fields. Thus, the reduction in dendritic inhibition—due to a reduction in SST interneuron activity, for example—might be responsible for opening a window for plasticity by promoting these dendritic events. Reduced inhibition could unmask small input inhomogeneities, leading to the rapid emergence of place cells during the first stages of exploration of novel environments. These

small inhomogeneities would then be amplified through synaptic plasticity. The role of increased somatic inhibition in novel environments, however, is less clear. Since soma-targeting interneurons receive inputs from local pyramidal cells, the increase in soma-targeting interneuron activity could be reflecting the increase in pyramidal cell activity. Somatic inhibition can also be responsible for regulating pyramidal cell activity to ensure that the overall level of excitatory activity is kept within a certain regime. In our simulations, we induced a quick switch between silent and place cells by injecting an excitatory current onto the perisomatic section of the CA1 pyramidal cell. Endogenously, this change in somatic input might be mediated by soma-targeting interneurons such as a subset of PV expressing cells. These cells would act as a gate and could quickly reassign which cells become active and therefore choose which cells encode the relevant spatial information. This control by PV interneurons might be important to ensure the development of sparse and robust representations. Overall, this dendrite- and soma-specific regulation could be a mechanism to separate the learning process into two stages such that spatial representations are first developed within the hippocampus before being communicated back to cortex. Furthermore, the increase in soma-targeting interneuron activity can also be responsible for controlling plasticity at CA1 pyramidal neurons.

Aside from direct dendritic disinhibition, place cells might be formed by alternative — probably complementary — mechanisms such as via neuromodulation. Several neuromodulators such as acetylcholine, noradrenaline, dopamine and serotonin, have been implicated in long-term synaptic plasticity [Froemke et al., 2007; Frémaux and Gerstner, 2016; Martins and Froemke, 2015; Palacios-Filardo and Mellor, 2019; Pedrosa and Clopath, 2017; Ruivo and Mellor, 2013]. These neuromodulators are responsible for changing the functional state of the hippocampal CA1 network and they might be responsible for modulating interneuron activity when the animal faces novel experiences [Hasselmo and McGaughy, 2004; Kentros et al., 2004; Ruivo et al.,

2017]. The action of neuromodulators, however, may have further implications such as an increase in pyramidal cell excitability or change in the plasticity rules governing glutamatergic synapses. The inclusion of these factors in future versions of our model could help unravelling further details of the mechanisms associated with place field development.

CA1 pyramidal cell depolarization has been shown to increase rapidly following exposure to novel environments [Cohen et al., 2017; Frank et al., 2004]. As suggested by Cohen et al. [Cohen et al., 2017], this increase is associated with increased excitatory inputs onto CA1 pyramidal cells in our model. Through exploration, pyramidal cell firing rate returns to baseline levels in familiar environments. This later reduction in place cell firing rate has been suggested to be associated with a reduction in excitatory input [Cohen et al., 2017]. Conversely, inspired by data from Sheffield et al. [Sheffield et al., 2017], our model suggests that the return to baseline firing rate might be associated with the combined increase in dendritic inhibition and decrease in somatic inhibition, while excitatory inputs remain strong. This strong dendritic inhibition and strong dendritic excitation might lead to a local balanced state, giving rise to experimentally observed dynamics [Vreeswijk and Sompolinsky, 1996].

In our model, we considered synaptic plasticity to be dependent on presynaptic activity and postsynaptic dendritic activation only. Additionally, we considered only direct dendrite to soma propagation. Although dendritic activation is necessary for NMDA-dependent synaptic potentiation, this activation can indeed be induced by local NMDA spikes [Brandalise et al., 2016; Gasparini et al., 2004; Major et al., 2008; Palmer et al., 2014; Schiller et al., 2000] and plateau potentials [Bittner et al., 2015; Grienberger et al., 2014; Takahashi and Magee, 2009], but also by back-propagating action potentials [Hill et al., 2013; Magee and Johnston, 1997; Spruston et al., 1995; Zhou et al., 2008]. Therefore, whereas somatic activation does not seem to be

necessary for place field formation, it might also promote synaptic plasticity. It would be interesting to include soma-to-dendrite propagation in future extensions of our model and investigate the consequences of somatic activation to place field formation and stability.

In all of our simulations, we assume that CA1 pyramidal cells inherit spacial tuning from input neurons which are likely to correspond to CA3 place cells. Furthermore, we assume that each of these input neurons might be strong enough to drive CA1 pyramidal cell activity. Since we are using rate-based models, these simulated neurons should actually be interpreted as a population of highly correlated neurons. These would then correspond to a group of CA3 neurons with similar spacial tuning. This assumption would not require that all the neurons in this CA3 population fire together but, instead, that the total input from this population to the CA1 neuron is spatially modulated. Therefore, our model does not assume that the spiking times of a large group of CA3 neurons are highly correlated, but that their place fields — a smoothed, multi-lap averaged version of their spiking rates — overlap.

Our model indicates that the balance between strong excitatory input and the interplay between dendritic and somatic inhibition leads to place field stabilization in familiar environments. Synaptic plasticity, in our model, leads to the strengthening of within-field inputs and weakening of out-of-field inputs. The importance of plasticity for place field stabilization is corroborated by experiments in which NMDA receptors have been shown to be important for place field stabilization [Cacucci et al., 2007; Kentros et al., 1998; McHugh et al., 1996]. The increase in dendritic inhibition in familiar environments in our model induces a reduction in dendritic events and, thus, a reduction in plasticity-induced changes in place fields. Additionally, the combination of weak out-of-field inputs and strong dendritic inhibition leads to higher robustness to noise. Overall, place fields stabilize following the exploration of novel environments, in agreement with experiments [Cohen et al., 2017]. Besides changes in excitatory

and inhibitory inputs, dendritic nonlinearities might also contribute to place field development and stabilization. In presence of noise, our model indicates that dendritic nonlinearities are crucial for reliable place field development. Therefore, our model offers a possible mechanism for place field stabilization and highlights the importance of interneuron diversity and the balance between strong excitatory and inhibitory inputs for this stabilization.

Our model provides a mechanistic understanding of the CA1 network. It reproduces a variety of observations, such as the dynamics of place fields during the exploration of novel and familiar environments. Furthermore, we demonstrate that place fields can be manipulated by artificial depolarization of CA1 pyramidal cells in our model.

4.4 Methods

Neuron model

We use two-compartment, rate-based neuron models. Each neuron is modeled as two compartments: one representing the perisomatic region and another representing the apical dendrites. The dendritic compartment's activity, r_{dend}, is determined by

$$\tau_0 \frac{dr_{dend}}{dt} = -r_{dend} + g_{dend}\left(p_{dend}\right) \ ,$$

where τ_0 is a time constant, and p_{dend} is the dendritic "potential" variable given by

$$p_{dend} = \sum_i w_i R_i - I_{dend} + I_{dend}^{ext} \ ,$$

where R_i is the firing rate of neuron i in the presynaptic layer, w_i is the synaptic weight from a neuron in the presynaptic layer, I_{dend} is the input from dendrite-targeting interneurons—simulating SOM+ interneuron inputs, and I_{dend}^{ext} is an external current applied to the dendritic compartment. The function g_{dend} is a non-linear function of

the input to the dendritic compartment given by

$$g_{dend}(I) = \alpha_1 \left[\tanh(I/I_0)\right]_+ + \alpha_2 \left(\frac{1}{2}(\tanh(2(I-I_0))+1)\right) ,$$

where $[\cdot]_+$ denotes a rectification that sets negative values to zero, α_1 controls the linear gain of the dendritic compartment, α_2 controls the amplitude of the non-linear term associated with dendritic spikes, and I_0 is proportional to the minimum input current necessary for the induction of a dendritic spike (figure S5A-B).

Inputs from dendrites are propagated to the soma following a non-linear propagation function that depends on the somatic "potential" $V_{soma} = I^{dep}_{soma} - I_{soma}$, where $I^{dep}_{soma} = I^{exc}_{soma} + I^{ext}_{soma}$ is sum of the excitatory input onto the perisomatic compartment, I^{exc}_{soma}, and the external current applied to the soma, I^{ext}_{soma}, and I_{soma} is the input from soma-targeting interneurons—simulating PV+ interneuron inputs. The activity of the somatic compartment, r_{soma}, is given by

$$\tau_0 \frac{dr_{soma}}{dt} = -r_{soma} + \left[g_{prop}\left(V_{soma}\right) r_{dend} + I^{dep}_{soma} - I_{soma} - N_{th}\right]_+ ,$$

where N_{th} is the threshold for somatic activation, and the non-linear dendrite-to-soma propagation function g_{prop} is given by

$$g_{prop}(V_{soma}) = \begin{cases} 0 & \text{if } V_{soma} \leq \theta_{prop} \\ 1 & \text{if } V_{soma} > \theta_{prop} \end{cases} ,$$

where θ_{prop} is a threshold for dendrite-to-soma propagation.

Synaptic plasticity model

The synaptic weights from input neurons onto CA1 neurons are plastic and depends on the activity of the presynaptic neuron, r_j, and the activity of the dendritic com-

partment of the postsynaptic neuron, r_{dend}, as a standard Hebbian term. We include a homeostatic term that takes into account the sum of all synaptic weights onto the postsynaptic neuron. The synaptic weight from input neuron j to the postsynaptic neuron i, w_{ij} is updated following

$$\frac{dw_{ij}}{dt} = \eta_{ex} r^i_{dend} r_j - \eta_{homeo} \left(\sum_j w_{ij} - \theta_{homeo} \right) ,$$

where η_{ex} is the learning rate of excitatory connections, η_{homeo} is the learning rate of the homeostatic term, and θ_{homeo} is a target homeostatic constant.

Position-modulated inputs

The simulated CA1 neurons receive feedforward input from N_{pre} neurons. These input neurons are tuned to specific locations and their firing rates span over the entire environment. All the place fields of input neurons have the same tuning width, σ_{pre}, and the same amplitude, A_{pre}. We assume that the animal explores an annular track of length L with speed v. The firing rate of an input neuron with place field centered at p_0 is

$$r^{input}(p) = A_{pre} \exp \left(-\frac{d^2}{2\sigma^2_{pre}} \right) , \tag{4.1}$$

where p is the animal's position, and d is the distance, along the track, between the animal's position and the center of the place field.

Novelty signal

When simulating the exploration of a novel environment, we assume that the interneuron activity changes over time and is interneuron-type specific. We define a quantity, named novelty signal, that modulates the interneuron activity

$$n(t) = \exp(-t/\tau_n) ,$$

where t is the time measured from the start of exploration, and τ_n is a time constant. The dendritic and somatic inhibition are then given by

$$I_{dend/soma}(t) = I^{\infty}_{dend/soma} - \left(I^{\infty}_{dend/soma} - I^{0}_{dend/soma}\right) n(t) \,,$$

where $I^{\infty}_{dend/soma}$ is the inhibitory activity in the dendrite/soma in familiar environments, and $I^{0}_{dend/soma}$ is the initial inhibitory activity in the dendrite/soma in novel environments. The initial level of dendritic inhibition is assumed to be lower than its level in familiar environments, $I^{0}_{dend} < I^{\infty}_{dend}$. The initial level of somatic inhibition is assumed to be higher than its level in familiar environments, $I^{0}_{soma} > I^{\infty}_{soma}$.

Measuring place field stability

In figure 4, we analyze the stability of place fields in the first and last lap of novel environment exploration. In order to measure the effect of noise in novel environments, we go through the following steps: (1) we take the network in the state it was at the beginning of lap 1; (2) we simulate one lap of exploration, without plasticity; (3) we measure the place field of the postsynaptic neuron; (4) we rescale this place field such that its peak is set to 1; (5) we change the state of the network by adding noise to it (see below); (6) we repeat (2)-(4); (7) we calculate the absolute distance between the two rescaled receptive fields; (8) we repeat (6)-(7) N_{noise} times and take an average over all samples (figure S5). To measure the effect of noise in familiar environments, we follow the same steps but using the state of the network at the beginning of the last lap (lap 100) in step (1).

We assume that place fields can be affected by three sources of noise: (i) noise at presynaptic place fields, (ii) noise at presynaptic firing rates, and (iii) noise at synaptic weights. In case (i), we multiply each presynaptic receptive field (equation 4.1) by a random variable taken from a normal distribution with mean 1 and variance N^2. In

case (ii), we assume that each presynaptic neuron receives an extra input, independent of its receptive field, and not tuned to the animal's position. This extra input is taken from a normal distribution with mean 0 and variance N^2 and then rectified to admit only positive values. In case (iii), we add a random number to each synaptic weight. This random number is taken from a normal distribution with mean 0 and variance N^2. In all three cases, we define N as the noise amplitude.

Parameters and simulations

All simulations were implemented in python and will be made available at ModelDB. The parameters used in our simulations can be found in table 4.1.

4.5 Data availability

All data and software supporting the findings of this study are available from the corresponding authors upon reasonable request. The code used to generate the results that are reported in this study will be made available at ModelDB.

Table 4.1: Parameters summary

Neuron Model		
Name	**Value**	**Description**
τ_0	5.0 ms	Firing rate time constant
α_1	4/3	Linear gain of dendritic compartment
α_2	2/3	Related to the amplitude of dendritic spikes
I_0	2.5	Minimum current to induce dendritic spikes
N_{th}	1.0	Threshold for somatic activation
θ_{prop}	- 0.2	Threshold for dendrite-to-soma propagation
Plasticity Model		
Name	**Value**	**Description**
η_{ex}	2×10^{-4} ms^{-1}	Excitatory plasticity learning rate
η_{homeo}	2×10^{-4} ms^{-1}	Homeostatic plasticity learning rate
θ_{homeo}	3.0 (Fig 5: 2.0)	Homeostatic target value
Place-tuned input		
Name	**Value**	**Description**
A_{pre}	2.2	Presynaptic place field amplitude
σ_{pre}	5.0	Presynaptic place field width
Novelty signal		
Name	**Value**	**Description**
τ_n	100 s	Time constant for novelty signal decay
I^0_{dend}	0.8	Initial dendritic inhibition
I^∞_{dend}	7.5 (fig2); 8.5 (fig3 & 5)	Target dendritic inhibition
I^0_{soma}	1.2	Initial somatic inhibition
I^∞_{soma}	0.0	Target somatic inhibition
Simulation parameters		
Name	**Value**	**Description**
N_{pre}	10	Number of presynaptic neurons
I^{exc}_{soma}	0.5 (fig2); 1.0 (fig3 & 5)	Excitatory current onto perisomatic compartment
T_{length}	50 a.u.	Track length (arbitrary units)
v	1×10^{-2} ms^{-1}	Animal speed
dt	1 ms	Integration time step

4.6 References

Barry, C., Lever, C., Hayman, R., Hartley, T., Burton, S., O'Keefe, J., Jeffery, K., and Burgess, (2006). The Boundary Vector Cell Model of Place Cell Firing and Spatial Memory. *Reviews in the Neurosciences*, 17:71–98.

Battaglia, F. P. and Treves, A. (1998). Attractor neural networks storing multiple space representations: A model for hippocampal place fields. *Physical Review E*, 58:7738–7753.

Bittner, K. C., Grienberger, C., Vaidya, S. P., Milstein, A. D., Macklin, J. J., Suh, J., Tonegawa, S., and Magee, J. C. (2015). Conjunctive input processing drives feature selectivity in hippocampal CA1 neurons. *Nature Neuroscience*, 18:1133–1142.

Bittner, K. C., Milstein, A. D., Grienberger, C., Romani, S., and Magee, J. C. (2017). Behavioral time scale synaptic plasticity underlies CA1 place fields. *Science*, 357:1033–1036.

Blair, H. T., Gupta, K., and Zhang, K. (2008). Conversion of a phase- to a rate-coded position signal by a three-stage model of theta cells, grid cells, and place cells. *Hippocampus*, 18:1239–1255.

Bliss, T. V. P. and Collingridge, G. L. (1993). A synaptic model of memory: long-term potentiation in the hippocampus. *Nature*, 361:31–39.

Brandalise, F., Carta, S., Helmchen, F., Lisman, J., and Gerber, U. (2016). Dendritic NMDA spikes are necessary for timing-dependent associative LTP in CA3 pyramidal cells. *Nature Communications*, 7:ncomms13480.

Burgess, N. and O'Keefe, J. (2011). Models of place and grid cell firing and theta rhythmicity. *Current Opinion in Neurobiology*, 21:734–744.

Cacucci, F., Wills, T. J., Lever, C., Giese, K., and O'Keefe, J. (2007). Experience-Dependent Increase in CA1 Place Cell Spatial Information, But Not Spatial Reproducibility, Is Dependent on the Autophosphorylation of the -Isoform of the Calcium/Calmodulin-Dependent Protein Kinase II. *The Journal of Neuroscience*, 27:7854–7859.

Cohen, J. D., Bolstad, M., and Lee, A. K. (2017). Experience-dependent shaping of hippocampal CA1 intracellular activity in novel and familiar environments. *eLife*, 6:e23040.

Conklin, J. and Eliasmith, C. (2005). A Controlled Attractor Network Model of Path Integration in the Rat. *Journal of Computational Neuroscience*, 18:183–203.

Diamantaki, M., Coletta, S., Nasr, K., Zeraati, R., Laturnus, S., Berens, P., Preston-Ferrer, P., and Burgalossi, A. (2018). Manipulating Hippocampal Place Cell Activity by Single-Cell Stimulation in Freely Moving Mice. *Cell reports*, 23:32–38.

Doron, M., Chindemi, G., Muller, E., Markram, H., and Segev, I. (2017). Timed Synaptic Inhibition Shapes NMDA Spikes, Influencing Local Dendritic Processing and Global I/O Properties of Cortical Neurons. *Cell Reports*, 21:1550–1561.

Dragoi, G. and Tonegawa, S. (2011). Preplay of future place cell sequences by hippocampal cellular assemblies. *Nature*, 469:397.

Dragoi, G. and Tonegawa, S. (2013). Distinct preplay of multiple novel spatial experiences in the rat. *Proceedings of the National Academy of Sciences*, 110:9100–9105.

Dragoi, G. and Tonegawa, S. (2014). Selection of preconfigured cell assemblies for representation of novel spatial experiences. *Philosophical Transactions of the Royal Society of London B: Biological Sciences*, 369:20120522.

Epsztein, J., Brecht, M., and Lee, A. K. (2011). Intracellular Determinants of Hippocampal CA1 Place and Silent Cell Activity in a Novel Environment. *Neuron*, 70:109–120.

Fanselow, M. S. (2000). Contextual fear, gestalt memories, and the hippocampus. *Behavioural Brain Research*, 110:73–81.

Frank, L. M., Stanley, G. B., and Brown, E. N. (2004). Hippocampal Plasticity across Multiple Days of Exposure to Novel Environments. *The Journal of Neuroscience*, 24:7681–7689.

Franzius, M., Vollgraf, R., and Wiskott, L. (2007). From grids to places. *Journal of Computational Neuroscience*, 22:297–299.

Froemke, R. C., Merzenich, M. M., and Schreiner, C. E. (2007). A synaptic memory trace for cortical receptive field plasticity. *Nature*, 450:nature06289.

Frémaux, N. and Gerstner, W. (2016). Neuromodulated Spike-Timing-Dependent Plasticity, and Theory of Three-Factor Learning Rules. *Frontiers in Neural Circuits*, 9:85.

Fyhn, M., Hafting, T., Treves, A., Moser, M.-B., and Moser, E. I. (2007). Hippocampal remapping and grid realignment in entorhinal cortex. *Nature*, 446:190.

Gasparini, S., Migliore, M., and Magee, J. C. (2004). On the Initiation and Propagation of Dendritic Spikes in CA1 Pyramidal Neurons. *The Journal of Neuroscience*, 24:11046–11056.

Golding, N. L., Staff, N. P., and Spruston, N. (2002). Dendritic spikes as a mechanism for cooperative long-term potentiation. *Nature*, 418:326.

Grienberger, C., Chen, X., and Konnerth, A. (2014). NMDA Receptor-Dependent Multidendrite Ca2+ Spikes Required for Hippocampal Burst Firing In Vivo. *Neuron*, 81:1274–1281.

Grienberger, C., Milstein, A. D., Bittner, K. C., Romani, S., and Magee, J. C. (2017). Inhibitory suppression of heterogeneously tuned excitation enhances spatial coding in CA1 place cells. *Nature Neuroscience*, 20:417–426.

Hartley, T., Burgess, N., Lever, C., Cacucci, F., and O'Keefe, J. (2000). Modeling place fields in terms of the cortical inputs to the hippocampus. *Hippocampus*, 10:369–379.

Hasselmo, M. E. and McGaughy, J. (2004). High acetylcholine levels set circuit dynamics for attention and encoding and low acetylcholine levels set dynamics for consolidation. *Progress in Brain Research*, 145:207–231.

Hill, A. (1978). First occurrence of hippocampal spatial firing in a new environment. *Experimental Neurology*, 62:282–297.

Hill, D. N., Varga, Z., Jia, H., Sakmann, B., and Konnerth, A. (2013). Multibranch activity in basal and tuft dendrites during firing of layer 5 cortical neurons in vivo. *Proceedings of the National Academy of Sciences*, 110:13618–13623.

Jarsky, T., Roxin, A., Kath, W. L., and Spruston, N. (2005). Conditional dendritic spike propagation following distal synaptic activation of hippocampal CA1 pyramidal neurons. *Nature Neuroscience*, 8:nn1599.

Kentros, C., Hargreaves, E., Hawkins, R. D., Kandel, E. R., Shapiro, M., and Muller, R. V. (1998). Abolition of Long-Term Stability of New Hippocampal Place Cell Maps by NMDA Receptor Blockade. *Science*, 280:2121–2126.

Kentros, C. G., Agnihotri, N. T., Streater, S., Hawkins, R. D., and Kandel, E. R. (2004). Increased Attention to Spatial Context Increases Both Place Field Stability and Spatial Memory. *Neuron*, 42:283–295.

Knierim, J. J. and Zhang, K. (2012). Attractor Dynamics of Spatially Correlated Neural Activity in the Limbic System. *Annual Review of Neuroscience*, 35:267–285.

Lee, D., Lin, B.-J., and Lee, A. K. (2012). Hippocampal Place Fields Emerge upon Single-Cell Manipulation of Excitability During Behavior. *Science*, 337:849–853.

Leutgeb, S., Leutgeb, J. K., Barnes, C. A., Moser, E. I., McNaughton, B. L., and Moser, M.-B. (2005). Independent Codes for Spatial and Episodic Memory in Hippocampal Neuronal Ensembles. *Science*, 309:619–623.

Leutgeb, S., Leutgeb, J. K., Treves, A., Moser, M.-B., and Moser, E. I. (2004). Distinct Ensemble Codes in Hippocampal Areas CA3 and CA1. *Science*, 305:1295–1298.

Levy, W. B. (1996). A sequence predicting CA3 is a flexible associator that learns and uses context to solve hippocampal-like tasks. *Hippocampus*, 6:579–590.

Magee, J. C. and Johnston, D. (1997). A Synaptically Controlled, Associative Signal for Hebbian Plasticity in Hippocampal Neurons. *Science*, 275:209–213.

Major, G., Polsky, A., Denk, W., Schiller, J., and Tank, D. W. (2008). Spatiotemporally graded NMDA spike/plateau potentials in basal dendrites of neocortical pyramidal neurons. *Journal of neurophysiology*, 99:2584–601.

Martins, A. R. O. and Froemke, R. C. (2015). Coordinated forms of noradrenergic plasticity in the locus coeruleus and primary auditory cortex. *Nature Neuroscience*, 18:1483–1492.

Mayford, M. (2013). The search for a hippocampal engram. *Philosophical transactions of the Royal Society of London. Series B, Biological sciences*, 369:20130161.

McHugh, T. J., Blum, K. I., Tsien, J. Z., Tonegawa, S., and Wilson, M. A. (1996). Impaired Hippocampal Representation of Space in CA1-Specific NMDAR1 Knockout Mice. *Cell*, 87:1339–1349.

Müller, C., Beck, H., Coulter, D., and Remy, S. (2012). Inhibitory Control of Linear and Supralinear Dendritic Excitation in CA1 Pyramidal Neurons. *Neuron*, 75:851–864.

O'Keefe, J. (1976). Place units in the hippocampus of the freely moving rat. *Experimental Neurology*, 51:78–109.

O'Keefe, J. and Dostrovsky, J. (1971). The hippocampus as a spatial map. Preliminary evidence from unit activity in the freely-moving rat. *Brain Research*, 34:171–175.

O'Keefe, J. and Nadel, L. (1978). *The hippocampus as a cognitive map*. Clarendon Press.

Palacios-Filardo, J. and Mellor, J. R. (2019). Neuromodulation of hippocampal long-term synaptic plasticity. *Current Opinion in Neurobiology*, 54:37–43.

Palmer, L. M., Shai, A. S., Reeve, J. E., Anderson, H. L., Paulsen, O., and Larkum, M. E. (2014). NMDA spikes enhance action potential generation during sensory input. *Nature Neuroscience*, 17:383–390.

Pedrosa, V. and Clopath, C. (2017). The Role of Neuromodulators in Cortical Plasticity. A Computational Perspective. *Frontiers in Synaptic Neuroscience*, 8:38.

Ruivo, L. M. T.-G., Baker, K. L., Conway, M. W., Kinsley, P. J., Gilmour, G., Phillips, K. G., Isaac, J. T., Lowry, J. P., and Mellor, J. R. (2017). Coordinated Acetylcholine

Release in Prefrontal Cortex and Hippocampus Is Associated with Arousal and Reward on Distinct Timescales. *Cell Reports*, 18:905–917.

Ruivo, L. M. T.-G. and Mellor, J. R. (2013). Cholinergic modulation of hippocampal network function. *Frontiers in Synaptic Neuroscience*, 5:2.

Samsonovich, A. and McNaughton, B. L. (1997). Path Integration and Cognitive Mapping in a Continuous Attractor Neural Network Model. *Journal of Neuroscience*, 17:5900–5920.

Schiller, J., Major, G., Koester, H. J., and Schiller, Y. (2000). NMDA spikes in basal dendrites of cortical pyramidal neurons. *Nature*, 404:285.

Schiller, J., Schiller, Y., and Clapham, D. E. (1998). NMDA receptors amplify calcium influx into dendritic spines during associative pre- and postsynaptic activation. *Nature Neuroscience*, 1:nn0698_114.

Sheffield, M., Adoff, M. D., and Dombeck, D. A. (2017). Increased Prevalence of Calcium Transients across the Dendritic Arbor during Place Field Formation. *Neuron*, 96.

Sheffield, M. E. and Dombeck, D. A. (2019). Dendritic mechanisms of hippocampal place field formation. *Current Opinion in Neurobiology*, 54:1–11.

Sheffield, M. E. J. and Dombeck, D. A. (2015). Calcium transient prevalence across the dendritic arbour predicts place field properties. *Nature*, 517:200.

Soman, K., Muralidharan, V., and Chakravarthy, V. S. (2018). A unified hierarchical oscillatory network model of head direction cells, spatially periodic cells, and place cells. *European Journal of Neuroscience*, 47:1266–1281.

Spruston, N., Schiller, Y., Stuart, G., and Sakmann, B. (1995). Activity-dependent action potential invasion and calcium influx into hippocampal CA1 dendrites. *Science*, 268:297–300.

Takahashi, H. and Magee, J. C. (2009). Pathway Interactions and Synaptic Plasticity in the Dendritic Tuft Regions of CA1 Pyramidal Neurons. *Neuron*, 62:102–111.

Treves, A. and Rolls, E. T. (1994). Computational analysis of the role of the hippocampus in memory. *Hippocampus*, 4:374–391.

Tsodyks, M. (1999). Attractor neural network models of spatial maps in hippocampus. *Hippocampus*, 9:481–489.

Vreeswijk, C. v. and Sompolinsky, H. (1996). Chaos in Neuronal Networks with Balanced Excitatory and Inhibitory Activity. *Science*, 274:1724–1726.

Weber, S. N. and Sprekeler, H. (2018). Learning place cells, grid cells and invariances with excitatory and inhibitory plasticity. *eLife*, 7.

Wilson, M. and McNaughton, B. (1993). Dynamics of the hippocampal ensemble code for space. *Science*, 261:1055–1058.

Zhou, W., Yan, P., Wuskell, J. P., Loew, L. M., and Antic, S. D. (2008). Dynamics of action potential backpropagation in basal dendrites of prefrontal cortical pyramidal neurons. *European Journal of Neuroscience*, 27:923–936.

Supplementary Figures

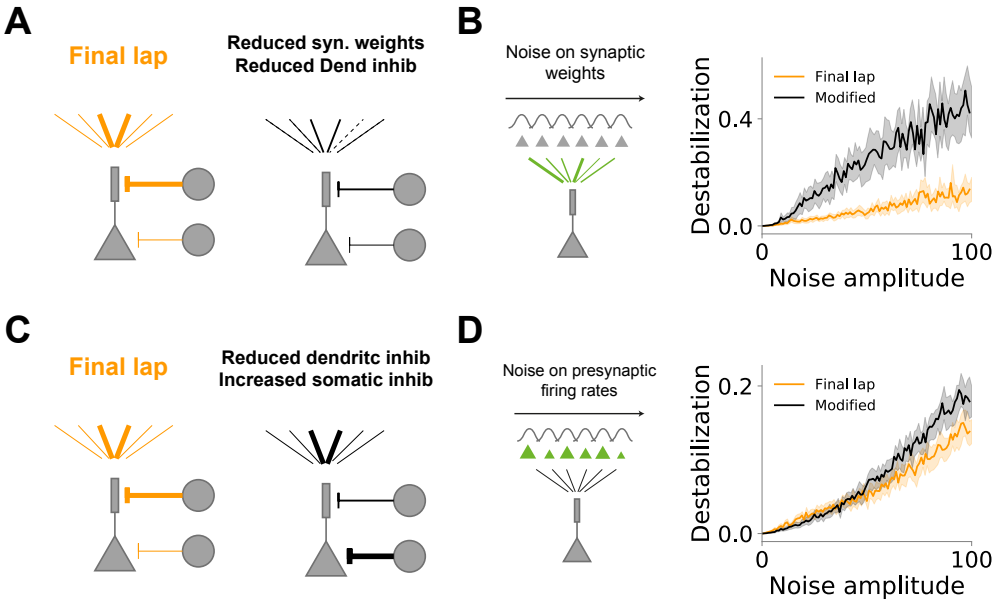

Figure S1 (related to figure 4). Strong synaptic weights and stronger dendritic inhibition ensures place field stability. **(A-B)** Strong synaptic weights provide stability to noise on synaptic connections. **(A)** Left: Network diagram for the network state at the last lap of exploration in figure 4. Right: Modified network with reduced synaptic weights and reduced dendritic inhibition. Importantly, the changes are determined such that the neuron's place field is kept unchanged. **(B)** Destabilization of place fields by noise on synaptic weights for final lap of exploration (orange) and modified network as in (B) (black). **(C)** Left: Network diagram for the network state at the last lap of exploration in figure 4. Right: Modified network with reduced dendritic inhibition and increased somatic inhibition. Importantly, the changes are determined such that the neuron's place field is kept unchanged. **(D)** Destabilization of place fields by noise on presynaptic firing rates for final lap of exploration (orange) and modified network as in (C) (black).

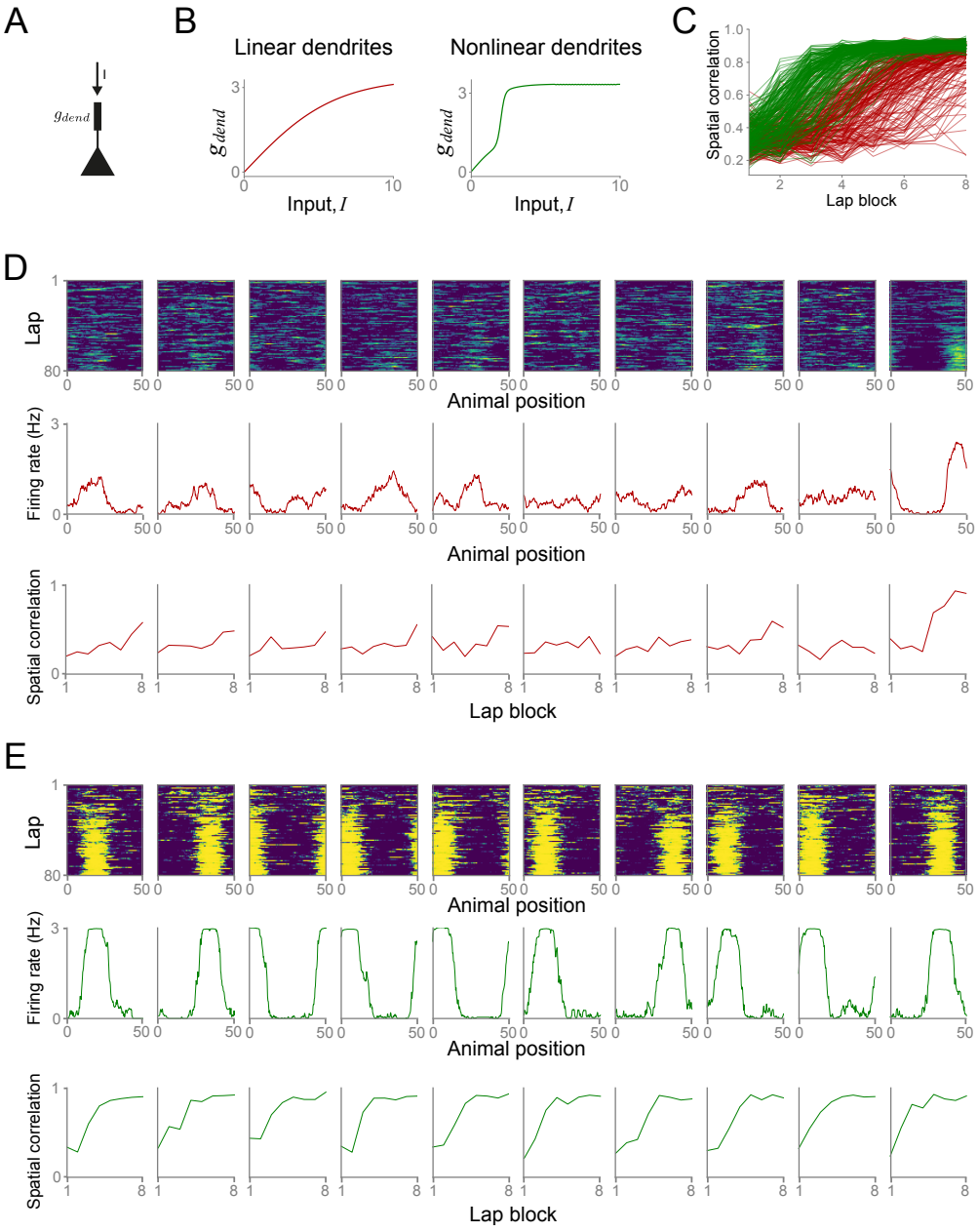
A
B
Linear dendrites
Nonlinear dendrites
C
Input, I
Spatial correlation
Lap block
D
Lap
Animal position
Firing rate (Hz)
E

Figure S2. Dendritic non-linearity leads to reliable place field development. (A) Single-cell diagram. A pyramidal neuron receives input I and integrates it through a function g_{dend}. **(B)** Dendritic transformation function g_{dend} as a function of the input I for linear dendrite (left, red) and nonlinear dendrites (right, green). **(C)** Spatial correlation between laps for blocks of 10 laps on simulations with nonlinear dendrites (green) and linear dendrites (red). Thick lines show averages over 200 cells for each group. Thin lines are individual cells. Note that the spatial correlation for several cells with linear dendrites does not increase over lap blocks. **(D)** Examples of individual pyramidal cells with linear dendrites. Top, evolution of neuron firing rate over laps as a function of the animal position. Middle, average neuron firing rate over the last 10 laps of exploration as a function of the animal position. Spatial correlation between laps for blocks of 10 laps. **(E)** Examples of individual pyramidal cells with nonlinear dendrites. Top, evolution of neuron firing rate over laps as a function of the animal position. Middle, average neuron firing rate over the last 10 laps of exploration as a function of the animal position. Spatial correlation between laps for blocks of 10 laps.

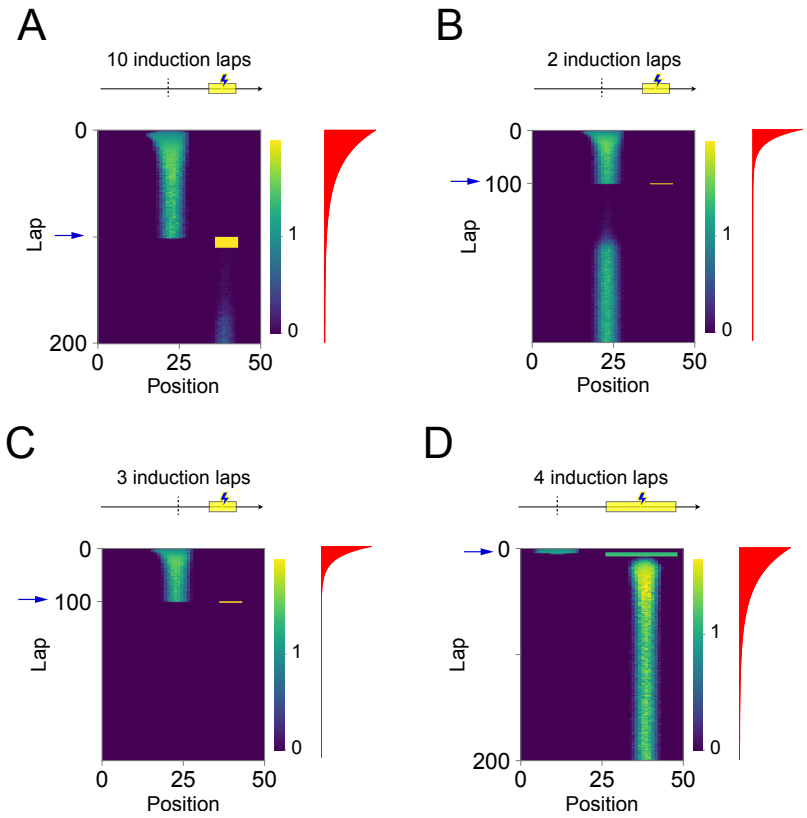

Figure S3 (related to figure 5). Artificially induced CA1 single cell activity can shift place field location. **(A-D)** Evolution of place fields for the case in which an extra current is applied to the postsynaptic neuron while the animal traverses a section of the track. Yellow bar indicates the induction region in which the extra current is applied. Dashed line indicates the position of the peak of the initial place field. Blue arrow indicates the first induction lap. Red curve shows the evolution of the novelty signal over laps. **(A)** Place field evolution for 10 induction laps and small induction region (15% of the track). Place fields are shifted towards new position determined by the region of extra current application. **(B)** Place field evolution for 2 induction laps and small induction region (15% of the track). Place fields are transiently removed by the application of extra current and reemerge at the initial location. **(C)** Place field evolution for 3 induction lap and small induction region (15% of the track). Place fields are removed following the application of extra current. **(D)** Same as figure 5I for a larger number of laps. Place field evolution for 5 induction laps and large induction region (45% of the track). The induction protocol is applied on lap 5, while the novelty signal is still strong. Place fields are shifted to new location.

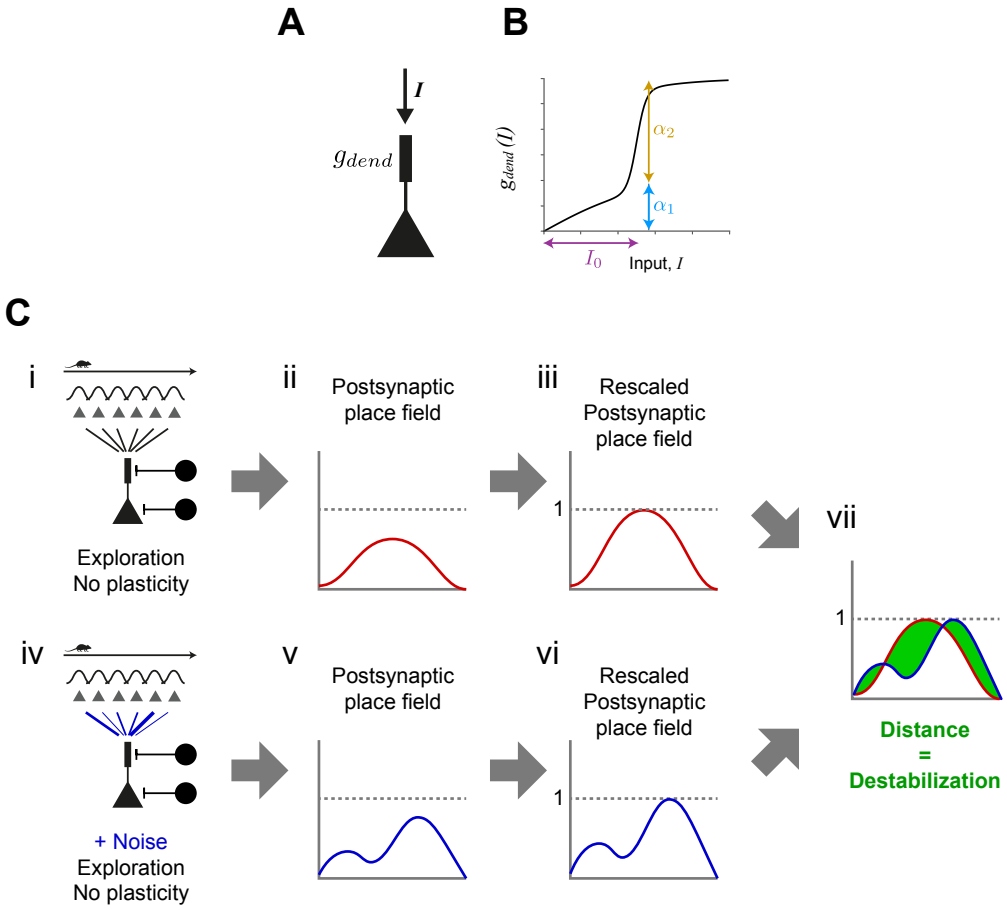

Figure S4. Dendritic non-linearity and stability analysis procedure. **(A)** Single-cell diagram. A pyramidal neuron receives input I and integrates it through a function g_{dend}. **(B)** Diagram of g_{dend} as a function of the input I (see methods). α_1 controls the linear gain of the dendritic compartment; α_2 controls the amplitude of the non-linear term related to dendritic spikes; and I_0 controls the minimum input to elicit dendritic spikes. **(C)** Place field stability analysis. For each measurement of place field stability (see methods) we perform the following steps: (i) we simulate one lap of exploration, without plasticity; (ii) we measure the place field of the postsynaptic neuron; (iii) we rescale this place field such that its peak is set to 1; (iv) we change the state of the network by adding noise to it; (v-vi) we repeat (ii)-(iii); (vii) we calculate the absolute distance between the two rescaled receptive fields.

Chapter 5

Interneuron-specific plasticity at parvalbumin and somatostatin inhibitory synapses onto CA1 pyramidal neurons shapes hippocampal output

Following our investigation into the role that excitation, excitatory plasticity, and inhibition play in learning, we next investigate the mechanisms regulating inhibitory plasticity onto CA1 pyramidal neurons. We present experimental data supporting the idea that different types of interneurons undergo undergo different synaptic plasticity rules. This result adds evidence to support the view that each interneuron type might fulfill a specific function. We then use computational modelling to predict the effect

of these interneuron-specific plasticity rules on pyramidal cell output. Upon further investigation, we confirm these prediction in hippocampal brain slices. Finally, our simulations suggest that the combination of plasticity rules leads to stable place field consolidation across environments.

The layout of the work will be presented in an article format as it has been submitted for publication. We would like to thank Matt Udakis, Sophie Chamberlain, and Jack Mellor for the experimental results and insightful discussions and idea, and Claudia Clopath for supervising and guiding the project.

Interneuron-specific plasticity at parvalbumin and somatostatin inhibitory synapses onto CA1 pyramidal neurons shapes hippocampal output

Summary

The formation and maintenance of spatial representations within hippocampal cell assemblies is strongly dictated by patterns of inhibition from diverse interneuron populations. Although it is known that inhibitory synaptic strength is malleable, induction of long-term plasticity at distinct inhibitory synapses and its regulation of hippocampal network activity is not well understood. Here, we show that inhibitory synapses from parvalbumin and somatostatin expressing interneurons undergo long-term depression and potentiation respectively (PV-iLTD and SST-iLTP) during physiological activity patterns. Both forms of plasticity rely on T-type calcium channel activation to confer synapse specificity but otherwise employ distinct mechanisms. Since parvalbumin and somatostatin interneurons preferentially target perisomatic and distal dendritic regions respectively of CA1 pyramidal cells, PV-iLTD and SST-iLTP coordinate a reprioritisation of excitatory inputs from entorhinal cortex and CA3. Furthermore, circuit-level modelling reveals that PV-iLTD and SST-iLTP cooperate to stabilise place cells while facilitating representation of multiple unique environments within the hippocampal network.

Keywords

Hippocampus, inhibition, plasticity, parvalbumin, somatostatin, LTD, LTP, STDP T-type calcium channel.

Introduction

GABAergic inhibitory interneurons form a diverse array of specialised cell types critical for the regulation of complex network functions within the brain. A defining feature of inhibitory interneurons is their precise axonal aborisations whereby inhibitory synapses target specific subdomains of pyramidal neurons and other inhibitory interneurons [1, 2]. Within the hippocampus and neocortex, parvalbumin (PV) and somatostatin (SST) expressing interneurons form two broad and occasionally overlapping subtypes of interneurons that preferentially target perisomatic and distal dendritic regions of pyramidal neurons respectively and are active on different phases of the theta cycle [2-6]. This endows them with unique roles in sculpting pyramidal neuron responses to excitatory inputs [7, 8]. Perisomatic inhibition by PV interneurons regulates pyramidal neuron spiking and network oscillations through feedforward and feedback inhibition [9-12]. In contrast, dendritic inhibition by SST interneurons regulates local synaptic and dendritic conductances, Ca^{2+} signal generation and excitatory synaptic plasticity principally through feedback inhibition [9, 13-15].

A defining feature of the hippocampus is the encoding of spatially relevant information via the formation of place cells [16]. Synaptic plasticity at glutamatergic synapses in the hippocampus accounts for the formation of location specific firing of individual place cells but it also plays a major role in the formation of place cell assemblies during exploration and offline replay of place cell activity [17-21]. Interestingly, individual CA1 pyramidal neurons can encode distinct place fields in different environments [22] presumably driven by ongoing excitatory synaptic plasticity. This feature of place cells and the persistent plasticity of their synaptic connections presents fundamental problems for hippocampal networks balancing flexibility versus stability of representations [23]. It is not clear how place cell

assemblies in the hippocampus can encode multiple different locations in separate environments without interference.

Inhibitory interneurons play an integral role within the hippocampus controlling place cell activity [8, 24-26], where short-term changes in SST and PV interneuron activity differentially regulate the emergence and firing patterns of place cells [8, 25] by controlling glutamatergic synaptic plasticity [13, 15]. But the consequences of long-term plasticity at inhibitory synapses on place cell activity has not been investigated.

Long-term inhibitory synaptic plasticity is a potentially important mechanism for learning within cortical networks [27-31] and GABAergic synapses in the hippocampus exhibit structural and functional plasticity [32-34]. Reductions in inhibitory strength via retrograde endocannabinoid signalling is well established [35-37] but multiple other mechanisms to regulate long-term inhibitory synaptic strength have also been proposed including $GABA_B$ receptors and BDNF [38], spike timing-dependent plasticity of chloride transporters [39], retrograde nitric oxide signalling [40] and NMDA receptors [41]. In the neocortex, synapses from PV and SST interneurons can undergo unique forms of plasticity [38, 41], whilst in the hippocampus, recent evidence suggests interneuron subtype specific inhibitory synapses are regulated in distinct ways [15, 42]. However, it is not clear whether long-term plasticity of inhibitory synapses is differentially engaged between interneuron subtypes during physiologically relevant activity and, furthermore, what the consequences of such plasticity would be for hippocampal network activity and place cell representations.

To address these questions, we utilised an optogenetic approach in hippocampal slices to selectively activate perisomatic and dendritically targeting inhibition onto CA1 pyramidal neurons by expression of channelrhodopsin in PV or SST interneurons. We found that synapses from PV and SST interneurons undergo interneuron-specific forms of inhibitory synaptic plasticity driven by the relative

timing of inhibitory and excitatory neuronal spiking and employing distinct signalling mechanisms. We go on to show these forms of cell-specific long-term inhibitory plasticity have profound effects on the output of CA1 pyramidal neurons and use computational modelling to demonstrate that these plasticity rules can provide a mechanism by which hippocampal place fields can remain stable over time whilst flexibly encoding location in multiple environments.

Results

Divergent inhibitory plasticity at PV and SST synapses

To achieve subtype specific control of inhibitory interneurons, we selectively activated either PV or SST interneurons by expressing the light-activated cation channel channelrhodopsin-2 (ChR2) in a cre-dependent manner using mice that expressed cre recombinase under control of the promoter for either the parvalbumin gene (PV-cre) or somatostatin gene (SST-cre) crossed with mice expressing cre-dependent ChR2 (PV-ChR2 and SST-ChR2 mice; methods). Immunohistochemisty confirmed that ChR2 expression was highest in the Stratum Pyramidal (SP) and Stratum Oriens (SO) layers for PV-ChR2 mice with cell bodies principally located in SP (Fig. 1a). Conversely, ChR2 expression was highest in the SO and Stratum Lacunosum Moleculare (SLM) layers for SST-ChR2 mice with cell bodies principally located in SO (Fig. 1b). These expression profiles are consistent with the established roles of PV and SST interneurons providing perisomatic and dendritic inhibition respectively [1, 2, 43]. To further confirm the spatially distinct inhibitory targets, we recorded interneuron subtype-specific inhibitory currents onto CA1 pyramidal neurons by activating ChR2 with 470nm blue light (Fig. 1c). The rise and decay kinetics of the resulting light evoked PV IPSCs were significantly faster compared to SST derived IPSCs (Fig. 1d,e) (Rise time: 3.8 ± 0.3 ms PV verses 6.1 ± 0.8 ms SST, $n = 8$, $p < 0.05$; Decay time: 16 ± 1.3 ms PV verses 28 ± 2.6 SST, $n = 8$, $p < 0.01$) supporting a more proximal location for PV synapses

compared to SST synapses. Light evoked PV IPSC kinetics were almost identical to IPSC kinetics recorded from paired whole-cell recordings made from PV expressing fast-spiking basket cells to CA1 pyramidal cells (Supplementary Fig. 1a) and similarly, selective activation of Oriens Lacunosum Moleculare (OLM) cells using Chrna2-cre mice [44, 45] revealed IPSC kinetics indistinguishable from SST-ChR mice (Supplementary Fig. 1e). Furthermore, measurement of synaptic response amplitudes as light was targeted to different regions of the slice confirmed the immunohistochemical characterisation of ChR2 expression supporting the selective stimulation of perisomatic vs dendritic targeted inhibition (Supplementary Fig. 1b,c,f,g). Therefore, whilst we cannot exclude the activation of other interneuron subtypes expressing PV or SST, these data suggest the majority of our synaptic inputs most likely arise from activation of PV basket cells and SST OLM cells that selectively target synapses to perisomatic and distal dendritic regions of CA1 pyramidal cells respectively.

Having established two populations of inhibitory synapses we investigated whether PV or SST synapses undergo long-term inhibitory synaptic plasticity and if so, whether induction and expression is similar at each synapse. IPSCs were recorded from CA1 pyramidal neurons held at 0 mv with glutamatergic transmission pharmacologically blocked. Interneuron subtype-specific IPSCs mediated by $GABA_A$ receptors were evoked by 5 ms light pulses and, importantly, an independent IPSC control pathway was evoked by electrical stimulation in the pyramidal layer (PV IPSCs) or Stratum Radiatum (SST IPSCs) (Fig. 1f and Supplementary Fig. 1d,h). Both PV and SST interneurons are entrained to theta frequency rhythms in the hippocampus [3] so we first tested whether bursts of IPSCs delivered at theta frequency could induce long-term inhibitory synaptic plasticity. Theta burst stimulation (TBS) of the light evoked pathway led to a prolonged pathway-specific reduction of PV-IPSC amplitude indicating a synapse specific long-term depression of PV synapses (PV-iLTD, 115% ± 14% control verses 61%

± 8% test pathway, n = 6, $p < 0.05$) (Fig. 1g). In contrast an identical light induced TBS led to a pronounced pathway-specific long-term potentiation of SST-IPSC amplitude (SST-iLTP, 87% ± 6% control verses 139% ± 8% test pathway, n = 6, $p < 0.01$) (Fig. 1h). These findings indicate that high frequency inhibitory synaptic stimulation can induce inhibitory synaptic plasticity at PV and SST synapses, but the direction of plasticity is diametrically opposite for the two different synapses.

A common feature of plasticity at inhibitory synapses is the requirement for postsynaptic depolarisation in conjunction with synaptic stimulation, despite the synaptic stimulation itself causing hyperpolarisation [15, 32-39, 41, 42]. To test the requirement for depolarisation in PV-iLTD and SST-iLTP we delivered TBS whilst voltage clamping neurons at -60mV during the TBS protocol. Under these conditions neither PV-iLTD nor SST-iLTP were induced (Supplementary Fig. 2a,b; PV: 84% ± 8% control verses 91% ± 4% test pathway, n = 5, $p > 0.05$; SST: 96% ± 6% control verses 106% ± 4% test pathway, n = 5, $p > 0.05$), indicating that both forms of inhibitory plasticity require coincident pyramidal neuron depolarisation and inhibitory input.

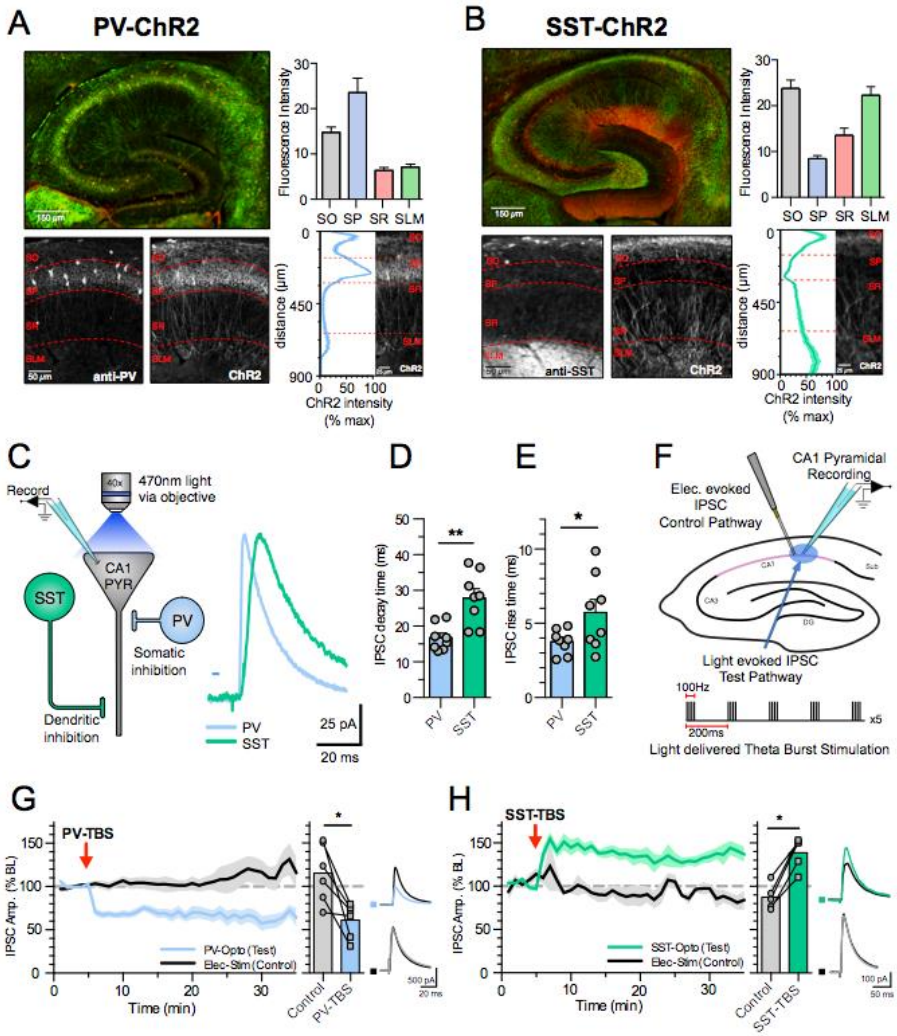

Figure 1: Somatically targeting PV and dendritically targeting SST inhibitory synapses undergo long-term synaptic plasticity.

(a) Immunohistochemistry showing expression of PV (red) and ChR2 (green) in PV-ChR2 mice. Histogram displaying mean ChR2 fluorescence expression levels in different hippocampal layers: Stratum Oriens (SO), Stratum Pyramidal (SP) Stratum Radiatum (SR) and Stratum Lacunosum Moleculare (SLM) (right top), ChR2 expression as a function of distance across hippocampal layers (right bottom). **(b)** Same as A but for SST-ChR2 mice. **(c)** Schematic and example IPSC traces highlighting the somatic and distal targeting of PV and SST synapses. **(d)** Summary of IPSC decay times for PV and SST IPSCs. **(e)** Summary of IPSC rise times for PV and SST IPSCs. **(f)** Schematic displaying the recording set up

for inhibitory plasticity experiments and the light induced theta burst (TBS) induction protocol. **(g)** TBS induced iLTD at PV synapses (left) average plasticity at control and test pathways (middle) and example traces before and after plasticity (right). **(h)** TBS induced iLTP at SST synapses (left) average plasticity at control and test pathways (middle) and example traces before and after plasticity (right). Data represent mean ± S.E.M statistical comparison via unpaired (d,e) and paired (g,h) t-tests where significance difference is indicated (*p < 0.05 and **p<0.01). See also Supplementary Fig. 1 and Supplementary Fig. 2.

PV and SST synapses undergo spike timing-dependent inhibitory plasticity

During exploratory behaviour, neurons in the hippocampus are entrained to the theta rhythm [46] with defined populations of neurons, including different subpopulations of interneurons, firing action potentials at specific phases of the theta cycle [2-4]. Having established a requirement for coincident synaptic activity and postsynaptic depolarisation for the induction of PV-iLTD and SST-iLTP we next sought to determine whether this was a Hebbian form of plasticity that could be induced by coincident pre- and post-synaptic action potentials and if so, what the precise spike timing requirements might be with respect to the preferred interneuron and pyramidal spiking phases of the theta cycle. The major subclasses of PV interneurons, basket cells and axo-axonic cells, fire on the descending phase of theta cycle roughly 60ms before pyramidal neurons, whilst both bistratified and OLM SST interneurons fire near coincident with pyramidal neurons at the trough of the cycle (Fig. 2a) [2-4, 6]. We therefore tested the induction of inhibitory spike timing-dependent plasticity (iSTDP) using spike timings of -60 ms, 0 ms and +60 ms to replicate spike patterns during exploratory behaviour and span the full width of a theta cycle (Fig. 2a).

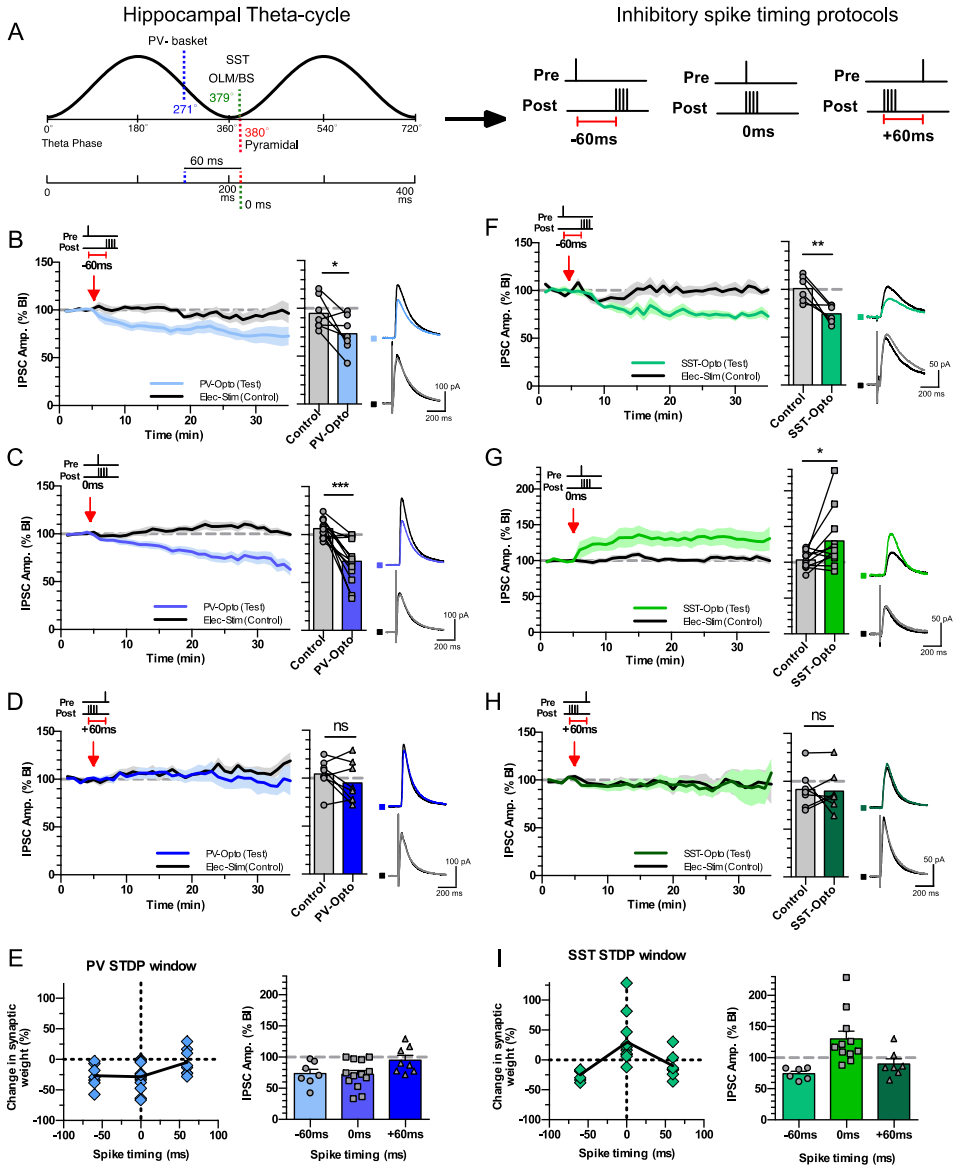

Figure 2. PV and SST inhibitory synapses undergo spike timing-dependent plasticity.

(a) Schematic highlighting the relative spike timing of PV and SST expressing interneurons during theta oscillations in relation to pyramidal neuron spiking (left). The three pairing protocols used for iSTDP experiments representing presynaptic stimulation and postsynaptic action potentials -60 ms pre before post, 0 ms pre and post together and +60 ms post before pre (right). **(b)** -60 ms pre before post pairing induced iLTD at PV synapses

(left) average plasticity at control and test pathways (middle) and example traces for before and after plasticity (right). **(c)** 0 ms pre and post pairing induced iLTD at PV synapses (left) average plasticity at control and test pathways (middle) and example traces for before and after plasticity (right). **(d)** +60 ms post before pre pairing failed to induce plasticity at PV synapses (left) average plasticity at control and test pathways (middle) and example traces for before and after plasticity (right). **(e)** Summary of the inhibitory STDP window at PV synapses. **(f-i)** Same as b-e but for SST synapses. Data represent mean ± S.E.M statistical comparison via paired t-tests where significance difference is indicated (*$p < 0.05$ and ***$p<0.001$). Scale bars b-d: 200ms, 100pA f-h 200ms, 50pA.

To test iSTDP, CA1 pyramidal neurons were voltage clamped at -50mV in the presence of AMPA and NMDA receptor blockers and light and electrically evoked IPSCs recorded as test and control synaptic pathways respectively. During the iSTDP protocol, recordings were switched to current clamp with the membrane potential maintained at -50 mV and single light evoked IPSCs were paired with a burst of 4 action potentials repeated 100 times at theta frequency (5 Hz). Stimulation of PV synapses with the theta-relevant -60 ms spike timing protocol resulted in pathway specific PV-iLTD (Fig. 2b, 95% ± 7% control verses 73% ± 7% test pathway, $n = 7$, $p < 0.05$). PV-iLTD was also observed when PV synapses were paired at 0 ms (Fig. 2c, 106% ± 3% control verses 72% ± 6% test pathway, $n = 13$, $p < 0.001$) but not at +60 ms (Fig. 2d, 105% ± 6% control verses 95% ± 8% test pathway, $n = 8$, $p > 0.05$) resulting in a pan-theta cycle iSTDP relationship incorporating iLTD but no iLTP (Fig. 2e). Surprisingly, SST synapses also displayed iLTD at -60 ms spike timings (Fig. 2f, 101% ± 7% control verses 70% ± 5% test pathway, $n = 6$, $p < 0.01$) but contrastingly underwent iLTP when paired at 0 ms (Fig. 2g, 104% ± 4% control verses 130% ± 13% test pathway, $n = 11$, $p < 0.05$). At pairings of +60 ms SST synapses also exhibited no plasticity similar to PV synapses (Fig. 2h, 92% ± 8% control verses 90% ± 8% test pathway, $n = 7$, $p > 0.05$). Therefore, SST synapses can undergo both iLTD and iLTP depending on the precise spike timing of pre- and post-synaptic action potentials in contrast to PV

synapses that only undergo iLTD. These results demonstrate that spike timings observed during theta rhythm entrainment lead to distinct rules for iSTDP at PV and SST synapses. Interestingly, we observed at both PV and SST synapses that pairing inhibitory inputs 60 ms after a burst of action potentials was insufficient to induce inhibitory plasticity, highlighting the importance of spike timing and the need for inhibitory synaptic input prior to pyramidal neuron activity.

PV-iLTD requires postsynaptic activation of T-type Ca^{2+} channels and calcineurin.

We next investigated the molecular mechanisms of spike timing-dependent PV-iLTD. First, we found that presynaptic input or postsynaptic spikes alone were insufficient to induce iLTD at PV synapses. (Presynaptic input only: 100% ± 12% control verses 94% ± 6% test pathway, n = 6, $p > 0.05$; Postsynaptic spikes only: 103% ± 10% control verses 94% ± 5% test pathway, n = 6, $p > 0.05$) (Fig. 3a,b). Consistent with PV-iSTDP and TBS induced PV-iLTD, these results show that coincident activity between PV interneurons and pyramidal neurons is required for PV-iLTD. Many forms of synaptic plasticity also depend on elevations in postsynaptic Ca^{2+} and we tested if this was the case for PV-iLTD by including the Ca^{2+} chelator BAPTA in the intracellular recording solution. BAPTA prevented PV-iLTD demonstrating a dependence on postsynaptic Ca^{2+} (100% ± 10% control verses 95% ± 8% test pathway, n = 6, $p > 0.05$) (Fig. 3c).

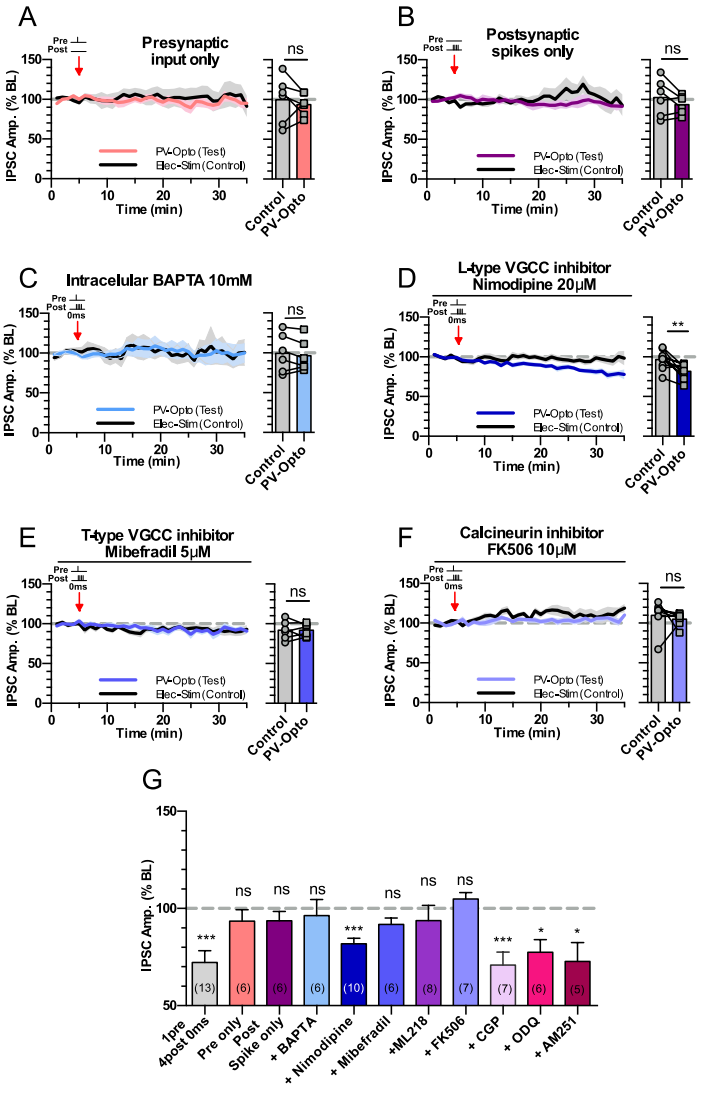

Figure 3. PV-iLTD requires activation of T-type VGCCs and calcineurin.

(a) Presynaptic stimulation of PV inputs alone induced no plasticity. **(b)** Postsynaptic spikes alone failed to induce plasticity at PV synapses. **(c)** Inclusion of BAPTA in the internal recording solution occludes PV iLTD upon 0 ms pre and post pairing. **(d)** L-type calcium channel antagonist Nimodopine doesn't block PV iLTD upon 0 ms pre and post pairing. **(e)** T-type calcium channel antagonist Mibefradil occludes PV iLTD upon 0 ms pre and post pairing. **(f)** Calcineurin inhibitor, FK506 occludes PV iLTD upon 0 ms pre and post pairing. In panels a-f, average plasticity in control and test pathways is shown on the right. **(g)** Summary histogram displaying the level of plasticity under each experimental condition. Data represent mean ± S.E.M statistical comparison via paired t-tests (a-f) and one sample t-tests (g). Significant difference is indicated (*p < 0.05, **p<0.01 and ***p<0.001). See also Supplementary Fig. 3.

Important sources of postsynaptic Ca^{2+} for the induction of excitatory and inhibitory synaptic plasticity are NMDA receptors and voltage-gated Ca^{2+} channels (VGCCs) [41, 47-49]. Since NMDA receptors are blocked in our experiments, we investigated the role of VGCCs in PV-iLTD. L-type VGCCs are the most prominent postsynaptic VGCCs, however, the L-type VGCC inhibitor nimodipine (20 µM) failed to block PV-iLTD (97% ± 4% control verses 82% ± 3% test pathway, $n = 10$, $p < 0.01$ (Fig. 3d). We next tested the role of T-type VGCCs using the inhibitor mibefradil (5 µM) which blocked PV-iLTD (92% ± 5% control verses 92% ± 3% test pathway, $n = 6$, $p > 0.05$ (Fig. 3e) and this was confirmed with the use of another T-type VGCC inhibitor ML218 (3 µM) [50] (99.4% ±5.3% control verses 93.8 ± 7.2% test pathway, $n = 8$, $p > 0.05$) (Supplementary Fig. 3e). Interestingly, T-type VGCCs have a low voltage threshold for activation and predominantly reside in an inactivated state at resting membrane potentials [51]. They therefore require hyperpolarisation to relieve voltage inactivation (de-inactivation), which corresponds precisely with the requirement for inhibitory synaptic input prior to postsynaptic depolarisation resulting in synapse specificity of PV-iLTD. These findings highlight a mechanism by which inhibitory synapses can provide a synapse-specific source of Ca^{2+} to induce inhibitory plasticity.

The downstream effects of Ca^{2+} can lead to release of retrograde signalling molecules which regulate presynaptic release of GABA [36, 40] or it can signal postsynaptically to reduce $GABA_A$ receptor function [32]. We therefore tested whether previously described retrograde signalling molecules nitrous oxide [40] and endocannabinoids [36] are involved in PV-iLTD. The nitrous oxide pathway antagonist ODQ (5 µM) and the CB1 receptor antagonist AM251 (1 µM) both failed to prevent PV-iLTD (Supplementary Fig. 3c,d and Fig. 3g, ODQ: 100% ± 8% control verses 78% ± 7% test pathway, $n = 6$, $p < 0.05$; AM251: 98% ± 8% control verses 73% ± 10% test pathway, $n = 5$, $p < 0.05$). An additional candidate mechanism could be the activation of the G-protein coupled $GABA_B$ receptor since

this has been shown to mediate a form of iLTD [38], however the $GABA_B$ receptor antagonist CGP 55845 (1 μM) also failed to prevent PV-iLTD (Supplementary Fig. 3b and Fig. 3g, 101% ± 10% control verses 71% ± 7% test pathway, n = 7, $p < 0.05$). One postsynaptic signalling pathway that has been implicated in iLTD is activation of the phosphatase calcineurin [32, 52, 53]. Application of the calcineurin inhibitor FK506 (10 μM) prevented PV-iLTD (110% ± 7% control verses 105% ± 3% test pathway, n = 7, $p > 0.05$) (Fig. 3f) indicating a postsynaptic target for Ca^{2+} signalling. In summary, PV-iLTD requires coincident pre- and post-synaptic activity, opening T-type VGCC to provide a postsynaptic Ca^{2+} signal that leads to activation of calcineurin to induce LTD at PV inhibitory synapses (Fig. 3g, 5a).

SST-iLTP requires postsynaptic activation of L- and T-type Ca^{2+} channels and CAMKII.

The molecular mechanisms of spike timing-dependent SST-iLTP were next investigated. Similar to PV-iLTD, and consistent with SST-iSTDP and TBS induced SST-iLTP, we found that SST-iLTP requires coincident pre- and post-synaptic activation as neither SST inputs nor postsynaptic action potentials alone were able to induce SST-iLTP (Presynaptic input only: 107% ± 6% control verses 91% ± 11% test pathway, n = 6, $p > 0.05$; Postsynaptic spikes only: 94% ± 5% control verses 100% ± 10% test pathway, n = 7, $p > 0.05$) (Fig. 4a,b). The inclusion of the Ca^{2+} chelator BAPTA also prevented the induction of iLTP at SST synapses (97.44% ± 10% control verses 92% ± 6% test pathway, n = 6, $p > 0.05$) (Fig. 4c), indicating SST-iLTP requires postsynaptic Ca^{2+}. Again, we assessed if L- and/or T-type VGCCs could provide the source of postsynaptic Ca^{2+} required for SST-iLTP. Interestingly, L-Type VGCC antagonist nimodipine and T-type VGCC antagonists mibefradil and ML218 both blocked SST-iLTP (nimodipine: 93% ± 7% control verses 101% ± 7% test pathway, n = 5, $p > 0.05$; mibefradil: 99% ± 9% control

verses 101% ± 10% test pathway, n = 7, p > 0.05; ML218: 113% ± 8% control verses 100% ± 6% test pathway, n = 7, p > 0.05) (Fig. 4d,e,h, Supplementary Fig. 4b) showing SST-iLTP requires activation of L-type and T-type VGCCs with the latter providing a synapse specific source of Ca^{2+} similar to PV-iLTD.

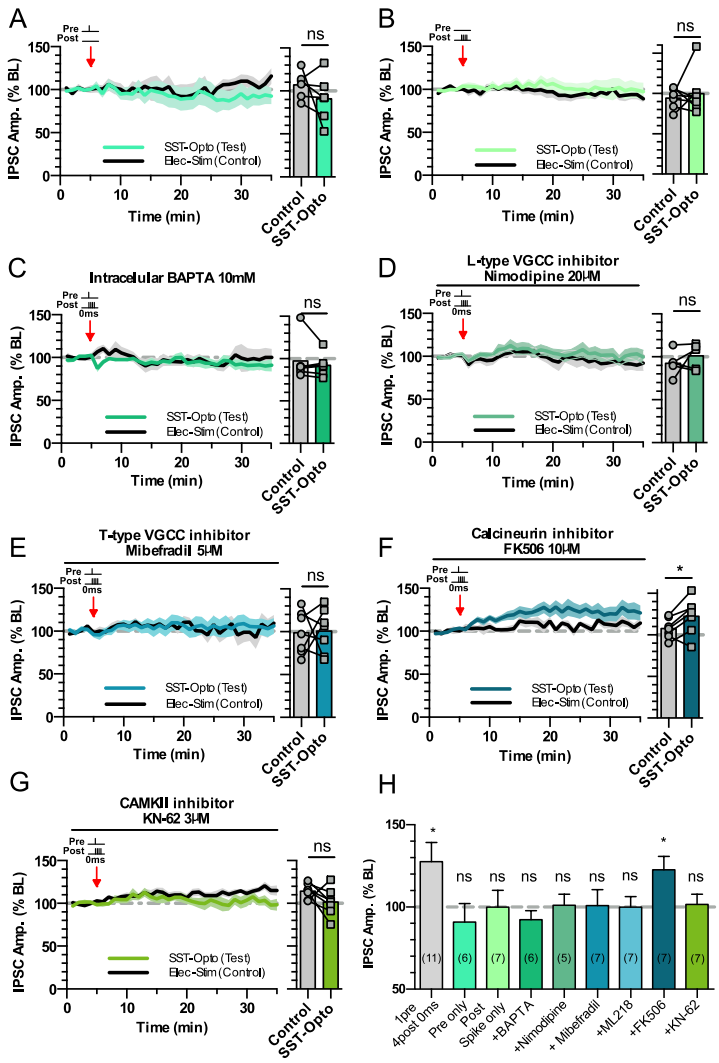

Figure 4. SST-iLTP requires activation of L-type and T-type VGCCs and CAMKII.

(a) Presynaptic stimulation of SST inputs alone failed to induce plasticity. **(b)** Post synaptic spikes alone failed to induce plasticity at SST synapses. **(c)** Inclusion of BAPTA in the internal recording solution occludes SST iLTP upon 0 ms pre and post pairing. **(d)** L-type calcium channel antagonist Nimodopine occludes SST iLTP upon 0 ms pre and post pairing. **(e)** T-type calcium channel antagonist Mibefradil occludes SST iLTP upon 0 ms pre and post pairing. **(f)** Calcineurin inhibitor, FK506 fails to block SST iLTP upon 0 ms pre and post pairing. **(g)** CAMKII inhibitor KN-62 occludes SST iLTP upon 0 ms pre and post pairing. In panels a-g, average plasticity in control and test pathways is shown on the right. **(h)** Summary

histogram displaying the level of plasticity under each experimental condition. Data represent mean ± S.E.M statistical comparison via paired t-tests (a-g) and one sample t-tests (h). Significant difference is indicated (*p < 0.05). See also Supplementary Fig. 4.

Since calcineurin is required for PV-iLTD, we next tested the possible involvement of calcineurin in SST-iLTP. However, inhibition of calcineurin failed to block SST-iLTP (108% ± 5% control verses 123% ± 8% test pathway, n = 7, p < 0.05) (Fig. 4f,h). As SST-iLTP requires both L-type and T-type VGCCs we hypothesised that SST-iLTP might be mediated by a molecular pathway engaged by high levels of postsynaptic Ca^{2+}. CAMKII is one such candidate and has been shown to mediate potentiation of inhibitory synapses including SST synapses within the cortex [41] and other inhibitory synapses within the hippocampus [54, 55] resulting in postsynaptic changes in $GABA_A$ receptors. We therefore tested the involvement of CAMKII activation on hippocampal SST-iLTP and found that the CAMKII inhibitor KN-62 (3 μM) prevented SST-iLTP (115% ± 3% control verses 102% ± 6% test pathway, n = 7, p > 0.05) (Fig. 4g,h), consistent with its role in mediating iLTP. In summary, SST-iLTP requires the coincident activation of SST synapses and pyramidal neurons, which activates L-type and T-type VGCCs providing a Ca^{2+} source able to activate CAMKII to induce SST-iLTP (Fig. 5b).

SST and PV plasticity shape pyramidal neuron responses to excitatory input pathways.

To understand the potential implications of PV-iLTD and SST-iLTP on network integration of inputs to a pyramidal neuron, we implemented a multi-compartment model of a CA1 pyramidal neuron in the presence of proximal (PV) and distal (SST) inhibition (Fig. 6a). The simulated CA1 pyramidal neuron receives distal excitatory input from entorhinal inputs via the temporoammonic (TA) pathway and proximal excitatory input from CA3 inputs via the Schaffer collateral (SC) pathway. We also

implemented rate-based inhibitory plasticity rules derived from our experiments under the most physiologically-relevant conditions (SST-iLTP and PV-iLTD).Inhibitory synaptic weights onto pyramidal cells were therefore updated following a Hebbian plasticity rule in which coincident pre- and postsynaptic activity leads to iLTD for PV synapses and iLTP for SST synapses. We then simulated activity within the network before and after the induction of inhibitory plasticity and compared the correlation between Schaffer collateral or temporoammonic inputs and pyramidal cell activity at these two stages. As expected, the correlation between Schaffer collateral inputs and CA1 pyramidal cell activity increased and the correlation between temporoammonic inputs and CA1 pyramidal cell activity decreased following the induction of interneuron plasticity (Fig. 6b). Therefore, if we assume that SST-iLTP occurs primarily at distal dendritic locations, interneuron-specific plasticity is a potential mechanism to change CA1 network state from being driven by both temporoammonic and Schaffer collateral inputs to being primarily driven by Schaffer collateral inputs.

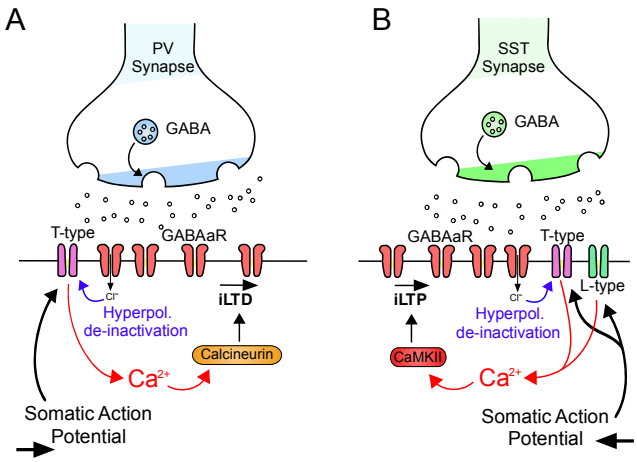

Figure 5. PV-iLTD and SST-iLTP mechanisms.

(a) Illustration of PV-iLTD mechanism. Hyperpolarisation by $GABA_A$ receptor currents relieves T-type VGCCs from voltage dependent inactivation (de-inactivation). Back-propagating action potentials then activate T-type VGCCs providing an inhibitory synapse specific source of Ca^{2+} to activate calcineurin resulting in LTD at PV synapses. **(b)** Illustration of SST-iLTP mechanism. Similar to PV-iLTD but requiring activation of T-type and L-type VGCCs that activates CAMKII resulting in LTP at SST synapses.

We next incorporated functionally-relevant feedforward and feedback connectivity for PV and SST interneurons within the CA1 network. PV interneurons receive strong feedforward innervation from the Schaffer collateral pathway but relatively limited input from the temporoammonic pathway and some feedback input from CA1 pyramidal neurons [7, 9, 43, 56]. In contrast, distally targeting SST interneurons receive almost no feedforward input and are driven by feedback input from CA1 pyramidal neurons [9, 43, 57, 58]. There is also evidence that bistratified interneurons that target inhibition to proximal dendrites in Stratum Radiatum and express both PV and SST can be feedforward in the Schaffer collateral pathway and also feedback within CA1 [9, 43].

Using these various functional connectivity arrangements, we first investigated the consequences of PV-iLTD on CA1 pyramidal cell output. For Schaffer collateral inputs with feedforward PV interneurons, PV-iLTD led to an increase in CA1 pyramidal cell activity due to a reduction in feedforward inhibition (Fig. 6c). The same result was achieved if we included feedback inhibition from PV interneurons (Supplementary Fig. 5a). When we considered the temporoammonic pathway without feedforward PV interneurons, PV-iLTD did not change pyramidal cell output (Fig. 6d). However, if we incorporated PV interneurons as feedforward and feedback inhibition, PV-iLTD led to an increase in pyramidal cell activity in response to temporoammonic stimulation (Supplementary Fig. 5b). Therefore, our model predicts that CA1 pyramidal cell activity in response to Schaffer collateral stimulation should increase following PV-iLTD whereas it is likely to remain unchanged in response to stimulation of the temporoammonic pathway unless PV interneurons participating in feedforward inhibition of the temporoammonic pathway or feedback inhibition are significantly activated and undergo PV-iLTD.

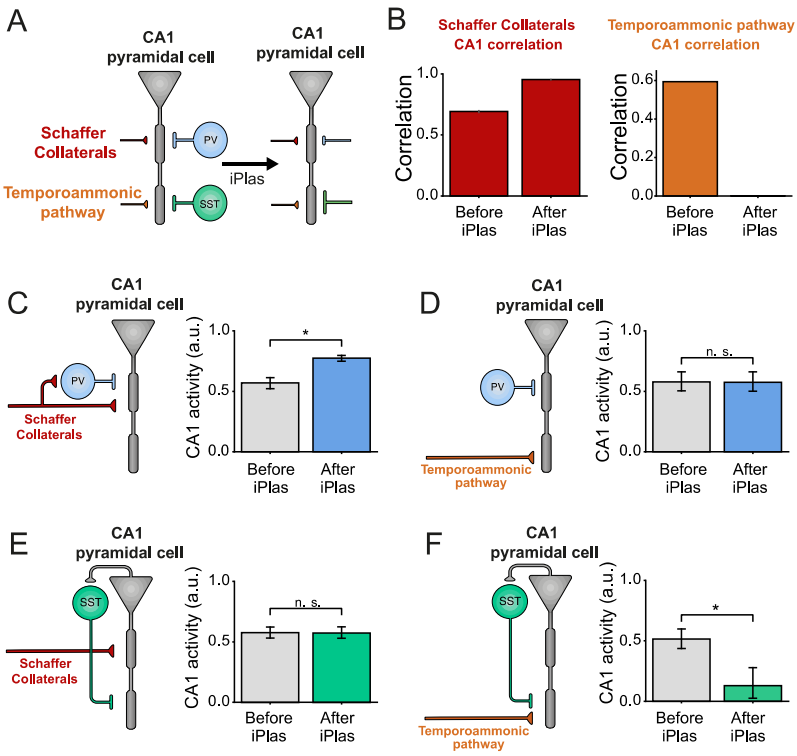

Figure 6. PV and SST plasticity differentially regulate Schaffer collateral and temporoammonic excitation of CA1 pyramidal neurons.

(a) Diagram of a simulated, rate-based CA1 pyramidal cell before and after the induction of inhibitory plasticity (iPlas). A single two-compartment neuron receives inputs from four sources: distally-targeting temporoammonic, proximally-targeting Schaffer collaterals, distally-targeting inhibition from SST interneurons, and proximally-targeting inhibition from PV interneurons. iPlas leads to PV-iLTD and SST-iLTP. **(b)** Correlation between Schaffer collateral activity and CA1 somatic activity (left) and temporoammonic activity and CA1 somatic activity (right) before and after iPlas at PV and SST synapses (PV-iLTD and SST-iLTP). **(c-f)** CA1 somatic activity before and after iPlas (either PV-iLTD or SST-iLTP) under the individual stimulation of either Schaffer collaterals or temporoammonic inputs. **(c)** Schaffer collateral-driven CA1 somatic activity is enhanced upon PV-iLTD. **(d)** CA1 somatic activity driven by temporoammonic input after PV-iLTD, is unchanged. **(e)** CA1 somatic activity driven via Schaffer collateral input after SST-iLTD is unchanged. **(f)** SST-iLTP leads to a reduction in CA1 somatic activity in response to temporoammonic input. Data represent mean ± S.E.M statistical comparison via unpaired t-tests. Significant difference is indicated (*$p < 0.05$). See also Supplementary Fig. 5.

We next investigated the implications of SST-iLTP on CA1 pyramidal cell output. Pyramidal cell activity in response to Schaffer collateral stimulation was not affected by SST-iLTP if SST synapses are located at the pyramidal cell's distal dendritic compartment (Fig. 6e) and this was true regardless of whether SST interneurons were activated in feedforward or feedback fashion (Supplementary Fig. 5c). Contrary to Schaffer collateral stimulation, temporoammonic-induced CA1 pyramidal cell activity was reduced after SST-iLTP (Fig. 6f) and this effect was stronger if SST interneurons were considered to be feedforward as well as feedback (Supplementary Fig. 5d). In summary, our model predicts that SST-iLTP does not affect Schaffer collateral-induced CA1 pyramidal cell activity whereas SST-iLTP decreases activity induced by temporoammonic stimulation.

If we assume the functional connectivity shown in Figures 6c-f, our model simulations therefore predict that PV-iLTD will increase CA1 pyramidal neuron responses to Schaffer collateral but not temporoammonic inputs and that SST-iLTP will decrease CA1 pyramidal neuron responses to temporoammonic but not Schaffer collateral inputs.

To test these predictions, we experimentally investigated the impact of PV-iLTD and SST-iLTP on the probability of spike generation in CA1 pyramidal neurons. By stimulating either the Schaffer collateral or temporoammonic pathways, action potential probability was recorded in response to 10 consecutive EPSPs where the stimulation intensity was set such that the baseline action potential probability for each EPSP was ~50%. Upon Schaffer collateral stimulation, PV-iLTD (0 ms timing) led to an increase in the spike probability (0.4 ± 0.07 baseline verses 0.78 ± 0.05 post plas, $n = 6$, $p < 0.05$) (Fig. 7a) that mirrored the timecourse of PV-iLTD, but for temporoammonic pathway stimulation spike probability was unaltered (0.44

± 0.04 baseline verses 0.47 ± 0.03 post plas, n = 6, p > 0.05) (Fig. 7b). Taken together these results confirm the predictions from the model and suggest that in our experiments the majority of PV interneurons recruited by Schaffer collateral stimulation are feedforward and undergo PV-iLTD whereas few PV interneurons are recruited by temporoammonic stimulation or via feedback excitation from CA1 pyramidal neurons. We next conducted experiments to examine the impact of SST-iLTP on spike generation. We found that the increase in SST inhibition with SST-iLTP had little effect on action potential generation from Schaffer collateral stimulation (0.53 ± 0.04 baseline verses 0.5 ± 0.08 post plas, n = 8, p > 0.05) (Fig. 7c) but led to a robust reduction in spike generation from the temporoammonic pathway (0.52 ± 0.03 baseline verses 0.27 ± 0.09 post plas, n = 6, p < 0.05 (Fig. 7d). Again, these results confirm the predictions from the model and suggest that in our experiments SST interneurons are primarily feedback and target distal dendritic regions of pyramidal neurons.

Taken together, these results demonstrate that long-term inhibitory plasticity changes the responses of CA1 pyramidal neurons prioritising inputs from the Schaffer collateral pathway over those from the temporoammonic pathway. Increased distal dendritic inhibition driven by SST-iLTP will also inhibit the induction of excitatory synaptic plasticity [44, 59] with important functional implications for the formation and stability of place cells.

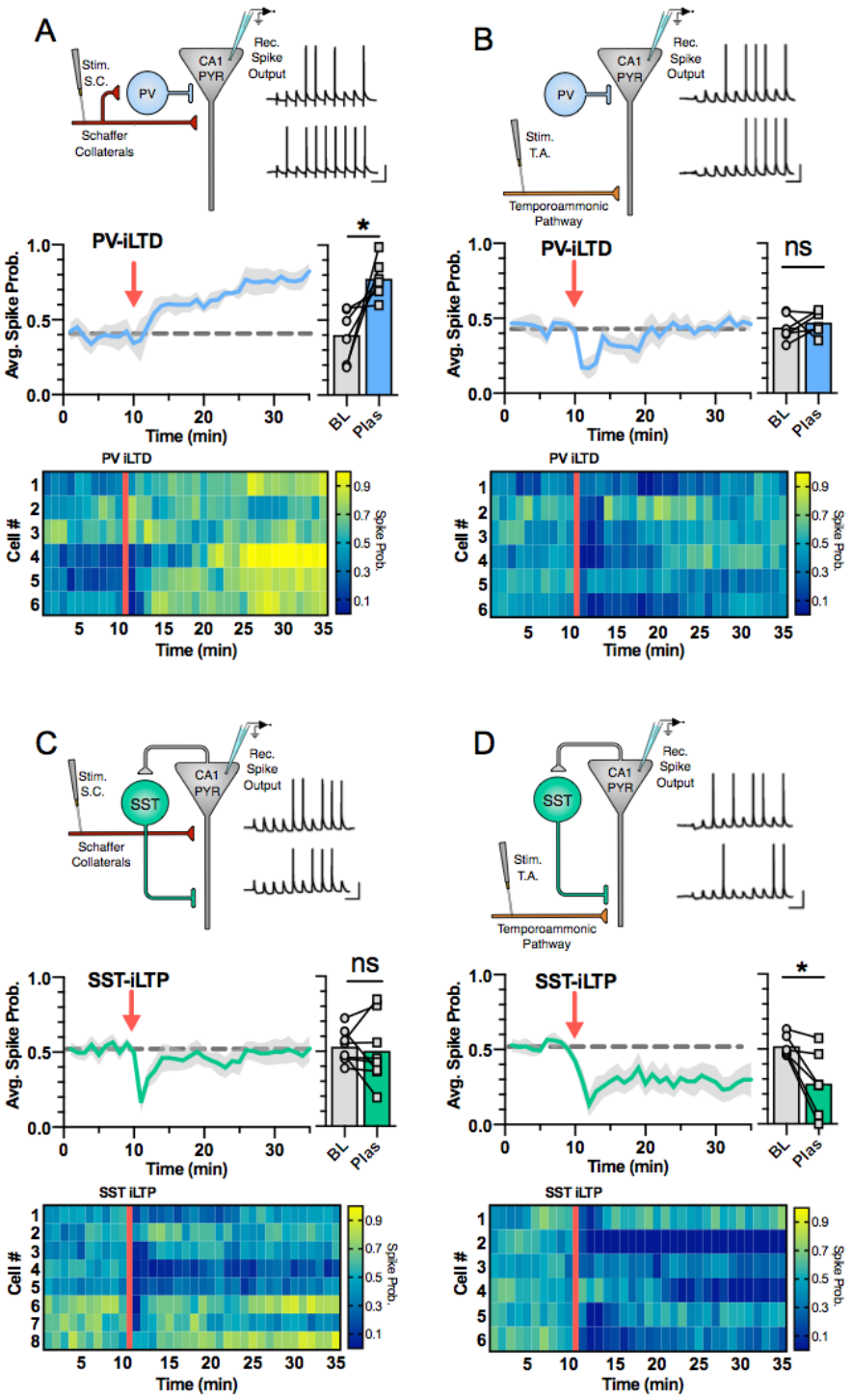
A
Stim. S.C.
PV
CA1 PYR
Rec. Spike Output
Schaffer Collaterals
PV-iLTD
Avg. Spike Prob.
Time (min)
BL
Plas
*
PV iLTD
Cell #
Spike Prob.
B
Stim. T.A.
Temporoammonic Pathway
ns
C
SST
SST-iLTP
SST iLTP
D

Figure 7. CA1 output driven by Schaffer collateral or temporoammonic inputs is differentially regulated by PV-iLTD and SST-iLTP.

(a) Diagram showing the experimental design where electrically stimulated Schaffer collaterals evoke action potentials in CA1 pyramidal neurons with example current-clamp traces before and after induction of PV iLTD (0 ms pre and post pairing) (top). Spike probability timecourse (left) and average spike probability during baseline (BL) and 20-25 minutes after induction of PV iLTD (Plas) (right). **(b)** Same as A but for the stimulation of the temporoammonic pathway. **(c)** Diagram showing electrical stimulation of Schaffer collaterals with example traces before and after induction of SST iLTP (0 ms pre and post pairing) (top). Spike probability timecourse (left) and average spike probability during baseline (BL) and after SST iLTP (Plas) (right). **(d)** same as C but for stimulation of the temporoammonic pathway. Data represent mean ± S.E.M statistical comparison via paired t-tests between baseline and post plasticity where significance difference is indicated (*p < 0.05). Scale bars: 100ms, 20mV.

Inhibitory plasticity at PV and SST synapses provides a mechanism for place cell stability across multiple environments.

We next explored the implications of long-term inhibitory plasticity on place cell physiology within hippocampal networks. The long-term nature of inhibitory plasticity suggests that its impact on place cell physiology will be evident as an animal traverses different environments. Key features of place cells are: (i) that in multiple different environments each place cell may represent distinct locations or switch to be silent, and (ii) that within any single environment place cell representations are broadly stable upon repeated exposures to that environment [22, 60]. However, these two features are somewhat contradictory since they require place cells to respond to different inputs without interference [23].

To investigate the functional implications of interneuron subtype-dependent long-term plasticity for place cell physiology in multiple different environments, we simulated a CA1 network receiving place-tuned input while an animal explored first an annular track (environment A) and then a different track (environment B) before finally returning to the original familiar environment A' (Fig. 8a). In our

simulations, CA1 pyramidal neurons receive inputs from Schaffer collaterals, temporoammonic pathway, SST interneurons and PV interneurons (Fig. 8b). Schaffer collateral inputs are spatially tuned while the other inputs are considered spatially uniform for simplicity. Schaffer collateral inputs are plastic and follow a Hebbian-type plasticity rule which depends on coincident pre- and post-synaptic activation. Following recent evidence that place fields are formed by synaptic plasticity at Schaffer collateral synapses following closely-timed temporoammonic and Schaffer collateral inputs [19, 61], we implemented the postsynaptic term of the Hebbian plasticity rule to be the product of the activities of the distal and proximal compartments of our two-compartment neuron model (see Methods). SST and PV inhibitory synapses onto pyramidal cells also follow a rate-based Hebbian-type plasticity rule inspired by the physiologically-relevant scenarios from our experimental data (as for Figure 6). Coincident pre- and post-synaptic activity leads to iLTP in the case of SST synapses, whereas pre- and post-synaptic coactivation leads to iLTD in the case of PV synapses.

For any trial simulation of the network, the simulated CA1 pyramidal neuron rapidly developed a place field at a random location within environment A that remained stable for subsequent laps of the track (Fig. 8b). These place fields were driven by rapidly evolving synaptic weight changes (Supplementary Fig. 6). When the track was switched to environment B, the indexes of Shaffer collateral inputs were shuffled. In this environment, the CA1 pyramidal neuron occasionally formed a new place field but was more often silent due to an inability to align and adapt synaptic weight increases after the inputs were shuffled (Fig. 8b and Supplementary Fig. 6a). On returning to the familiar environment A', the initial place field location was reinstated immediately (Fig. 8b,d,e). These results are qualitatively in line with the experimentally observed physiology of place cell activity in different environments [22].

To determine the role of inhibitory plasticity, we first removed PV-iLTD and SST-iLTP from the model. Simulations of this model lacking inhibitory plasticity showed similar place cell activity in environment A. In contrast, when the track was switched to environment B without inhibitory plasticity engaged, synaptic weight changes drove the generation of new place fields in every trial and the overall spiking rates were not reduced (Fig. 8c and Supplementary Fig. 6b). Furthermore, on returning to environment A, the place fields were no longer reinstated but instead new representations evolved (Fig. 8c,d,f). Thus, without inhibitory plasticity novel environments generate interference and the network is no longer capable of creating stable place field representations.

We next sought to distinguish the roles of PV-iLTD and SST-iLTP within this network. Simulations of a model with only PV-iLTD (SST-iLTP OFF) showed similar lack of place cell stability across environments A-B-A' to simulations with no inhibitory plasticity and overall spiking rates were unchanged in environments B and A' due to prior spiking rate saturation (Fig. 8g,i,j). With implementation of only SST-iLTP (PV-iLTD OFF), place cell stability across environments A-B-A' was reinstated but overall spiking rates were reduced compared to simulations with full inhibitory plasticity (Fig. 8i,i,k).

These circuit-level modelling data show how long-term inhibitory plasticity can provide a mechanism for the experimentally observed phenomenon that newly formed place cells are stable with repeated exposure to an environment and don't undergo interference from experiencing other environments. This stability is principally due to SST-iLTP which also reduces the efficiency of forming new place fields in different environments. The overall spike output of place cells is maintained by PV-iLTD which counteracts the reduction in spike output caused by SST-iLTP.

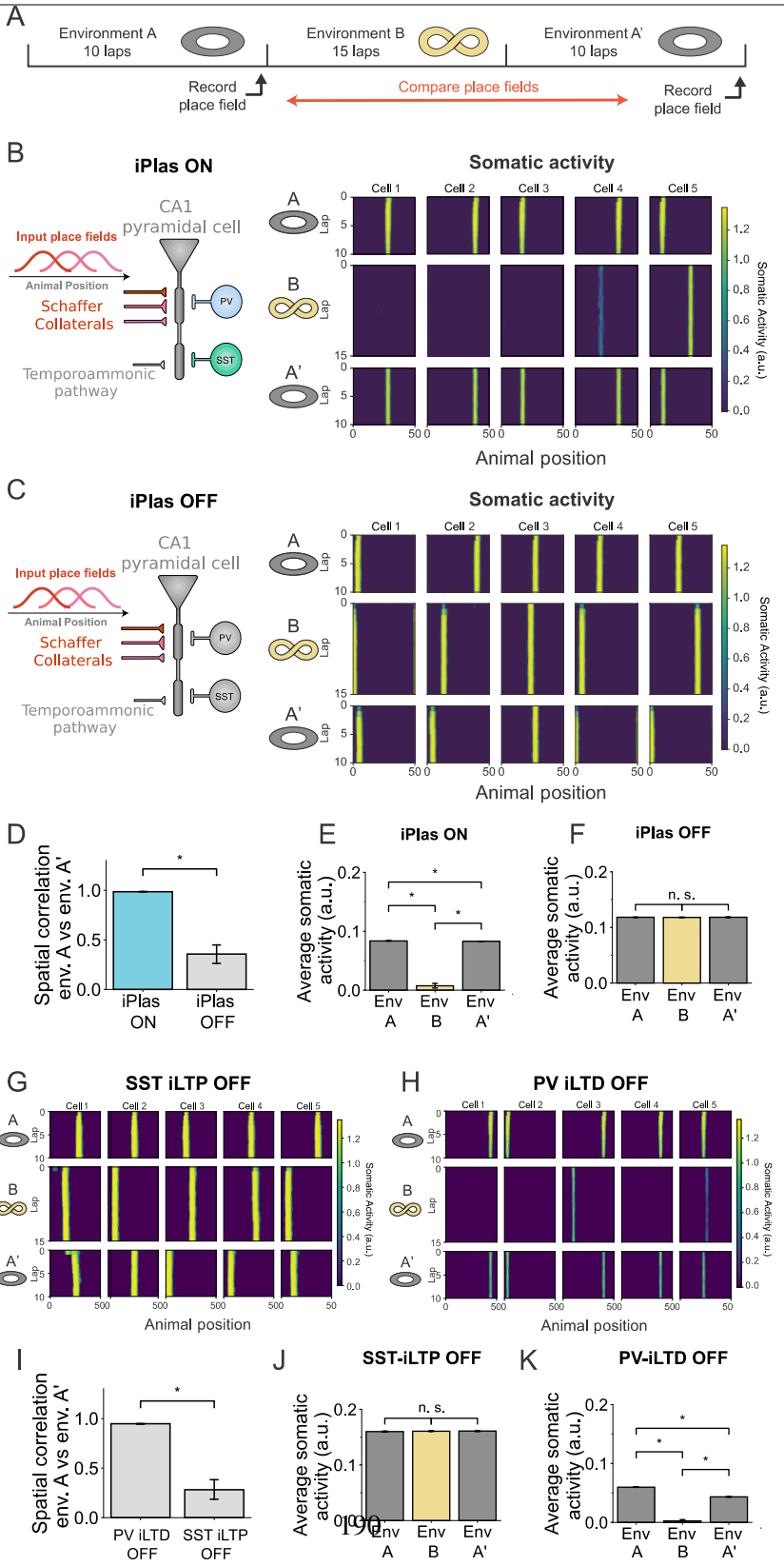
A
Environment A
10 laps
Environment B
15 laps
Environment A'
10 laps
Record place field
Compare place fields
Record place field
B
iPlas ON
CA1 pyramidal cell
Input place fields
Animal Position
Schaffer Collaterals
PV
SST
Temporoammonic pathway
Somatic activity
Cell 1
Cell 2
Cell 3
Cell 4
Cell 5
Lap
Somatic Activity (a.u.)
Animal position
C
iPlas OFF
D
Spatial correlation env. A vs env. A'
iPlas ON
iPlas OFF
E
iPlas ON
Average somatic activity (a.u.)
Env A
Env B
Env A'
F
iPlas OFF
n. s.
G
SST iLTP OFF
H
PV iLTD OFF
I
PV iLTD OFF
SST iLTP OFF
J
SST-iLTP OFF
K
PV-iLTD OFF

Figure 8. PV and SST plasticity ensure place cell stability and fidelity across multiple environments.

(a) Simulation protocol. An animal explores environment A for 10 laps. It is then moved to environment B and explores it for 15 laps. Finally, the animal is moved back to the first environment (A') and is allowed to run for another 10 laps. Throughout this protocol, two-compartment CA1 pyramidal cells are simulated receiving spatially-tuned Schaffer collateral inputs, temporoammonic input, and PV and SST inhibitory inputs. Schaffer collateral synapses follow a Hebbian-type excitatory plasticity dependent on the co-activation of dendritic and somatic compartments (see methods). PV and SST synapses undergo rate-based iPlas (PV-iLTD and SST-iLTP). We simulate the switch from environment A to environment B by randomly shuffling the identity of the SC inputs to the CA1 pyramidal neuron. Schematic depictions of environments A and B indicate their cyclical nature. **(b)** Diagram of simulated CA1 pyramidal cell and examples of somatic activity during exploration for iPlas ON. With iPlas (PV-iLTD and SST-iLTP) ON, place field location formed in environment A (top & bottom panel) remains stable after exposure to novel environment B (middle panel). **(c)** Diagram of simulated CA1 pyramidal cell and examples of somatic activity during exploration for iPlas OFF. Location of place fields formed in environment A are not maintained after exposure to a novel environment. **(d)** Spatial correlation between environment A before and after exposure to novel environment is maintained when iPlas is present but is reduced without iPlas. **(e)** When iPlas is ON, average somatic activity of recently formed place cell is significantly reduced in new environment B but returns to higher levels when the animal returns to environment A'. **(f)** When iPlas is OFF, average somatic activity remains high in both environments. **(g)** When SST-iLTP is turned off, leaving just PV-iLTD, place cell locations are not retained after exposure to a new environment. **(h)** When PV-iLTD is turned off, leaving just SST-iLTP, place cell locations are maintained across multiple environments. **(i)** Spatial correlation between environment A before and after exposure to novel environment is maintained when only PV-iLTD is turned off but is reduced when only SST-iLTP is turned off. **(j)** SST-iLTP is turned off, leaving just PV-iLTD, average somatic activity remains high in both environments. **(k)** When PV-iLTD is turned off, leaving just SST-iLTP, average somatic activity is lower and thus less robust. Data represent mean ± S.E.M statistical comparison via unpaired t-tests. Significant difference is indicated (*$p < 0.05$). See also Supplementary Fig. 6.

Discussion

Inhibitory GABAergic synapses are known to undergo long-term plasticity but very few studies have defined which subpopulations of inhibitory interneurons are engaged and whether plasticity is induced by physiological firing patterns. This is important since distinct interneuron subtypes play highly specific roles within neuronal networks [1] and therefore plasticity at one inhibitory synapse may have very different effects to another. In this study we address this complexity and show that proximal and distal dendritically targeting interneuron synapses on CA1 pyramidal neurons have distinct plasticity rules within the hippocampus. These inhibitory synapses undergo homosynaptic plasticity in a Hebbian manner relying on the coincident activation of interneurons and pyramidal neurons (Fig. 1,2). This coincident activity enables recruitment of VGCCs to provide local sources of Ca^{2+} able to alter inhibitory synapse strength (Fig. 3,4,5).

By computationally modelling the effects of inhibitory plasticity at a single neuron level, we predicted that altered inhibition at distinct dendritic compartments dramatically alters pyramidal neuron output (Fig. 6). We confirmed this experimentally showing action potential generation from proximally and dendritically targeting excitatory inputs is modulated by inhibitory plasticity in corresponding dendritic compartments (Fig. 7).

By expanding our computational model, we show how plasticity at these distinct inhibitory synapses can play roles in the stabilisation of place cell activity within the hippocampus (Fig. 8). This inhibitory plasticity stabilisation ensures place cell fidelity and resilience to interference from activity in multiple different environments.

Inhibitory plasticity at distinct inhibitory synapses

The mechanisms and network implications of long-term plasticity at glutamatergic synapses have been extensively characterised. However, less attention has been paid to long-term plasticity at inhibitory synapses which are known to undergo dynamic changes in efficacy [1, 27, 28]. An array of unique mechanisms discovered for inhibitory plasticity suggests a lack of uniformity across the multiple subtype-specific inhibitory synapses.

Within the hippocampus, synapses from CCK expressing proximally targeting basket cells onto CA1 pyramidal neurons undergo an endocannabinoid mediated iLTD [36]. Here, mobilisation of retrograde endocannabinoid signalling results in long term suppression of GABA release [36, 62]. We demonstrate that a similar morphological subtype of interneuron, the proximally targeting PV interneurons can also undergo iLTD but in an endocannabinoid independent mechanism (Fig. 3), highlighting the diversity of plasticity mechanisms even among interneurons with similar morphology [63].

Other long-term inhibitory plasticity mechanisms include a persistent shift in the chloride reversal potential caused by coincident activity-dependent modulation of the KCC2 chloride transporter [39, 64, 65]. Interestingly, in the hippocampus this iLTD is reported in the feedforward inhibitory pathway for Schaffer collateral innervation of CA1, commensurate with PV basket cell innervation, and is dependent on L-type VGCC and NMDA receptor activation. An alternative set of mechanisms for PV synapse plasticity is reported in the auditory cortex where PV synapses undergo bidirectional iSTDP via BDNF and $GABA_B$ dependent mechanisms [38]. However, these mechanisms do not appear to apply to PV-iLTD in the hippocampus and moreover, we found no evidence for PV-iLTP. The lack of PV-iLTP is also reported in the prefrontal cortex where SST but not PV synapses undergo iLTP [41]. This suggests that inhibitory plasticity rules may not be conserved across brain regions or that PV synapses undergo multiple forms of inhibitory plasticity. In contrast, the

mechanism for iLTP at SST synapses may be broadly conserved, at least between prefrontal cortex and hippocampus, where activation of CAMKII via Ca^{2+} influx to dendrites is found to induce iLTP [41]. The mechanistic differences here relate to the source of Ca^{2+} influx, arising from NMDA receptors in prefrontal cortex and L- and T-type VGCCs in hippocampus. We further show that hippocampal SST synapses can be depressed by non-coincident pre- and post-synaptic spike timing and it will be interesting to find out if this is also the case for synapses in prefrontal cortex.

Inhibitory plasticity relies on recruitment of T-type VGCC.

We show that plasticity at both PV and SST synapses exhibits several key properties: (i) it depends on the coincident activity of inhibitory synapses and postsynaptic action potentials, (ii) it is synapse specific, and (iii) it relies on postsynaptic Ca^{2+} signalling. These properties are apparently contradictory since synapse-specific inhibition is hyperpolarising which usually inhibits Ca^{2+} influx and signalling. We show that this apparent contradiction is resolved by recruitment of T-type VGCCs. At resting membrane potentials, T-type VGCCs are in an inactivated state, which can be de-inactivated by a hyperpolarising membrane potential [51, 66], this activation profile lends itself perfectly to recruitment by GABAergic synapse activity. Importantly, we show that pairing action potentials before inhibitory input or inhibitory input alone is insufficient to induce inhibitory plasticity. These observations suggest GABA synapse dependent de-inactivation of T-type VGCC is required prior to action potential activation of T-type VGCC, leading to a local synapse specific source of Ca^{2+} to drive inhibitory plasticity.

Indeed, there is considerable evidence linking GABA signalling and T-type VGCC activation. In the cerebellum and thalamus where T-type VGCCs are widely expressed, T-type VGCCs regulate inhibitory synapse strength [64, 67-69]. In the thalamus GABAergic synapses onto thalamocortical neurons de-inactivate T-type

VGCCs and reduce inhibitory synaptic strength [68]. This thalamocortical inhibitory plasticity is also dependent on the interaction of calcineurin with $GABA_A$ receptors, similar to findings in the hippocampus [32, 52] and those we present here.

A striking finding in our results shows that identical induction protocols PV and SST synapses induce opposing forms of plasticity via the differential recruitment of calcineurin and CaMKII. Since CaMKII requires higher [Ca^{2+}] to activate, the differential recruitment of calcineurin and CaMKII could be explained if postsynaptic [Ca^{2+}] is higher at SST vs PV inhibitory synapses. In support of this hypothesis, we show that SST-iLTP relies on L-type as well as T-type VGCCs suggesting a higher level of Ca^{2+} entry. Alternatively, expression levels of VGCCs may increase at more distal dendritic locations and there is evidence that T-type VGCC expression is higher in dendritic regions of pyramidal neurons causing differential regulation of glutamatergic plasticity along the proximal-distal axis of pyramidal neurons [70].

The consequences of inhibitory synaptic plasticity on hippocampal network function.

Our data support two separate functions of interneuron subtype-specific inhibitory plasticity on hippocampal network function. Firstly, increasing inhibitory inputs to distal dendritic locations on CA1 pyramidal neurons whilst reducing inhibition at proximal locations prioritises response to inputs from CA3 pyramidal neurons via the Schaffer collateral pathway over those from entorhinal neurons via the temporoammonic pathway. Secondly, in our computational model, increasing inhibition at distal dendritic locations inhibits the induction of synaptic plasticity at excitatory synapses [44, 59] thereby reducing adaptability of hippocampal representations.

Interneuron-specific inhibitory plasticity at proximal and distal dendritic locations coupled with the anatomical arrangement of Schaffer collateral inputs to proximal dendrites and temporoammonic inputs to distal dendrites intuitively predicts that inhibitory plasticity will rebalance the weighting of excitatory inputs in favour of Schaffer collaterals. We formalised these predictions using computational modelling of the CA1 network and then tested them experimentally. We confirmed that PV-iLTD increases CA1 pyramidal neuron responses to Schaffer collateral stimulation whereas SST-iLTP decreases responses to temporoammonic stimulation. Our combination of computational modelling and experimental approaches also showed that the majority of PV interneurons activated by our optogenetic approach are feedforward in the Schaffer collateral pathway but not the temporoammonic. Furthermore, our data indicate a limited feedback role for the PV interneurons we activate since PV-iLTD did not impact CA1 pyramidal neuron spike output in response to temporoammonic input. This broadly corresponds to anatomical and functional data for PV interneurons in the hippocampus [7, 9, 43, 56]. In contrast, the SST interneurons we stimulate are distally targeting, receive almost no feedforward input and are driven by feedback input from CA1 pyramidal neurons and therefore have all the hallmarks of OLM cells [9, 43, 57, 58].

The implications of reprioritising CA3 input over entorhinal input to CA1 are not straightforward but parallels can be drawn with the short-term reprioritisation caused by neuromodulator or thalamocortical inputs in cortical circuits [59, 71-73]. Often these mechanisms also involve reconfiguration of inhibitory interneuron circuits which are proposed to prioritise input of new sensory information over internal representation on short timescales including theta cycle timescales [74, 75]. The long-term inhibitory plasticity described here is predicted to achieve the reverse outcome prioritising previously learnt associations and making the network less receptive to new information.

Such a scenario would fit with the second role of inhibitory plasticity inhibiting excitatory plasticity and therefore the formation of new representations. SST inhibitory input regulates dendritic excitability and therefore NMDA receptor activation and excitatory synaptic plasticity [15]. Long-term plasticity of SST synapses will change the ability for CA1 pyramidal neurons to undergo induction of excitatory LTP [44, 59]. We show that this has major implications for the stability and flexibility of place cells since their formation and remapping depends on excitatory synaptic plasticity driven by dendritic spikes generated by coincident Schaffer collateral and temporoammonic inputs [19, 61, 76]. SST-iLTP prevents place cell representations in environment A being disrupted by different representations in environment B and indeed reduces the ability for place cells to be active in multiple environments. Interestingly, short-term changes in PV and SST interneuron firing rates in response to novel environments may provide a countermechanism to enable new place fields to be formed in novel environments [25]. Our data and modelling therefore provide a mechanism to reconcile the observed stability of place cells across time and their ability to remap in distinct environments [22].

In summary, our data reveal a novel form of inhibitory plasticity in the hippocampus induced by physiological patterns of firing. It has major implications for hippocampal function controlling input-output relationships in CA1 and providing a mechanism to explain a long-standing conundrum regarding place cell stability versus flexibility.

Methods

Animal strains and breeding

All procedures and techniques were conducted in accordance to the UK animals scientific procedures act, 1986 with approval of the University of Bristol ethics committee. To express ChR2 within either PV,SST or Chrna2 expressing interneurons C57/Bl6 homozygous Ai32 mice (Gt(ROSA)26Sor$^{tm32(CAG-COP4*H134R/EYFP)Hze}$ Jax Stock number: 024109) were bred with either homozygous PV-Cre (Pvalb$^{tm1(cre)Arbr/J}$ Jax stock number: 017320), SST-Cre (Sst$^{tm2.1(cre)Zjh/J}$ Jax stock number: 013044) or Chrna2-cre [44] mice creating heterozygous offspring with interneuron specific expression of ChR2. For brain slice electrophysiology both male and female mice were used.

Brain slice preparation

Brain slices were prepared from 4-9 week old mice following cervical dislocation and decapitation and brains removed and dissected in ice cold cutting solution containing in mM: 205 Sucrose, 10 Glucose, 26 $NaHCO_3$, 2.5 KCl, 1.25 NaH_2PO_4, 0.5 $CaCl_2$, 5 $MgCl_2$, constantly bubbled with 95% O_2 and 5% CO_2. Horizontal brain slices, 400 µM thick containing the hippocampus were prepared via a vibratome (Leica LS1200). Brain slices were transferred to ACSF containing in mM: 124 NaCl, 3 KCl, 24 $NaHCO_3$, 1.25 NaH_2PO_4 10 Glucose, 2.5 $CaCl_2$, 1.3 $MgCl_2$, constantly bubbled with 95% O_2 and 5% CO_2. and incubated at 35 °C for 30 min before being stored at room temperature for at least 30 min before experimentation.

Whole cell patch clamp recordings.

Brain slices were transferred to a submerged slice recording chamber with a constant 2.5 ml/min flow of ACSF (see above), held at 32 °C. Inhibitory plasticity experiments were recorded in the presence of DAP5 (50 µM) and NBQX (20 µM) to isolate GABAergic events. Slices were visualised using infrared DIC optics using

a Scientifica SliceScope microscope. Patch electrodes with a resistance of 3-6 MΩ were pulled from borosilicate glass capillaries using a horizontal puller (P-97, Sutter-instruments) and filled with internal solution. For whole cell voltage clamp recordings where neurons were held at 0 mV internal solution consisted of in mM: 130 Cs-$MeSO_4$, 4 NaCl, 10 HEPES, 0.5 EGTA, 10 TEA-Cl, 2 Mg-ATP, 0.5 Na2-GTP, 1 QX-314.Cl, adjusted to pH 7.3 with CsOH and ~ 290 mOsm, Cl^- reversal potential -57 mV. For iSTDP experiments an intracellular solution consisting of in mM: 140 K-gluconate, 5 NaCl, 1 $MgCl_2$, 10 HEPES, 4 Mg-ATP, 0.3 Na_2-GTP, 0.2 EGTA adjusted to pH 7.3 with KOH and ~ 290 mOsm, Cl^- reversal potential -77 mV. For current clamp recordings the intracellular solution consisted of in mM: 130 K-gluconate, 8 NaCl, 1 $MgCl_2$, 10 HEPES, 4 Mg-ATP, 0.3 Na_2-GTP, 0.2 EGTA adjusted to pH 7.3 with KOH and ~290 mOsm, Cl^- reversal -67 mV. In all experiments a junction potential of ~ -15 mV was not compensated.

Recordings of CA1 pyramidal neurons were conducted via a Multiclamp 700A amplifier (Molecular devices) filtered at 6 kHz and digitised at a sampling frequency of 20 kHz using a Micro 1401 data acquisition board (CED). Data was acquired using Signal5 software (CED) and data analysed using custom MATLAB Scripts.

Synaptic stimulation and plasticity protocols.

For inhibitory plasticity experiments subtype specific IPSCs were evoked via optical stimulation of ChR2 via a 470 nm LED (Thorlabs) through a 40x objective lens using 2-5 ms square pulses of light. Control pathway IPSCs were evoked via 100 μs square pulse electrical stimulation delivered via a monopolar stimulating electrode placed in the pyramidal layer or Stratum Radiatum. For plasticity experiments each pathway was stimulated every 15 sec in an interleaved fashion and synapses from each pathway were checked for independence by a paired pulse protocol (Supplementary Fig. 1).

For light evoked TBS plasticity, neurons were voltage clamped at 0 mV for the duration of the experiment, light evoked TBS was applied in voltage clamp and consisted of 5 bursts delivered at 5 hz, each burst containing 4 light pulses at 100 hz with the protocol repeated 5 times at 0.033 hz. For inhibitory spike time dependent plasticity experiments, neurons were voltage clamped at -50 mV. Pairing protocol consisted of 100 pairings at 5 hz in current clamp (neurons maintained at -50 mV), each consisting of presynaptic light stimulation with a burst of action potentials initiated via somatic current injections (2 ms duration, 1 nA amplitude). For all plasticity experiments the series resistance was monitored and cells that showed a >20% change were excluded from analysis.

Spike probability experiments were conducted in current clamp where 10 EPSPs were evoked at 10 hz via a bipolar stimulating electrode placed in either the SR or SLM layer to stimulate the Schaffer collateral or temporoammonic pathway. Stimulation intensity was adjusted to evoked action potentials in roughly half of the EPSP stimulations.

Immunohistochemistry

Brains were fixed via cardiac perfusion of Phosphate buffered saline (PBS) followed by 4% Formaldehyde in PBS. Brains were removed and stored in PFA for 24hrs and then transferred to 30% sucrose PBS solution for 2 days. 50 µm thick slices were then obtained via cryostat sectioning. Slices were incubated in a blocking solution containing 5% donkey serum and 0.2% Triton X-100 for 90 min at room temperature. Slices were then incubated in room temperature overnight in PBS containing 1% donkey serum and either anti-PV (1:10000, Sigma P3088) anti-SST (1:10000 Santa Cruz SC-7819) or anti-GFP (1:1000 LifeTech A11122) antibodies for PV, SST and ChR2 visualisation respectively. Slices were then washed with PBS and incubated with secondary antibodies, Alexa-594 (1:1000, LifeTech) or Alexa-488 (1:1000, LifeTech) for 2hrs at room temperature, before

washing with PBS and mounting on microscope slides with 1:1000 DAPI staining. Slices were then visualised, and images acquired using a widefield fluorescence microscope. Hippocampal layer regions within the CA1 were defined based on DAPI staining and ChR2 mean fluorescence intensity was quantified using ImageJ software.

In vitro data analysis

Experimental unit was defined as cell with only one cell recorded per slice. Up to 3 cells were recorded from each animal with an average of 1.6 cells per animal. Measurements were taken as an average of 4 responses to obtain a data point per min, averages represent mean ± S.E.M. Time series data was normalised to the last 5 min of baseline and plasticity was assessed by comparing the average IPSC amplitude 20-30 min after plasticity induction between the control and test pathway. Owing to the within cell control, data were analysed using a paired two-tailed Student's t-test between the two pathways. For histograms comparing the average test pathway plasticity, statistical significance was assigned as a one-sample t-test compared to 100. In all cases significance assigned if $p < 0.05$.

Computational modelling

Neuron Model and network structure

We investigate a feedforward network consisted of a single postsynaptic neuron receiving inputs from the temporoammonic pathway, Schaffer collaterals, and SST and PV interneurons. The postsynaptic neuron is modelled using a two-compartment, rate-based neuron model. The first compartment represents the distal dendrites of CA1 pyramidal cells, receiving excitatory inputs from the temporoammonic pathway and inhibitory inputs from SST interneurons. The second compartment represents the perisomatic region of CA1 pyramidal cells,

receiving excitatory inputs from Schaffer Collaterals and inhibitory inputs from PV interneurons.

The dendritic compartment's activity, r_{dend}, is given by

$$\tau_0 \frac{dr_{dend}}{dt} = -r_{dend} + \left[TA_{input} - w_{SST} r_{SST}\right]_+ ,$$

where $[\cdot]_+$ denotes a rectification that sets negative values to zero, τ_0 is a time constant, TA_{input} is the temporoammonic pathway input, w_{SST} is the synaptic weight from SST interneurons to the CA1 pyramidal cell, and $r_{SST} = 1$ is the SST interneuron activity.

The somatic compartment's activity, r_{soma}, is given by

$$\tau_0 \frac{dr_{soma}}{dt} = -r_{soma} + g\left(r_{dend} + w_{SC} SC_{input} - w_{PV} r_{PV}\right)$$

where SC_{input} is the activity of Schaffer Collateral input neurons, w_{SC} are the synaptic weights from SC inputs, w_{PV} is the synaptic weight from PV interneurons to the CA1 pyramidal cell, $r_{PV} = 1$ is the PV interneuron activity, and g is a non-linear function given by

$$g(x) = \frac{4}{3}\left[\tanh\left(\frac{2x}{5}\right)\right]_+ .$$

TA and SC inputs

The simulated CA1 pyramidal cells receive excitatory inputs from the temporoammonic pathway and Schaffer Collaterals (SC). The input from the temporoammonic pathway is simulated as $TA_{input} = \mu_{TA} + \xi_{TA}$, where μ_{TA} is a constant and ξ_{TA} is generated from an Ornstein-Uhlenbeck process with a time constant of 50 ms, mean 0 and variance 0.5. The SC inputs are generated from N_{SC} input neurons and each input neuron is tuned to a specific location such that their

firing rates span over the entire environment. All place fields of SC input neurons have the same tuning width σ_{SC} and amplitude A_{SC}.

For the simulations involving exploration, the simulated animal explores an annular track of length L with speed v. The activity of a SC input neuron with place field centered at position p_0 is

$$SC_{input}(p) = A_{SC} exp\left(-\frac{d^2}{2\sigma_{SC}^2}\right) + A_{noise}\xi_{SC} \ ,$$

where p is the animal's position, d is the distance between the p and p_0 along the track, A_{noise} is a constant, and ξ_{SC} is generated from an Ornstein-Uhlenbeck process with a time constant of 50 ms, mean 0 and variance 0.5.

In Fig. 6, we simulate an artificial stimulation of TA and SC. Therefore, for these simulations, SC inputs are not spatially tuned. Instead, they are simulated as $SC_{input} = \mu_{SC} + \xi_{SC}$, where μ_{SC} is a constant.

Excitatory plasticity model

In Fig. 8, synaptic weights from SC input neurons to CA1 pyramidal neurons are plastic. These connections follow a Hebbian-type plasticity rule in which changes in synaptic weights depend on coincident pre- and postsynaptic activity. The postsynaptic term is given by the product of dendritic and somatic activity. This is motivated by recent findings suggesting that place fields are modified and formed following coincident TA and SC inputs [19, 61]. The excitatory synaptic weight w_{ij} from input neuron j to postsynaptic neuron i is updated following

$$\frac{dw_{ij}}{dt} = \eta_{SC}\left(r_{dend}^i r_{soma}^i - 0.1\right)_+ r^j \ ,$$

where η_{SC} is the learning rate for SC connections, r^j is the presynaptic neuron activity, r_{soma}^i is the somatic activity of the postsynaptic neuron, and r_{dend}^i is the

dendritic activity of the postsynaptic neuron. Because this rule is inherently unstable, synaptic weights are also normalized as commonly done [77]. After every weight update, we subtract the average synaptic weight $\sum_j w_{ij}/N_{SC}$ from all weights and add a constant term (here 2). Negative weights are then rectified to zero.

Inhibitory plasticity model

We implement an inhibitory plasticity rule inspired by our experimental findings. Under a rate-based framework, these plasticity rules are assumed to mirror those found during theta oscillations. Synaptic weights from PV interneurons onto CA1 pyramidal cells follow a rate-based Hebbian plasticity rule in which the coactivation of pre- and postsynaptic neurons leads to LTD:

$$\frac{dw_{PV}}{dt} = -\eta_{PV} r_{PV} r_{soma} \ ,$$

where η_{PV} is the learning rate for PV connections, and r_{soma} is pyramidal cell somatic activity. Synaptic weights from SST interneurons onto CA1 pyramidal cells follow a Hebbian plasticity rule in which the coactivation of pre- and postsynaptic neurons leads to LTP:

$$\frac{dw_{SST}}{dt} = \eta_{SST} r_{SST} r_{soma} \ ,$$

where η_{SST} is the learning rate for SST connections. Both PV and SST synaptic weights are bounded between w_{min} and w_{max}.

Environment switch

In Fig. 8, we simulate a feedforward network while an animal runs through an annular track. When the animal starts exploring environment A for the first time, the initial synaptic weights for the SC inputs are drawn from a lognormal distribution with underlying normal distribution with mean zero and standard deviation 0.1. The synaptic weights are then multiplied by 0.1 and two neighbouring

inputs are randomly chosen and their synaptic weights are set to 0.6. This imposes a small structure in the synaptic weights and ensures that input neurons are able to induce postsynaptic activity. The animal then explores environment A for 10 laps. Next, the animal is moved to a novel environment (environment B). We simulate the switch to a novel environment by randomly shuffling the identity of the SC inputs to the CA1 pyramidal neuron. The animal then explores environment B for 15 laps. Subsequently, the animal is moved back to environment A (environment A'), which is implemented by returning the SC inputs to the original identity. Finally, the animal explores environment A' for another 10 laps.

Parameters and simulations

All simulations were implemented in python and can be made available upon request. The parameters used in our simulations can be found in table 1.

Neuron Model		
Name	**Value**	**Description**
τ_0	1.25 ms	Time constant for the dynamics
Network parameters		
Name	**Value**	**Description**
N_{SC}	40	Number of SC input neurons
N_{SST}	1	Number of SST interneurons
N_{PV}	1	Number of PV interneurons
Plasticity Model		
Name	**Value**	**Description**
η_{SST}	2.0×10^{-4} ms $^{-1}$	SST plasticity learning rate
η_{PV}	2.0×10^{-4} ms $^{-1}$	PV plasticity learning rate
η_{SC}	2.5×10^{-5} ms $^{-1}$	Learning rate for Schaffer Collaterals
Place-tuned input		
Name	**Value**	**Description**
A_{SC}	6.0	Presynaptic place field amplitude
σ_{SC}	2.0	Presynaptic place field width
Simulation parameters		
Name	**Value**	**Description**
L	50	Track length
v	2.5×10^{-3} ms $^{-1}$	Animal speed

References

1. Pelkey, K.A.*, et al.* Hippocampal GABAergic Inhibitory Interneurons. *Physiol Rev* **97**, 1619-1747 (2017).
2. Klausberger, T. & Somogyi, P. Neuronal diversity and temporal dynamics: the unity of hippocampal circuit operations. *Science* **321**, 53-57 (2008).
3. Klausberger, T.*, et al.* Brain-state- and cell-type-specific firing of hippocampal interneurons in vivo. *Nature* **421**, 844-848 (2003).
4. Varga, C., Golshani, P. & Soltesz, I. Frequency-invariant temporal ordering of interneuronal discharges during hippocampal oscillations in awake mice. *Proc Natl Acad Sci U S A* **109**, E2726-2734 (2012).
5. Harris, K.D.*, et al.* Classes and continua of hippocampal CA1 inhibitory neurons revealed by single-cell transcriptomics. *PLoS biology* **16**, e2006387 (2018).
6. Katona, L.*, et al.* Sleep and movement differentiates actions of two types of somatostatin-expressing GABAergic interneuron in rat hippocampus. *Neuron* **82**, 872-886 (2014).
7. Milstein, A.D.*, et al.* Inhibitory Gating of Input Comparison in the CA1 Microcircuit. *Neuron* **87**, 1274-1289 (2015).
8. Royer, S.*, et al.* Control of timing, rate and bursts of hippocampal place cells by dendritic and somatic inhibition. *Nat Neurosci* **15**, 769-775 (2012).
9. Sun, Y.*, et al.* Cell-type-specific circuit connectivity of hippocampal CA1 revealed through Cre-dependent rabies tracing. *Cell reports* **7**, 269-280 (2014).
10. Geiger, J.R., Lubke, J., Roth, A., Frotscher, M. & Jonas, P. Submillisecond AMPA receptor-mediated signaling at a principal neuron-interneuron synapse. *Neuron* **18**, 1009-1023 (1997).
11. Pouille, F. & Scanziani, M. Enforcement of temporal fidelity in pyramidal cells by somatic feed-forward inhibition. *Science* **293**, 1159-1163 (2001).

12. Sohal, V.S., Zhang, F., Yizhar, O. & Deisseroth, K. Parvalbumin neurons and gamma rhythms enhance cortical circuit performance. *Nature* **459**, 698-702 (2009).
13. Chiu, C.Q.*, et al.* Compartmentalization of GABAergic inhibition by dendritic spines. *Science* **340**, 759-762 (2013).
14. Maccaferri, G. Stratum oriens horizontal interneurone diversity and hippocampal network dynamics. *J Physiol* **562**, 73-80 (2005).
15. Schulz, J.M., Knoflach, F., Hernandez, M.C. & Bischofberger, J. Dendrite-targeting interneurons control synaptic NMDA-receptor activation via nonlinear alpha5-GABAA receptors. *Nature communications* **9**, 3576 (2018).
16. O'Keefe, J. Place units in the hippocampus of the freely moving rat. *Exp Neurol* **51**, 78-109 (1976).
17. Isaac, J.T., Buchanan, K.A., Muller, R.U. & Mellor, J.R. Hippocampal place cell firing patterns can induce long-term synaptic plasticity in vitro. *J Neurosci* **29**, 6840-6850 (2009).
18. Mishra, R.K., Kim, S., Guzman, S.J. & Jonas, P. Symmetric spike timing-dependent plasticity at CA3-CA3 synapses optimizes storage and recall in autoassociative networks. *Nature communications* **7**, 11552 (2016).
19. Bittner, K.C., Milstein, A.D., Grienberger, C., Romani, S. & Magee, J.C. Behavioral time scale synaptic plasticity underlies CA1 place fields. *Science* **357**, 1033-1036 (2017).
20. Cohen, J.D., Bolstad, M. & Lee, A.K. Experience-dependent shaping of hippocampal CA1 intracellular activity in novel and familiar environments. *Elife* **6** (2017).
21. Sadowski, J.H., Jones, M.W. & Mellor, J.R. Sharp-Wave Ripples Orchestrate the Induction of Synaptic Plasticity during Reactivation of Place Cell Firing Patterns in the Hippocampus. *Cell reports* **14**, 1916-1929 (2016).

22. Colgin, L.L., Moser, E.I. & Moser, M.B. Understanding memory through hippocampal remapping. *Trends Neurosci* **31**, 469-477 (2008).
23. Chaudhuri, R. & Fiete, I. Computational principles of memory. *Nat Neurosci* **19**, 394-403 (2016).
24. Del Pino, I.*, et al.* Abnormal wiring of CCK(+) basket cells disrupts spatial information coding. *Nat Neurosci* **20**, 784-792 (2017).
25. Sheffield, M.E.J., Adoff, M.D. & Dombeck, D.A. Increased Prevalence of Calcium Transients across the Dendritic Arbor during Place Field Formation. *Neuron* **96**, 490-504 e495 (2017).
26. Trouche, S.*, et al.* Recoding a cocaine-place memory engram to a neutral engram in the hippocampus. *Nat Neurosci* **19**, 564-567 (2016).
27. Chiu, C.Q., Barberis, A. & Higley, M.J. Preserving the balance: diverse forms of long-term GABAergic synaptic plasticity. *Nat Rev Neurosci* **20**, 272-281 (2019).
28. Kullmann, D.M., Moreau, A.W., Bakiri, Y. & Nicholson, E. Plasticity of inhibition. *Neuron* **75**, 951-962 (2012).
29. Donato, F., Rompani, S.B. & Caroni, P. Parvalbumin-expressing basket-cell network plasticity induced by experience regulates adult learning. *Nature* **504**, 272-276 (2013).
30. Hellyer, P.J., Jachs, B., Clopath, C. & Leech, R. Local inhibitory plasticity tunes macroscopic brain dynamics and allows the emergence of functional brain networks. *NeuroImage* **124**, 85-95 (2016).
31. Vogels, T.P., Sprekeler, H., Zenke, F., Clopath, C. & Gerstner, W. Inhibitory plasticity balances excitation and inhibition in sensory pathways and memory networks. *Science* **334**, 1569-1573 (2011).
32. Muir, J.*, et al.* NMDA receptors regulate GABAA receptor lateral mobility and clustering at inhibitory synapses through serine 327 on the gamma2 subunit. *Proc Natl Acad Sci U S A* **107**, 16679-16684 (2010).

33. Nusser, Z., Hajos, N., Somogyi, P. & Mody, I. Increased number of synaptic GABA(A) receptors underlies potentiation at hippocampal inhibitory synapses. *Nature* **395**, 172-177 (1998).
34. Schuemann, A., Klawiter, A., Bonhoeffer, T. & Wierenga, C.J. Structural plasticity of GABAergic axons is regulated by network activity and GABAA receptor activation. *Front Neural Circuits* **7**, 113 (2013).
35. Alger, B.E. & Pitler, T.A. Retrograde signaling at GABAA-receptor synapses in the mammalian CNS. *Trends Neurosci* **18**, 333-340 (1995).
36. Chevaleyre, V. & Castillo, P.E. Heterosynaptic LTD of hippocampal GABAergic synapses: a novel role of endocannabinoids in regulating excitability. *Neuron* **38**, 461-472 (2003).
37. Lee, S.H., Foldy, C. & Soltesz, I. Distinct endocannabinoid control of GABA release at perisomatic and dendritic synapses in the hippocampus. *J Neurosci* **30**, 7993-8000 (2010).
38. Vickers, E.D.*, et al.* Parvalbumin-Interneuron Output Synapses Show Spike-Timing-Dependent Plasticity that Contributes to Auditory Map Remodeling. *Neuron* **99**, 720-735 e726 (2018).
39. Woodin, M.A., Ganguly, K. & Poo, M.M. Coincident pre- and postsynaptic activity modifies GABAergic synapses by postsynaptic changes in Cl- transporter activity. *Neuron* **39**, 807-820 (2003).
40. Nugent, F.S., Penick, E.C. & Kauer, J.A. Opioids block long-term potentiation of inhibitory synapses. *Nature* **446**, 1086-1090 (2007).
41. Chiu, C.Q.*, et al.* Input-Specific NMDAR-Dependent Potentiation of Dendritic GABAergic Inhibition. *Neuron* **97**, 368-377 e363 (2018).
42. Horn, M.E. & Nicoll, R.A. Somatostatin and parvalbumin inhibitory synapses onto hippocampal pyramidal neurons are regulated by distinct mechanisms. *Proc Natl Acad Sci U S A* **115**, 589-594 (2018).

43. Booker, S.A. & Vida, I. Morphological diversity and connectivity of hippocampal interneurons. *Cell Tissue Res* **373**, 619-641 (2018).
44. Leao, R.N.*, et al.* OLM interneurons differentially modulate CA3 and entorhinal inputs to hippocampal CA1 neurons. *Nat Neurosci* **15**, 1524-1530 (2012).
45. Mikulovic, S., Restrepo, C.E., Hilscher, M.M., Kullander, K. & Leao, R.N. Novel markers for OLM interneurons in the hippocampus. *Front Cell Neurosci* **9**, 201 (2015).
46. Buzsaki, G. Theta oscillations in the hippocampus. *Neuron* **33**, 325-340 (2002).
47. Griffith, T., Tsaneva-Atanasova, K. & Mellor, J.R. Control of Ca2+ Influx and Calmodulin Activation by SK-Channels in Dendritic Spines. *PLoS computational biology* **12**, e1004949 (2016).
48. Magee, J.C. & Johnston, D. A synaptically controlled, associative signal for Hebbian plasticity in hippocampal neurons. *Science* **275**, 209-213 (1997).
49. Tigaret, C.M., Olivo, V., Sadowski, J.H., Ashby, M.C. & Mellor, J.R. Coordinated activation of distinct Ca(2+) sources and metabotropic glutamate receptors encodes Hebbian synaptic plasticity. *Nature communications* **7**, 10289 (2016).
50. Xiang, Z.*, et al.* The Discovery and Characterization of ML218: A Novel, Centrally Active T-Type Calcium Channel Inhibitor with Robust Effects in STN Neurons and in a Rodent Model of Parkinson's Disease. *ACS Chem Neurosci* **2**, 730-742 (2011).
51. Randall, A.D. & Tsien, R.W. Contrasting biophysical and pharmacological properties of T-type and R-type calcium channels. *Neuropharmacology* **36**, 879-893 (1997).

52. Wang, J., *et al.* Interaction of calcineurin and type-A GABA receptor gamma 2 subunits produces long-term depression at CA1 inhibitory synapses. *J Neurosci* **23**, 826-836 (2003).
53. Luscher, B., Fuchs, T. & Kilpatrick, C.L. GABAA receptor trafficking-mediated plasticity of inhibitory synapses. *Neuron* **70**, 385-409 (2011).
54. Marsden, K.C., Beattie, J.B., Friedenthal, J. & Carroll, R.C. NMDA receptor activation potentiates inhibitory transmission through GABA receptor-associated protein-dependent exocytosis of GABA(A) receptors. *J Neurosci* **27**, 14326-14337 (2007).
55. Petrini, E.M., *et al.* Synaptic recruitment of gephyrin regulates surface GABAA receptor dynamics for the expression of inhibitory LTP. *Nature communications* **5**, 3921 (2014).
56. Ganter, P., Szucs, P., Paulsen, O. & Somogyi, P. Properties of horizontal axo-axonic cells in stratum oriens of the hippocampal CA1 area of rats in vitro. *Hippocampus* **14**, 232-243 (2004).
57. Lacaille, J.C., Mueller, A.L., Kunkel, D.D. & Schwartzkroin, P.A. Local circuit interactions between oriens/alveus interneurons and CA1 pyramidal cells in hippocampal slices: electrophysiology and morphology. *J Neurosci* **7**, 1979-1993 (1987).
58. Blasco-Ibanez, J.M. & Freund, T.F. Synaptic input of horizontal interneurons in stratum oriens of the hippocampal CA1 subfield: structural basis of feed-back activation. *Eur J Neurosci* **7**, 2170-2180 (1995).
59. Williams, L.E. & Holtmaat, A. Higher-Order Thalamocortical Inputs Gate Synaptic Long-Term Potentiation via Disinhibition. *Neuron* **101**, 91-102 e104 (2019).
60. Ziv, Y., *et al.* Long-term dynamics of CA1 hippocampal place codes. *Nat Neurosci* **16**, 264-266 (2013).

61. Bittner, K.C.*, et al.* Conjunctive input processing drives feature selectivity in hippocampal CA1 neurons. *Nat Neurosci* **18**, 1133-1142 (2015).
62. Younts, T.J.*, et al.* Presynaptic Protein Synthesis Is Required for Long-Term Plasticity of GABA Release. *Neuron* **92**, 479-492 (2016).
63. Freund, T.F. & Katona, I. Perisomatic inhibition. *Neuron* **56**, 33-42 (2007).
64. Wang, L., Kitai, S.T. & Xiang, Z. Activity-dependent bidirectional modification of inhibitory synaptic transmission in rat subthalamic neurons. *J Neurosci* **26**, 7321-7327 (2006).
65. Ormond, J. & Woodin, M.A. Disinhibition-Mediated LTP in the Hippocampus is Synapse Specific. *Front Cell Neurosci* **5**, 17 (2011).
66. Perez-Reyes, E. Molecular physiology of low-voltage-activated t-type calcium channels. *Physiol Rev* **83**, 117-161 (2003).
67. Aizenman, C.D., Manis, P.B. & Linden, D.J. Polarity of long-term synaptic gain change is related to postsynaptic spike firing at a cerebellar inhibitory synapse. *Neuron* **21**, 827-835 (1998).
68. Pigeat, R., Chausson, P., Dreyfus, F.M., Leresche, N. & Lambert, R.C. Sleep slow wave-related homo and heterosynaptic LTD of intrathalamic GABAAergic synapses: involvement of T-type Ca2+ channels and metabotropic glutamate receptors. *J Neurosci* **35**, 64-73 (2015).
69. Sieber, A.R., Min, R. & Nevian, T. Non-Hebbian long-term potentiation of inhibitory synapses in the thalamus. *J Neurosci* **33**, 15675-15685 (2013).
70. Isomura, Y., Fujiwara-Tsukamoto, Y., Imanishi, M., Nambu, A. & Takada, M. Distance-dependent Ni(2+)-sensitivity of synaptic plasticity in apical dendrites of hippocampal CA1 pyramidal cells. *J Neurophysiol* **87**, 1169-1174 (2002).
71. Fu, Y.*, et al.* A cortical circuit for gain control by behavioral state. *Cell* **156**, 1139-1152 (2014).

72. Hasselmo, M.E. & Schnell, E. Laminar selectivity of the cholinergic suppression of synaptic transmission in rat hippocampal region CA1: computational modeling and brain slice physiology. *J Neurosci* **14**, 3898-3914 (1994).
73. Hasselmo, M.E. The role of acetylcholine in learning and memory. *Curr Opin Neurobiol* **16**, 710-715 (2006).
74. Lopes-Dos-Santos, V.*, et al.* Parsing Hippocampal Theta Oscillations by Nested Spectral Components during Spatial Exploration and Memory-Guided Behavior. *Neuron* **100**, 940-952 e947 (2018).
75. Dupret, D., O'Neill, J. & Csicsvari, J. Dynamic reconfiguration of hippocampal interneuron circuits during spatial learning. *Neuron* **78**, 166-180 (2013).
76. Sheffield, M.E. & Dombeck, D.A. Calcium transient prevalence across the dendritic arbour predicts place field properties. *Nature* **517**, 200-204 (2015).
77. Lazar, A., Pipa, G. & Triesch, J. SORN: a self-organizing recurrent neural network. *Frontiers in computational neuroscience* **3** (2009).

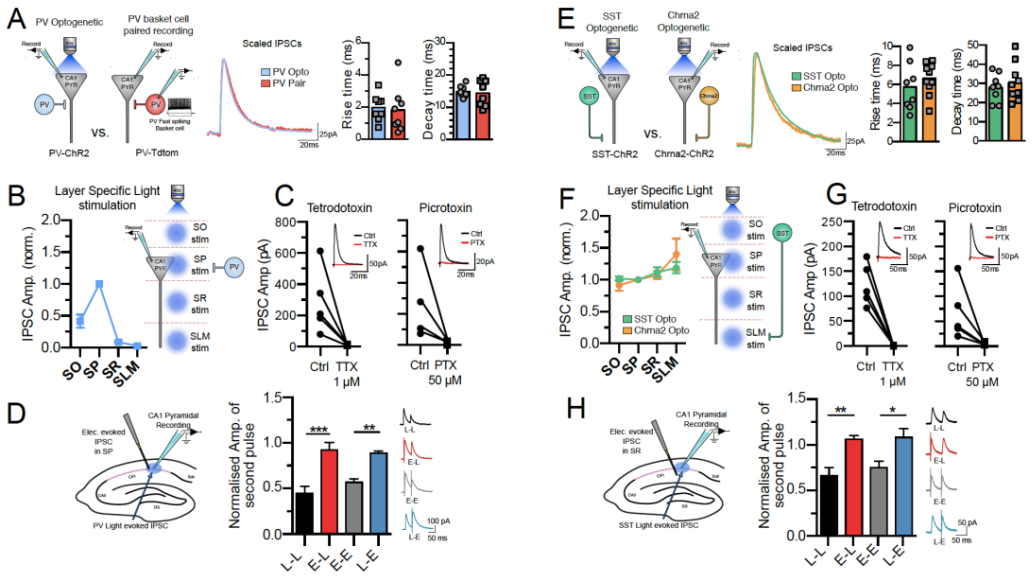

Supplementary Figure 1 (related to Fig. 1). Characterisation of PV and SST optogenetic responses.

(a) Comparison of optogenetically evoked PV IPSCs and IPSCs recorded via PV fast-spiking basket cell and CA1 pyramidal neuron paired recordings. Both rise and decay times were indistinguishable.

(b) PV IPSCs evoked via light stimulation through the objective lens positioned over different layers of the hippocampus. PV IPSC amplitude was highest in the pyramidal layer consistent with PV basket cell activation.

© PV IPSCs were completely blocked by 1µM tetrodotoxin and 50µM picrotoxin showing optogenetic IPSCs are action potential and $GABA_A$ receptor dependent.

(d) Check of pathway independence between PV-optogenetic light-evoked pathway and electrically-evoked IPSC control pathway in SP. Electrical stimulation failed to depress light responses whilst light responses failed to depress electrical responses indicating separate discrete inhibitory synapse activation.

(e) Comparison of optogenetically evoked IPSCs SST and Chrna2 expressing OLM interneurons. Both rise and decay times were indistinguishable.

(f) SST and Chrna2 IPSCs evoked via light stimulation of different layers of the hippocampus. Both SST and Chrna2 IPSC amplitudes were maintained across all layers and highest in stratum lacunosum moleculare layer consistent with SST OLM interneuron activation.

(g) SST IPSCs were completely blocked by 1μM tetrodotoxin and 50μM picrotoxin showing optogenetic IPSCs are action potential and $GABA_A$ receptor dependent.

(h) Check of pathway independence between SST-optogenetic light-evoked pathway and electrically-evoked IPSC control pathway in the SR. Electrical stimulation failed to depress light responses whilst light responses failed to depress electrical responses indicating separate discrete inhibitory synapse activation. Data represent mean ± S.E.M statistical comparison via unpaired t-tests (d,h) (*$p < 0.05$, **$p < 0.01$, ***$p < 0.001$).

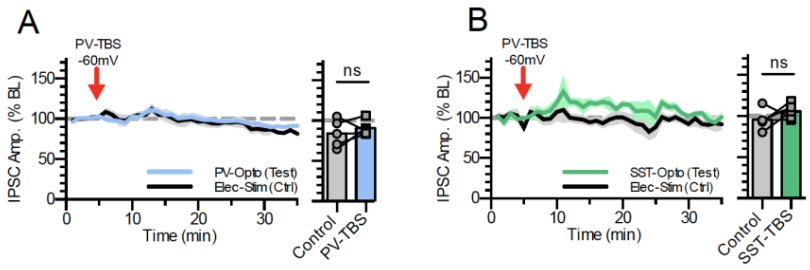

Supplementary Figure 2 (related to Fig. 1). TBS induced PV-iLTD and SST-iLTP are dependent on postsynaptic depolarisation

CA1 pyramidal neurons were recorded at 0 mV for the duration of the experiment except for during the light induced TBS protocol in which the neuron was held at -60 mV.

(a) PV-iLTD was not induced if CA1 pyramidal neurons were held at -60 mV during the induction protocol.

(b) SST-iLTP failed to be induced when CA1 pyramidal neurons were held at -60 mV during the induction protocol. Data represent mean ± S.E.M statistical comparison via paired t-tests.

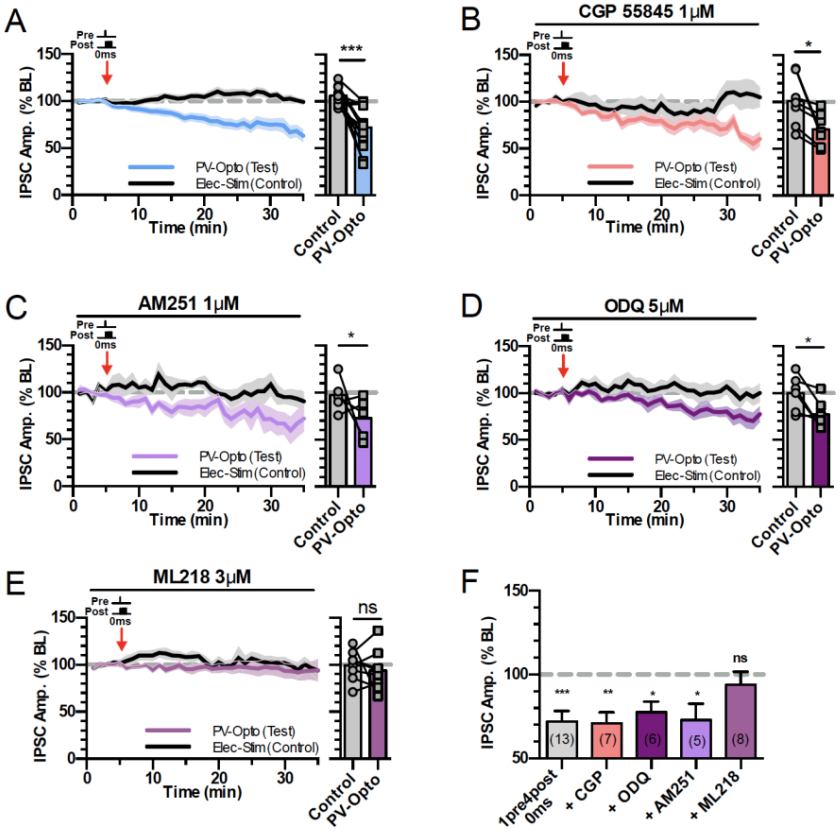

Supplementary Figure 3 (related to Fig. 3). PV-iLTD is not dependent on endocannabinoid, GABAB receptors or nitrous oxide signalling.

(a) PV-iLTD induced by 0 ms 1pre 4post timing (data from Fig. 2c).

(b) GABAB antagonist CGP55845 (1 µM) failed to block PV-iLTD.

(c) CB1 receptor antagonist AM251 (1 µM) failed to block PV-iLTD.

(d) Inhibiting the Nitrous oxide pathway via inhibition of guanylyl cyclase with ODQ (5 µM) failed to block PV-iLTD.

(e) The selective T-type VGCC inhibitor ML218 (3 µM) blocked PV-iLTD **(f)** Summary histogram displaying the level of plasticity under each experimental

condition. Data represent mean ± S.E.M statistical comparison via paired t-tests (a-e) and one sample t-tests

(f). Significant difference is indicated (*$p < 0.05$).

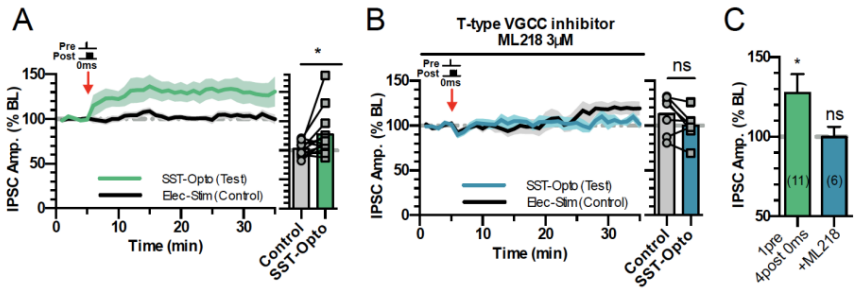

Supplementary Figure 4 (related to Fig. 4). SST-iLTP requires T-type VGCC activation.

(a) SST-iLTP induced by 0 ms 1pre 4post timing (data from Fig. 2g).

(b) The selective T-type VGCC inhibitor ML218 (3 µM) blocked SST-iLTP.

(c) Summary histogram displaying the level of plasticity under each experimental condition. Data represent mean ± S.E.M statistical comparison via paired t-tests (a,b) and one sample t-tests (c). Significant difference is indicated (*p < 0.05).

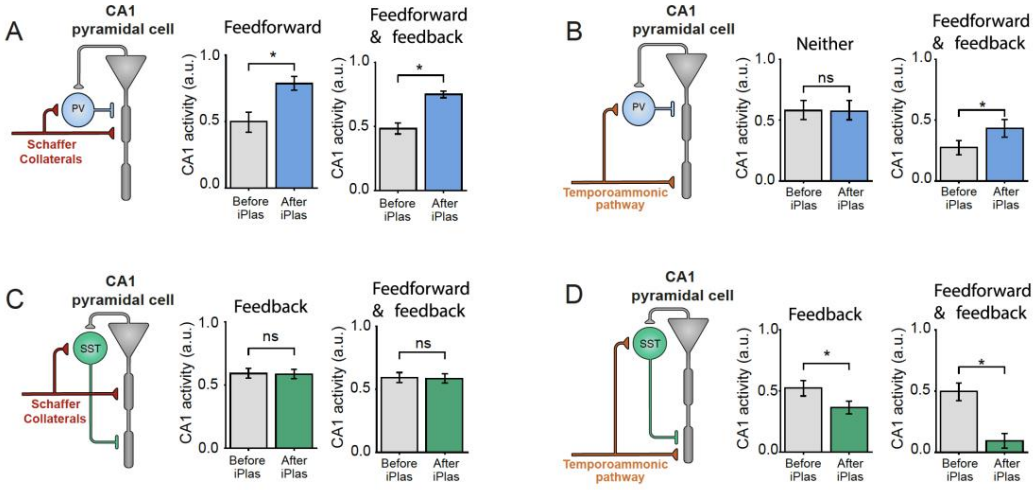

Supplementary Figure 5 (related to Fig. 6). PV and SST plasticity regulate CA1 pyramidal neuron excitability via feedback and feedforward inhibition.

(a) PV-iLTD increased CA1 pyramidal neuron activity in responses to Schaffer collateral input if PV interneurons are engaged via feedforward inhibition or feedforward and feedback inhibition.

(b) PV-iLTD had no effect on temporoammonic excitation of CA1 pyramidal neurons due to lack of feedforward or feedback inhibition. If the temporoammonic pathway recruits PV interneurons via feedforward or partake in feedback inhibition PV-iLTD increased temporoammonic pathway driven CA1 activity.

(c) SST-iLTP had no effect on the Schaffer collateral induced CA1 pyramidal neuron excitability if it is engaged via feedback or feedback and feedforward inhibition.

(d) SST-iLTP reduced the temporoammonic pathway driven excitability of CA1 pyramidal neurons when engaged via feedback or feedforward and feedback inhibition. Data represent mean ± S.E.M statistical comparison via unpaired t-tests. Significant difference is indicated (*$p < 0.05$).

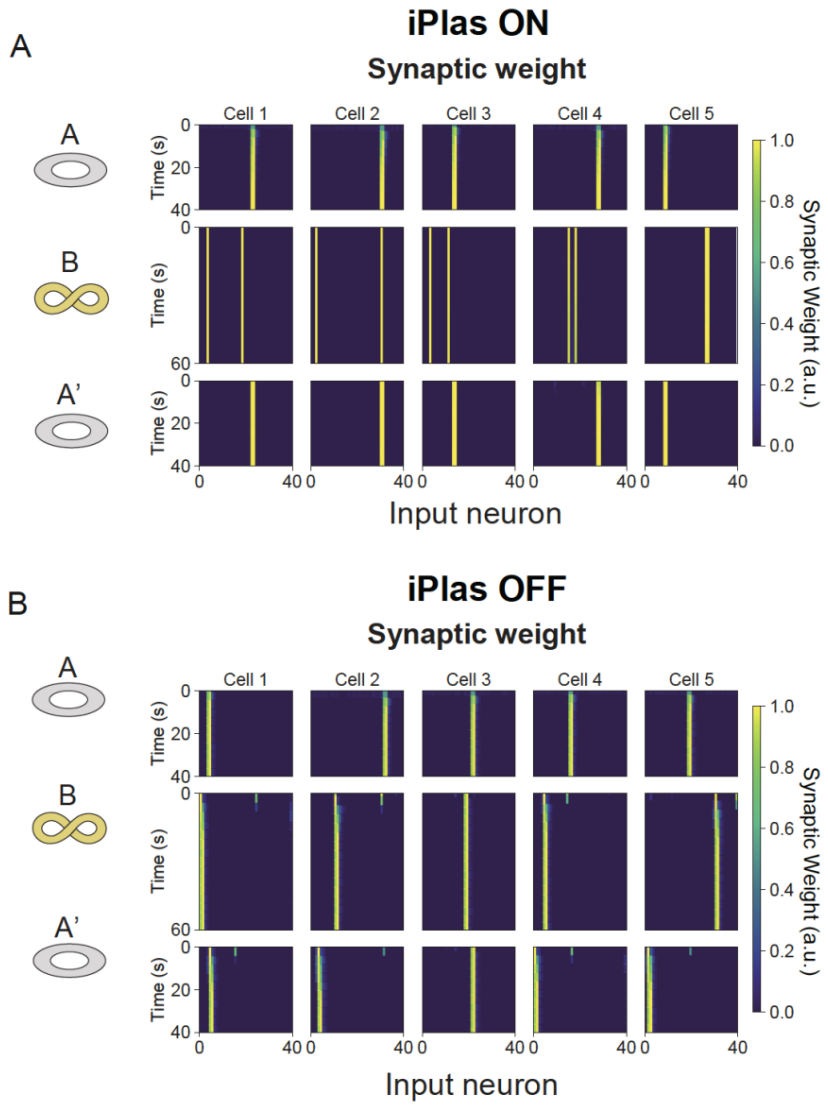

Supplementary Figure 6 (related to Fig. 8). Simulated synaptic weight evolution during exploration in different environments.

(a) Evolution of synaptic weights over time for the example cells shown in Fig. 8b. During these simulations, iPlas is active.

(b) Evolution of synaptic weights over time for the example cells shown in Fig. 8c. During these simulations, iPlas is turned off.

Chapter 6

Voltage-based inhibitory plasticity as a flexible model for network homeostasis

Our experiments involving inhibitory plasticity onto CA1 pyramidal cells suggested that this form of plasticity might be intimately related the the postsynaptic membrane voltage. More specifically, inhibitory synaptic plasticity could only be induced by presynaptic theta burst stimulation when the postsynaptic membrane voltage was clamped at a high voltage. Inspired by these findings, we propose a voltage-based inhibitory synaptic plasticity model. This model regulates network activity by setting a target value for the postsynaptic membrane potential over a long timescale. As a consequence of this rule, the network activity is regulated by the imposition of a natural maximum firing rate. Importantly, unlike previous spike-based models, our voltage-based inhibitory synaptic plasticity model does not restrict the postsynaptic

firing rate to a narrow range.

The layout of the work will be presented in an article format as it is soon to be submitted for publication. We would like to thank Claudia Clopath for supervising and guiding the project.

Voltage-based inhibitory plasticity as a flexible model for network homeostasis

Abstract

The balance between excitatory and inhibitory inputs (E/I balance) can ensure network stability. Moreover, inhibitory neurons are directly involved in neural computations and can shape sensory representations. Therefore, in face of excitatory synaptic plasticity, inhibitory connections are likely to adapt to maintain network stability. A widely used inhibitory synaptic plasticity rule regulates network dynamics by imposing a target firing rate. This results in a network in which all neurons fire, on average, at the same firing rate. Here, we propose a model of inhibitory synaptic plasticity in which synaptic updates depend on presynaptic spike arrival and postsynaptic membrane voltage. Our plasticity rule regulates the network activity by setting a target value for a low-pass-filtered version of the postsynaptic membrane potential. We then simulate a feedforward network composed of excitatory and inhibitory neurons receiving uncorrelated input. Similarly to what has been shown in a theoretical work using a non-spike-based plasticity model, our inhibitory plasticity

model regulates E/I ratio while allowing for a broad range of postsynaptic firing rates and thus network diversity. The change in inhibitory synaptic weight increases with the initial E/I ratio. In a feedforward network in which excitatory and inhibitory neurons receive correlated input, our plasticity rule allows for the development of co-tuned excitation and inhibition, in agreement with recordings in rat auditory cortex. Therefore, our voltage-dependent inhibitory plasticity model accounts for network homeostasis while allowing for diverse neuronal dynamics observed in vivo.

Keywords: synaptic plasticity, inhibitory plasticity, spike-timing-dependent plasticity, voltage-based plasticity.

6.1 Introduction

Cortical neurons receive balanced excitatory and inhibitory inputs [D'amour and Froemke, 2015; Froemke et al., 2007; Monier et al., 2008; Wehr and Zador, 2003]. This balance between excitation and inhibition is thought to be important for network stability and signal processing [Carvalho and Buonomano, 2009; Ecker et al., 2010; Renart et al., 2010; Rocha et al., 2008; Van Vreeswijk and Sompolinsky, 1996; Vogels and Abbott, 2009; Vogels et al., 2011]. Additionally, cortical neurons have been shown to receive co-tuned excitatory and inhibitory inputs in a stimulus-specific manner [Anderson et al., 2000; Froemke et al., 2007; Monier et al., 2008; Wehr and Zador, 2003]. The mechanisms that support and promote this balanced state in biological conditions, however, are still under intense debate. Inhibitory synaptic plasticity has been proposed as a potential candidate to fulfill this role [Hennequin et al., 2017; Luz and Shamir, 2012; Vogels et al., 2011]. By modulating inhibitory connections, the network can recover to a balanced state even in face of continuously-changing excitatory connections [Clopath et al., 2016; Vogels et al., 2013, 2011].

The most widely used inhibitory synaptic plasticity model modulates inhibitory

connections depending on the timing of pre- and postsynaptic spikes [Vogels et al., 2011]. This spike-based inhibitory synaptic plasticity (sISP) rule regulates the balance between excitatory and inhibitory inputs while imposing a target firing rate for the postsynaptic neuron [Vogels et al., 2011]. When combined with correlated excitatory and inhibitory inputs, this plasticity model produces co-tuned excitatory and inhibitory receptive fields [Clopath et al., 2016; Vogels et al., 2011]. Because of the restrictions that this model imposes onto postsynaptic firing rates, however, once the balanced state is achieved, responses to stimuli can only be perceived transiently [Vogels et al., 2011]. The timescales at which these responses can be observed are determined by the timescales at which inhibitory synapses are updated. Moreover, in a recurrent network, the average firing rate of all excitatory cells converge to the same value, independently of their feedforward inputs.

Excitatory synaptic plasticity has been vastly explored and several plasticity models have been proposed, including spike-timing-dependent plasticity (STDP) [Gerstner et al., 1996] and voltage-based models [Clopath et al., 2010a; Clopath and Gerstner, 2010]. Contrastingly, inhibitory synaptic plasticity models have only recently started being investigated and the range of proposed plasticity models and applications is still limited. Recent experimental data has suggested that the rules governing the change in inhibitory connections might depend on concurrent excitatory inputs [D'amour and Froemke, 2015]. Theoretical studies have shown that co-dependent excitatory and inhibitory synaptic plasticity rules can regulate network activity without setting a target firing rate for postsynaptic excitatory cells [Agnes and Vogels, 2018]. Moreover, accumulating evidence indicates that inhibitory plasticity rules are interneuron-type specific [Chiu et al., 2018; Udakis et al., 2019; Vickers et al., 2018], a characteristic that has been suggested to be important for controlling place field formation and consolidation in CA1 pyramidal cells [Udakis et al., 2019]. Additionally, inhibitory synaptic plasticity in hippocampal CA1 interneuron synapses could only be induced

by presynaptic theta burst stimulation if the postsynaptic membrane voltage was clamped at a hyperpolarized potential [Udakis et al., 2019]. Under spike-timing-dependent protocols, inhibitory synaptic changes could not be observed using single postsynaptic spikes. Instead, inhibitory plasticity required postsynaptic bursts [Udakis et al., 2019].

We propose a voltage-based inhibitory synaptic plasticity (vISP) model in which the updates in inhibitory synaptic weights depend on the postsynaptic membrane voltage and presynaptic spikes. According to our plasticity model, inhibitory synaptic weights are updated to regulate the postsynaptic membrane voltage over a long timescale. We next explore the effects of this plasticity model using a feedforward network of excitatory and inhibitory inputs. We show that our model can modulate pyramidal cell activity by imposing a natural maximum firing rate. Contrary to previous models of sISP, however, our model does not impose a unique target postsynaptic firing rate. Therefore, our voltage-based model regulates network activity while allowing for a diversity in pyramidal cell firing rates.

6.2 Results

Voltage-based inhibitory synaptic plasticity model

We propose an inhibitory plasticity model in which the update in synaptic connections from inhibitory neurons onto pyramidal cells depends on the postsynaptic membrane voltage. In our voltage-based inhibitory synaptic plasticity model, the update in inhibitory weights aims to maintain the average postsynaptic membrane voltage at a target value over a long timescale. Moreover, this update is only applied if the postsynaptic membrane voltage is depolarized and the presynaptic cell spikes within a short time window (figure 1A, see methods). Additionally, to ensure a minimum level of neuronal activity, inhibitory presynaptic spikes lead to a depression in synaptic

weights.

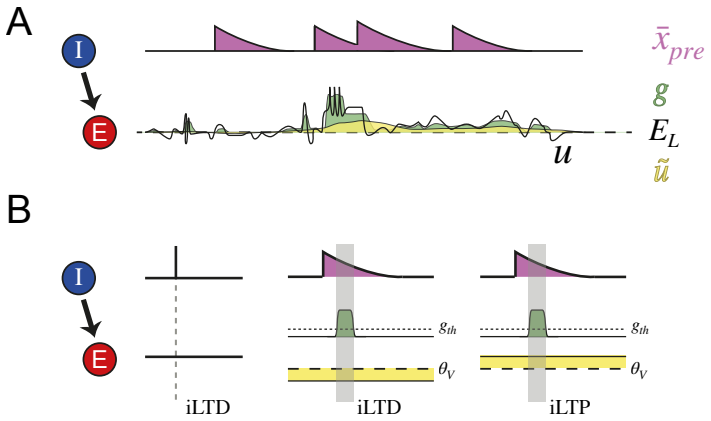

Figure 1: **Illustration of the voltage-dependent inhibitory synaptic plasticity model. (A)** Illustration of the main variables used in the model. The inhibitory synaptic plasticity rule modulates the strength of connections from inhibitory neurons (blue) to excitatory neurons (red). The presynaptic trace $\bar{x}_{pre}$ (purple) increases for every presynaptic inhibitory spike and decays exponentially otherwise. The gating variable g (green) is a low-pass-filtered version of the difference between the membrane voltage (u, black) and the resting potential (E_L dashed line) with a fast time constant. The variable $\tilde{u}$ (yellow) is a low-pass-filtered version of the postsynaptic membrane potential with a slow time constant. **(B)** Illustration of the model. Every presynaptic spike leads to the depressed of the respective inhibitory synaptic weights (left, iLTD). Further synaptic changes occur if the presynaptic inhibitory trace is non-zero—i.e a presynaptic spike occurred recently—and the gating variable is above a threshold g_{th} (dotted line). In this case, inhibitory synaptic weights are depressed (middle) if $\tilde{u}$ is below a target value θ_V (dashed line) or strengthened (right) if $\tilde{u}$ is above θ_V. See methods for more details.

vISP regulates pyramidal cell firing rate without setting a unique target value

We first investigate whether our inhibitory plasticity model can regulate pyramidal cell firing rate. We simulate a feedforward network composed of 20 excitatory and 20 inhibitory neurons projecting onto one postsynaptic neuron (figure 2A). The input neurons fire, on average, with the same firing rate and the synaptic weights from excitatory input neurons are all fixed at the same value. The weights for inhibitory synapses are initialized at a small value and are updated following the vISP

model. We then run these simulations for several levels of excitatory input firing rate. Independently of the initial conditions, the vISP model regulates the inhibitory connections such that the ratio between excitatory and inhibitory inputs onto the postsynaptic cell (E/I ratio) converges to the same level (figure 2B). Interestingly, our inhibitory plasticity rule sets a natural maximum firing rate for the postsynaptic neuron (figure 2B). Importantly, this model does not restrict the postsynaptic activity to a narrow range. Instead, the postsynaptic firing rate can assume any value from zero to the maximum firing rate imposed by the inhibitory plasticity rule (figure 2B). Therefore, the vISP model regulates pyramidal cell activity by setting a target E/I ratio and a maximum firing rate without overconstricting the postsynaptic activity.

To compare the effects of our model with previous models, we run the same simulations replacing our inhibitory plasticity model with a spike-based inhibitory plasticity rule [Vogels et al., 2011]. Under this rule, near-coincident pre- and postsynaptic spikes lead to synaptic potentiation whereas each presynaptic spike leads to synaptic depression (see methods). This synaptic plasticity rule has been shown to set a target firing rate for the postsynaptic neuron [Vogels et al., 2011]. Indeed, in our simulations, the sISP model sets a target value for both the E/I ratio and the postsynaptic firing rate (figure 2C). Therefore, the sISP model regulates pyramidal cell activity by constraining the postsynaptic firing rate to a narrow range around the target firing rate.

vISP and correlated excitatory and inhibitory inputs lead to co-tuned E/I receptive fields

We next investigate the effect of the vISP model on inhibitory receptive field formation. In particular, we wonder whether this inhibitory plasticity model can account for the co-tuning of excitatory and inhibitory currents observed in cortical neurons [Anderson et al., 2000; Froemke et al., 2007; Monier et al., 2008; Rocha et al., 2008; Wehr

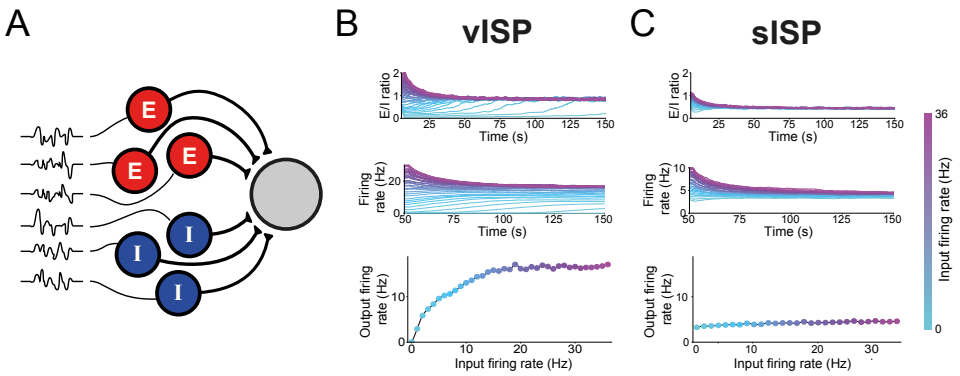

Figure 2: **vISP regulates pyramidal cell firing rate without setting a unique target value.** **(A)** Network diagram. We simulate a feedforward network composed of N_E presynaptic excitatory neurons (red) and N_I presynaptic inhibitory neurons (blue) projecting onto one postsynaptic cell (gray). Presynaptic cells are activated independently with the same average firing rate. Inhibitory connections are initialized at the same value and are updated following either vISP or sISP models (see methods). Excitatory connections are fixed throughout the simulations. Simulations are run for several levels of average excitatory input firing rate. **(B)** Simulations in which inhibitory synapses are updated following vISP. Top: evolution of the ratio between excitatory and inhibitory inputs (E/I ratio) into the postsynaptic cell over time. Middle: evolution of the postsynaptic firing rate over time. These firing rates were measured as a rolling average over a time window of 25 seconds. Bottom: final postsynaptic firing rate measured at the end of the simulation (150 s) as a function of the excitatory input firing rate. The different colors represent simulations under different levels of excitatory input firing rate. Each curve is an average over 50 simulations under the same initial conditions. The final postsynaptic firing rates are naturally bounded by the voltage-dependent inhibitory plasticity rule. They can, however, take any values from zero to this upper bound, depending on the overall excitatory input to the postsynaptic cell. Contrarily, the E/I ratio converges to the same value for all levels of input firing rates. **(C)** Analogous to B for simulations in which inhibitory synaptic weights are updated following sISP model. This inhibitory plasticity model sets a target firing rate for the postsynaptic cell, regardless of the total excitatory input.

and Zador, 2003]. To test that, we simulate a feedforward network of excitatory and inhibitory neurons projecting onto one postsynaptic neuron. Those two populations of neurons are organized in pairs such that each pair of excitatory and inhibitory neurons fire with the same time-varying firing rate (figure 3A). The excitatory synaptic weights are initialized such that the excitatory receptive field is Gaussian shaped with a peak at input neuron 10. Those synaptic weights are kept fixed throughout the simulations. The inhibitory synaptic weights are initialized at a low value and

evolve following the vISP model. Similarly to the case with homogeneous excitatory connections, the change in inhibitory connections regulates the E/I ratio, forcing it towards a target value close to 1 (figure 3B). Interestingly, although the vISP model allows for a wide range of postsynaptic firing rates, the re-scaled inhibitory synaptic weights converge to the same values of their corresponding excitatory counterparts (figure 3B). Therefore, the vISP model supports the emergence of a co-tuning between excitation and inhibition.

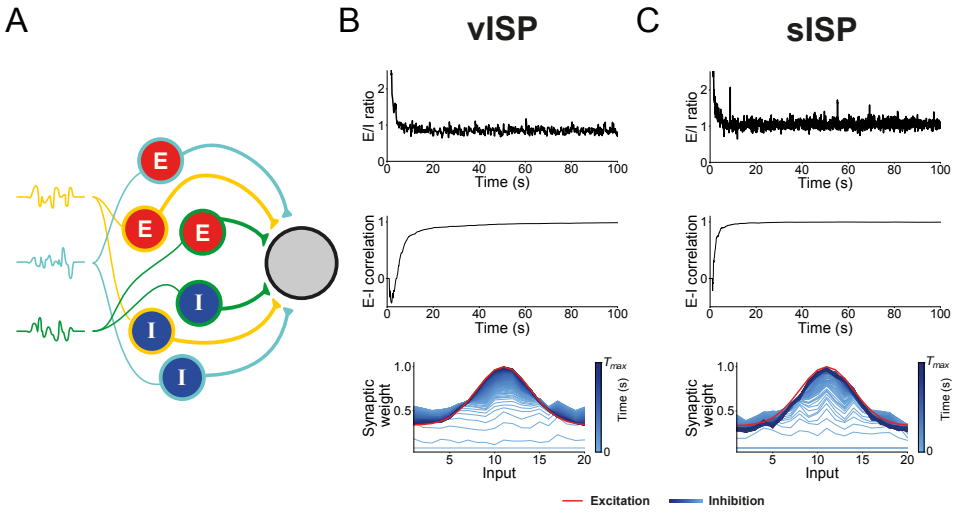

Figure 3: **vISP and correlated excitatory and inhibitory inputs lead to co-tuned E/I receptive fields. (A)** Network diagram. We simulate a feedforward network composed of N_E presynaptic excitatory neurons (red) and N_I presynaptic inhibitory neurons (blue) projecting onto one postsynaptic cell (gray). The different colour—yellow, blue, and green—represent different inputs. Each excitatory cell is modelled as a Poisson neuron with a cell-specific, time-varying firing rate which is shared with a corresponding inhibitory cell (same input color). Inhibitory connections are initialized at the same value and are updated following either vISP or sISP models (see methods). Excitatory connections are fixed throughout the simulations. **(B)** Simulations in which inhibitory connections follow vISP model. Top: evolution of E/I ratio over time. Middle: Evolution of E-I correlation over time. The E-I correlation is measured as the correlation between excitatory and inhibitory synaptic weights, i.e. the correlation between excitatory and inhibitory receptive fields. Bottom: excitatory (red) and inhibitory (blues) synaptic weights for each input. Each blue curve represents the inhibitory synaptic weights for one specific time of the simulation. **(C)** Same as B for the simulations in which inhibitory connections follow sISP model.

The co-tuning between excitatory and inhibitory receptive fields has also been observed using a spike-timing dependent inhibitory plasticity rule [Vogels et al., 2011] or its rate-based version [Clopath et al., 2016]. To test this under the same conditions as the ones used with the vISP model, we run the same simulations as before while replacing the inhibitory plasticity rule with a spike-based model. As expected, the inhibitory synaptic inputs converge to the same levels as their corresponding excitatory input (figure 3C). In summary, both voltage- and spike-based inhibitory plasticity rule account for the development of co-tuned excitatory and inhibitory receptive fields when E and I inputs are correlated.

Inhibitory connections adapt to changes in excitatory input while allowing for diversity in pyramidal cell firing rate

In biological neural networks, excitatory connections are constantly changing and the network should be provided with mechanisms to adjust to these changes. To test whether a network governed by the vISP model can adapt to changes in excitatory inputs, we simulate a feedforward network analogous to the one we simulated before but with an excitatory receptive field centered around input 7 (figure 4A). The activities of excitatory and inhibitory neurons associated to the same input index are correlated in time. The excitatory synaptic weights are kept fixed while the inhibitory synaptic weights evolve following the vISP model. Similarly to what we observed in the previous case, the inhibitory receptive field converges to match the excitatory inputs (figure 4A). Consequently, the E/I ratio is modulated and converges to a value close to 1 (figure 4C) whereas the postsynaptic firing rate decays to an almost-silent stage (figure 4D). After 450 s, the excitatory synaptic weights are shifted instantly such that the peak of the excitatory receptive field is centered around input 15 and its amplitude is twice the original amplitude (figure 4B). The excitatory synaptic weights are then kept constant for another 450 s while the inhibitory synaptic weights are

allowed to change. The inhibitory receptive field adapts to the changes in excitatory inputs moves towards the new excitatory receptive field (figure 4B), forcing the E/I ratio to return to the same level as in the first half of the simulation (figure 4C). Remarkably, the postsynaptic firing rate does not return to the same level. Instead, it decays to a higher level when compared to the first 450 seconds of simulation (figure 4D). Therefore, the vISP model provides a mechanism with which a network can adapt to changes in excitatory inputs and still allow for diversity in neuronal activity.

6.3 Discussion

We propose a voltage-based inhibitory synaptic plasticity model as a mechanism to regulate network activity. Our model imposes a target value for a low-passed-filtered version of the postsynaptic membrane potential. This allows for short-term fluctuations while imposing a long-term regulation of the neuron's membrane potential. We analyse the effect of our inhibitory plasticity model on a feedforward network composed of excitatory and inhibitory neurons projecting onto one single neuron. The vISP model regulates the postsynaptic activity by imposing a natural maximum firing rate and a unique target value for the ration between excitatory and inhibitory inputs. Surprisingly, the vISP model does not restrict the postsynaptic firing rate to a narrow range. Instead, the postsynaptic neuron firing rate is only bounded by a maximum firing rate. This result contrasts with previous results observed under spike-based inhibitory synaptic plasticity rules [Hennequin et al., 2017; Luz and Shamir, 2012; Vogels et al., 2013, 2011].

This wider range of possible postsynaptic firing rates gives support for a more flexible network. While the E/I ratio and the maximum firing rates are imposed, the different levels of postsynaptic firing rate allow for a more stable rate-based code. Since spike-based inhibitory plasticity models impose a fixed target firing rate, differences in firing rate can only be encoded in the transient network dynamics. Following our vISP

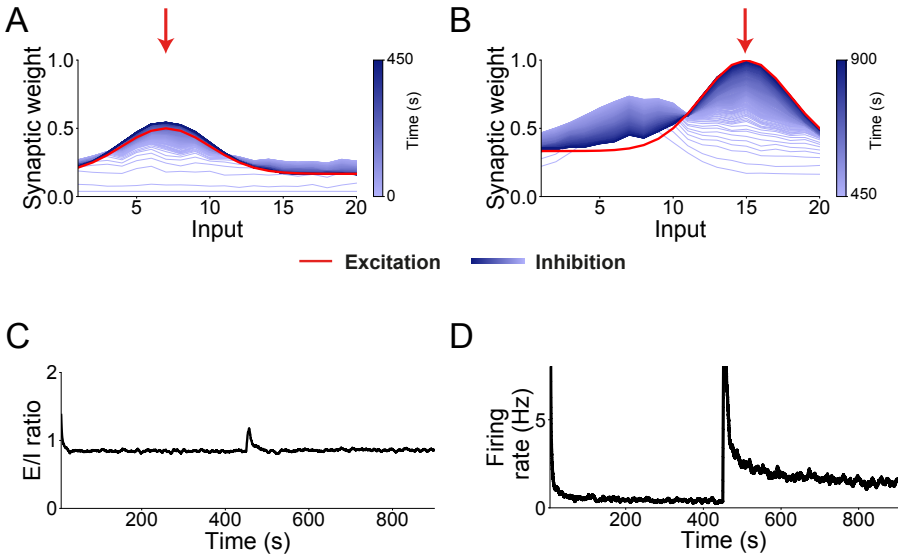

Figure 4: **Inhibitory connections adapt to changes in excitatory input while allowing for diversity in pyramidal cell firing rate.** **(A)** Excitatory (red) and inhibitory (blues) synaptic weights for each input. The simulations run for 450 seconds. Excitatory synaptic connections are fixed throughout the simulations whereas inhibitory synaptic weights are initialized at a low level and evolve following the vISP model. Red arrow indicated the preferred input (input 6) for excitatory connections. Blue curves represent the inhibitory synaptic weights for specific times of the simulation. **(B)** Excitatory (red) and inhibitory (blues) synaptic weights for each input. The simulations run for 450 seconds. The peak of the excitatory tuning curve is instantly shifted to input 15 and its amplitude is twice the amplitude of the simulations in A. The excitatory weights are then kept fixed throughout the simulations. Inhibitory synaptic weights are initialized at the final state of the simulations in A and evolve following the vISP model. Red arrow indicated the preferred input (input 15) for excitatory connections. Blue curves represent the inhibitory synaptic weights for specific times of the simulation. **(C)** Evolution of E/I ratio over time for the entire simulation (900 seconds). **(D)** Evolution of the postsynaptic firing rate over time for the entire simulation (900 seconds). Although the E/I ratio returns to the same value after the excitatory synaptic weights are disturbed, the firing rate converges to a higher level.

model, the network can converge to different states depending on the feedforward inputs. The neuronal response to sensory stimulation, for example, would abruptly increase at the stimulus onset but would decay to different levels depending on the amplitude of the stimulus. Therefore, the vISP model supports long-term, rate-based encoding. More importantly, our voltage-based model supports quick changes in

rate-based codes caused, for example, by changes in context. Although a spike-based model could be combined with diversity in firing rates by assigning different target firing rates to each neuron, the entire network would still be limited in terms of possible steady states.

The interaction between excitatory and inhibitory synaptic plasticity has been shown to lead to complex dynamics [Clopath et al., 2016]. Under the right conditions, this interaction leads to the development of receptive fields and co-tuning between excitation and inhibition [Clopath et al., 2016]. Importantly, the details of the excitatory plasticity rule—more specifically, the choice of synaptic normalization—determine whether or not receptive fields are developed [Clopath et al., 2016]. In all of our simulations, excitatory synaptic connections were fixed. It would be interesting to test whether the interaction between a spike-based excitatory synaptic plasticity rule and our vISP model could lead to a more robust receptive field development. Since our inhibitory plasticity model supports different levels of postsynaptic firing rate, small differences in excitatory input would lead to small differences in firing rate that would not be compensated by a change in inhibitory weights. Therefore, this difference in excitatory synaptic weight would lead to a positive feedback loop and finally to receptive field development.

In all of our simulations, the parameters for our neuron model were extracted from previous studies [Brette and Gerstner, 2005; Clopath et al., 2010a] (see methods). Although we used exactly the same parameters used in these previous studies, the results from our simulations should be robust to variations in these parameters. Since our conclusions from our simulations not not depend on exact values, parameters in the same range should be enough to ensure the neuronal dynamics are within the experimentally observed regime and should lead to the same conclusions in our simulations.

The dynamics of the membrane voltage vary drastically depending on the location within the neuron. At the soma, action potentials follow a stereotypical shape spanning over a few of milliseconds [Antic et al., 2010]. At dendrites, however, NMDA spikes can last for dozens of milliseconds [Antic et al., 2010]. Therefore, our voltage-based inhibitory plasticity rule might have different effects depending on the targeting site of the inhibitory synapse. Since different types of interneurons generally target different layers of pyramidal cells, our vISP model could possibly explain the different learning rules observed for different types of interneurons [Chiu et al., 2018; Udakis et al., 2019; Vickers et al., 2018].

Inhibitory synaptic plasticity has been shown to be an ideal candidate to regulate network activity while supporting the existence of multiple cell assemblies [Vogels et al., 2011]. When the connections between clusters of neurons—the cell assembly—are strengthened to store a memory, the sISP model leads to the potentiation of inhibitory connection onto the cell assembly. This strengthening of inhibitory connections ultimately pushes the cell assembly activity back to baseline level [Vogels et al., 2011]. At this stage, the memory is stored in the synaptic weights but the activity of the cell assembly is indifferentiable from the activity of the rest of the network. The memory can be transiently recovered by the application of an external input onto the assembly [Vogels et al., 2011]. It would be interesting to extend our analysis of the vISP model to recurrent networks and investigate whether this model would support the storage of quiescent memories within the network.

Our voltage-based inhibitory plasticity model provides a mechanism to regulate network activity while supporting network diversity and flexibility. Our model poses interesting questions for further theoretical exploration when moving towards either large, recurrent networks or more biologically detailed neuron models. Several of the results observed in our analysis could be tested experimentally and further experiments could help constraining the model.

6.4 Methods

Neuron model

In our simulations, neurons are modelled by an adaptive exponential integrate-and-fire (AdEx) model [Brette and Gerstner, 2005]. As such, the neuronal membrane voltage u follows

$$C\frac{du}{dt} = -g_L\left(u - E_L\right) + g_L\Delta_T \exp\left(\frac{u - V_T}{\Delta_T}\right) - w_{ad} + I \quad ,$$

where C is the membrane capacitance, g_L is the leak conductance, E_L is the resting potential, Δ_T is the slope factor, V_T is the threshold potential, and I is the total input current. The adaptation current w_{ad} is described by

$$\tau_{ad}\frac{dw_{ad}}{dt} = a\left(u - E_L\right) - w_{ad} \quad ,$$

where τ_{ad} is the adaptation time constant and a is a parameter. The neuron spikes when its membrane voltage reaches a spiking threshold V_{th}. At this point, the membrane voltage is reset to V_{reset} and w_{ad} is increased by an amount b. After spiking, the neuron's membrane voltage is kept at V_{reset} for a refractory time τ_{ref}.

Additionally, we implement a conductance-based model for synaptic connections. Therefore, the total input current is described by

$$I = g^E\left(V^E - u\right) + g^I\left(V^I - u\right) + I^{ext} \quad ,$$

where g^E is the excitatory synaptic conductance, g^I is the inhibitory synaptic conductance, V^E is the excitatory reversal potential, V^I is the inhibitory synaptic conductance, and I^{ext} is the external current. When the neuron receives an action potential

from presynaptic neuron j, the postsynaptic conductance is increased by an amount $\Delta g_j^E = \bar{g}^E w_j^E$, for excitatory synapses, and $\Delta g_j^I = \bar{g}^I w_j^I$, for inhibitory synapses. Both g_j^E and g_j^I are parameters. The postsynaptic conductance decay otherwise with time constant τ_E, for excitatory synapses, and τ_I, for inhibitory synapses. The excitatory synaptic weights w_j^E are fixed throughout the simulations and the inhibitory synaptic weights w_j^I are updated following an inhibitory synaptic plasticity rule (see below).

This neuron model has been previously used in voltage-dependent excitatory plasticity models [Clopath et al., 2010b] and has been shown to be important when used to fit experimental data [Badel et al., 2008]. All the parameters for the neuron model were extracted from previous studies [Brette and Gerstner, 2005; Clopath et al., 2010a].

Synaptic plasticity model (vISP)

We propose a voltage-dependent inhibitory synaptic plasticity rule (vISP). Our synaptic plasticity model acts as a homeostatic mechanism to regulate the average postsynaptic membrane voltage. The weight of the synaptic connection from presynaptic inhibitory neuron j follows

$$\frac{dw_j^I}{dt} = \eta_I \left(g - g_{th}\right)_+ \left(\tilde{u} - \theta_V\right) \bar{x}_j - \alpha S_j \quad ,$$

where η_I is the inhibitory plasticity learning rate, g_{th} is a fixed threshold, θ_V is a target membrane voltage, α is a parameter, and $S_j = \sum \delta(t - t_j^f)$ is the presynaptic spike train—where t_j^f are the presynaptic spiking times. The presynaptic trace $\bar{x}_j$ is increased by 1 whenever there is a presynaptic spike and decays exponentially otherwise with time constant τ_{trace}. The gating variable g is used to determine whether the postsynaptic neuron has been recently depolarized and it evolves following

$$\tau_f \frac{dg}{dt} = -\left[g - \left(u - E_L\right)_+\right] \quad ,$$

where τ_f is a fast time constant. The variable $\tilde{u}$ is an exponential low-pass-filtered version of the postsynaptic membrane potential

$$\tau_s \frac{d\tilde{u}}{dt} = -\left(\tilde{u} - u\right) \quad ,$$

where τ_s is a slow time constant.

Synaptic plasticity model (sISP)

To compare the effect of our voltage-based inhibitory plasticity model with previous models, we run some of the simulations under the same conditions but replacing the plasticity rule with an spike-timing-dependent inhibitory synaptic plasticity model (sISP) [Vogels et al., 2011]. Under this model, the weight of the synaptic connection from presynaptic inhibitory neuron j to postsynaptic neuron i is updated such that

$$w_{ij}^I \longrightarrow w_{ij} + \eta_{sISP}\left(x_i^{sISP} - \alpha^{sISP}\right) \quad ,$$

for every presynaptic spike, and

$$w_{ij}^I \longrightarrow w_{ij} + \eta_{sISP} x_j^{sISP} \quad ,$$

for every postsynaptic spike, where η_{sISP} is the sISP learning rate, α^{sISP} is the depression factor, and x^{sISP} is the synaptic trace which is increased by 1 whenever the neuron spikes and decays exponentially otherwise with time constant τ_{sISP}.

Parameters and simulations

All data and software supporting the findings of this study are available from the corresponding authors upon reasonable request. The parameters for all the simulations can be found in tables 1-2.

Table 6.1: Parameters summary 1.

Neuron Model		
Name	**Value**	**Description**
$\boldsymbol{E_L}$	**-60 mV**	**Resting potential**
g_L	10 nS	Leak conductance
Δ_T	4 mV	Slope factor
V_T	-50.4 mV	Threshold potential
τ_{ad}	144 ms	Adaptation time constant
a	2 nS	Subthreshold adaptation
b	1 nS	Spike-triggered adaptation
V_{th}	-30 mV	Spiking threshold
V_{reset}	-60 mV	Reset membrane potential
τ_{ref}	5 ms	Refractory time
C	281 pF	Membrane capacitance
Network parameters		
Name	**Value**	**Description**
N_E	20	Number of excitatory input neurons
N_I	20	Number of inhibitory input neurons
Synapse Model		
Name	**Value**	**Description**
τ_E	5 ms	Decay constant for excitatory conductance
τ_I	10 ms	Decay constant for inhibitory conductance
$\bar{g}_E$	2 nS	Excitatory conductance amplitude
$\bar{g}_I$	2 nS	Inhibitory conductance amplitude
V^E	-10 mV	Excitatory reversal potential
V^I	-100 mV	Inhibitory reversal potential

Table 6.2: Parameters summary 2.

Plasticity model (vISP)		
Name	**Value**	**Description**
η_I	4×10^{-6}	Inhibitory plasticity learning rate
g_{th}	0.1 mV	Threshold for gating variable
θ_V	-60 mV	Target membrane voltage
α	0.08	Depression parameter
τ_{trace}	2 ms	Decay time constant for presynaptic trace
τ_f	20 ms	Fast decaying time constant
τ_s	200 ms	Slow decaying time constant
Plasticity model (sISP)		
Name	**Value**	**Description**
η_{sISP}	5×10^{-3}	Inhibitory plasticity learning rate (sISP model)
α^{sISP}	0.08	Presynaptic offset
τ_{sISP}	20 ms	Decay constant for synaptic trace

6.5 References

Agnes, E. and Vogels, T. P. (2018). Learn, forget, relearn, amplify: codependent synaptic plasticity in spiking networks. *Cosyne Abstract*, page 66589.

Anderson, J. S., Carandini, M., and Ferster, D. (2000). Orientation tuning of input conductance, excitation, and inhibition in cat primary visual cortex. *Journal of Neurophysiology*, 84(2):909–926.

Antic, S. D., Zhou, W. L., Moore, A. R., Short, S. M., and Ikonomu, K. D. (2010). The decade of the dendritic NMDA spike.

Badel, L., Lefort, S., Berger, T. K., Petersen, C. C., Gerstner, W., and Richardson, M. J. (2008). Extracting non-linear integrate-and-fire models from experimental data using dynamic I-V curves. *Biological Cybernetics*, 99(4-5):361–370.

Brette, R. and Gerstner, W. (2005). Adaptive exponential integrate-and-fire model as an effective description of neuronal activity. *Journal of Neurophysiology*, 94(5):3637–3642.

Carvalho, T. P. and Buonomano, D. V. (2009). Differential effects of excitatory and inhibitory plasticity on synaptically driven neuronal input-output functions. *Neuron*, 61(5):774–85.

Chiu, C. Q., Martenson, J. S., Yamazaki, M., Natsume, R., Sakimura, K., Tomita, S., Tavalin, S. J., and Higley, M. J. (2018). Input-Specific NMDAR-Dependent Potentiation of Dendritic GABAergic Inhibition. *Neuron*, 97(2):368–377.e3.

Clopath, C., Büsing, L., Vasilaki, E., and Gerstner, W. (2010a). Connectivity reflects coding: a model of voltage-based stdp with homeostasis. *Nature neuroscience*, 13(3):344–352.

Clopath, C., Büsing, L., Vasilaki, E., and Gerstner, W. (2010b). Connectivity reflects coding: a model of voltage-based STDP with homeostasis. *Nature neuroscience*, 13(3):344–52.

Clopath, C. and Gerstner, W. (2010). Voltage and spike timing interact in stdp - a unified model. *Frontiers in synaptic neuroscience*, 2:25.

Clopath, C., Vogels, T., Froemke, R. C., and Sprekeler, H. (2016). Receptive field formation by interacting excitatory and inhibitory synaptic plasticity. *bioRxiv*, page 66589.

D'amour, J. and Froemke, R. (2015). Inhibitory and excitatory spike-timing-dependent plasticity in the auditory cortex. *Neuron*, 86(2):514–528.

Ecker, A. S., Berens, P., Keliris, G. A., Bethge, M., Logothetis, N. K., and Tolias, A. S. (2010). Decorrelated neuronal firing in cortical microcircuits. *Science (New York, N.Y.)*, 327(5965):584–7.

Froemke, R. C., Merzenich, M. M., and Schreiner, C. E. (2007). A synaptic memory trace for cortical receptive field plasticity. *Nature*, 450:nature06289.

Gerstner, W., Kempter, R., van Hemmen, J. L., and Wagner, H. (1996). A neuronal learning rule for sub-millisecond temporal coding. *Nature*, 383(6595):76.

Hennequin, G., Agnes, E. J., and Vogels, T. P. (2017). Inhibitory Plasticity: Balance, Control, and Codependence. *Annual review of neuroscience*, 40:557–579.

Luz, Y. and Shamir, M. (2012). Balancing feed-forward excitation and inhibition via hebbian inhibitory synaptic plasticity. *PLoS Computational Biology*, 8(1):e1002334.

Monier, C., Fournier, J., and Frégnac, Y. (2008). In vitro and in vivo measures of evoked excitatory and inhibitory conductance dynamics in sensory cortices. *Journal of neuroscience methods*, 169(2):323–65.

Renart, A., De La Rocha, J., Bartho, P., Hollender, L., Parga, N., Reyes, A., and Harris, K. D. (2010). The asynchronous state in cortical circuits. *Science*, 327(5965):587–590.

Rocha, J. d. l., Marchetti, C., Schiff, M., and Reyes, A. D. (2008). Linking the response properties of cells in auditory cortex with network architecture: Cotuning versus lateral inhibition. *The Journal of Neuroscience*, 28(37):9151–9163.

Udakis, M., Pedrosa, V., Chamberlain, S. E. L., Clopath, C., and Mellor, J. R. (2019). Interneuron-specific plasticity at parvalbumin and somatostatin inhibitory synapses onto CA1 pyramidal neurons shapes hippocampal output. *bioRxiv*, page 774562.

Van Vreeswijk, C. and Sompolinsky, H. (1996). Chaos in neuronal networks with balanced excitatory and inhibitory activity. *Science*, 274(5293):1724–1726.

Vickers, E. D., Clark, C., Osypenko, D., Fratzl, A., Kochubey, O., Bettler, B., and Schneggenburger, R. (2018). Parvalbumin-interneuron output synapses show spike-timing-dependent plasticity that contributes to auditory map remodeling. *Neuron*, 99(4):720–735000000.

Vogels, T. P. and Abbott, L. F. (2009). Gating multiple signals through detailed balance of excitation and inhibition in spiking networks. *Nature Neuroscience*, 12(4):483–491.

Vogels, T. P., Froemke, R. C., Doyon, N., Gilson, M., Haas, J. S., Liu, R., Maffei, A., Miller, P., Wierenga, C. J., Woodin, M. A., Zenke, F., and Sprekeler, H. (2013). Inhibitory synaptic plasticity: spike timing-dependence and putative network function. *Frontiers in Neural Circuits*, 7:119.

Vogels, T. P., Sprekeler, H., Zenke, F., Clopath, C., and Gerstner, W. (2011). Inhibitory plasticity balances excitation and inhibition in sensory pathways and memory networks. *Science*, 334(6062):1569–1573.

Wehr, M. and Zador, A. M. (2003). Balanced inhibition underlies tuning and sharpens spike timing in auditory cortex. *Nature*, 426(6965):442–446.

Chapter 7

Conclusion and future work

In this thesis, we investigated the ways by which excitation and inhibition are involved in learning and memory formation. We explored how neuromodulators affect learning by directly altering the excitatory STDP window or by modulating neuronal activity. Furthermore, we investigate the effect of upregulating neuronal activity on receptive fields. We show that the increase in neuronal activity can lead to either the broadening or sharpening of the receptive field, depending on the neuron's initial excitatory input. Additionally, we investigate whether the upregulation of the excitatory plasticity learning rate would lead to the same outcome. Surprisingly, the increase in learning rate leads to the sharpening of the neuron's place field independently of the level of excitatory inputs.

We then presented a novel type of STDP observed in our experiments in vivo. We observed that connections from L4 to L2/3 neurons in barrel cortex follow a network-state dependent plasticity rule. In anaesthetised mice, the brain network alternates between Up and Down states, similarly to the cycles observed in mice during sleep.

During Up states, we found that presynaptic spikes lead to synaptic depression whereas pre- followed shortly by postsynaptic spikes prevents this depression but does not lead to potentiation. Since neurons are unlike to fire during Down states, synaptic connections are unlike to go through activity-dependent plasticity. Therefore, we simulated a network and implemented an excitatory plasticity rule based on our observations during Up states. Our simulations indicated that this plasticity rule provides a potential mechanism for the refinement of sensory representations.

In order to understand how interneurons interact with and guide excitatory plasticity, we analysed the emergence and stabilization of place fields in the hippocampal CA1 region. In particular, we investigated how the modulation of interneuron activity in novel environments promotes the emergence of new receptive fields. This modulation of interneuron activity happens in an interneuron-type-specific manner and is likely to be related to the release of neuronmodulators associated with novelty. Our simulations suggest that dendrite-targeting interneurons play a crucial role in place field development and consolidation whereas soma-targeting interneurons can quickly and reversibly turn silent cells into place cells.

Next, we delved deeper into the mechanisms regulating inhibitory plasticity onto CA1 pyramidal neurons. We presented experimental data suggesting that different types of interneurons undergo different forms of plasticity. We then used computational simulations to predict the effect of these plasticity rules on pyramidal cell output and confirmed those predictions with further experiments. Finally, our simulations suggested that the combination of plasticity rules leads to stable place field consolidation across environments.

Our experiments involving inhibitory plasticity onto CA1 pyramidal cells indicated

that the postsynaptic membrane voltage plays an important role in gating synaptic plasticity. Inspired by these findings, we proposed a voltage-based inhibitory synaptic plasticity model. This model regulates network activity by setting a target value for the E/I ratio and by imposing a maximum postsynaptic firing rate. Importantly, unlike previous spike-based models, our voltage-based inhibitory synaptic plasticity model does not restrict the postsynaptic firing rate to a narrow range.

7.1 Future Work

This project opened a wide range of possible future explorations. On a theoretical and simulation point of view, we would like to extend the analysis of the effect of neuromodulation on receptive fields to recurrent networks. A similar extension of the Up-state-modulated excitatory plasticity rule towards recurrent networks could offer interesting insights into the processes involving memory refinement. We restricted our simulations to feedforward networks due to the supporting experimental evidence being restricted to connections from cortical L4 to L2/3 neurons. However, since the extension of network-wide activity is widespread throughout multiple brain regions, the same learning rules may be governing connections in non-cortical areas. Therefore, it would be interesting to investigate the effect of those learning rules on recurrent networks and on refinement of cell assemblies.

We investigated the effect of the modulation of interneuron activity induced by novelty in an interneuron-type-specific manner. We also investigated the specific plasticity rules regulating connections from those interneurons. The natural next step is to combine both. When an animal explores a novel environment, neuromodulators are released, and concurrently, synaptic connections are reshaped. Therefore, it would

be interesting to explore how these two effects combine and interact in our model.

In terms of the voltage-based inhibitory synaptic plasticity we proposed, there are multiple routes to be explored. Firstly, moving towards larger, recurrent networks, there is an open question of whether memories can be stored in the form of cell assemblies under this plasticity rule. At this stage, we will also probe the network and test whether it can perform different tasks, such as encode a rate-based code. On a different direction, we will move towards a more biologically detailed neuron model. Using such models, we will test whether the vISP model behaves differently depending on the site of the inhibitory connection along the neuron. That could lead to a generalization of the model for different types of interneurons. This could then account for the diversity in inhibitory plasticity rules observed for different interneuron types.

On an experimental point of view, there are several directions worth pursuing. The Up-state-modulated plasticity was observed in barrel cortex on anesthetized mice. Whether the same or a similar plasticity rule modulates excitatory connections in other brains regions is an open question. In our investigation of the effects of somatic and dendritic inhibition on place field stabilization, we made several predictions regarding the artificial induction of place field plasticity. These predictions are yet to be probed. Finally, regarding our voltage-based inhibitory plasticity rule, there are several experiments that could be performed to constrain the model. Although the postsynaptic membrane voltage seems to be relevant for the induction of inhibitory plasticity onto hippocampal CA1 pyramidal cells, the exact relationship between them has not been explored yet.

7.2 Conclusion

In summary, we investigated the effect of excitation and inhibition in learning. To that end, we investigated how third factors such as neuromodulators and network state affect excitation and inhibition, ultimately exerting an effect on learning. Through multiple stages of interactions between experiments and computational simulations, we explored several systems, proposed mechanistic explanations for experimental data, and suggested possible functional implications of experimental findings. Finally, we proposed a novel, voltage-based inhibitory plasticity model as a mechanism for network homeostasis.

In the appendix, we present some additional work investigating the mechanisms underlying the stabilization of CA1 spatial maps. This work is an extension of part of chapter 4 to recurrently connected networks.

Chapter 8

Bibliography

Bakin, J. S. and Weinberger, N. M. (1996). Induction of a physiological memory in the cerebral cortex by stimulation of the nucleus basalis. *Proceedings of the National Academy of Sciences of the United States of America*, 93(20):11219–24.

Bear, M. F. and Singer, W. (1985). Modulation of visual cortical plasticity by acetylcholine and noradrenaline. *Nature*, 320(6058):172–176.

Bi, G. Q. and Poo, M. M. (1998). Synaptic modifications in cultured hippocampal neurons: dependence on spike timing, synaptic strength, and postsynaptic cell type. *The Journal of neuroscience : the official journal of the Society for Neuroscience*, 18(24):10464–10472.

Bienenstock, E., Cooper, L., and Munro, P. (1982). Theory for the development of neuron selectivity: orientation specificity and binocular interaction in visual cortex. *The Journal of Neuroscience*, 2(1):32–48.

Bittner, K. C., Grienberger, C., Vaidya, S. P., Milstein, A. D., Macklin, J. J., Suh, J.,

Tonegawa, S., and Magee, J. C. (2015). Conjunctive input processing drives feature selectivity in hippocampal CA1 neurons. *Nature Neuroscience*, 18:1133–1142.

Bittner, K. C., Milstein, A. D., Grienberger, C., Romani, S., and Magee, J. C. (2017). Behavioral time scale synaptic plasticity underlies CA1 place fields. *Science*, 357:1033–1036.

Brette, R. and Gerstner, W. (2005). Adaptive exponential integrate-and-fire model as an effective description of neuronal activity. *Journal of Neurophysiology*, 94(5):3637–3642.

Chun, S., Bayazitov, I. T., Blundon, J. A., and Zakharenko, S. S. (2013). Thalamocortical long-term potentiation becomes gated after the early critical period in the auditory cortex. *The Journal of neuroscience : the official journal of the Society for Neuroscience*, 33(17):7345–57.

Clopath, C., Büsing, L., Vasilaki, E., and Gerstner, W. (2010). Connectivity reflects coding: a model of voltage-based STDP with homeostasis. *Nature Neuroscience*, 13(3):344–352.

Dorrn, A. L., Yuan, K., Barker, A. J., Schreiner, C. E., and Froemke, R. C. (2010). Developmental sensory experience balances cortical excitation and inhibition. *Nature*, 465(7300):932–6.

Drever, B. D. (2011). The cholinergic system and hippocampal plasticity. *Behavioural Brain Research*, 221(2):505–514.

Froemke, R. C., Merzenich, M. M., and Schreiner, C. E. (2007). A synaptic memory trace for cortical receptive field plasticity. *Nature*, 450(7168):425–429.

Gerstner, W., Kempter, R., van Hemmen, J. L., and Wagner, H. (1996). A neuronal learning rule for sub-millisecond temporal coding. *Nature*, 383(6595):76–78.

Gerstner, W. and Kistler, W. (2002). *Spiking Neuron models*. Cambridge University Press.

Gjorgjieva, J., Clopath, C., Audet, J., and Pfister, J.-P. (2011). A triplet spike-timing-dependent plasticity model generalizes the Bienenstock-Cooper-Munro rule to higher-order spatiotemporal correlations. *Proceedings of the National Academy of Sciences of the United States of America*, 108(48):19383–8.

González-Rueda, A., Pedrosa, V., Feord, R. C., Clopath, C., and Paulsen, O. (2018). Activity-dependent downscaling of subthreshold synaptic inputs during slow-wave-sleep-like activity in vivo. *Neuron*, 97(6):1244 – 1252.e5.

Gu, Q. (2002). Neuromodulatory transmitter systems in the cortex and their role in cortical plasticity. *Neuroscience*, 111(4):815–835.

Hebb, D. O. (1949). The Organization of Behavior. *The Organization of Behavior*, 911(1):335.

Kilgard, M. P. and Merzenich, M. M. (1998). Cortical Map Reorganization Enabled by Nucleus Basalis Activity. *Science*, 279(5357).

Ma, X. and Suga, N. (2005). Long-term cortical plasticity evoked by electric stimulation and acetylcholine applied to the auditory cortex. *Proceedings of the National Academy of Sciences of the United States of America*, 102(26):9335–40.

Markram, H., Lubke, J., Frotscher, M., and Sakmann, B. (1997). Regulation

of synaptic efficacy by coincidence of postsynaptic APs and EPSPs. *Science*, 275(5297):213–215.

Martins, A. R. O. and Froemke, R. C. (2015). Coordinated forms of noradrenergic plasticity in the locus coeruleus and primary auditory cortex. *Nature neuroscience*, 18(August):1–12.

O'Keefe, J. (1976). Place units in the hippocampus of the freely moving rat. *Experimental Neurology*, 51(1):78–109.

O'Keefe, J. and Dostrovsky, J. (1971). The hippocampus as a spatial map. preliminary evidence from unit activity in the freely-moving rat. *Brain Research*, 34(1):171–175.

O'keefe, J. and Nadel, L. (1978). The hippocampus as a cognitive map.

Pfister, J.-P. and Gerstner, W. (2006). Triplets of spikes in a model of spike timing-dependent plasticity. *The Journal of neuroscience : the official journal of the Society for Neuroscience*, 26(38):9673–82.

Shulz, D. E., Sosnik, R., Ego, V., Haidarliu, S., and Ahissar, E. (2000). A neuronal analogue of state-dependent learning. *Nature*, 403(6769):549–553.

Sjöström, P. J., Rancz, a., Roth, a., and Häusser, M. (2010). Dendritic Excitability and Synaptic Plasticity Dendritic Excitability and Synaptic Plasticity. *Physiological Reviews*, 88(November 2009):1–28.

Vogels, T. P., Sprekeler, H., Zenke, F., Clopath, C., and Gerstner, W. (2011). Inhibitory plasticity balances excitation and inhibition in sensory pathways and memory networks. *Science (New York, N.Y.)*, 334(6062):1569–73.

Wilson, M. A. and McNaughton, B. L. (1993). Dynamics of the hippocampal ensemble code for space. *Science*, 261(5124):1055–1058.

Appendix A

Additional work - Mechanism underlying homeostasis of CA1 spatial representation

Mechanism underlying homeostasis of CA1 spatial representation

Results

Data-driven model of the CA1 network

In our network model, we divide the population of pyramidal cells into groups such that all neurons in each group receive place-tuned input with the same tuning—although with different amplitudes (figure 1A). Pyramidal cells are not recurrently connected, as shown by anatomical studies Deuchars and Thomson [1996]; Thomson and Radpour [1991], but are connected to inhibitory neurons which feed back the excitatory population. Taken together, all the elements described above form a simple yet effective model of the hippocampal CA1 network.

We then test whether this model can reproduce—or postdict—the following experimental findings: During exploration of a familiar environment, if all place cells encoding this environment are silenced, another set of cells (the so-called alternative cells) emerges and their activity spans over the whole environment Trouche et al. [2016]. Additionally, the repeated suppression of the initial place cells leads to the consolidation of the alternative map Trouche et al. [2016].

Lateral inhibition as a mechanism for fast remapping

Trouche et al. Trouche et al. [2016] have shown that optogenetically silencing all place cells active in a familiar environment leads to the emergence of a new set of cells, the so-called alternative cells. This emergence of alternative cells is fast and reversible once the initial (called tagged) cells are allowed to fire again. After several repetitions of this protocol, the alternative set of cells stays active even without

optogenetic manipulation (figure 1B). Therefore, silencing place cells leads to a fast remapping and later consolidation of this alternative map.

We wondered whether our model would be able to account for this fast remapping. To that end, we simulate a network of CA1 neurons composed of 100 excitatory cells randomly connected to 40 inhibitory cells. We split the excitatory cells into groups and each group receives inputs with the same tuning but different amplitudes (figure 1A, see methods). Due to lateral inhibition and input heterogeneity, the network forms a set of active cells and another set of silent cells (figure 1C). As it was done in Trouche et al. Trouche et al. [2016], we tag all the cells that are active during exploration and force those cells to be silent. The silencing of pyramidal cells lowers the input to inhibitory neurons, leading to the release of a set of initially silent cells, named alternative cells (figure 1D-E). Because silent cells receive place-tuned input that overlaps with place field input, the activity of the alternative cells covered the entire track (figure 1D-E). After a few laps, we release the tagged neurons, allowing them to fire again. Since there was not enough time for plasticity to act, the initial map dominates. The initial pyramidal cells drive the lateral inhibition, which in turn suppresses the activity of the alternative cells (figure 1F). Therefore, our model suggests that the fast and reversible remapping is a result of disinhibition of pyramidal cells induced by the decrease in lateral inhibition.

Inhibitory plasticity and network heterogeneity avoids rebound during fast remapping

Trouche et al. Trouche et al. [2016] have shown that optogenetic silencing CA1 place cells in an environment leads to a fast emergence of a new set of alternative place cells. Following place cell silencing, they observed an abrupt increase in alternative neuron activity followed by a slower, seconds-long change towards a stable level Trouche et al. [2016]. We hypothesize that this slower change is due to plasticity in order to

ensure that the overall activity is kept within a target range. Since CA1 interneurons are broadly tuned, local inhibitory plasticity rules might be able to regulate network-wide activity. We therefore test whether an input-dependent inhibitory plasticity rule is responsible for the experimentally observed dynamics. The plasticity rule is such that high inputs onto inhibitory neurons lead to an increase in inhibitory excitability. Conversely, low inputs onto inhibitory neurons lead to a decrease in inhibitory excitability (see methods for details). Importantly, there is no individual target firing rate for excitatory neurons, which is essential for the development of active and silent cells. Therefore, this local, input-dependent inhibitory plasticity rule is consistent with the formation of place and silent cells, and is able to control network-wide activity.

We next investigate whether the implementation of this plasticity rule would lead to a slower increase in alternative neuron firing rate following place cell silencing (light-ON). In order to do that, we implement the inhibitory plasticity rule in a network of interneurons randomly connected to CA1 pyramidal neurons (figure 2A). We run the silencing protocol by silencing all active pyramidal cells. The instantaneous decrease in input to interneurons leads to an abrupt increase in alternative neuron firing rate. This increase is not sufficient to compensate for the reduction in place cell activity. The low network firing rate results in a decrease in interneuron excitability and a further, slower increase in alternative neuron activity (figure 2B). The combination of input-dependent inhibitory plasticity and heterogeneous connections leads to a slow ramp in network activity in light-ON epochs, and a quick return to baseline level in light-OFF epochs, in agreement with experiments. If inhibitory plasticity is not taken into account, the firing rate of alternative neurons increases abruptly and quickly reaches a stable, lower level (figure 2G-H). Furthermore, this inhibitory plasticity acts as a homeostatic mechanism to maintain overall activity when the neuronal network is disturbed (figure 2C).

We then compare a homogeneously connected network with a heterogeneously connected one. In a homogeneously connected network, the input-dependent inhibitory plasticity regulates network-wide connectivity (supplementary figure 2). In a heterogeneously connected network, however, the functional consequences of this rule are not straightforward. In order to investigate this, we simulate a simple network of two pyramidal cells and two interneurons. The interneurons are connected to pyramidal cells such that each interneuron receives inputs from one pyramidal cell and inhibits the other one (supplementary figure 2A). Even for small divergences in feedforward input to pyramidal cells, the inhibitory plasticity amplifies this difference and ensures the development of an active and a silent cell (supplementary figure 2B). Equivalently, in a sparse, randomly connected network, the inhibitory plasticity amplifies the network structure, ensuring the development of place and silent cells. Conversely, in heterogeneously connected networks, tagged cell activity returns to the original level following tagged cell release (when tagged cells stop receiving silencing current), in agreement with experiments. For homogeneously connected networks, however, there is a rebound in the activity of original place cells (supplementary figure 2D-E).

Excitatory plasticity as a mechanism for map consolidation

We next investigate the mechanism underlying the consolidation of the alternative map. In order to do that, we silence the tagged cells for several laps (light-ON). We release the tagged neurons every 10 laps—on testing sessions—to measure the network activity without manipulations (light-OFF, figure3B). As a result of activity-dependent synaptic plasticity, the connections onto alternative cells are strengthened whereas the connections onto tagged cells are weakened. Over testing sessions, the set of active cells gradually shifts from tagged cells to alternative cells (figure 3C), in agreement with Trouche et al. Trouche et al. [2016].

Functional implication: Map-homeostasis

In order to investigate the functional consequences of this plasticity, we quantify the network's decoding efficiency—by measuring the error in position estimation from neuronal activity—in different stages of the simulation (see methods). During the first lap of the silencing protocol (light-ON), the network's decoding efficiency decreases. After several laps of the silencing protocol, however, synaptic plasticity recovers the network decoding efficiency (figure 4). We next apply the place cell suppression protocol on a network with homogeneous excitatory-to-inhibitory (E-I) connections. In heterogeneously connected networks, the suppression of tagged cell activity leads to a decrease in the activity of some interneurons (supplementary figure 1A-B), in agreement with experiments Trouche et al. [2016]. In homogeneously connected networks, however, silencing place cells inevitably leads to a decrease in the activity of every inhibitory neuron. Again, repeated suppression leads to remapping (supplementary figure 1C-G). Therefore, our model suggests that synaptic plasticity of feedforward inputs onto CA1 pyramidal cells, i.e. plasticity of Schaffer collaterals, is a good candidate for the mechanism underlying place map consolidation. Moreover, pyramidal neurons might be heterogeneously connected to interneurons.

In summary, our model indicates that the fast remapping after silencing place cells is due to the release of lateral inhibition. Additionally, the consolidation of the alternative map in our model is promoted by synaptic plasticity of feedforward inputs onto CA1 pyramidal cells. This plasticity recovers the network's decoding efficiency.

Methods

Neuron model

We use a rate-based neuron model where the rate r is determined by

$$\tau_0 \frac{dr}{dt} = -r + \left[\sum_i w_i R_i \right]_+ .$$

where $[\cdot]_+$ denotes a rectification that sets negative values to zero, τ_0 is a time constant, R_i is the firing rate of neuron i in the presynaptic layer, w_i is the synaptic weight from a neuron in the presynaptic layer.

Network structure

In our network simulations, we simulate a network of N_E excitatory neurons and N_I inhibitory neurons. Excitatory neurons are not recurrently connected but are all connected to inhibitory neurons. All excitatory neurons are connected to all inhibitory neurons with the same synaptic strength. The excitatory neurons are divided in N_G groups and each group receives, initially, inputs with the same spatial tuning.

Synaptic plasticity model

The synaptic weights from input neurons onto CA1 neurons are plastic and depends on the activity of the presynaptic neuron r_j and the activity of the postsynaptic neuron as a standard Hebbian term. We include a homeostatic term that takes into account the sum of all synaptic weights onto the postsynaptic neuron. The synaptic weight from input neuron j to the postsynaptic neuron i, w_{ij}, is updated following

$$\frac{dw_{ij}}{dt} = \eta_{ex} r_i r_j - \eta_{homeo} \left(\sum_j w_{ij} - \theta_{homeo} \right) ,$$

where η_{ex} is the learning rate of excitatory connections, η_{homeo} is the learning rate of the homeostatic term, and θ_{homeo} is a target homeostatic constant.

Inhibitory plasticity model

In section , we implement a form of inhibitory plasticity which dependents on the total input current received by each inhibitory neuron. In our implementation, the intrinsic excitability of inhibitory neurons is plastic. However, this implementation is equivalent, in our model, to changing all synaptic connections from each inhibition neuron. The firing rate of each inhibitory neuron, r_i^{inh}, is given by

$$\tau_0 \frac{dr_i^{inh}}{dt} = -r_i^{inh} + \left[\sum_j w_{ij}^{IE} r_j^{ex} - \theta_{inhib} \right]_+ ,$$

where w_{ij}^{EI} is the synaptic weight from excitatory neuron j to inhibitory neuron i, and θ_{inhib} is a threshold that controls the excitability of the inhibitory neuron. This excitability is modulated by the input received by the inhibitory neuron as follows

$$\frac{d\theta_{inhib}}{dt} = -\eta_{in} \left(\theta_{inhib} - \theta_{target} \right) ,$$

and

$$\theta_{target} = A_{inhib} (I_0^{ex} - I^{ex}) ,$$

where η_{th} is the inhibitory learning rate, A_{inhib} is the inhibitory plasticity strength, I_0^{ex} is a constant, and $I^{ex} = \sum_j w_{ij}^{IE} r_j^{ex}$ is the total excitatory input received by the inhibitory neuron.

Position-modulated inputs

The simulated CA1 neurons receive feedforward input from N_{pre} neurons. These input neurons are tuned to specific locations and their firing rates span over the entire

environment. All the place fields of input neurons have the same tuning width, σ_{pre}, and the same amplitude, A_{pre}. We assume that the animal explores an annular track of length L with speed v. The firing rate of an input neuron with place field centered at p_0 is

$$r^{input}(p) = A_{pre} \exp\left(-\frac{d^2}{2\sigma_{pre}^2}\right) , \tag{1}$$

where p is the animal's position, and d is the distance, along the track, between the animal's position and the center of the place field.

Position decoding from network activity

The animal's position was decoded from the network activity using a population vector method. For each neuron i, we assigned a preferred location p_i^0, determined by the neuron's place field peak location. The position of the animal at time t was then estimated as the weighted sum of all neuron's preferred location

$$p^{est}(t) = \frac{\sum_i r_i(t) p_i^0}{\sum r_i(t)} , \tag{2}$$

where $r_i(t)$ is the firing rate of neuron i. The position estimate error was measured as the integral of the distance between the estimated position and the animal's real position.

Parameters and simulations

All simulations were implemented in python and are available at ModelDB. The parameters used in our simulations can be found in table 1

Table 1: Parameters summary

	Name	Value	Description
Neuron Model	τ_0	2.0 ms	Firing rate time constant
	N_{th}	1.0	Threshold for somatic activation
Network Model	N_E	100	Number of excitatory neurons in the network
	N_I	20	Number of inhibitory neurons in the network
	N_G	10	Number of groups of excitatory neurons
Plasticity Model	η_{ex}	5×10^{-4} ms^{-1}	Excitatory plasticity learning rate
	η_{homeo}	5×10^{-5} ms^{-1}	Homeostatic plasticity learning rate
	θ_{homeo}	2.0	Homeostatic target value
	η_{in}	1×10^{-4} ms^{-1}	Inhibitory plasticity learning rate
	I_0^{ex}	8.0	Target excitatory input (for inhibitory plasticity)
	A_{inhib}	1.0	Strength of inhibitory plasticity
	A_{inhib} (S3H)	10.0	Strength of inhibitory plasticity for supp fig 3H
Input	A_{pre}	2.0	Presynaptic place field amplitude
	σ_{pre}	5.0	Presynaptic place field width

References

Deuchars, J. and Thomson, A. M. (1996). Ca1 pyramid-pyramid connections in rat hippocampus in vitro: Dual intracellular recordings with biocytin filling. *Neuroscience*, 74(4):1009–1018.

Thomson, A. M. and Radpour, S. (1991). Excitatory connections between ca1 pyramidal cells revealed by spike triggered averaging in slices of rat hippocampus are partially nmda receptor mediated. *European Journal of Neuroscience*, 3(6):587–601.

Trouche, S., Perestenko, P. V., Ven, G. M. v. d., Bratley, C. T., McNamara, C. G., Campo-Urriza, N., Black, S. L., Reijmers, L. G., and Dupret, D. (2016). Recoding a cocaine-place memory engram to a neutral engram in the hippocampus. *Nature Neuroscience*, 19(4):564–567.

Figure 1. Lateral inhibition as a mechanism for fast remapping (A) Network diagram. Pyramidal neurons (triangles) are split into groups such that neurons in each group receive place-tuned input with the same spatial tuning but different amplitudes. Pyramidal neurons receive feedback inhibition from inhibitory point neurons (circles). Each pyramidal neuron can be active (green triangles) or silent (gray triangles). **(B)** Protocol mimicking Trouche et al. experimental design Trouche et al. [2016]. The animal is allowed to explore a familiar environment and all CA1 pyramidal cells active in that particular environment are tagged. The tagged cells are silenced (light-ON) and an alternative set of cells becomes active. After a few laps, tagged cells are allowed to fire again (light-OFF) and the initial place map is recovered. After many repetitions of this protocol, the alternative set of cells is stabilized and remain active even without optogenetic manipulation. In our simulations, the tagging-and-silencing protocol is implemented by injecting an extra (negative) current onto initial place cells to ensure they are kept silent. **(C)** Neuronal activity as a function of the animal's position for all pyramidal neurons during the first lap of exploration. **(D)** Neuronal activity as a function of the animal's position for all pyramidal neurons following tagged cell silencing. Pyramidal cell activity is weaker and noisier, but covers the whole environment. Note that the neural index is sorted with respect to its field. **(E)** Difference between pyramidal cell activity in (D) and (C).

Figure 2. Inhibitory plasticity and inhibitory homogeneity avoids rebound during fast remapping (A-C) Inhibitory plasticity in heterogeneously connected networks. **(A)** Network diagram. Pyramidal cells (triangles) are randomly connected to inhibitory cells (circles) and those are randomly connected back to pyramidal cells. Some pyramidal cells (green triangles, named tagged cells) are active in the first stage of the simulations. When those cells are silenced, an alternative set of cells (purple triangles) becomes active. The remaining pyramidal cells (gray triangles) are silent over the entire simulation. **(B)** Evolution of tagged (green) and alternative (magenta) cell activity over one silencing protocol under inhibitory plasticity. Lateral inhibition leads to an instantaneous increase in alternative cell activity following tagged cell silencing, whereas inhibitory plasticity leads to a seconds-long adaptation of alternative cell activity. Yellow bar indicates time window in which tagged cells are silenced. **(C)** Average firing rate for all active cells in light-OFF (no external current) and light-ON (tagged cells silencing) epochs. Gray circles indicate individual trials. Black circles indicate average over all 50 trials. **(D-F)** Inhibitory plasticity in uniformly connected networks. **(D)** Network diagram. Pyramidal cells (triangles) are uniformly, bidirectionally connected to inhibitory cells (circles). Some pyramidal cells (green triangles, named tagged cells) are active in the first stage of the simulations. When those cells are silenced, an alternative set of cells (purple triangles) becomes active. The remaining pyramidal cells (gray triangles) are silent over the entire simulation. **(E-F)** Same as in (B)-(C) for a homogeneously connected network. **(G-I)** Network dynamics in a homogeneously connected network without plasticity. **(G)** Network diagram. Pyramidal cells (triangles) are uniformly, bidirectionally connected to inhibitory cells (circles). All connections and neuron excitability are fixed. **(H-I)** Same as in (B)-(C) for a homogeneously connected network without plasticity.

Figure 3. Excitatory plasticity leads to map consolidation **(A)** Simulation timeline. Initially, the animal explores the environment for 70 laps. During lap 70, all active cells are tagged. Following the exploration phase, the following protocol is applied 8 times: 1) tagged cells are silenced for 9 laps through the application of a strong inhibitory current onto tagged cells, 2) tagged cells are released (no extra current) for 1 lap (testing session) and we record the activity of all neurons. **(B)** Tagged cell and alternative cell activity on testing sessions. Total firing rate of tagged (green) and alternative (magenta) cells over testing sessions divided by the initial firing rate of tagged cells. **(C)** Neuronal activity as a function of the animal's position for all pyramidal neurons during the first lap of exploration. **(G)** Neuronal activity as a function of the animal's position for all pyramidal neurons during the final lap of exploration (after plasticity). Pyramidal cell activity covers the whole environment and is stronger after synaptic plasticity. **(E)** Difference between pyramidal cell activity in (F) and (D).

Figure 4. Functional implication: Map homeostasis Position decoding error during initial light-OFF, light-ON and after plasticity. The animal's position was decoded from the network activity using a population vector algorithm (see methods). We used the network activity from the first lap of exploration (light-OFF), the first lap of exploration following tagged cell silencing (light-ON), and the last lap of exploration (after plasticity). $*p < 10^{-185}$, $**p < 10^{-150}$, and $***p < 10^{-34}$ by Student's t test. Error bars indicate SD.

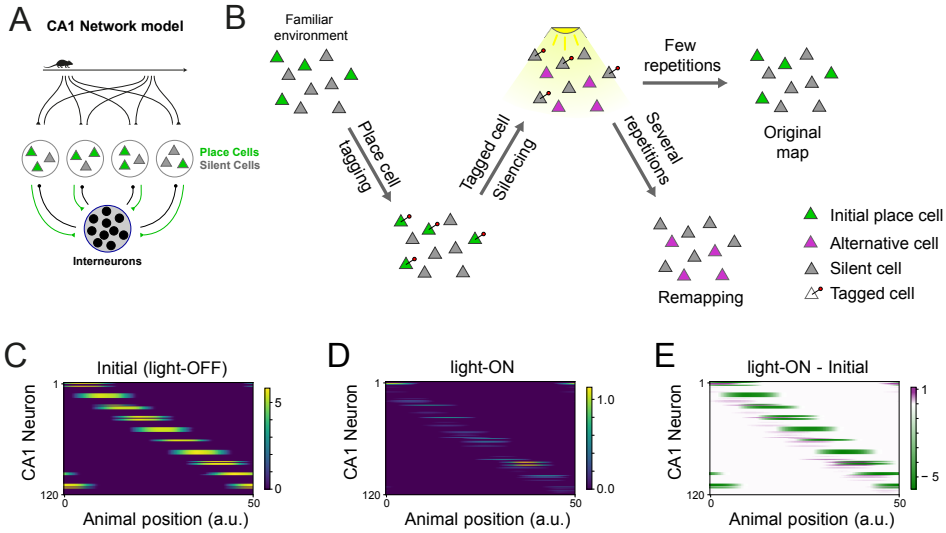
A
CA1 Network model
Place Cells
Silent Cells
Interneurons
B
Familiar environment
Place cell tagging
Tagged cell
Silencing
Few repetitions
Several repetitions
Original map
Remapping
Initial place cell
Alternative cell
Silent cell
Tagged cell
C
Initial (light-OFF)
CA1 Neuron
Animal position (a.u.)
D
light-ON
CA1 Neuron
Animal position (a.u.)
E
light-ON - Initial
CA1 Neuron
Animal position (a.u.)

Figure 1

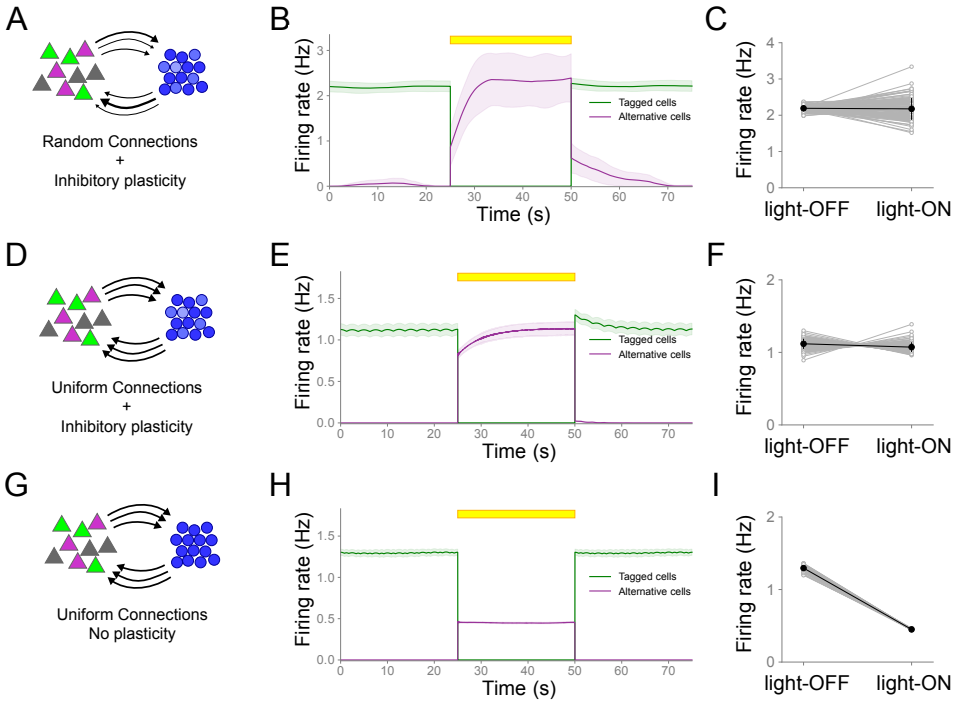
A
Random Connections
+
Inhibitory plasticity
B
Firing rate (Hz)
Time (s)
Tagged cells
Alternative cells
C
Firing rate (Hz)
light-OFF
light-ON
D
Uniform Connections
+
Inhibitory plasticity
E
Firing rate (Hz)
Time (s)
Tagged cells
Alternative cells
F
Firing rate (Hz)
light-OFF
light-ON
G
Uniform Connections
No plasticity
H
Firing rate (Hz)
Time (s)
Tagged cells
Alternative cells
I
Firing rate (Hz)
light-OFF
light-ON

Figure 2

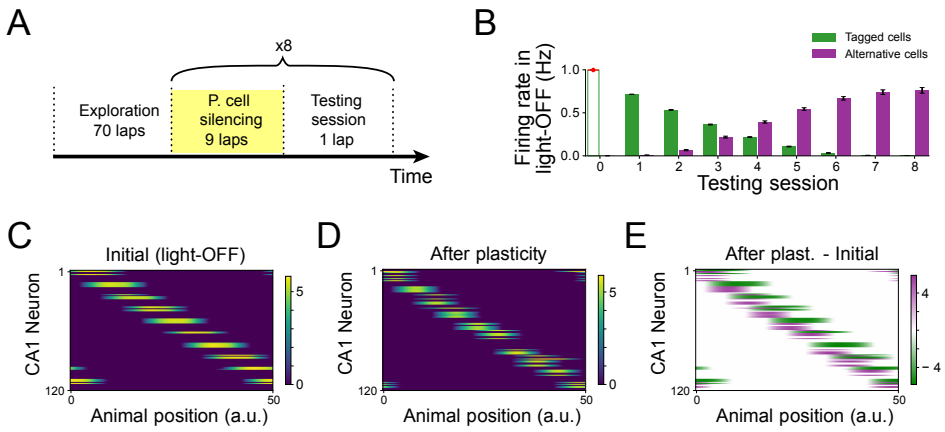
A
x8
Exploration
70 laps
P. cell
silencing
9 laps
Testing
session
1 lap
Time
B
Tagged cells
Alternative cells
Firing rate in
light-OFF (Hz)
1.0
0.5
0.0
0
1
2
3
4
5
6
7
8
Testing session
C
Initial (light-OFF)
CA1 Neuron
1
120
0
50
5
0
Animal position (a.u.)
D
After plasticity
CA1 Neuron
1
120
0
50
5
0
Animal position (a.u.)
E
After plast. - Initial
CA1 Neuron
1
120
0
50
4
−4
Animal position (a.u.)

Figure 3

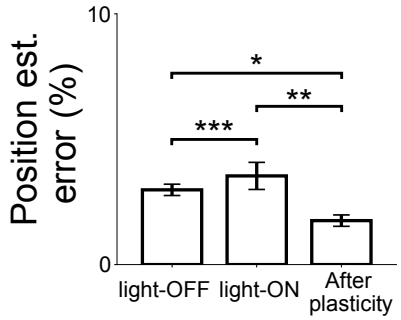

Figure 4

Supplementary Figures

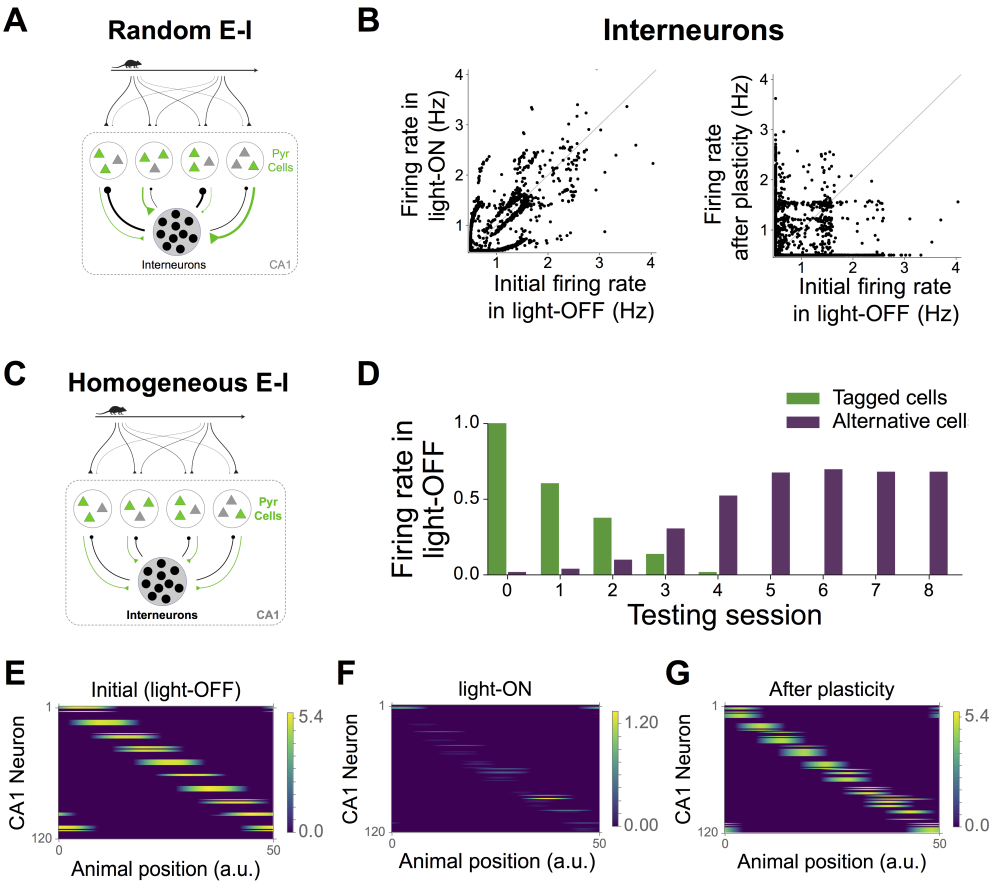

Supplementary Figure 1 (related to figure 3).

Supplementary Figure 1 (related to figure 3). Place cell silencing in uniformly connected networks leads to remapping. **(A)** Network diagram. Pyramidal neurons (triangles) are split into groups such that neurons in each group receive place-tuned input with the same spatial tuning but different amplitudes. Pyramidal neurons receive feedback inhibition from inhibitory point neurons (circles). Each pyramidal neuron can be active (green triangles) or silent (gray triangles). Pyramidal neurons are randomly connected to interneurons. **(B)** Interneuron activity. Left: interneuron firing rate in light-ON (tagged cell silencing) versus initial interneuron firing rate in light-OFF (no silencing). Right: final interneuron firing rate after plasticity versus initial interneuron firing rate in light-OFF. Because of the random E-I connections, some interneuron firing rates increase whereas others decrease, as observed experimentally [Trouche et al., 2016]. **(C)** Network diagram as in A. Pyramidal neurons are uniformly connected to interneurons. **(D)** Tagged cell and alternative cell activity on testing sessions. Total firing rate of tagged (green) and alternative (purple) cells over testing sessions divided by the initial firing rate of tagged cells. **(E)** Neuronal activity as a function of the animal's position for all pyramidal neurons during the first lap of exploration. **(F)** Neuronal activity as a function of the animal's position for all pyramidal neurons following tagged cell silencing. Pyramidal cell activity is weaker and noisier, but cover the whole environment. **(G)** Neuronal activity as a function of the animal's position for all pyramidal neurons during the final lap of exploration (after plasticity). Pyramidal cell activity cover the whole environment and is stronger after synaptic plasticity.

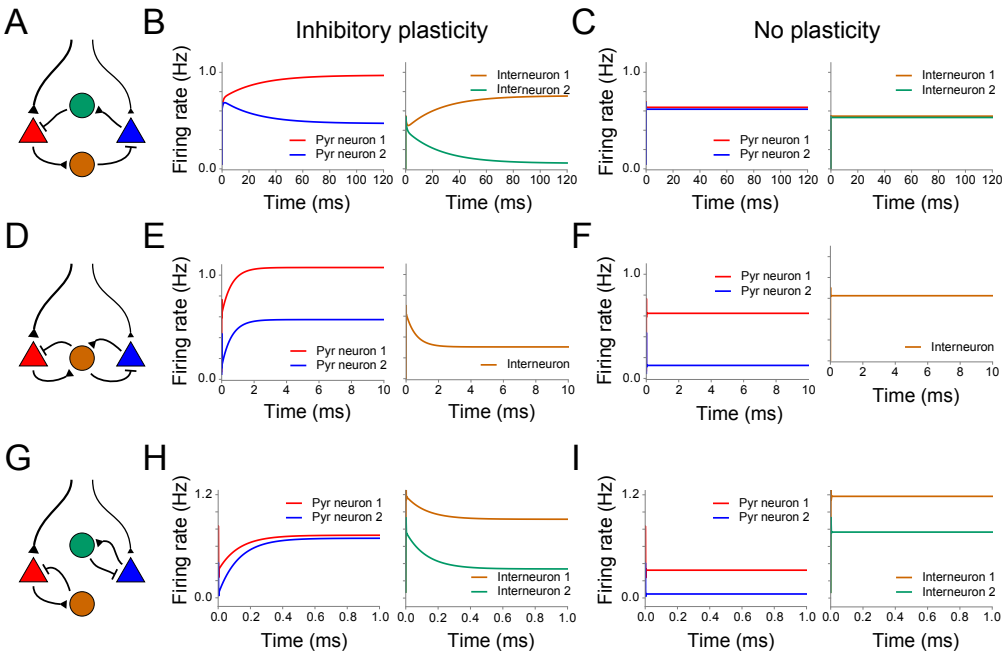

Supplementary Figure 2.

Supplementary Figure 2. Inhibitory plasticity amplifies input heterogeneity in randomly connected networks. (A) Network diagram, two pyramidal cells (triangles) and two interneurons (circles) are simulated. One of the pyramidal cells (red) receives a slightly (1%) stronger feedforward input. One interneuron (orange) receives input from the pyramidal neuron that is more active and projects onto the remaining pyramidal cell. The second interneuron (green) receives input from the less active pyramidal cell and projects onto the more active pyramidal cell. **(B)** Evolution of neuronal firing rates for pyramidal cells (left) and interneurons (right). Interneuron intrinsic excitability is modulated by an input-dependent plasticity rule. The small (1%) difference in feedforward input is amplified by the inhibitory plasticity. **(C)** Evolution of neuronal firing rates for pyramidal cells (left) and interneurons (right). Interneuron intrinsic excitability is fixed (no plasticity). **(D)** Network diagram, two pyramidal cells (triangles) and one interneuron (orange circle) are simulated. One of the pyramidal cells (red) receives 50% stronger feedforward input. The interneuron receives input from both pyramidal neurons and projects back onto both pyramidal neurons. **(E-F)** Same as (B)-(C) for a network as described in (D). The input-dependent inhibitory plasticity regulates the overall network activity. **(G)** Network diagram, two pyramidal cells (triangles) and two interneurons (circles) are simulated. One of the pyramidal cells (red) receives 75% stronger feedforward input. One interneuron (orange) receives input from the pyramidal neuron that is more active and projects back onto the same pyramidal cell. The second interneuron (green) receives input from the less active pyramidal cell and projects back onto the same pyramidal cell. **(H-I)** Same as (B)-(C) for a network as described in (G). The input-dependent inhibitory plasticity regulates the activity locally.

References

[Trouche et al., 2016] Trouche, S., Perestenko, P. V., Ven, G. M. v. d., Bratley, C. T., McNamara, 532 C. G., Campo-Urriza, N., Black, L. S., Reijmers, L. G., and Dupret, D. (2016). Recoding a 533 cocaine-place memory engram to a neutral engram in the hippocampus. Nature Neuroscience, 534 19(4):564–567.